DESIGN, MODELING AND CONTROL OF CONTINUUM ROBOTS FOR MULTI-SCALE MOTION AND OCT-GUIDED MICRO-SURGERY

By

Giuseppe Del Giudice

Dissertation

Submitted to the Faculty of the

Graduate School of Vanderbilt University

in partial fulfillment of the requirements

for the degree of

DOCTOR OF PHILOSOPHY

in

Mechanical Engineering

August 31, 2021

Nashville, Tennessee

Approved:

Nabil Simaan, Ph.D	
Nilanjan Sarkar Ph.D	
Thomas J. Withrow Ph.D	
Jason Mitchell Ph.D	
Karen Joos MD, Ph.D	

To my parents

Angelo and Felicia,

a mio nonno Michele.

ACKNOWLEDGMENTS

I didn't think that this would have been the hardest page to write of this dissertation. I'm struggling to figure out where to start here. It has been a long, beautiful, hard, challenging, unforgettable unique journey in which I have been extremely lucky to have had many people around me that pushed me, motivated me, helped me, loved me, believed in me, and never let me down or left me alone, and without some of these people, I would have never been the person I'm or the engineer I became. Part of this dissertation is dedicated to all of you.

I want to thank my supervisor Professor Nabil Simaan, for being a great mentor, a sincere friend, and a role model for me during these years in the lab. His dedication, his passion for his job and his students, his constant search for excellence in every project in the lab will always be for me font of inspiration. I can't acknowledge enough how thankful I am to him.

A big sincere thanks goes to my colleagues and former colleagues of the ARMA Lab: Colette Abah, Neel Shiora, Andrew Orekhov, Garrison Johnston, Elan Ahronovich, Rashid Yasin, Jared Lawson, Jason Pile, Haoran Yu, Rajarshi Roy, and Aditya Bhowmick.

A special thanks goes to Long Wang and Nima Sarli for putting up with all my questions and messy codes. To all of you, Thanks!!!

I want to thanks all my friends here in the USA and back in Italy for always being with me, motivated me, pushed me, and made these past six years even more unforgettable.

Then there are those friends, that I can't call anything less than brothers, that have always been there no matter what no matter when, always walking with me: Andrea, Philip,

Ben, Nick. To all of you, Thanks!!

The biggest thanks goes to my family and my wife Doris. I get my strength, my motivation from your constant, unconditional love. Thanks for being on my side for all these years supporting me, thanks for your patience when I was at my worst, and thanks for your smiles and laughter and tears of joy when I succeed. This thesis is dedicated to you.

The research reported in this thesis was supported by the NIH under award numbers #1R01EY028133, and #1R21EB015623-01A1 and NSF under award numbers #1537659, and #1734461. The content is solely the responsibility of the author and does not necessarily represent the official views of the funding agencies.

TABLE OF CONTENTS

Page

LIST OF TABLES

LIST OF FIGURES

CHAPTER 1

INTRODUCTION

1.1 Overview of this Dissertation

The applications of Continuum Robots (CRs) in surgery have seen a rapid growth in the last two decades. The design of these robots requires unique electro-mechanical architectures of Actuation Units (AUs) and their End-Effector (EE) that satisfy operational requirements of precision, workspace, and payload capabilities. The ability of these robots to circumvent anatomical obstacles while preserving distal dexterity for surgical manipulation has motivated research on a variety of surgical applications. Examples include trans-oral surgery of the upper airways [2, 3, 4], trans-esophageal surgery [5], trans-nasal surgery [6, 7], frontal sinus exploration [8], single port access surgery [9, 10], transurethral bladder cancer exploration [11] and resection [12], neurosurgery and skull base surgery [13, 14], and orthopedics [15, 16, 17, 18]. Moreover, CRs can navigate deep into human anatomy for surgical intervention showing dexterous motion capabilities in confined spaces for applications involving natural orifice surgery as shown in [19, 20, 21, 22, 23].

Despite the recent rapid growth of research activity on continuum robots for surgery, there are limited number of commercial robotic platforms that use continuum robots. The vast majority use catheters for neurological applications, pulmonology (Monarch Platform by AURIS), and cardiac catheterization ([24, 25]). Unlike the mechanical architecture of most of these systems, a new class of continuum robots called multi-backbone continuum robots (MBCR) was presented in [26, 2]. These robots present challenges that require unique approaches to modeling, control, and design.

In this work, we focus on several critical aspects for successful MBCR use for surgery. The first part of the thesis (chapter 2) presents design considerations for custom actuation units for MBCRs with key considerations of pre-clinical deployability for transurethral bladder tumor resection (TURBT). The second part of the thesis (Chapters 3) focuses on a new class of continuum robots capable of providing multi-scale manipulation. These robots achieve their micro-motion in a unique way by altering their static equilibrium. We, therefore, call this class of robots "continuum robots with equilibrium modulation" and use the acronym CREM to designate them. At the micro-motion scale, these robots present unique challenges in terms of motion tracking, kinematic modeling, and control. These challenges are addressed in chapters 4, 5, 6 respectively. To further extend the investigation of continuum robots design feasible for surgical application, chapter **??** presents preliminary design consideration and testing of a new design for an antagonistic pair actuated continuum robot and its preliminary study on neurological and ophthalmic application

The following sections present the detailed motivation for each one of the areas related to the design embodiment and control of MBCRs and CREM robots. These sections aim to identify the scientific/technical need in each one of the three core areas of this thesis. Figure 1.1 presents the areas of research covered by this work along with the clinical applications motivating these works.

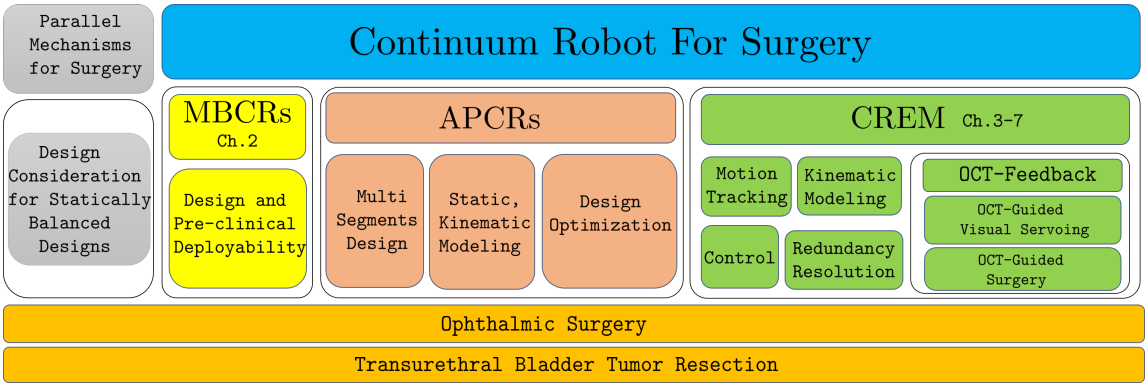

Figure 1.1: Overview of the research areas covered in this dissertation.

1.2 Motivating Clinical/Technical Needs and Contributions of this Work

This work was motivated by observations of challenges and potential for improvement in several surgical domains. These challenges include dexterity enhancement, the design of robots for deep access while considering clinical needs, precision enhancement for microsurgery, and the use of imaging feedback for microsurgery. The following are the three core areas where we identified technical and application needs in robot-assisted surgery:

1.2.1 Design of highly dexterous robots and their actuation mechanisms

In the area of dexterous manipulation in confined spaces, TURBT presents unique challenges discussed in detail in [27, 19]. Although TURBT is a commonly performed procedure, it is still challenging for surgeons. Patients are often required to undergo re-TURs (repeat TURBT) multiple times during their course of treatment due to inaccurate or insufficient resection of the tumorous tissues. Insufficient resections may be due to tool limitations such as lack of intracavitary distal dexterity, ability to precisely control depth of resection, and to optimize in-vivo visualization.

The need for multi-segment highly-dexterous continuum robots arises from access challenges and the need to operate in confined spaces. To date, most catheter systems are limited to one segment or at most two segments that are separated with a large distance (e.g. see [28, 29]). When designing these robots several considerations for actuation unit design need to be simultaneously accounted for when designing the robot itself. Separating these steps may produce a design that requires very expensive actuators due to unrealistic precision and speed requirements. Furthermore, prior works rarely discuss design considerations for pre-clinical deployability within the context of continuum robots. In certain scenarios, detachability of the actuation unit is a strong requirement for successful system deployability. In Chapter 2 we discuss these challenges within the context of TURBT and present the task-based design process of a compact nine degrees of freedom (DoF) actuation

unit (AU) for transurethral resection of bladder tumor (TURBT). This AU has a unique modular architecture allowing partial decoupling of actuation, force, and position sensing in a compact modular format. The derivation of task specifications based on kinematic simulations takes into account workspace, accuracy, and force application capabilities for TURBT. Design considerations for supporting modularity, serviceability, sterilization, and compactness are also presented. Finally, experimental evaluation of performances and animal lab testing are reported. The detailed exposition of the design process serves as a case study that will be helpful for other groups interested in the development and integration of surgical continuum robots.

1.2.2 Challenges of precision and the need for both macro and micro-scale motion

In addition to motion maneuverability in confined spaces, surgical robots often need millimetric-level precision for most clinical applications (e.g. see [30]). The previously mentioned applications typically require a large range of motion and millimeter-level precision. There are, however, a host of potential applications that require a very small micro-motion workspace with micrometer-level precision. Most challenging micro-surgical tasks such as micro-anastomosis and micro-vascular reconstruction (e.g. in hand and plastic surgery) are currently performed with an open surgical approach (e.g. see [31, 32, 33, 34]). Some of the challenges of microsurgery relate to reconciling motion scaling and magnification [35, 36] and lack of force or tactile feedback [37, 38, 39, 40, 41] which are important for micro-vascular reconstruction [42, 43, 44]. In this direction, works on CRs have focused mostly on several architectures reviewed in [45, 46]. The multi-backbone continuum robot (MBCR) architecture is a parallel robot architecture with constrained flexible legs. By extending the length of these legs, these robots can achieve controllable bending. Such robots can obtain a large workspace and high precision approaching the limits of visible motion when operated under normal endoscope visualization. For example, the Insertable Robotic Effector Platform (IREP) [47] has been shown to achieve $\approx 300\mu m$ precision

under telemanipulation and a much higher motion resolution [10]. Other continuum robot architectures such as concentric tube robots [48, 49] can offer large motion. Such robots achieve their motion through changes in the static equilibrium of antagonistic pre-bent tube pairs. Although these robots could theoretically be designed to achieve micro-motion, they are incapable of providing multi-scale motion because macro-scale motion requires a large curvature difference between their antagonistic tube pairs. This requirement is contrary to achieving high-motion resolution for micro-scale motion. Additionally, the increased task completion times (e.g. see [50]) occurring when a large motion scaling factor is used throughout the robot workspace impedes robotic technique adoption since surgical time is associated with increased complications [51, 52] and cost. Furthermore, while the limitation presented by precision and physiological tremor have been addressed with robotic assistance, image-guided diagnosis and intervention have generated better outcomes of surgical procedures and improved surgeon performance. Several applications could benefit from the combination of robots with micromotion capabilities and image feedback modalities. Such applications include micro-surgery, cellular-level surgery, and image-based biopsy which was motivated by the early works of [53] of optical coherence tomography (OCT). The needs of such a system and the potential applications previously mentioned have motivated the investigation (presented in Chapter 3) on the design, modeling, and control of CRs and CRs with multi-scale motion capabilities (defined as macro-motion and micro-motion capabilities).

Most works focusing on multi-scale motion use serial stacking of a micro-motion and a macro-motion robot. Such solutions may be difficult to miniaturize or to design in a manner that respects size, cost, and sterilizability constraints imposed by the surgical scene. For example, miniature parallel robots have been designed for surgical applications [54, 55]. Other systems incorporated parallel mechanisms on top of serial mechanisms for surgery, e.g., [56]. To date, there are no robotic systems capable of offering macro-scale and micro-scale motion capabilities in a form factor that can be easily miniaturized for dexterous

surgical intervention. The main goal of this work is to address this need for robots capable of multi-scale motion in a form factor that respects cost and deployability constraints in surgery. The goal is achieved by offering a new design of MBCRs capable of multi-scale motion. These robots achieve macro-motion in the same way MBCRs do through the direct actuation of their backbones. They achieve micro-motion through modulation of their static equilibrium as explained in Section 3.3.

However, one of the challenges of controlling robots implementing equilibrium modulation is the difficulty in achieving an accurate closed-form solution for their equilibrium pose as a function of the location of the equilibrium modulation joints. This difficulty stems from the lack of a direct functional relationship between input variables and the resulting change in the shape of these robots. This difficulty is further compounded by uncertainty about material properties and friction and a lack of control feedback sensory data at the end-effector level. This work comes as a first step in creating verifiable modeling and control techniques for the system using continuum robots with equilibrium modulation. To achieve this, there is a need for a high-precision motion tracking solution. While commercially existing trackers are suitable for motion resolution on the order of millimeters to meters, there is a sparsity of trackers capable of sensing resolutions below 200 μm. Recent advances in sensor technology have produced new trackers (e.g. Optical 3D measuring system CamBar B1 by AXIOS 3D Services GmbH) capable of 15μm accuracy. With applications of image-based biopsies, there is a need for tracking accuracies of 1-3 μm to obtain very high-resolution images. The needs of tracking such fine motion are addressed in Chapter 4. This chapter focused on offering a solution for visual tracking with sub-micron precision, validating the micro-motion capabilities of these robots.

In this direction, the contribution of this work relative to prior studies is in offering a solution for a continuum robot that can provide multi-scale motion. The work presented in chapter 5 offers new modeling insights that explain the micro-motion of these robots. Specifically, the explanation of the *turning point* phenomenon reported in 4.10.2, which

was observed in the early stage of the project. In addition to explaining this phenomenon using different approaches, detailed kinematic models are depicted to achieve closed-loop control of the multi-backbone CRs.

1.2.3 Image-guided surgery using micro-scale imaging feedback

OCT for image feedback in a robotic system to enable OCT-guided robotics telemanipulation is a fairly new approach and still in its infancy. Besides early works about OCT guidance presented in [57, 58], there are very few examples of OCT integrated into a robotic system like in [59], where a concept of OCT-guided intervention using a parallel robot and a custom B-mode OCT probe was introduced. Other works in this domain include [60, 61, 62] where a hand-held robot was introduced for stabilizing the depth of a needle-based on an integrated A-mode OCT probe. This work was extended in [62] for 3-axis needle tip stabilization using an A-mode OCT probe. Balicki et al. [63] also used depth virtual fixtures using A-mode OCT. OCT-guided needle placement using an external OCT was demonstrated in [64] for deep anterior lamellar keratoplasty.

Despite the progress, to date, there are no works that present a deployable B-mode OCT probe that can be integrated within a continuum robot for enabling micro-motion closed-loop control and in-situ 3D OCT imaging. Chapter 6 demonstrates a system-level integration and validation of volumetric 3D OCT and demonstrates micro-macro motion control with an application of visual servoing OCT-guided injection using CREM robot.

1.2.4 APCR Device for surgical application

With the recent trend in more minimally invasive surgical techniques, the need for very small, very flexible structures that can be used as part of surgical manipulators has increased. Similar previous works have explored flexure-based designs [65] for miniature wrists that can explore small features. Moreover, surgical applications are often requiring high distal dexterity and the ability to deploy extra tool or visualization devices. These

requirements can be satisfied by offering a working channel throughout the device that would allow tool deployability or an extra vision/diagnostic modality such as OCT.

The work presented in chapter 7 discusses the preliminary results of design effort and kinematic modeling of a miniaturized 2 DoF 2 segment antagonistic pair actuated continuum robot (APCR). The design effort and preliminary testing of a task-based experiment within the context of enabling dexterous intravenous navigation for ischemic stroke treatment are presented. Moreover, the preliminary constrained kinematic model for intraocular motion is derived and verified through an intraocular task-based simulation analysis.

1.2.5 Statically balanced parallel mechanism

Balancing parallel robots throughout their workspace while avoiding the use of balancing masses and respecting design practicality constraints is difficult. Medical robotics demands such compact and lightweight designs. It is convenient to consider the difficult task of achieving optimal balancing of a parallel robot throughout a desired task-based dexterous workspace. While it is possible to achieve perfect balancing in a path, only optimal balancing may be achieved without the addition of balancing masses.

The work presented in chapter 8 discusses design considerations of optimal robot base placement and the effects of placement of torsional balancing springs represents a relatively advantageous solution in terms of design simplicity. Using a modal representation for the balancing torque requirements, we use recent results [66] on the design of wire-wrapped cam mechanisms to achieve balancing throughout the workspace.

A simulation study shows that robot base placement can have a detrimental effect on the attainability of a practical design solution for static balancing. Also, we show that optimal balancing using torsional springs is best achieved when all springs are at the actuated joints and that the wire-wrapped cam design can significantly improve the performance of static balancing. The methodology presented provides practical design solutions that

yield simple, lightweight, and compact designs suitable for medical applications where such traits are paramount.

CHAPTER 2

TURBT - CONTINUUM ROBOT ENABLING DEXTEROUS TRANSURETHRAL BLADDER CANCER RESECTION

The following chapter introduces the design and testing of a telemanipulated transurethral robotic system for Transurethral Resection of Bladder Tumors (TURBT). The work presented in this chapter focuses on design considerations for actuation unit of surgical continuum robots. This work has been published in [67]. Other aspects of this work were published in [68, 69, 19] where experimental evaluation of TURBT system was presented.

2.1 Introduction

Bladder cancer is the fourth most common cancer among men in the US, with an estimated 74,000 new cancer diagnoses and 16,000 related deaths predicted for 2015 [1]. Beside few improvement of the instrumentation for transurethral procedures over the past few decades [70, 71, 72]. With the use of new technologies, important progress and significant improvements on the surgical tools are suitable for urology procedure in terms of dexterity, accuracy and repeatability.

Transurethral Resection of Bladder Tumor (TURBT) is the current gold standard for staging and diagnosis of bladder cancers and treatment of non-muscle invasive tumors (NMIBC) but despite recent improvements, TURBT is still characterized by high patient morbidity [73, 74]. Because of the high recurrence rate, Bladder Cancer is the most expensive treatment per patient of all the cancers [75, 76], this is mainly associated with incomplete cancerogenic tissue resection on initial Trans-Urethral Resection [77, 78] or

bladder wall perforations during TURBT [79, 78]. During this procedure, a urologist inserts a rigid device called a resectoscope inside the bladder through the urethra. Diagnosis or treatment is achieved by first locating the tumors on the bladder surface and then resecting them using an electrocautery loop deployed through the resectoscope by moving the loop back and forth through the tumorous tissue and cutting it away. Typically, TURBT is performed using the standard imaging technique, called white light cystoscopy and the visualization is provided through an endoscope rod lens. Although TURBT is a commonly performed procedure, it is still challenging for surgeons and patients are often required to undergo re-TURs (repeat TURBT) multiple times during their course of treatment. Repeat resections are often due to high recurrence rate, multifocality of disease, and insufficient resection to allow for critical disease staging. Insufficient resections may be due to tool limitations such as lack of intracavitary distal dexterity, ability to precisely control depth of resection, and optimize in-vivo visualization. To help overcome these dexterity limitations, this work aims to offer robotic assistance for dexterous surveillance and resection of bladder tumors in a manner currently impossible using instrumented rigid endoscopes.

One key type of snake-like robots is the multi-backbone continuum robot (MBCR) shown in figure 2.3. This design is a variant of previous wire-actuated continuum robot designs such as [80]. For the particular TURBT application, the new design of this robot consists of three segments. Each segment includes one central backbone, three secondary backbones, a base disk, spacer disks and an end disk. In our most recent embodiment, the central backbone is made of a Polytetrafluoroethylene (PTFE) elastomer and the secondary backbones are made of superelastic NiTi tubes. The spacer disks can be made from metallic disks or from a PTFE elastomer as shown in figure 1. The backbones connect only to the end disk and pass through the spacer disks via adequately dimensioned holes to ensure circular bending without significant stress concentration. By pushing or pulling on the secondary backbones, each segment can bend in two degrees of freedom (DoF) controlling the pitch and the yaw of the end disk relative to the base disk. A more detailed description

of the MBCR design are available in [3].

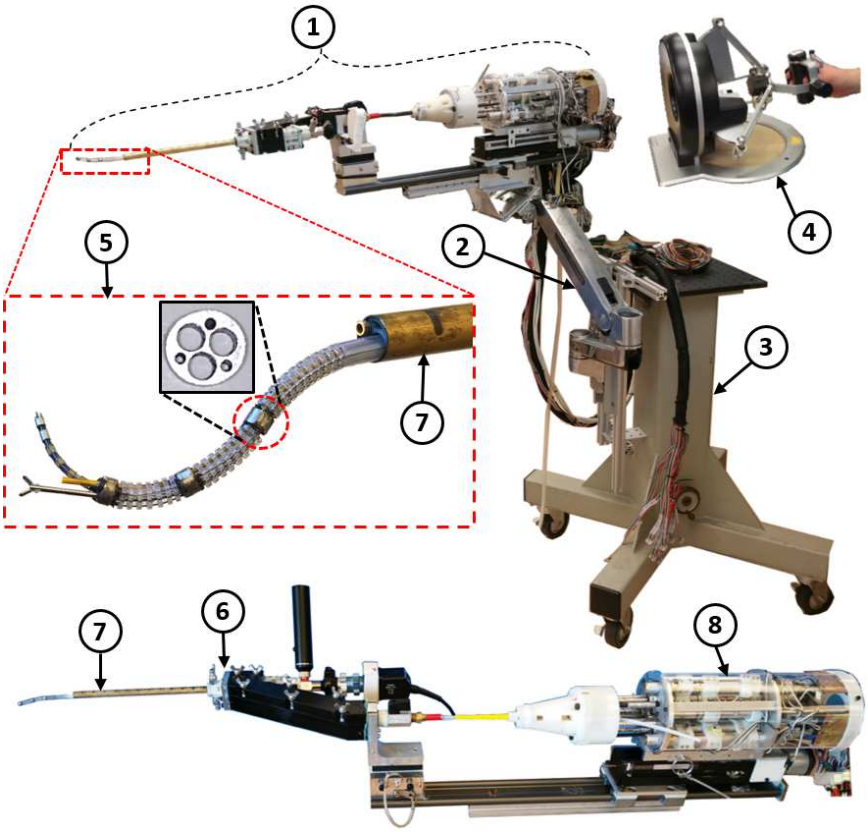

Figure 2.1: TURBot system: (A) Full System, ① TURBot surgical slave, ②Statically balanced arm, ③ Mobile base, ④ Master haptic interface. (B) 3-segment MBCR, ⑤ Spacer/End disk, ⑥ Robot-integrable resectoscope, ⑦ 3mm endoscope. (C) TURBot surgical slave, ⑧ Actuation Unit.

The clinical application motivating the design of the actuation unit presented in this chapter was described in detail in [12] where a proof-of-concept telemanipulation platform, shown if FIgure 2.2 using a two-segment MBCR slave for TURBT was presented. Figure 2.1 shows the current design of a TURBT slave robot arm that has been used in a series of swine studies comparing the accuracy of robotic resection with manual resections. The figure also shows the three-segment continuum robot and its actuation unit. A key component of this system is the robot-integrable resectoscope which was described in detail in [69]. The focus of this chapter will be mainly on the mechanical design of the actuation unit.

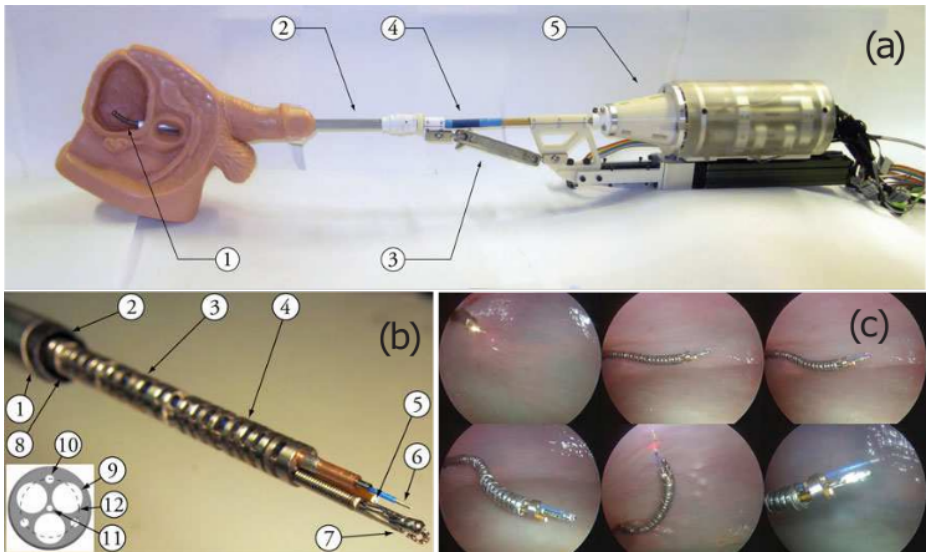

Figure 2.2: (a) Surgical slave of earlier bladder robot deployed into a mockup bladder, (b) Tooling includes fiberscope with light, biopsy cup, ablation laser fiber, (c) The robot operating inside an explanted bovine bladder

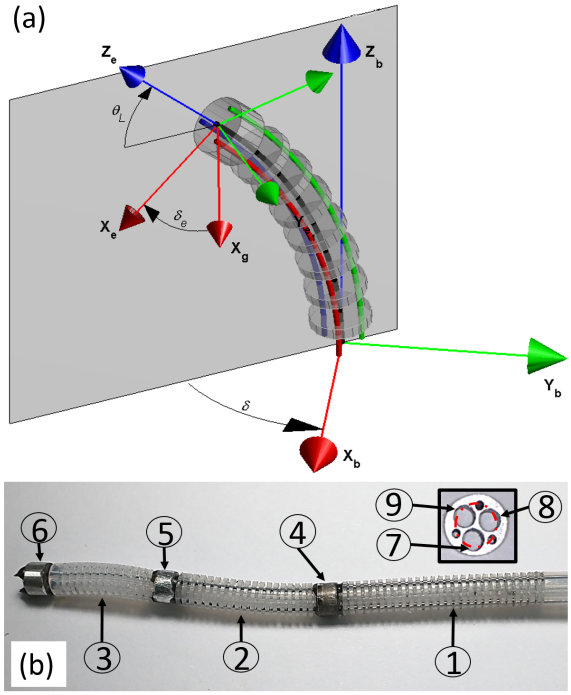

Figure 2.3: (a) A single segment of the continuum robot showing its two configuration variables $\psi = [\theta_L, \delta]^{\mathrm{T}}$, (b) Continuum robot design: ① First segment (26 mm length), ② Second Segment (18 mm length), ③ Third segment (14 mm length), ④⑤⑥ End-disks b)End disk design: ⑦ Tools deployment channel, ⑧ Backbone lumen, ⑨ Pitch circle

The segments of the MBCR are serially stacked to provide six degrees of freedom. The secondary backbones of each segment pass through the corresponding secondary backbones of its preceding segment. With three segments in an MBCR, three groups of three concentric NiTi backbones need to be actuated to control all nine backbones. The use of three secondary backbones to actuate each two-DoF segment improves payload distribution and miniaturization [26] and also provides a fail-safe operation in case one of the backbones fails. The rationale for using concentric deployment of secondary backbones stems from the resulting simplification as a result of actuation decoupling between snake segments. If the backbones are not aligned concentrically, the length of the backbones of the distal segments are not constant when the proximal segments are bent. This complicates the control and potentially degrades the accuracy of the end effector's motion.

The decoupled kinematics of multi-segment MBCR's as a result of concentric placement of secondary backbones poses a challenge in for design of the actuation unit as it demands the actuation of three concentric backbones. Other works on concentric tube robots (often used as steerable needles) have had to tackle this challenge [81, 82] but they typically had less numbers of DoFs. However, MBCR's require many more degrees of actuation due to the use of actuation redundancy. In addition, the surgical application requires compactness, sterilizability, and portability of the actuation unit. These combined challenges require a unique approach to the design of the actuation unit of such MBCR's. Examples of such designs have been presented in an ad-hoc manner in [3, 12] for MBCR's with two segments. This chapter aims to provide the rationale and the design considerations for such actuation units in a level of detail that has not been previously presented.

2.2 Previous system limitations

As mentioned above, the TURBoT system naturally derived form Goldman's system reported in [12] which was the only robot designed for TURBT procedure. Goldman's system however lacked in very important aspects required for a preclinically/clinically

deployable system, which leads to define areas of needed improvements. The original robotic system was lacking on a collaborative telemanipulation mode oriented in the image frame which would help the surgeon to navigate into the anatomy. On the same line, the imaging capabilities provided were not sufficient as it only uses a 10k-resolution fiberscope deployed in a working channel so, the new system should offer better imaging quality and modules than the single 10K-resolution fiberscope previously used. Moreover, the confined space anatomy requires increase dexterity with at least 7 Dof of movement within the bladder and it should allow independent control of ablation/resection instrument from the main MBCR to furthermore improve dexterity. Addressing these limitations guided the development of TURBot. The eventual goal of this system is to offer surgeons for the first time a system that can ensure full surveillance coverage, provide accurate dissection and enable en-block resection.

2.3 Design requirements

The design of the actuation unit started with consideration of conceptual attribute requirements and task specifications followed with a methodical derivation of joint-level design requirements. The conceptual attribute requirements guided the design architecture of the actuation unit as described in section 2.3.1 while the task specification requirements guided the detailed design and component selection for each joint as described in section 2.5.

2.3.1 Attribute requirements and task specifications

The following attribute requirements guided the conceptual design of our actuation unit.

1. *Portability and compactness* of the actuation unit. This requirement is due to the fact that this actuation unit needs to be manipulated by the surgeon in initial stages of system deployment hence the actuation unit needs to be as compact and the least

obtrusive as possible.

2. *Sterilizability* which requires that lumens that come into contact with the patient can be sterilized and other parts that do not come into direct contact with the patient can be covered with sterile draping while maintaining a sterile and open conduit for deployment of the *interventional functions* listed below.

3. *Modularity* in order to facilitate assembly, part interchangeability and for cost reduction.

4. *Separability of actuation* to allow easy disassembly of the actuation unit from the continuum robot and to ensure that the continuum robot can be serviced without having to disassemble the entire actuation unit, thereby avoiding the loss of prior calibration of the actuators.

5. *Robustness to sensory error* is required in order to ensure safety of robot operation in case one of the position sensors (motor encoders) malfunctions.

In addition to the above attribute requirements, the following *task specifications* are required by the surgical application of TURBT:

1. *Multi-functionality* of the robot requires it to support of manipulation, biopsy, ablation, suction and visualization. To achieve these functions, the continuum robot was designed to provide three working lumens as depicted first in [12].

2. *Force sensing* is required to facilitate trans-urethral deployment using complaint motion control as in [83] and sensing and control of interaction forces as in [84, 85]. The actuation unit is hence designed to accommodate load cells on each backbone of the robot.

3. *Intra-vesicular dexterity* is needed to support six degrees of freedom motion and coverage of the bladder volume. This requirement motivated the need for a snake-like robot having at least three segments since each segment provides two degrees of

freedom. Consequently, the actuation unit needs to have at least nine actuators since each segment of the continuum robot uses three actuated backbones to bend it using push-pull actuation.

4. *Precision of motion* is required to ensure high precision of ablation during TURBT. We have chosen $0.1mm$ as the target motion accuracy. There is no known quantification of resection accuracy in the literature so we have conservatively chosen $0.1mm$ since it is significantly better than the expected tip precision when manually manipulating a resectoscope having a length of in excess of 250 mm.

5. *Motion responsiveness* is needed to provide the surgeon the ability to move the snake robot with the necessary bending rate. Based on consultation with our clinician authors, we determined a bending rate of $\pm 90^{\circ}$ within 1 seconds as the desired maximal bending rate for each segment.

6. *Force interaction* was specified as a desirable functionality to support the ability of the robot's gripper to pull on mucosa during laser-aided resection. Although during normal cautery and laser resection the forces are minimal, we have conservatively specified a desired force application capability of 1 newton at the tip of the robot.

2.3.2 Derivation of Joint-Level Design Requirements

The kinematics of MBCR was addressed previously by [2, 86, 80]. The configuration of each segment is represented by $\psi_i = [\theta_{iL}, \delta_i]^T$, where $i = 1,2,3$ is the segment number, θ_{iL} is the bending angle and δ_i is the bending plane angle as shown in Figure 2.3. The kinematic relation between configuration space and joint space is

$$\begin{aligned} q_{1j} &= rcos(\delta_{1j})(\theta_{1L} - \theta_0), \\ q_{2j} &= rcos(\delta_{2j})(\theta_{2L} - \theta_0), \\ q_{3j} - q_{2j} &= rcos(\delta_{3j})(\theta_{3L} - \theta_0), \end{aligned} \tag{2.1}$$

where $j = 1,2,3$ is the secondary backbone number, q_{ij} is the j joint variable of the segment i ($\boldsymbol{q}_i = [q_{i1}, q_{i2}, q_{i3}]^T$) and $r = 1.725mm$ is the radius of the pitch circle determining the positions of the secondary backbones in the snake disks (See Figure 2.3).

To meet the motion responsiveness design requirement, i.e. bending rate of $\pm 90^\circ$ within 1 second (section 2.2), each segment actuators are required to provide maximal speeds of $4.7mm/sec, 4.7mm/sec$ and $9.4mm/sec$ respectively. These values are obtained by substitution in equation (2.1).

In order to satisfy the prescribed motion accuracy of $0.1mm$, the instantaneous Jacobian relating the configuration space and the joint space should be determined. Three vector spaces are involved in this process, namely task space, configuration space and joint space. These spaces are related by the Jacobians $\mathbf{J}_{x_c\psi}$ and $\mathbf{J}_{q\psi}$ such that

$$\mathbf{J}_{x_c\psi}\Delta\boldsymbol{\psi} = \Delta\mathbf{x_c}, \qquad \mathbf{J}_{q\psi}\Delta\boldsymbol{\psi} = \Delta\mathbf{q} \tag{2.2}$$

where $\mathbf{q} \in \mathbb{R}^{9\times 1} = [\boldsymbol{q}_1, \boldsymbol{q}_2, \boldsymbol{q}_3]^T, \boldsymbol{\psi} \in \mathbb{R}^{6\times 1} = [\boldsymbol{\psi}_1, \boldsymbol{\psi}_2, \boldsymbol{\psi}_3]^T, \mathbf{x}_c \in \mathbb{R}^{3\times 1}$ are joint-space, configuration-space and Cartesian-space vectors respectively. Derivation of the Jacobians is not mentioned here for brevity and the reader is referred to [3, 87] for a thorough discussion. Note that the formulations did not involve the base translation of the robot.
From equation (2.2) we obtain:

$$\Delta\boldsymbol{\psi} = \mathbf{J}^{\dagger}_{q\psi}\Delta\mathbf{q} \tag{2.3}$$

where $\mathbf{J}^{\dagger}_{q\psi}$ is Moore-Penrose pseudo-inverse of $\mathbf{J}_{q\psi}$ as determined by the following equation:

$$\mathbf{J}^{\dagger}_{q\psi} = (\mathbf{J}^{t}_{q\psi}\mathbf{J}_{q\psi} + \varepsilon\mathbf{I}_6)^{-1}\mathbf{J}^{t}_{q\psi} \tag{2.4}$$

ε term is added to regularize singular configurations and $\mathbf{I}_6 \in \mathbb{R}^{6\times 6}$ is the identity matrix. Substitution of equation (2.3) in (2.2) yields:

$$\mathbf{J}_{x_c q}\Delta\mathbf{q} = \Delta\mathbf{x}_c \tag{2.5}$$

where $\mathbf{J}_{x_c q} \triangleq \mathbf{J}_{x_c \psi} \mathbf{J}_{q\psi}^{\dagger} \in \mathbb{R}^{3\times 9}$.

Equation (2.5) can be used to determine the maximal tolerable joint space error vector to guarantee a task-space motion error having norm of of less than 0.1 mm in a specified configuration ψ. Figure 2.4 shows the contour plots of the reciprocal of the individual joint motion accuracy to impart a 0.1 mm motion in three world coordinate unit directions $\mathbf{e}_i, \mathbf{e}_j, \mathbf{e}_k$. The values of the reciprocals are represented for $\theta_{3L} = 0°, 45°, 90°$. The horizontal and vertical axes are θ_{1L} and θ_{2L} respectively. Note that δ_i's do not affect the joint motion norm significantly, therefore they are assumed as zero. The minimum joint motion is 0.0037,0.0014 and 0.0015 mm for $\Delta\mathbf{x}_c = 0.1\mathbf{e}_i$, $\Delta\mathbf{x}_c = 0.1\mathbf{e}_j$ and $\Delta\mathbf{x}_c = 0.1\mathbf{e}_k$ respectively.

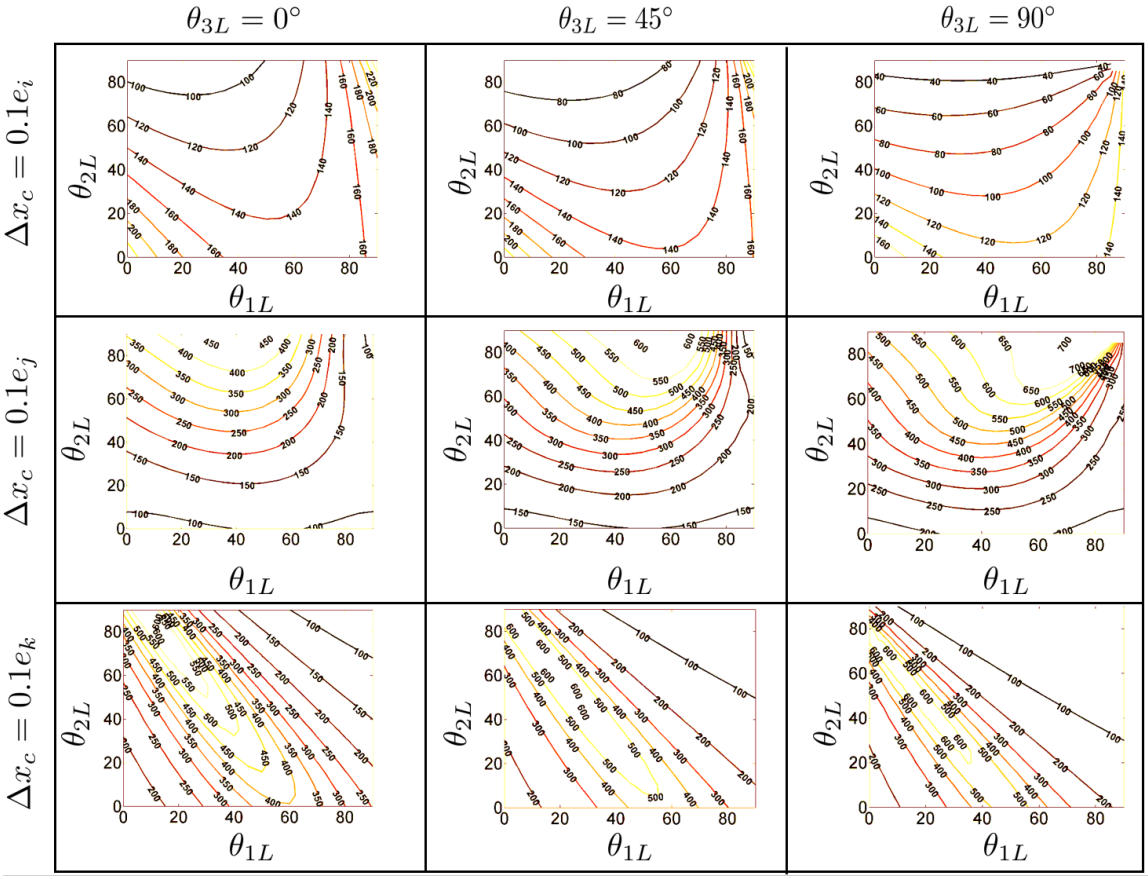

Figure 2.4: Contour plots of $\frac{1}{\|\Delta q_i\|}$ versus θ_{1L}(horizontal axis) and θ_{2L} (vertical axis) for $\delta_1 = \delta_2 = \delta_3 = 0$, $\theta_{3L} = 0°, 45°, 90°$, $\Delta\mathbf{x}_c = 0.1\mathbf{e}_i, 0.1\mathbf{e}_j, 0.1\mathbf{e}_k$

In order to determine the minimum required joint motion for all possible $\Delta\mathbf{x}_c$ directions, we consider equation (2.5) again. Using singular value decomposition and matrix algebraic

manipulations, it can be proved that

$$\|\Delta \mathbf{q}\| \geq \frac{\|\Delta \mathbf{x}_c\|}{\overline{\sigma}(\mathbf{J}_{x_c q})} \tag{2.6}$$

where $\|.\|$ and $\overline{\sigma}(.)$ represent Euclidean norm and maximum singular value respectively. Therefore,

$$\|\Delta \mathbf{q}\|_{min} = \frac{\|\Delta \mathbf{x}\|}{\max\limits_{\mathbb{Q}} \overline{\sigma}(\mathbf{J}_{x_c q})} \tag{2.7}$$

where $\mathbb{Q}$ denotes the the entire robot configuration space.

Equation (2.7) determines the required joint-level motion accuracy to meet a demanded positional accuracy. The robot configuration space was discretized and the maximum singular value was computed numerically at each configuration. The maximum value among the maximum singular values was determined. Using a 0.1 mm task-space accuracy and $\varepsilon = 10^{-7}$, the required joint-level motion accuracy was calculated as 0.0013 mm.

The first three columns of Table 2.1 summarize the simulation results using the task specifications of motion responsiveness as specified in section 2.3.1. The last column summarizes the simulation results for actuator torques using the interaction force task specification while considering particulars of the actuation unit architecture. At the outset, static simulations using the statics model in [26] were used to determine the required actuator forces for a three segment continuum robot having backbones as in [12], but with additional consideration for flexural rigidity of deployable tools such as a fiberscope and a flexible gripper. The simulations resulted in joint force requirements that ranged from 55 N to 30 N when considering all segments. Taking into account the design architecture of the actuation unit where the actuator of the first segment carries the actuators of the other segments, we have conservatively set the required joint force of the first segment actuator to 150N.

Table 2.1: Required joint-level specifications and the corresponding requisite gearmotor torques

Segment #	Joint stroke required	Min. joint -level position resolution	Max joint speed	Max joint force
1	4.7 mm	0.0013 mm	4.7 mm/s	150 N
2	4.7 mm	0.0013 mm	4.7 mm/s	30 N
3	9.4 mm	0.0013 mm	9.4 mm/s	30 N

2.4 Actuation Unit Architecture

2.4.1 Key actuation unit modules

The continuum robot is actuated by a compact, modular and portable 9-DoF *actuation unit* described in detail in Figure 2.5. Referring to Figure 2.5.A, the actuation unit ① connects to the continuum robot backbones using a *detachable actuation interface* ②. The backbones are routed from the detachable actuation interface to the continuum robot through an *actuation cone* ③. The detachable actuation interface provides the conceptual attribute of separability of actuation and supports sterilizability since all the actuation unit components can be contained in a sterile draping while keeping the continuum robot, cone and actuation interface as a contained assembly which has to undergo sterilization.

To satisfy the conceptual attribute of modularity, and compactness, the core of the actuation unit was designed based on three identical *backbone actuation modules* (100), (200), (300). Each sub-assembly has three *cylinders* (101) (102) (103) designated for actuating the first, second and third segments of the continuum robot. The three sub-assemblies are held in place between the *front plate* ④ and *rear plate* ⑥. The structural stiffness of the actuation unit is provided by three structural elements, two *Aluminum beams* ⑨ on the sides and the *attachment base plate* ⑤ on the bottom. When these three elements are connected to the front plate and the rear plate they form the chassis of the actuation unit. Moreover, the attachment base plate connects the slave robot to the insertion stage mounted on an adjustable passive arm shown in Figure 2.1.

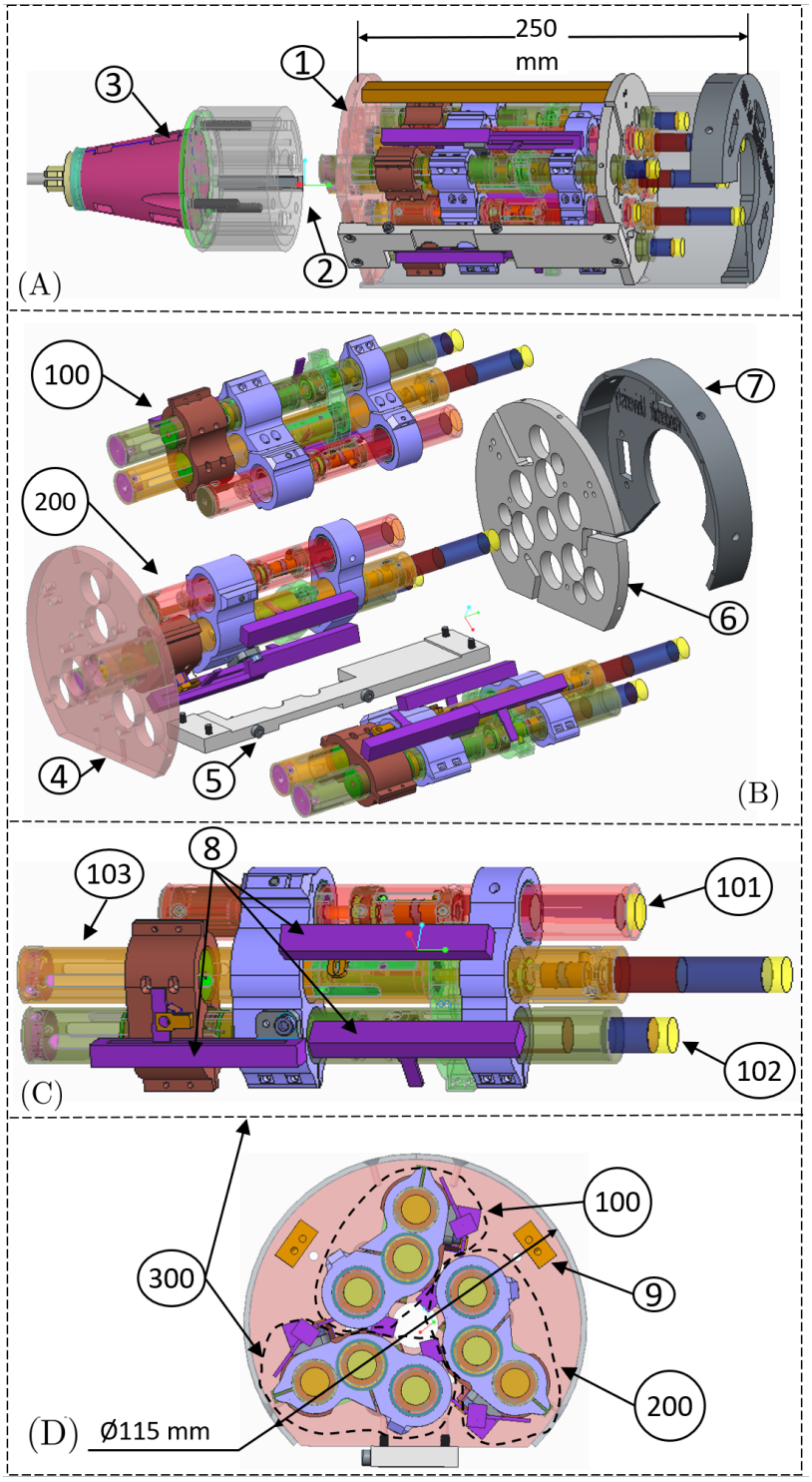

Figure 2.5: Actuation Unit Exploded view: (A) Assembly showing the actuation unit ①, the detachable actuation interface ②, and the actuation cone ③; (B) Exploded view showing the three backbone actuation modules (100)(200)(300), (C) bottom view showing axial symmetry, (D) backbone actuation module assembly

The conceptual attribute of robustness to sensory error is satisfied by concurrent use of encoder and potentiometer feedback. Figure 2.5.C shows the potentiometers ⑧ (Panasonic EWA-P10C15A14). These potentiometers also facilitate fast startup time since they provide absolute position feedback while the incremental magnetic encoders are used for high precision real-time control feedback. A significant discrepancy of feedback based on potentiometers and encoders is used to flag an erroneous feedback condition, which triggers a system halt or warning signal based on preference of the user.

2.4.2 Backbone Actuation Modules

The cross-sectional view in Figure 2.6 illustrates the internal structure of the first cylinders (101) and (103) also shown in Figure 2.5. The cylinders are equipped with selected motors combinations (18) (20) shown in Table 2.2. They are secured in place using custom made internal collars (22) (19) that rigidly connect the motor to the cylinder. The motors drive pistons (14) (29) (26) using internal lead screws (10). To compensate eventual small axis misalignment, an Oldham coupling (23) is used to connect the motor shaft and the lead screw. Moreover, the lead screws are also supported by ball bearings (25) held in place using custom-made collars (24) (11). Each piston contains two plastic nuts (28) that could be tightened on the respective lead screws with respect to another in order to remove the backlash between the lead screw and the piston.

The first cylinder is rigidly attached to the front plate by a dummy spacer (12)) (It can later be replaced by a load cell HONEYWELL Model 31 to measure backbones forces, as well the dummy spacer (15) can be replace with a load cell HONEYWELL Model 11) and is connected to the second and third cylinder using two connection frames (21) (27). The connection frames are clamped on the outer surface of the second and third cylinder and are free to slide on the first cylinder. The second connection frame (27) is also rigidly connected to the first cylinder piston trough a press-fit pin that ensures motion transmission. This motion of the first cylinder drives the backbone of the first segment of the continuum robot.

Table 2.2: Motor Combinations

First Cylinder			
Motor Combination	Gearhead	Motor	Encoder
Maxon Motor 324553	GP13A 110314 (Series 17:1 3249/196 16.57653061:1 ratio)	Maxon Motor RE13 118638	MR 241062, 256 CPT
Second and Third Cylinder			
MICROMO 1331T006SRIE2-400+14/1 14:1+X0437	14/1 14:1 (Series 14/1 676/49 13.795918:1 ratio)	MICROMO 1331T006SRIE2	X0437 magnetic Encoder digital outputs, 2 channels, 400 lines per revolution

The cross-sectional view in Figure 2.7 shows the internal structure of the second cylinder (102) and the third cylinder (103). The second piston is also equipped with the same motor combination (18), main piston, lead screw, collars and bearings of the previous cross section description. Moreover, there are two secondary pistons in these two cylinders. The *secondary driving cylinder* (32) is rigidly connected to the primary piston by an aluminum dummy spacer (15). The *secondary driven piston* (17) is free to slide in the third cylinder. A *bridge connector* (30) slides to the outer surface of the second and the third cylinder and is rigidly connected to the secondary pistons using shoulder screws. This entire design allows driving three concentric backbones. The first segment backbone is held by the custom-made holder (13), the second segment backbone is carried by the secondary driven piston (17) while the inner most backbone that drives the first segment is held by the custom-made gripper (16).

2.5 Component Selection

Tables 2.3 and 2.4 summarize the specifications and expected performance of the gear-motors combined with lead screws for driving the backbones of each segment. To arrive at the choice of gear-motors and screws a Matlab code was written to parse the specifications

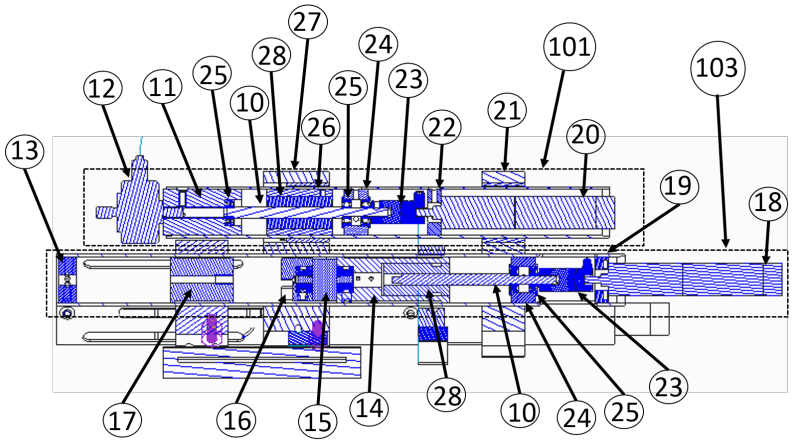

Figure 2.6: Cross section of the main cylinder and the third cylinder

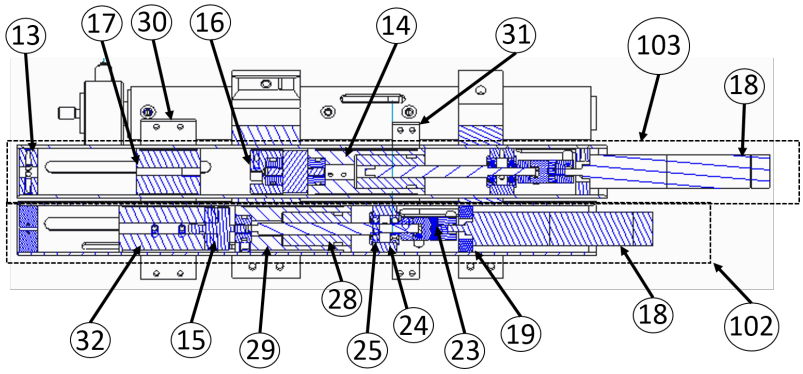

Figure 2.7: Cross section of the second cylinder and the third cylinder

Table 2.3: Motor combination design requirement

	Output gear torque		Power for maximal speed	
	Required	Provided	Required	Provided
Maxon motor	36.206 Nmm	39.28 Nmm	2.205 W	3 W
Micromo	9.320 Nmm	15.411 Nmm	2.711 W	3.11 W

Table 2.4: Motor combination design requirement

	Power for nominal speed		Max linear speed		Lead screw pitch
	Required	Provided	Required	Provided	
Maxon motor	2.115 W	2.37 W	4.7 mm/s	4.899 mm/s	0.60911 mm/turn
Micromo	0.688 W	1.003 W	9.4 mm/s	10.417 mm/s	0.60911 mm/turn

of available lead screws and motors that fit the cylinders. To obtain a first order estimate of the power requirements of the actuators were calculated based on task specification assuming gearhead efficiency of 80% and lead screw efficiency of 70%. Once a list of motors that satisfies the power requirements was made, the Matlab code was used to cull the list down to motor and screw combinations that can satisfy force and speed requirements.

The required torque to raise/lower the piston against/along the direction of an external loaf F is calculated as:

$$\tau_{r,l} = \frac{F dp}{2} \tan(\gamma \pm \lambda) + F \frac{dp_b}{2} \mu_{roll} b \tag{2.8}$$

where subscript r is for raising and l is for lowering a load. The first part accounts for friction between the screw and nut and the second part accounts for friction in the bearings supporting the lead screw. The lead screw friction angle γ is a function of screw geometry and friction coefficient between the screw and nut. The lead angle λ is a function of the screw pitch diameter d_p and lead L. Details of calculation of these angles can be found in [88].

2.5.1 Continuum robot actuation interface

2.5.1.1 Detachable actuation interface

A new feature introduced in this design allows to detach the actuation unit from the cone easily and quickly. The most important aspect of this new feature is that it allows to detach the front part of the system without acting at all on the actuation unit. The actuation unit will be totally preserved from re-calibration requirement or mechanical issues coming from a repetitive disassembling process. The concept is based on a concentric system of quick connectors shown in Figure 2.9.

Referring to Figure 2.9, the tubes ①, ②, ③ are placed inside each other and connected to their respective quick connectors by shear pins. The aluminum tubes on the actuation unit side are connected to their respective joint actuators using set-screws and metal glue, on the cone side, each brass tube is glued to each relative NiTinol backbone using custom-made aluminum adapters ④.

In case of a failure of the backbones, this new design allows an easy and quick replacement of the front part of the robot. A total time of 10 minutes (2 mins in average for disassembly of the front part and 8 minutes in average for re-assembly) is needed to replace the entire continuum robot and connect a new one to the actuation unit.

2.5.1.2 Actuation cone

The central part of the actuation cone called cone, is a rapid-prototyped part that routes the backbones inside the continuum robot tube. There are three channels inside the cone that curve smoothly converging into the stem. Along the central axis of the cone, there is a channel that drives the tools coming from the back of the actuation unit into the stem.

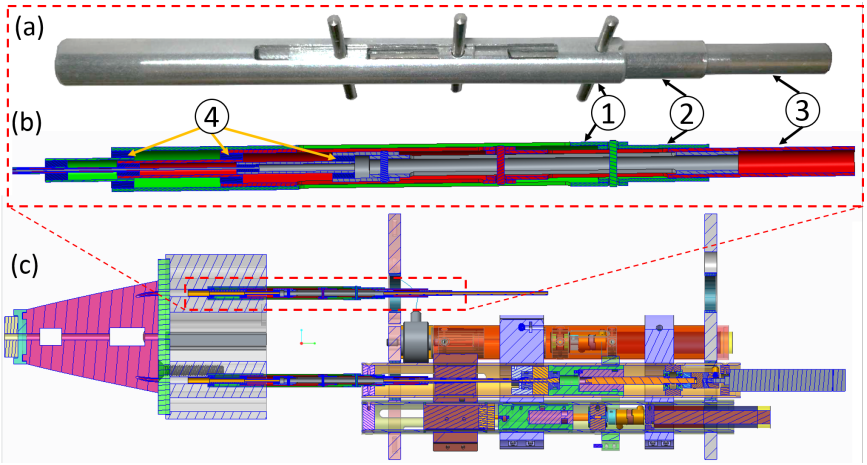

Figure 2.8: (a)Custom made detachable actuation interface, (b) Cross Section, (c) Actuation unit and the cone connection trough the detachable actuation interface

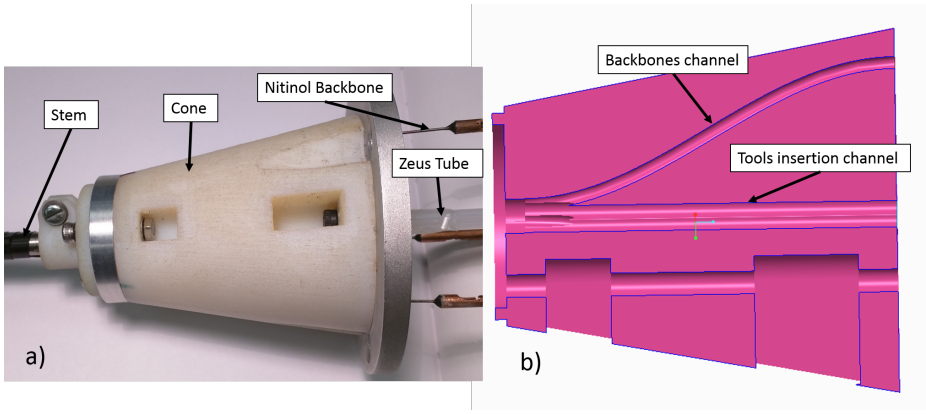

Figure 2.9: Actuation cone: (a) assembly, (b) cross section

2.6 Distal Microsnake

To increase distal dexterity inside the bladder and to be able to operate an ablating laser fiber independently from the main continuum robot, we deployed a 1.6*mm* in diameter, 2 DoF, single segment continuum robot (Figure 2.10.A) through one of the 3 lumens of the TURBT continuum segment. This section presents the design and system integration of the single segment snake-like robot used in the TURBT system.

2.6.1 Actuation unit and continuum segment

Figure 2.10.B shows the TURBT system (semi-transparent) with the distal microsnake actuation unit integrated on the main system, and the distal microsnake continuum segment deployed through one of the lumens of the 3 segments snake-like robot. The close up view in Figure 2.10.C shows an *Holmium Laser fiber* ① carried by the *distal microsnake continuum segment* ② and in turn deployed through the TURBT 3 segment continuum robot ③.

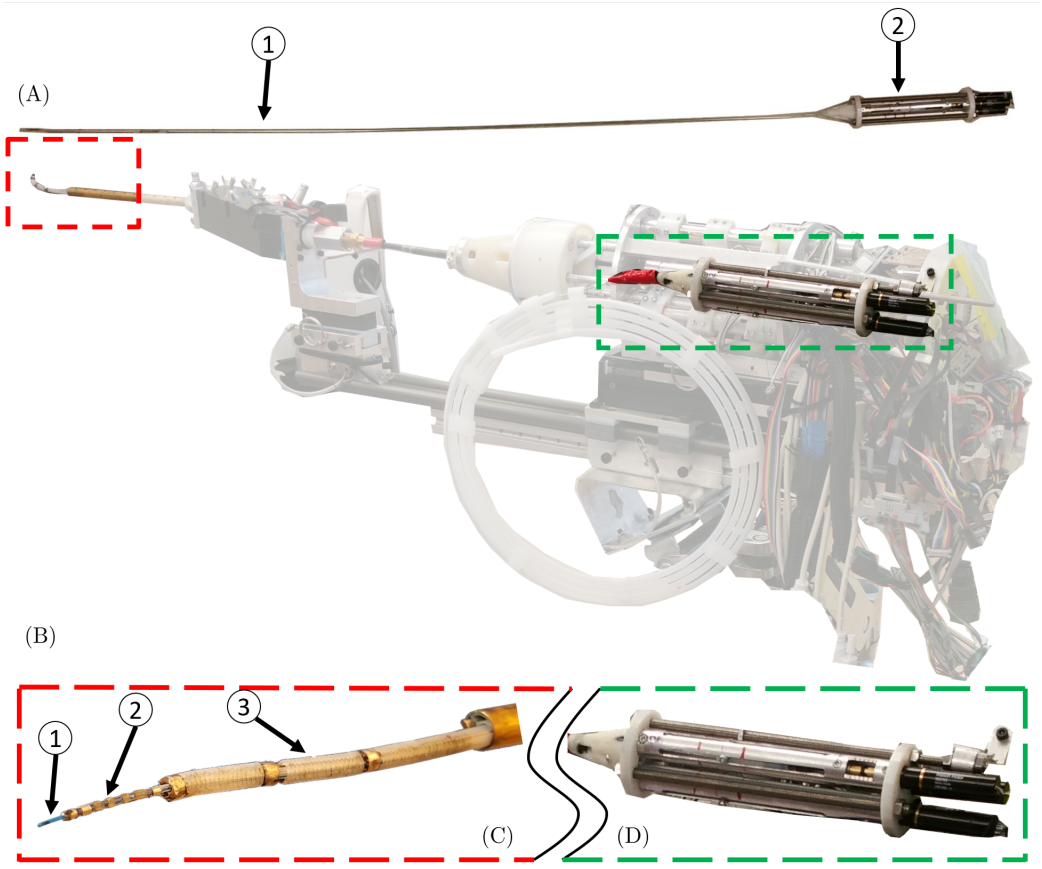

Figure 2.10: Distal Microsnake system integration: (A) Distal Microsnake: ① Continuum segment ② Actuation unit. (B) TURBT system(semi-transparent) with embedded distal microsnake actuation unit and the distal microsnake continuum segment deployed. (C) Continuum Segment close up view: ① Holmium Laser ② Distal Microsnake ③ TURBT 3 segment continuum robot (D) Distal microsnake actuation unit

The distal multibackbones continuum segment (Figure 2.11.A) has 3 NiTi backbones (0.22 mm in diameter) that are rigidly attached to an *End-disk* ①. The backbones are then

routed through 5 *intermediate disks* ③ that are equally spaced by 6 *spacer disks* ② and a *base disk* ④, forming a single continuum segment of 22 mm in length.

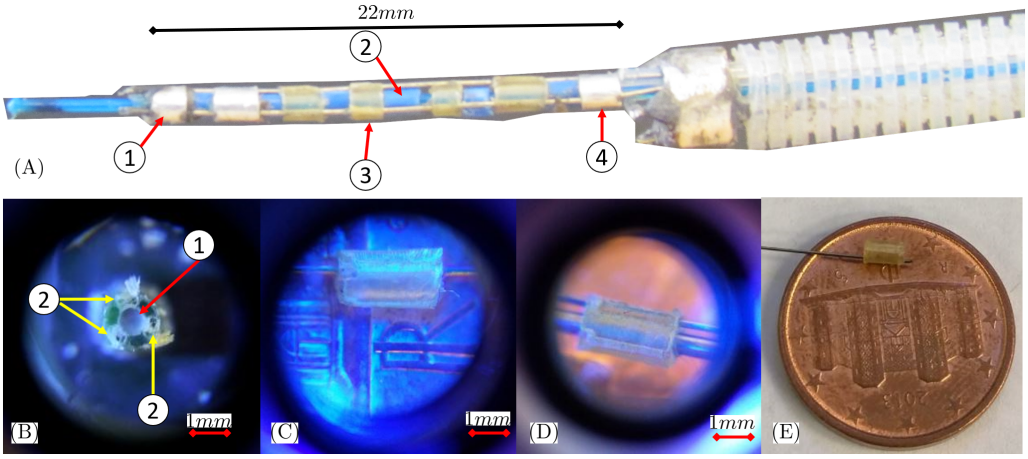

Figure 2.11: Distal Microsnake continuum segment: (A) Distal microsnake continuum segment ① End-disk ② Spacer disk ③ Intermediate disk ④ Base disk (B) Microscope top view of continuum segment intermediate-disk ① Central lumens for laser deploying ② Side backbone lumens (C) Microscope side view of a spacer disk with a 0.22 mm backbone passing through (D) Microscope side view of a spacer disk with all the 3 backbones passing through (E) Intermediate disk

The 2 DoF of the distal microsnake are actuated pushing and pulling on the 3 redundant backbones using a custom made actuation unit showed in Figure 2.12.A. The 3 backbones are routed from the continuum segment to the actuation unit through an *actuation cone* ① and a *snake holder* ② which ensure the backbone to not cross on each other. The actuation cone has 3 internal channels which direct the 3 backbone to three identical *single backbone actuation module* (Figure 2.12.B).

Referring to Figure 2.12.C, each single backbone actuation module have an outer *aluminum shell* ① that is rigidly attached to the NiTi backbone through one of the two *telescopic anti-buckling tubes*. To avoid the backbone to buckle, these tubes slide into each other in order to constantly support the backbone when it is pushed forward. The second anti-buckling tube is fixed on the *bottom holder collar* which rigidly connect to the aluminum shell. The anti-backlash piston is driven by a 0.60911 mm/turn *lead screw* ④ which is connected to a Maxon motor combination ⑨ # 300765 (Gearhead GP10A

218416(Series 16:1 ratio) + Motor RE10 256105 + MR Encoder 138061 (12 CPT)) through and *Oldham coupling* ⑧. In order to place coaxially the lead screw and the motor, we are using a *bearing holder collar* ⑥ to support the lead-screw, and a *top holder collar* ⑦ to hold the motor.

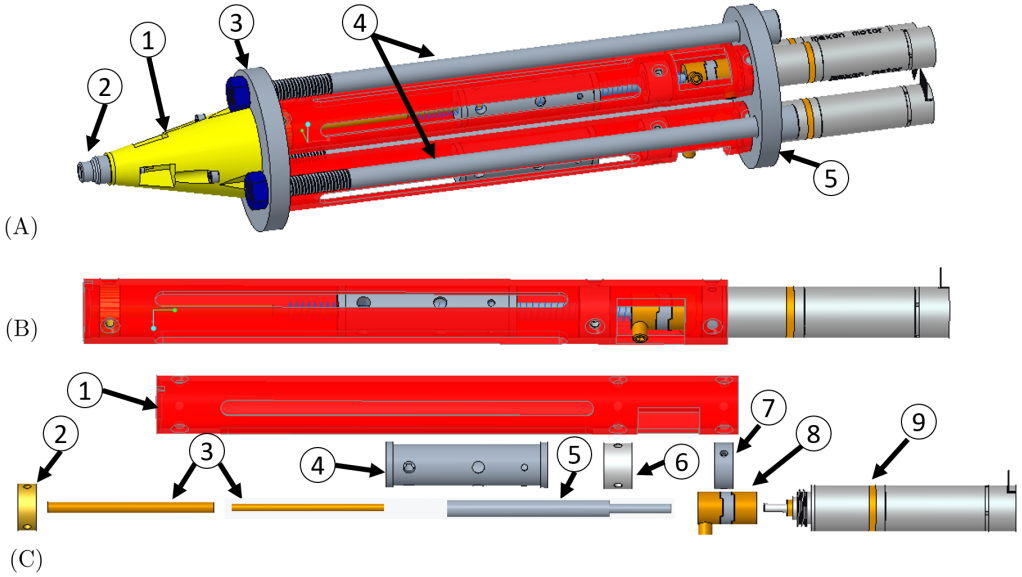

Figure 2.12: Distal Microsnake CAD Model: (A) Distal microsnake actuation unit: ① Actuation Cone ② Snake holder ③ Front Plate ④ M5 screws ⑤ Rear Plate. (B) Single backbone actuation module. (C) Exploded view of a single backbone actuation module: ① Aluminum cylinder ② Bottom holder collar ③ Telescopic anti-buckling tubes ④ Anti-backlash Piston ⑤ Lead screw ⑥ Bearings holder collar ⑦ Top holder collar ⑧ Oldham coupling ⑨ Maxon motor combination

Finally, the three actuation modules, forming the actuation unit, are assembled between a *front plate* (Figure 2.12.A ③) and a *rear plate* (Figure 2.12.A ⑤). To ensure structural rigidity, 3 M5 screws (Figure 2.12.A ④)are used to connect the two plates, forming the chassis of the actuation unit.

2.7 Experimental evaluation

In order to asses the capabilities and performances of the TURBoT, a series of different experimental validation procedure were performed. In this section a brief overview of this tests and their related results will be presented. For a more deep and thorough description

of all the experiments and for a more extensive explanation of the results obtained we refer the reader to [19, 68, 67].

2.7.1 Bending test

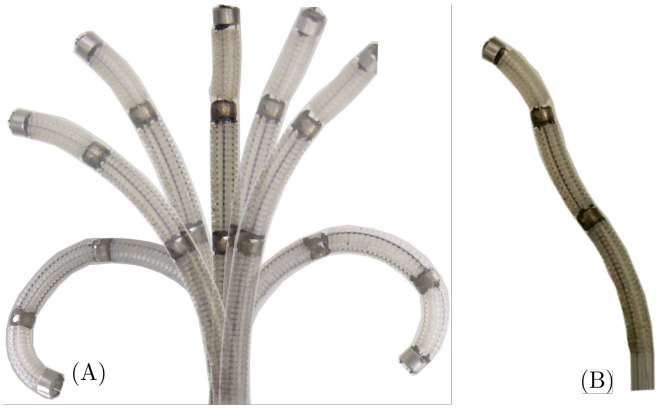

Figure 2.13: Sample motions generated by the continuum robot: (A) banding angles between 0° and 250°, (B) S shape-snake

Figure 2.13 shows the motion of the snake robot in an early experiment aimed to verify the functionality of the concentric actuation scheme with quick-connectors. The control code was written in Simulink package (Version 7.5) and the real-time code generation and implementation was carried out using xPC Target toolbox in Matlab (Presently known as Simulink Real-Time). The MBCR was actuated in the configuration space by trying different banding angle planes (δ_i) and bending angles (θ_{iL}) of each segment. Figure 2.13 illustrates the MBCR bending in the $\mathbf{x}_b\mathbf{z}_b$ plane (See Figure 2.3). To achieve this, the bending angles of each segment were independently controlled. Note that the maximum achievable bending angles are higher than illustrated and are only limited by the plastic deformation of the backbones.

2.7.2 Animal Study

The following was presented in [68, 69, 19, 89]

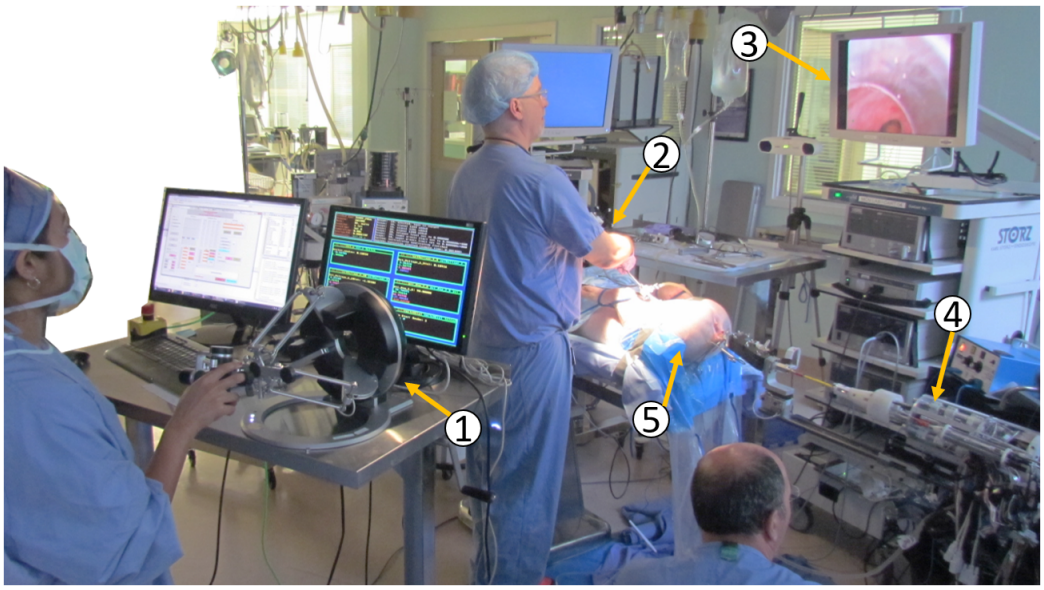

Figure 2.14: Animal lab experimental setup: ① Omega.7 master haptic interface, ② Transvesical endoscope camera, ③Surgeon monitor, ④ TURBot, ⑤ Swine

In order to assess the capability of the robotic system, we completed the first known animal study using the robot-assisted TURBT (Operative Room setup in Figure 2.14). The aim of the In-vivo experiment was to ablate mock-up generated tumors inside of a swine bladder. We successfully developed the cancerous lesions (Figure 2.15) using a blue dye (HistoGel specimen processing gel, Ref HG-4000-012 Thermo Scientific) injected on the bladder wall transabdominally in multiple locations. The colored tissues were successfully ablated using the TURBot and an indipendent two-Dof distal laser deployed within the robot. We showed the feasibility of en-block resection using a manually actuated griper deployed within the continuum robot.

The animal experiments identified several points of success on using the robotic system in the operative room. A qualitative verification of the robot's abilities to carry out resection at all regions of the bladder was shown by successfully ablating the lesions from all the locations, including the neck and the dome of the bladder, without the needs of deflate the bladder or applying any pubic compression, this was also facilitated by the statically balanced arm moving the robot in and out of the urethra and tilting the resectoscope

to adjust the angle of approach, helping on reaching into all quadrants of the bladder. Furthermore, we shown the feasibility of en-block resection using a manually actuated griper deployed within the continuum robot.

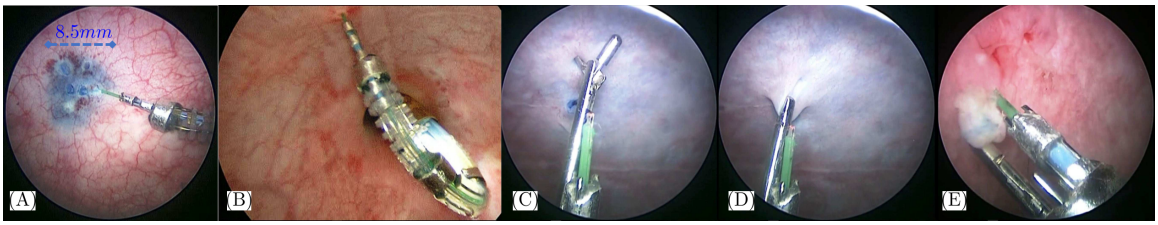

Figure 2.15: (A)HystoGel leasion and TURBot EE, (B) TURBot retroflexing to reach bladder neck, (C-E) En-block resection using manually actuated griper and 2-Dof distal laser

The experiments also pointed to limitations of our system that could be addressed in future work. The main limitation comes for the serious difficulties in visualization during the procedure enhancing the needs of a better intravesical visualization. Moreover, the disparity between the geometry of swine bladder and human bladder caused various difficulties. The small bladder size and the need for an additional balloon port to provide visualization meant we were left with very little space to create more than 2-3 tumors per pig and the more acute angle of the swine bladder neck left even less space to operate in that area.

In order to obtain more quantifiable performance a new set of experiments was conducted comparing manual resection performances against robot assisted resection using a precise human bladder model obtained by computer tomography scans and use the robot in an evaluation study on this bladder.

2.7.3 User Study

Figure 2.16.A shows the robotic system integrated in the experimental setup using 3D printed bladder phantoms (Figure 2.16.A3) obtained from patient CT scans. In order to adjust the approaching angle of TURBot to the urethra, the system uses a PUMA560 robot to

adjust the location and orientation of the phantom bladder model, shown in Figure 2.16.A1. The bladder model has been modified in order to accomodate resection plates using agar at key sites including the bladder neck. The EE of the CR has been equipped with a standard cautery resection loop and used cautery to carry out resection.

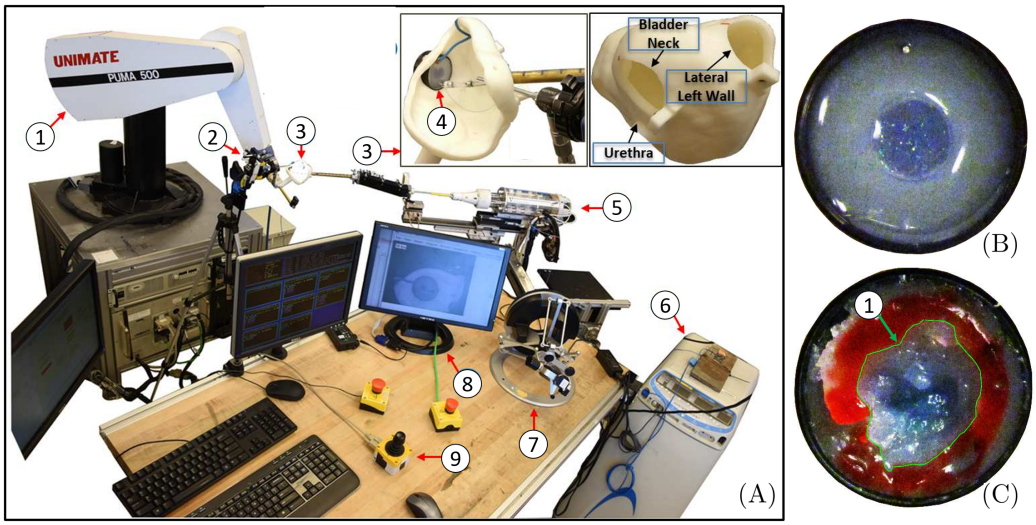

Figure 2.16: (A)Experimental setup: ① PUMA560 for phantom placement, ② Endoscope camera for in bladder visualization, ③ Bladder phantom, ④ Mockup tumor, ⑤ TURBot, ⑥ Cautery machine, ⑦ Omega.7 as master haptic interface, ⑧ In bladder visualization monitor, ⑨ PUMA560 Master controller. (B) Mockup tumor before resection (C) Mockup tumore processed after resection, ① resected area contour.

Each resection plate was imaged before and after resection, Figure 2.16.B and C respectively. The dimension of the tumors were carefully controlled and therefore images before and after the resection allowed measurements of tangential resection errors for each tumor. Repetition of the experiments using standard manual tools verified that one cannot carry out resection close to the bladder neck without resorting to aggressive deformation of the bladder. TURBot was able to resect a tumor at the left superior and at the neck region with an accuracy of $0.94 \pm 1.08mm$ and $0.27 \pm 1.56mm$ respectively. Considering both tumor locations, the accuracy of TURBot is evaluated as $0.60 \pm 1.33mm$. In comparison, manual resection accuracy is $0.2 \pm 1.1mm$. Note that however this value does not include the neck region where manual resection was not possible.

Based on the experiments, we noted that part of the reason for reduced accuracy of

the robot is related to visualization quality and blockage when using the robot. Since the electro-cautery resection loop was placed right at the tip of the robot there were some end point angles of the robot where it was hard to see the resection loop.

2.8 Conclusion

This chapter presented the design considerations that guided the design, fabrication and testing of a modular actuation unit for a continuum robot aimed at transurethral bladder cancer resection. A methodological process for guiding the design of this actuation unit was presented based on taking into consideration conceptual design attributes and task specifications. The conceptual design attributes were used to guide the choice of mechanical architecture of the actuation unit. The task specifications were used to guide the detailed design and component selection for each actuator. The resultant actuation unit is comprised of three modules allowing for modularity, ease of sterilization and actuation separability, and robustness to sensor errors. Preliminary testing shows that the actuation unit achieves its primary function. The system was tested in phantom and in-vivo studies where the robot successfully ablated tumors in several critical regions of swine bladders using laser. Though the design posed several bottlenecks particularly in terms of fabrication, the most critical aspect which demanded several iterations was the actuation detachment module since the backbone are deployed concentrically. Though previous works have presented some actuation units suitable for actuation of continuum robots, the design exposition has been predominately ad-hoc. We believe that this work provides an example that could benefit others when considering design of actuation units of continuum robots for specific surgical applications.

CHAPTER 3

INTRODUCTION TO CREM - CONTINUUM ROBOT WITH EQUILIBRIUM MODULATION

3.1 Overview and Clinical Motivation

Current robotic slave arms for minimally invasive surgery (MIS) offer excellent distal dexterity for surgical tasks requiring large workspaces and position accuracy ranging between 0.5 to 1.5 mm. For example, Kwartowitz et al. [90] experimentally determined the root mean square (RMS) localization accuracy of the da-Vinci Classic and da-Vinci S to be 1.02 mm and 1.05 mm, respectively. Despite their limited accuracy, these robots are able to perform well when tele-manipulated since their repeatability usually exceeds their accuracy and the users can use visual feedback to overcome accuracy errors. Despite increases in precision, existing surgical systems are unable to traverse curved anatomical passageways; therefore, researchers have pursued the use of snake-like robots [91] and continuum robots [81, 92, 13, 93, 94, 95] to increase the depth of minimally invasive reach into the anatomy.

While current continuum robots satisfy the requirements for large workspace and deep access into the anatomy, there are medical applications that could benefit from extreme precision (sub 100 μm). Examples include high-precision micro-surgical tasks (e.g. micro-vascular reconstruction, nerve repair and grafting) and image-based diagnosis and surgery at a tissue level. Micro-vascular reconstruction/anastomosis of blood vessels having small diameters ($\varnothing 1-3mm$) requires precision on the order of better than $100\mu m$. Also, the advent of image-based diagnosis and surgery at the tissue level creates new demand for ultra-precision robots. Fujimoto's [53] demonstration of OCT for image-based diagnosis

and Luo's [96] use of OCT biopsy of lymph nodes using an OCT with imaging resolutions of $1-3\mu m$ create new opportunities for robots that can enable in-vivo discernment of negative tumor margins. These opportunities can be achieved through micro motions to allow effective 3D OCT image reconstruction or mosaicing of confocal microscopy images.

Existing robots for multi-scale motion (MSM) are unsuitable for micro-surgery in deep surgical sites where miniaturization and traversal of often tortuous anatomical passageways is required. Also, new emerging surgical paradigms for natural orifice surgery and image-based diagnosis and guidance at the micro-scale level promise to provide accurate verification of tumor resection margins. To overcome the limitations of current robot architectures, and to enable image-based biopsy and micro-surgery in confined spaces, in this chapter, a new concept of continuum robots with equilibrium modulation (CREM) is presented. CREM robots are a modification of multi-backbone continuum robots that achieve micro-motion by using indirect actuation through modulation of their static equilibrium by change of the distribution of their cross-sectional flexural rigidity.

To overcome the challenges outlined above, there is a need for new robots capable of multi-scale motion (MSM) for satisfying gross motion during surgery and extreme precision to enable micro-scale task execution. To achieve this, we put forth the new concept of *CREM*. These robots are able to use *direct* and *indirect actuation* to produce motion of their end effectors. In contrast to typical robots, which rely on direct actuation of their active joints to move their end effectors, these robots are able to use a secondary set of actuators that change material and stiffness distribution along the body of the robot. By modulating these distribution, the static equilibrium of these robots is altered (modulated) by minute amounts; thereby resulting in end effector micro-motion.

In response to the needs outlined above, this work is presented as a first step towards modeling the micro-scale kinematics of these robots, solutions for micro-motion tracking approaches including color and shape-based markers and verified to achieve tracking accuracies of better than $2\mu m$. Preliminary evaluation of the micro-motion capabilities of a first

prototype demonstrates motion resolutions at $1\mu m$ level and hysteresis of less than $10\mu m$ - despite the use of inexpensive actuators with significant backlash.

3.2 Relevant Works on Micro-Macro Motion

The concept of CREM to achieve MSM is wholly new since previous works on MSM have primarily focused on serially-stacked architecture where a dedicated micro-manipulator is stacked on top of a serial manipulator. Examples of such works are found in Egeland's pioneering work [97] and followed by several works such as [98, 99, 100, 101, 102, 103]. Other works such as Portman, et al. [104] developed a Stewart/Gough parallel robot driven by hydraulic micro-actuators thereby providing high stiffness and accuracy better than 0.1 μm. Shoham [105] presented the concept of twisted wire actuators to demonstrate a planar parallel robot with micro-scale motion. Rul, et al. [106] developed a micromanipulation tool using SMA (Shape Memory Alloy) for actuation and implemented closed-loop feedback control using a displacement measurement laser. Yun, et al. presented a piezo-electrically actuated 3-degrees of freedom (DOF) micro/macro parallel platform for micro/nano positioning applications [107] with a limited workspace of $\pm 5mm$ in all directions.

Although these works achieved micron-scale resolution, the designs are not down-scalable in size and the micro-actuator technology is typically expensive. More importantly, these designs are not suitable for MSM in confined spaces while having to circumvent obstacles. As a result, these designs are not suitable for emerging applications where robots have to traverse curvilinear passageways to perform micro-precision tasks such as the cases in natural orifice surgery of micro-assembly/inspection in cluttered environments. The CREM concept presented in this chapter fills this need.

3.3 Continuum Robots with Equilibrium Modulation

Figure 3.1 depicts the concept of CRs for equilibrium modulation (CREM). This concept was introduced in [108] as a modification of the design proposed in [2]. A multi-backbone continuum segment includes four tubular backbones made of superelastic NiTi. These backbones include a central backbone ② surrounded by 3 secondary backbones ⑥ which are responsible for the macro-motion actuation. All the backbones slide through a base disk ⑤ and spacer disks ③ that maintain a constant radial distance between them. All the backbones rigidly connect to the end disk ①.

The (green) double line arrows in Figure 3.1A indicate the direct actuation of the secondary backbones in order to bend the continuum segment to achieve a desired end-disk orientation in two degrees of freedom. Micro-motion capability is obtained by controlling the insertion of Niti wires ④ inside the secondary tubular backbones. This motion is designated by (red) single line arrows in Figure 3.1A. By controlling the portion of the wires inserted into the secondary backbones, the flexural rigidity along the length of the continuum robot is changed. The equilibrium modulation actuation therefore causes an *indirect* actuation of the end effector (EE) that changes its static equilibrium pose to a new pose. In [109] we presented experimental results that show that the micro-motion path follows the general shape depicted in Figure 3.1B, but offered no explanation to the source of this phenomenon.

3.4 Design Modifications

For experimental evaluation, we have modified a pre-existing experimental apparatus that has been first presented in [84, 87]. This setup is shown in Figure 3.2.A ①-②. Originally, the setup was designed to control a multi-segment robot (up to three segments). The design modification required to fully disassemble the pre-existing continuum robot and fabricate a new single segment continuum robot to be used for equilibrium modulation

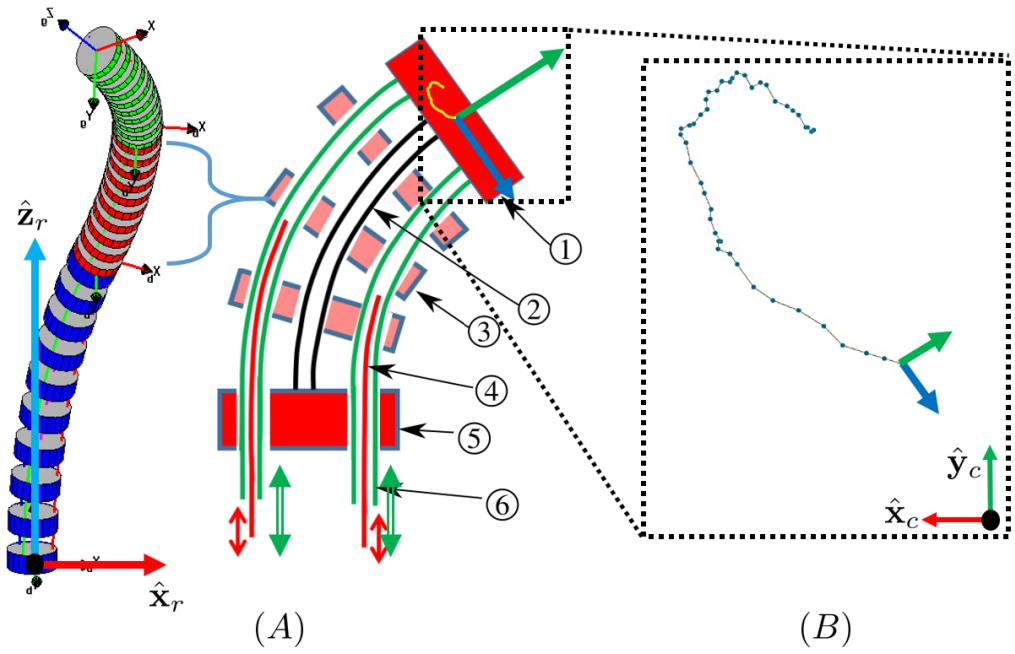

Figure 3.1: (A) Continuum robot with equilibrium modulation (B) Micro-motion trajectory of end-effector.

experiments and to allow the attachment of tracking markers to the disks of the continuum robot for the purpose of validating micro-motion. A new design and fabrication was done for the actuation unit in order to control the insertion wires. Furthermore, the new actuation unit was equipped with proper wires attachments to the actuation module. Beside the modification of the mechanical parts of the system, also the electronics setup was adjusted accordingly and it was redone in order to be able to use a newer written control code to enable independent control of the insertion wired and the backbones of the continuum robot.

The result of the modification is shown in Figure 3.2, where ③, the Micro-Motion Actuation Unit (MIMAC), has been added on top of the existing Large Snake Actuation Unit ②. At the bottom, marked as ①, is the continuum robot. The MIMAC is composed of three custom designed sub-assemblies, each called a Velmex Linear Insertion Stage (VLIS). The detailed design of the MIMAC and VLIS can be seen in figure 3.3.

As the name implies, the VLIS is a linear actuator to which the micro motion wires

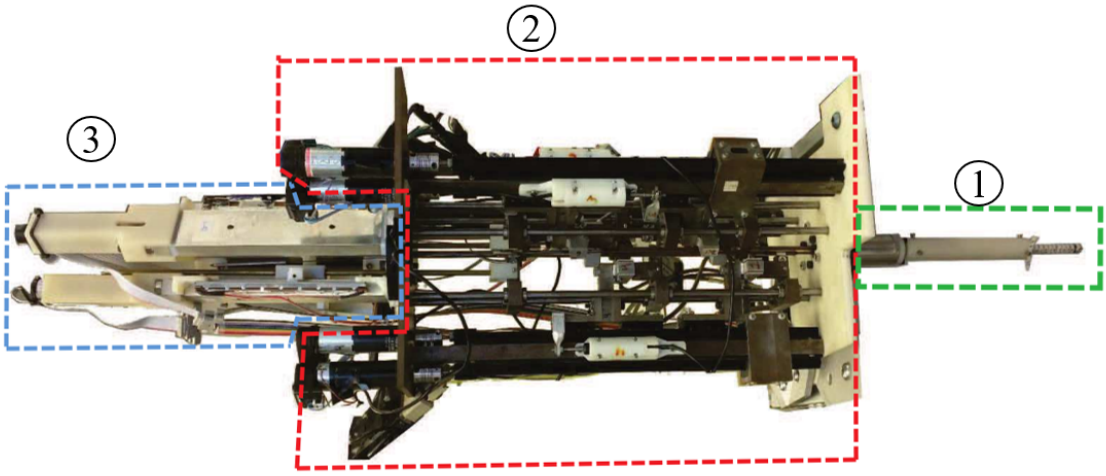

Figure 3.2: CREM Actuation Unit: ① Continuum robot, ② Continuum robot macro-motion actuation unit, ③ Micro-motion actuation unit.

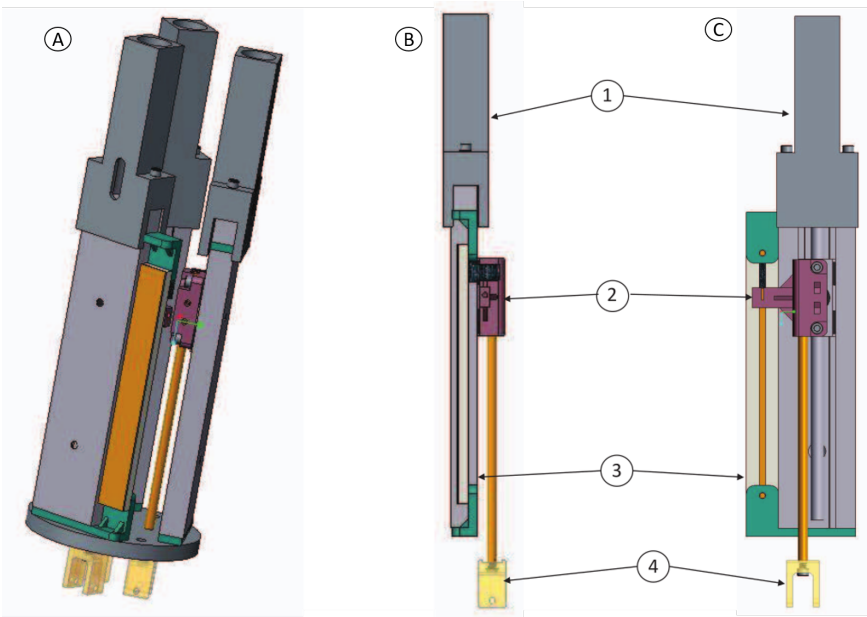

Figure 3.3: (A) The Micro-Motion Actuation Unit. (B) Velmex Linear insertion stage side view. (C) Velmex Linear insertion stage front view - ① Motor connection adaptor, ② Potentiometer shaft connector ③ Linear potentiometer ④ Micro motion wire connector

are attached to induce micro motion on the robot. The linear slide is equipped with a lead screw which have a 4.5 inches travel and pitch of 20 turns/inch. The carriage of the lead screw is mounted on a Velmex linear slide [A1506B-S1.5]. The position of the carriage is measured by a linear potentiometer [Bourns 652-PTB1432010BPB103]. The lead screw is actuated by a Maxon Motor [RE16 118733], attached with an Oldham coupling. The motor gearhead has a 29:1 ratio [Maxon 118185], and the encoder has 512 counts per turn [Maxon 201940]. The carriage, and all pieces attaching the various parts together have been designed and fabricated in-house. The three VLIS modules forming the MIMAC are mounted on a Delrin (polyoxymethylene) plate which attaches the MIMAC to the Large Snake Actuation Unit as shown in Figure 3.4.

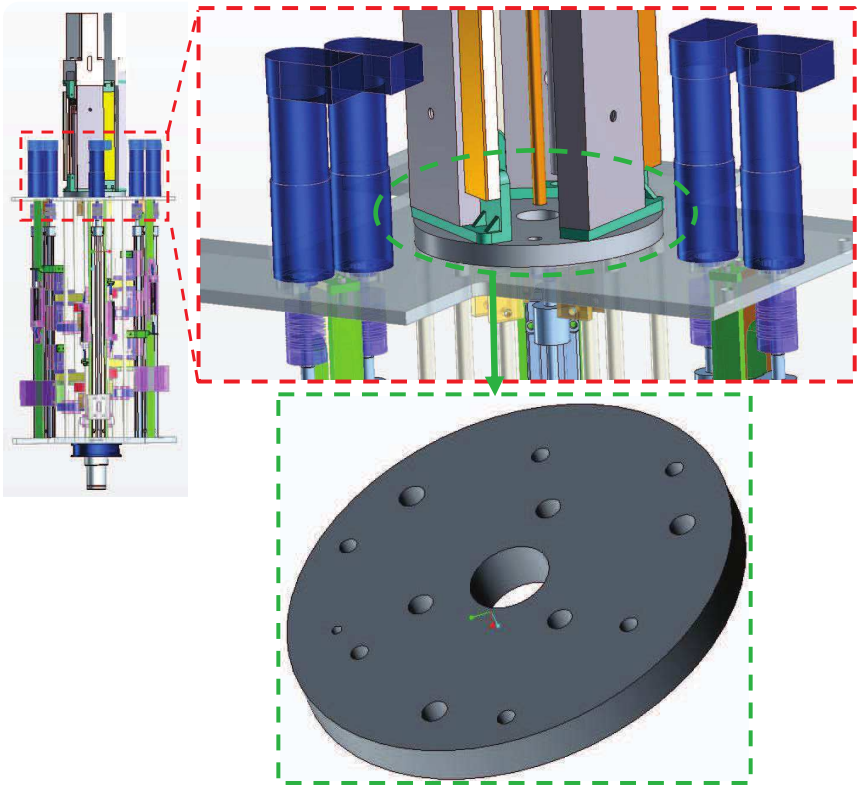

Figure 3.4: DELRIN plate

The MIMAC controls the insertion depth of three Nickel-Titanium (NiTi) wires inside the secondary backbones of the continuum robot. In order to maintain straight insertion of the wires, the wires and the ends of the actuators from the MIMAC are connected to a

double rail assembly built into the Large Snake Actuation Unit, shown in Figure 3.5.

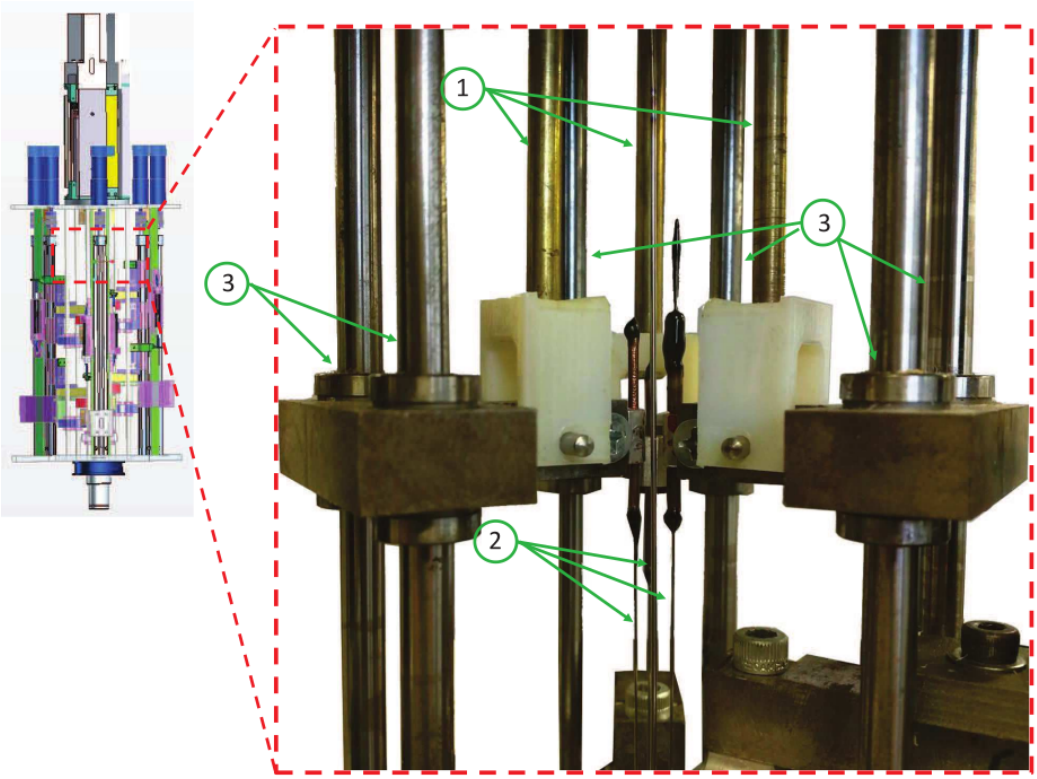

Figure 3.5: Double rail system: ① Linear stage rods ② Micro-motion NiTi Wires ③ Double rails

The length of each NiTi wire from its tip to the middle of the attachment point on the VLIS is 470 mm. This length ensures that the tip of the NiTi wire is at the end of the first segment of the continuum robot when the carriage of the VLIS is in the middle of its stroke.

In order to use the NiTi wires to accurately define micro motions of the robot, it is necessary to define a zero-point for measuring the insertion depth of the wires. This reference point is chosen to be at the end of the snake when it is straight, as shown in Figure 3.6. The zero-point for each wire is defined when the insertion wires are almost coming out of the 1st segment. The positive direction of insertion is defined away from the actuation unit, so that when the wires are inside the first segment the insertion depth is negative, whereas if they were to be inserted into a second segment, the values would be positive. Currently, no second segment has been attached to the robot, so all values for

insertion depths will range from 0 mm to -50 mm, which is the total length of the continuum robot when straight.

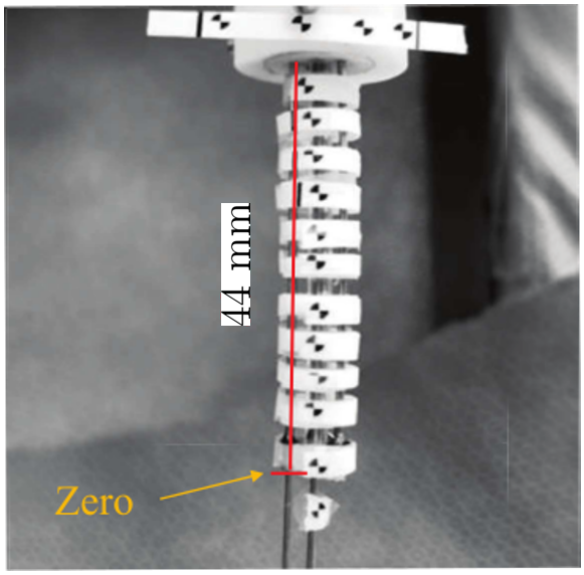

Figure 3.6: Zero depth location for Micro Wire Insertion

Once the position of the insertion wires has been determined to be at the zero location, that configuration must be saved. The potentiometer values for each joint were captured and saved to file. Additional measurements of the location of the connection point between the actuation unit and the NiTi wires were also taken using calipers as seen in Figure 3.7.

Wire 1

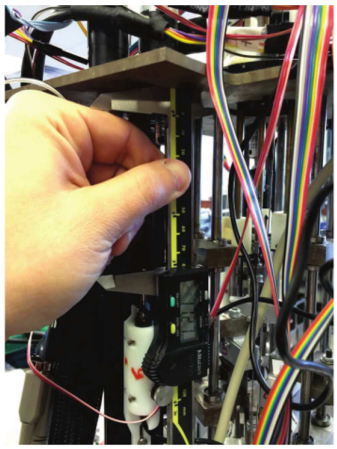

Wire 2

Wire 3

Figure 3.7: Caliper measurements of joint displacement when zero insertion depth was defined

3.5 Conclusion

This chapter introduced a new design concept for continuum robots achieving micro and macro scale motion and the upgrade of the existing hardware. The concept of micro-motion through equilibrium modulation was introduced and a first prototype of a continuum robot using equilibrium modulation (CREM) was presented. This concept differs from prior works on micro-macro motion by presenting a single device capable of multi-scale motion (compared to prior works using serially stacked micro-motion robots on top of a gross motion robot).

To validate the modeling of the micro-motion kinematics of CREM robots (presented in Chapter 5), the motion resolutions required to validate the modeling are beyond capabilities of commercial trackers,therefore the next chapter presents the efforts on investigating methods for achieving micron resolution tracking.

CHAPTER 4

MICRO-MOTION TRACKING FOR CREM ROBOTS

4.1 Introduction

In the following sections are presented the efforts for developing a real-time tracking solution for micro-motion control of CREM. Such continuum robots have a macro motion capability, covering a workspace of approximately $(30 \times 30mm)$ while its micro motion mode has only a range of approximately $(100-500\mu m)$. In the macro motion experiments, an imaging method is needed to capture the kinematic status of the entire continuum robot segment (about $45mm$), i.e. the central backbone curve of the robot. In the micro motion mode, an imaging method under a microscope scale (about $45X$) is desired to track tip position motion. The lack of a commercial tracker device, sensible enough to track sub-micron motion displacements, rose the need to build a custom made system, in term of hardware as well as software, able to perform at such high definition.

4.2 Micro-Motion Tracking and Image Segmentation

The micro-motion images are acquired using a Point Grey DragonFly2 camera shown in Figure 4.1⑤, equipped with a $4.5\times$ magnification microscope lens. The image segmentation discussed in the following sections were performed using MATLAB2016a.

In order to define the continuum robot tip in position and orientation at every pose over the workspace during micro-motion, images are acquired at each robot configuration as shown in Figure 4.1.C.

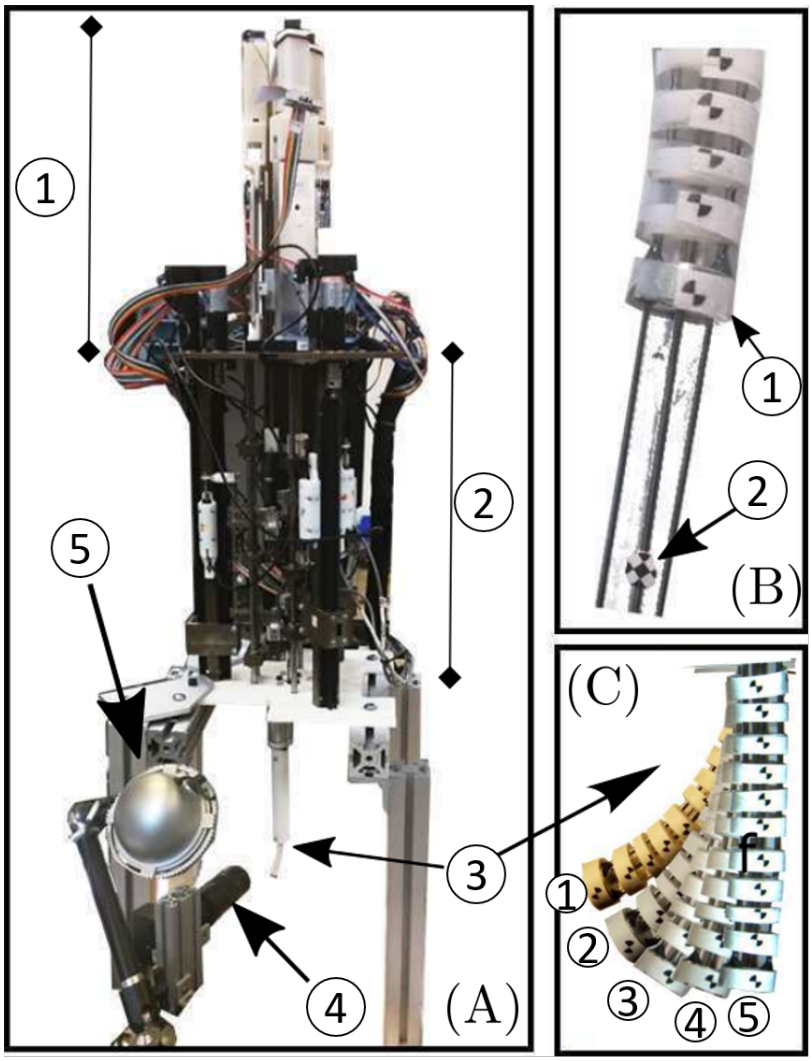

Figure 4.1: CREM experimental Setup: (A) System setup: ① Micro-motion Wires Actuation Unit, ② Continuum Robot Actuation Unit, ③ Continuum robot, ④ Microscope Camera, ⑤ - Macro Camera and Light Source. (B) Continuum Robot tip: ① - Continuum robot end-disk, ② Micro-motion marker. (C) Continuum Robot configurations: ① $\theta_1 = 75°$, ② $\theta_1 = 60°$, ③ $\theta_1 = 45°$, ④ $\theta_1 = 35°$, ⑤ $\theta_1 = 15°$

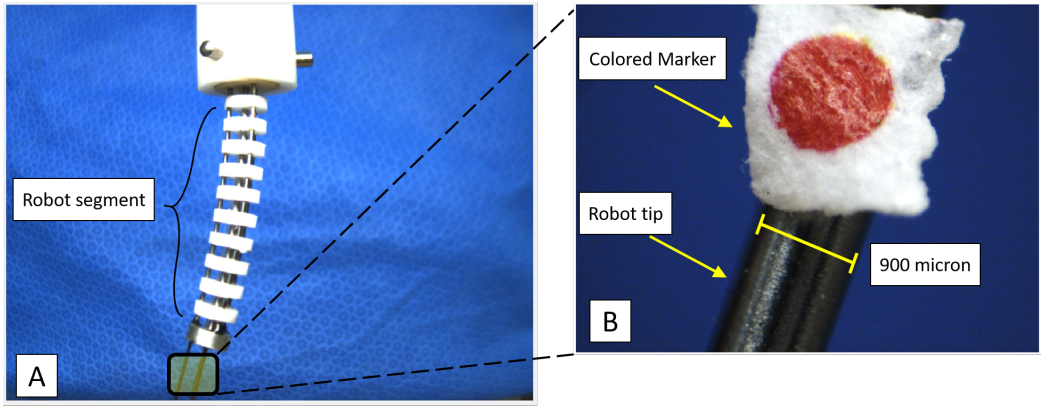

Figure 4.2: Examples of images from macro-micro robot experiments: (A) captures the macro motion of the robot and (B) is taken from the micro motion experiment where a red colored dot is attached to the tip of the robot

As shown in Figure 4.2, two images are acquired simultaneously at each robot configuration. In Figure 4.2 (A), the macro motion image, the goal is to capture the shape information of the bent continuum robot segment, which includes the following specific target goals:

(a) Obtain the end disk position and orientation, the position unit should be in pixels while the orientation should be expressed with a 2D rotation matrix.

(b) Obtain the position and orientation of sample locations along the central backbone.

(c) Fit a spline/polynomial curve to express the curvature profile.

In Figure 4.2 (B), the goal is to capture the tip position and orientation. The position can be captured, for example, using the center of the red colored dot or another type of marker that will be introduced in the following sections. The orientation can be either estimated using the parallel lines on the tip of the robot, or it may be estimated using another marker.

In the following sections, the technical development is discussed to obtain the shape information in macro motion mode of the continuum robot and the tip information in micro motion mode. Two strategies are explored:

(i) A strategy is discussed in section 4.8, that only uses a red dot and the robot outline

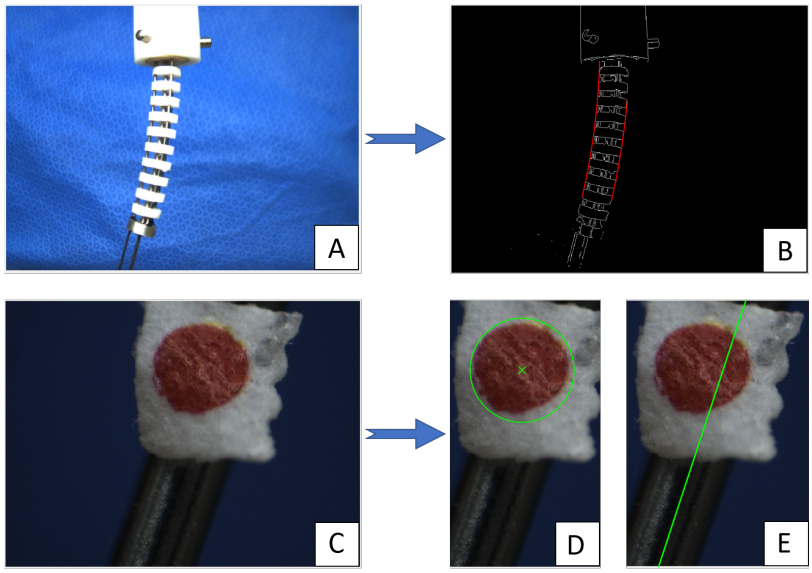

Figure 4.3: Results of markerless strategy using RGB color original images: (A,C) Acquired images (B,D,E) Post processed Images.

itself (example images as in Figure 4.2);

(ii) A strategy that uses a "X" shape marker is discussed in section 4.5(example images as in Figure 4.9).

4.3 Development of a Tracking Method using Color Circle Marker

A strategy is discussed in this section about combining a markerless tracking method for the shape of a continuum robot and a color circle marker tracking method for motion under microscope. As shown in Figure 4.3 and Figure 4.4, both macro and micro motion images were acquired and segmented. In both Figure 4.3 and 4.4: (A) and (C) are original images for macro and micro motion respectively; (B) is the resultant segmenting image with the snake curve boundary; (D) and (E) are the resultant segmenting images with the center of circle as position and the tip direction line respectively.

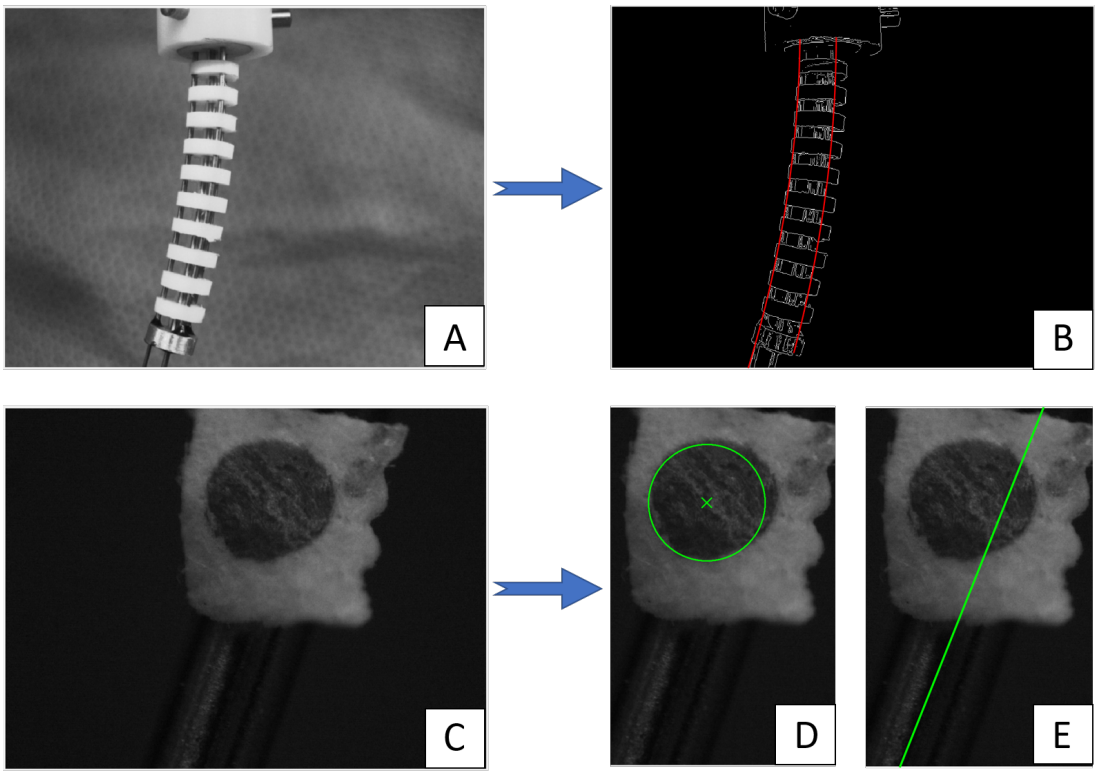

Figure 4.4: Results of markerless strategy using gray scale original images.

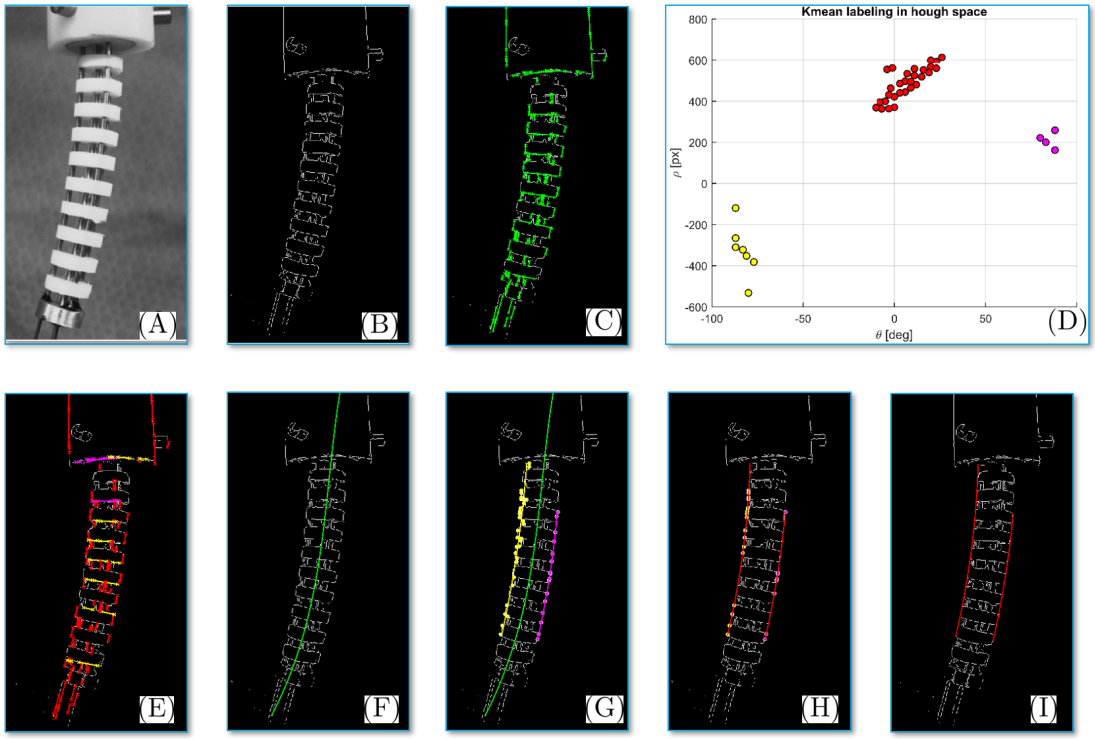

Figure 4.5: Image segmentation steps of markerless method for continuum robot shape: : (A,C) Acquired images (B,D,E) Post processed Images.

4.3.1 A markerless method to segment the shape of continuum robots

To segment the shape of the continuum robots in a markerless fashion, the following steps are applied, shown in Figure 4.5:

(i) A "RGB2Gray" conversion is applied first if the source image is in color(Figure 4.5.A). Then a *Sobel* intensity edge finder is applied, resulting in a binary image of the edgeFigure 4.5.B.

(ii) A *Hough* line transformation is used on the binary edge image where the detected line segments are marked in green color(Figure 4.5.C). The detected line segments cover most of the outline of the continuum robot, which naturally leads to the next step - selecting the edges that lie along the robot bending curve.

(iii) A *K-means clustering* method is applied to automatically label all the detected lines in three groups (red, yellow and magenta) (Figure 4.5.D-E). The color labeled lines are drawn in both the binary edge image and the hough space to shown correspondence. The K-means clustering is applied in hough space based on the moment of line and the orientation of line, resulting in a good selection that will eliminate outliers and lines that are perpendicular to the robot bending curve tangent directions (e.g. the yellow and magenta samples are deleted from this step forward). Both ends of all the selected lines are stored as sample points to be used for curve fitting procedures.

(iv) A polynomial curve fitting is applied on all of the sample points (Figure 4.5.F). This is used as a initial guess of the rough centerline of the continuum robot.

(v) The guessed centerline is used to split all of the samples and then the distances to the centerline are used to remove outliers that are either too far or too close to it. This results in nice selection of the sample points that are on the outline of the continuum robot (yellow and magenta scatters in Figure 4.5.G).

(vi) A refining procedure is applied again to select the final outline sample points to characterize the outline curve (Figure 4.5.H-I).

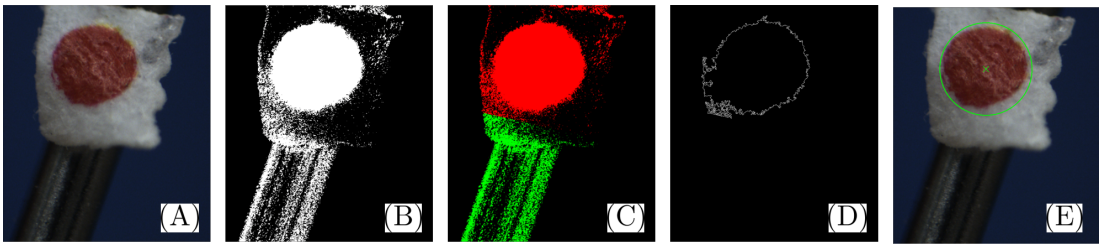

Figure 4.6: Image segmentation steps of markerless method for tip position of continuum robots using color images

4.3.2 Segmenting the tip position and orientation using a colored circle marker

The image segmentation of the tip position of a continuum robot in a microscopic scale using a simple red dot marker is shown in both Figure 4.6. The image processing steps are explained as follows for using the color image source:

(i) A *Hue Mask* is applied to select the red pixels, resulting in a binary image containing both the red circle and the tip of the robot (Figure 4.6.A).

(ii) A *K-means clustering* method is applied to automatically group all the pixels into two groups based on the locations of the bright pixels (Figure 4.6.B).

(iii) Then a *Sobel* intensity edge finder is applied, resulting in a binary image of the circle edge (Figure 4.6.C).

(iv) A *Hough Circle* transformation is applied to determine the radius and center of the circle in the edge binary image (Figure 4.6.D).

The steps for using gray image source are the same as the steps for color except that Otsu threshold method is used to generate a binary image.

The image segmentation of the tip orientation of a continuum robot on a microscopic scale is continued from the position segmentation and is combined with the Hough line transform and line clustering in the previous markerless shape segmentation, as shown in Figure 4.8. The detailed explanation of each step used is listed as follows:

(i) This step is continued from previous intermediate images in tip position segmenta-

tion. In color image cases, the group of pixels of the tip after hue mask is selected (Figure 4.8.A-B). In gray cases, the area that Otsu threshold selected previously is removed and reapply Otsu again to the background for inverse selection (Figure 4.8.G-H).

(ii) Then a *Sobel* intensity edge finder is applied, resulting in a binary image of the edge (Figure 4.8.c-I).

(iii) A *Hough* line transformation is used on the binary edge image where the detected line segments are marked in green color (Figure 4.8.D-L).

(iv) A *K-means clustering* method is applied to automatically label all of the detected lines in three groups (red, yellow and magenta). Both ends of all the selected lines are stored as sample points to be used for curve-fitting procedures (Figure 4.8.E-M).

(v) A line fitting is applied to obtain the centerline of the tip of the robot in the images (Figure 4.8.F-N).

4.4 Experimental results

These particular examples presented above, show that by using RGB color images we get slightly better results, infact, the detected edges are better representing the continuum robot macro shape. Furthermore, the segmentation presents a detected circle better represents the red dot marker and a line that better aligns with the center line of the robot tip.

However, all imaging processing was preliminarily implemented in Matlab2016a and the computation times were listed in Table 4.1, showing that using gray scale images in this strategy can significantly cut down the computation cost. In order to explore different solutions that could better identify position and orientation of the CR, limiting the segmentation-noise generated by the different filters applied on the images and rely, instead, more on unambiguous geometric feature, the next section presents the efforts of tracking a different kind of markers.

Image sources	Macro Im. Proc. Time [sec]	Micro Im. Proc. Time [sec]		Total Time [sec]
		Position	Tip Ang.	
RGB color	0.1681	2.0395	0.5775	2.7851
Gray scale	0.1361	1.4962	0.0956	1.7279

Table 4.1: Computation time comparison between using RGB color images or gray scale images

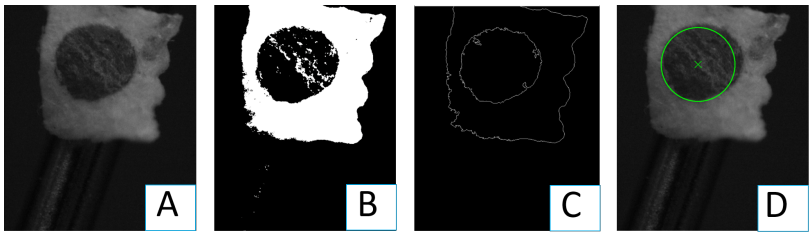

Figure 4.7: Image segmentation steps of markerless method for tip position of continuum robots using gray images

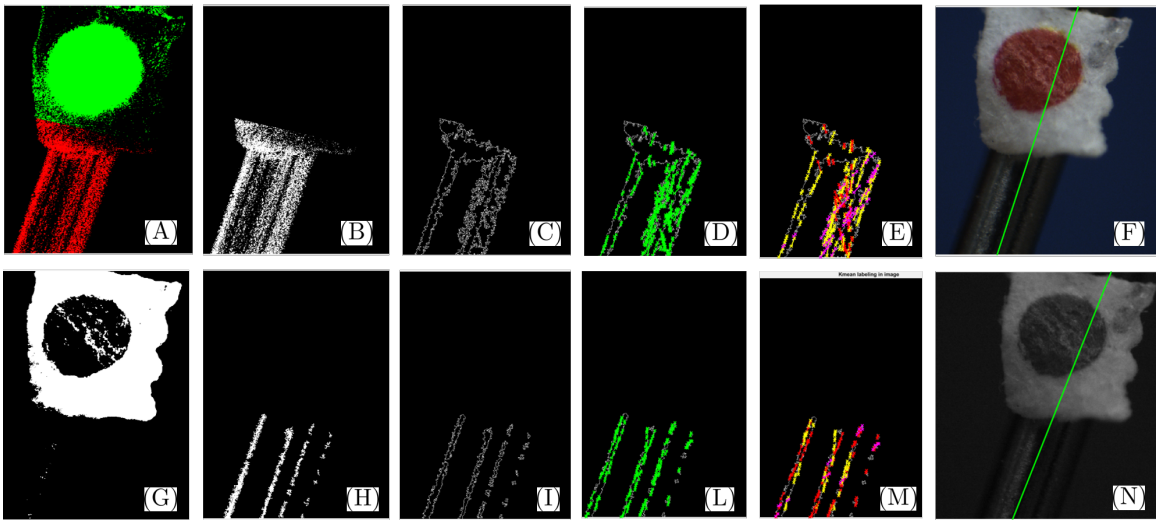

Figure 4.8: Image segmentation steps of markerless method for tip orientation of continuum robots

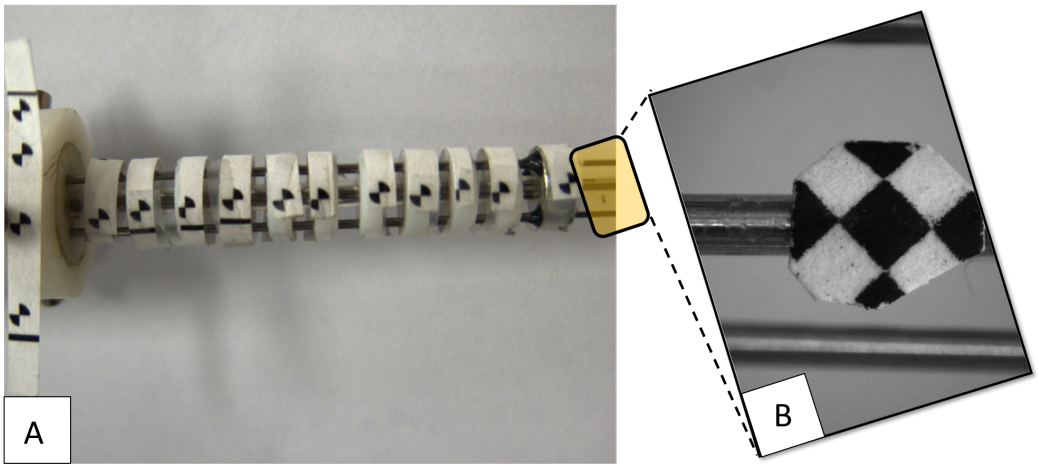

Figure 4.9: Examples of images where *X* markers are attached on both the robot segment body and the tip: (A) captures the macro motion of the robot and (B) is taken from the micro motion experiment

4.5 Development of a Tracking Method using *X* Markers

A method is described in this section to segment both the shape of a continuum robot and the tip and orientation on microscopic scale using *X* markers. An example is shown in Figure 4.9, where multiple *X* pattern markers are attached to the body of a continuum robot and are tracked under a HD camera. From each *X* marker, the position can be provided by the intersection of the edges of the pattern while the orientation can be provided by the orthogonal edges. With the measurements provided by multiple markers along the body of the continuum robot, the shape curvature profile can be obtained.

In addition, another marker with the same pattern is attached to the tip of this continuum robot but is tracked under a microscope camera view, as shown in the same example from Figure 4.9. By focusing on this single *X* marker in a magnifying view, as in Figure 4.9(B), a very high-resolution measurement of position and orientation is provided.

4.5.1 Tracking a single *X* marker under microscope

We will start with the description of the segmentation steps of a single *X* marker because it is easier since:

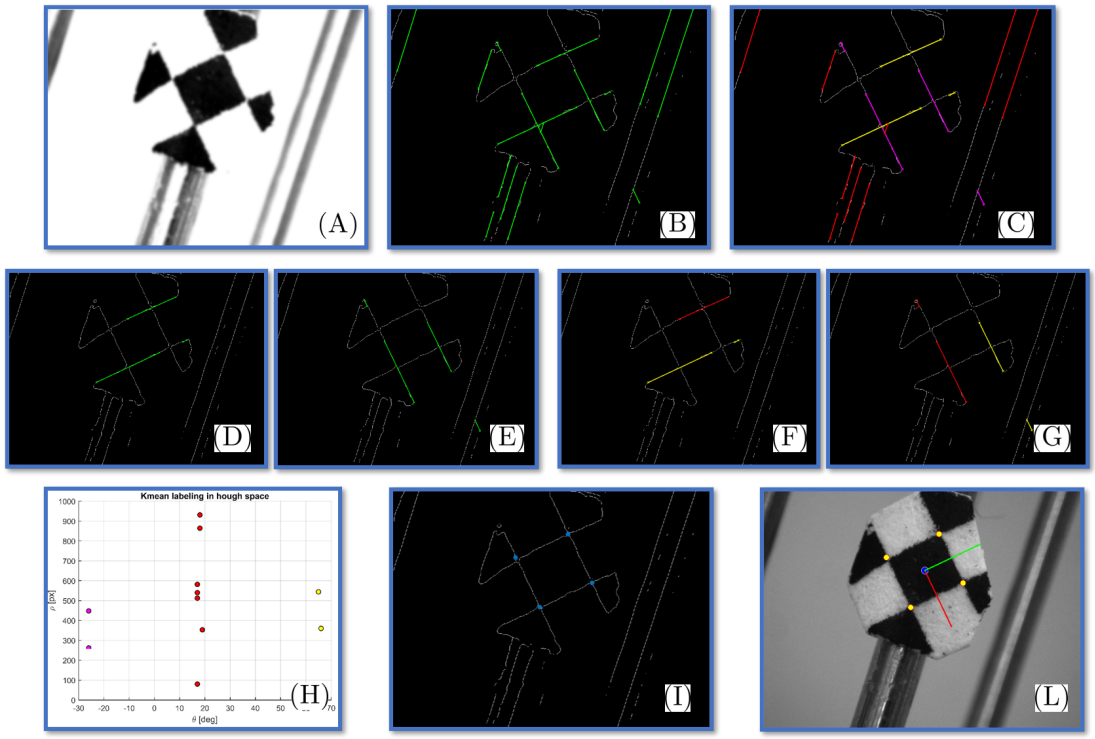

Figure 4.10: Image segmentation steps of one single *X* marker under microscope that provides position and orientation

- The marker occupies a big portion of the image.
- No other markers are in the same view.
- The characteristic features of the marker are easily distinguishable from one sample image (four edge lines and four intersection points).

The segmentation steps are depicted as follows, as shown in Figure 4.10:

(i) A contrast adjustment is applied to the original image to provide a brighter contrast of the black/white feature. Then a Gaussian filter is applied for smoothing the noisy edges in the image (Figure 4.10.A).

(ii) The *Sobel* edge detector is used to generate a binary edge image. A hough transform is used then to segment all lines in the image (Figure 4.10B).

(iii) All the lines detected are clustered to multiple groups only based on their directions (Figure 4.10.C).

(iv) Using the mean angle of each line group to represent it, from all groups, one pair of groups with the most orthogonality are selected (Figure 4.10D-E).

(v) Inside each of the groups selected, the lines are clustered again to another two subgroups based on the moment of lines (Figure 4.10.F-G-H). By averaging each subgroup, the four edge lines are obtained.

(vi) The four intersection points are calculated based on the four detected edge lines (Figure 4.10.I).

(vii) The position of this marker is calculated as the centroid of the four intersection points. The orientation is obtained by averaging the parallel lines and then re-adjusting to satisfy the orthogonality (Figure 4.10.L).

4.5.2 Tracking multiple *X* markers attached on a continuum robot

Segmenting multiple *X* markers simultaneously is much more challenging than segmenting a single *X* marker under microscope because:

- The black/white edges or corners are not occupying most of the view making these features not unique anymore.
- The difficulty in balancing between maximizing the number of markers attached and maximizing the size of each individual marker, which eventually leads to almost pixelated images of individual markers.

To solve these challenges, a method is implemented here based on Harris feature detection, Delaunay triangulation and an extrema intensity gradient method [110].

The segmentation steps are shown in Figure 4.11 and explained as follows:

(i) The original image is first adjusted automatically to have stronger contrast, making the *X* marker features more detectable (Figure 4.11.A).

(ii) A Harris feature detection is applied (Figure 4.11.B). All of the red scatters are detected as Harris corner features, which introduce many false undesirable corners.

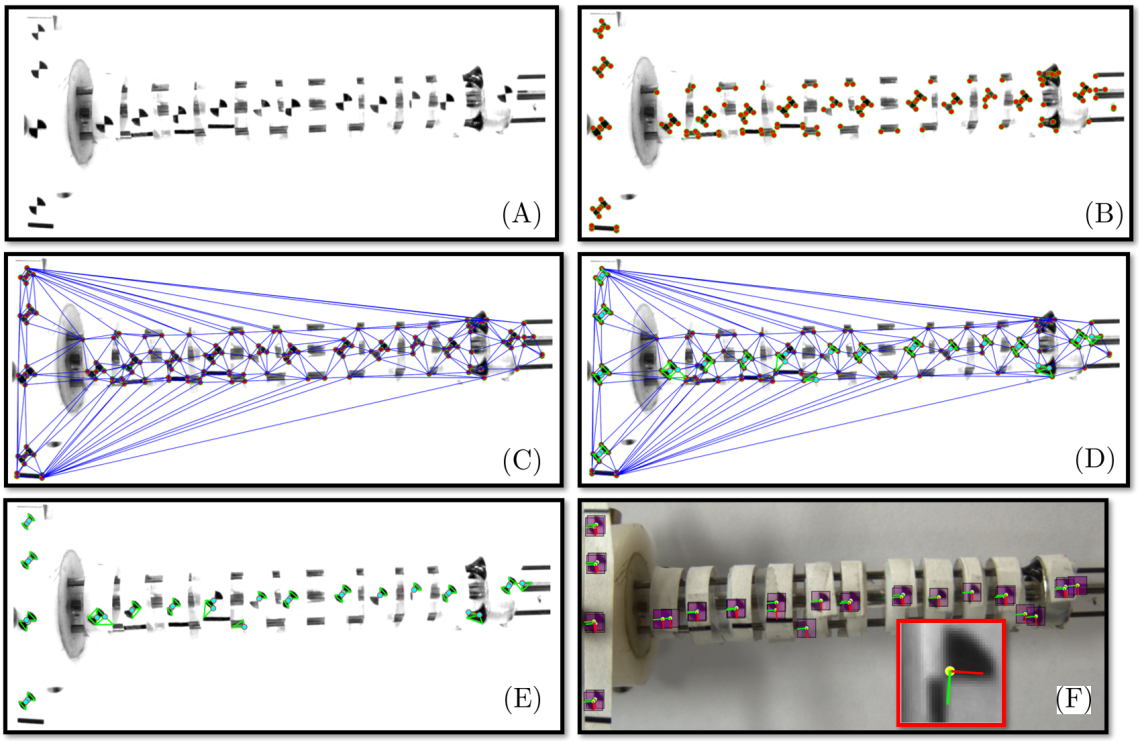

Figure 4.11: Image segmentation steps of multiple *X* markers attached to the body of a continuum robot for capturing the shape information

(iii) A Delaunay triangulation process is applied (Figure 4.11.C), resulting in a triangle mesh that connects all the detected points from the previous step.

(iv) Special features are noticed from each *X* marker:

- Right angle triangle
- An approximal range lengths of legs

Taking advantage of these conditions, the triangles that are close to *X* markers are identifiable (Figure 4.11.D).

(v) The triangles that are not qualified for the previous conditions are removed, leaving approximately most of the centers of all *X* markers. (Figure 4.11.E)

(vi) Square masks that are centered at the selected corners are used to process each *X* marker (Figure 4.11.F).

The size of the square mask is approximately the diameter of the *X* marker. From this

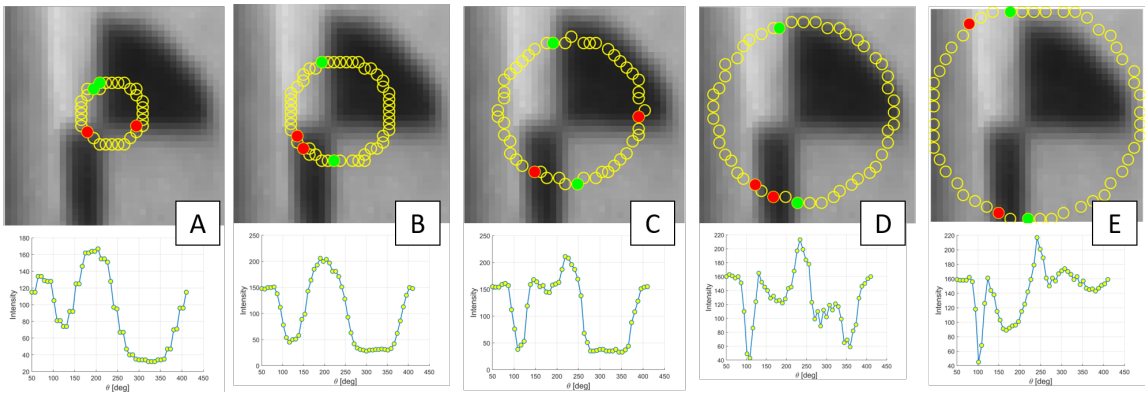

Figure 4.12: Image segmentation of one X marker from multiple marker arrangement

step, a position and an orientation is provided from each marker following [110]. The implementation details are shown in Figure 4.12 and explained below.

As shown in Figure 4.12, a set of discrete pixels along a circle with a given radius are used to sample the intensity. Considering all the points on this circle, four extrema can be found if the circle is complete and these four points can be used to identify the position and orientation of this marker. The key challenge in segmenting one of multiple X markers is to maintain a strong stability even in cases where the image is pixelated. This is achieved by first calculating extrema points using different radii then finding global maximal and minimal intensity gradients.

4.6 Experimental results

Tracking Method	**Macro Im. Proc. Time [sec]**	**Micro Im. Proc. Time [sec]**		**Total Time [sec]**
		Position	Tip Ang.	
Color circle	0.1681	2.0395	0.5775	2.7851
Gray circle	0.1361	1.4962	0.0956	1.7279
X marker	0.4925	0.1097		0.6022

Table 4.2: Computation time using X markers compared to the color circle marker method.

The results of segmenting the two example images using the method in this section

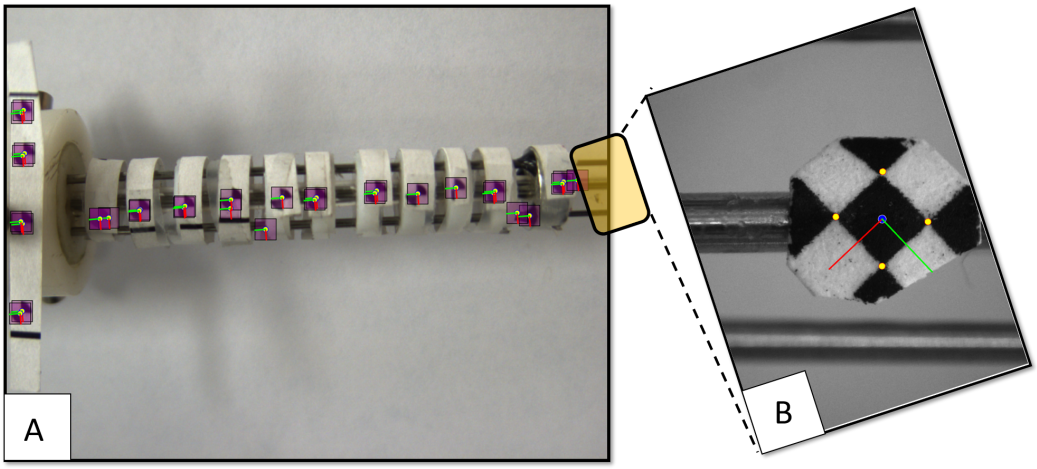

Figure 4.13: Examples of segmentation results using *X* markers: (A) captures the shape the continuum robot by segmenting the positions and orientations of multiple *X* markers and (B) captures the position and orientation under a microscope using an *X* marker

are shown in Figure 4.13 and the computational cost compared to the previously discussed methods is shown in Table 4.2. From the comparison table, one can see that using a single *X* marker can significantly reduce the computation cost for tracking micro motion under a microscope. However it is more expensive computationally to capture the robot shape in the current stage of implementation than the previous *markerless* method.

4.7 Micro Markers Tracking Testing and experimental setup

Using results from the previous section, Figure 4.14.A shows an acquired image of a marker mounted on the tip of the continuum robot. The image is processed to obtain position and orientation of the marker in order to track the position and orientation of the continuum robot tip. In a single experiment the equilibrium modulation wires are fully inserted through the entire length of continuum robot and an image is acquired every insertion step. The Figure 4.14.B shows the position of the marker center over a single experiment. The unclear position of the points, due to the poor resolution of the marker and image processing method, sensitivity to environmental lighting conditions, required significant improvement in the image segmentation ,optical tracking and optical marker

design. Therefore, to achieve micro-motion real time tracking it is required to investigate different building materials and different designs for a new marker to obtain its position and orientation, together with a more accurate and faster image segmentation method for real time marker tracking.

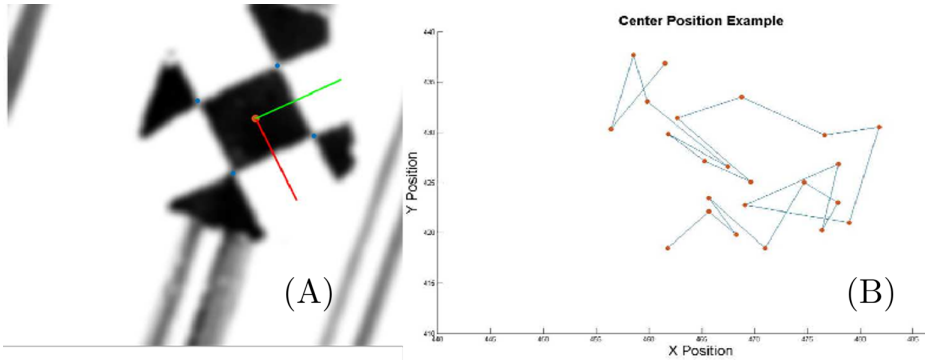

Figure 4.14: Single X marker segmentation: (A) Captured and processed micro-motion image of the robot. (B) Recorded position of the marker center during a single experiment

In the following sections, a new marker along with a new image processing and real time tracking of the continuum robot tip during micro-motion are described.

4.8 Micro-Motion Tracking Using Photomask Circle Markers

To overcome robustness and accuracy limitations of micro-motion tracking methods tested in the previous section, a new design for the micro marker and a new image segmentation method for tracking it in real time are presented. While X markers were more robust than color-based markers, they still exhibited errors due to poor definition of their edges and sensitivity to environmental lighting. These problems led to use a different material and marker fabrication method and the use of dedicated lighting. To overcome limitations of edge definition in printed markers, a single circle marker (Figure 4.15.A) was fabricated using a photomask sheet made by www.outputcity.com. To segment the circles in the new marker, the following steps are applied:

- A "RGB2bw" conversion is applied first to convert the image to black an white.

- A *Hough* circle transformation is applied to identify circles in the image as shown in Figure 4.15 (B)
- The last step is removing other undesired circles by thresholding the radius of detected marker in order to obtain the identify the desired circle 4.15 (C).

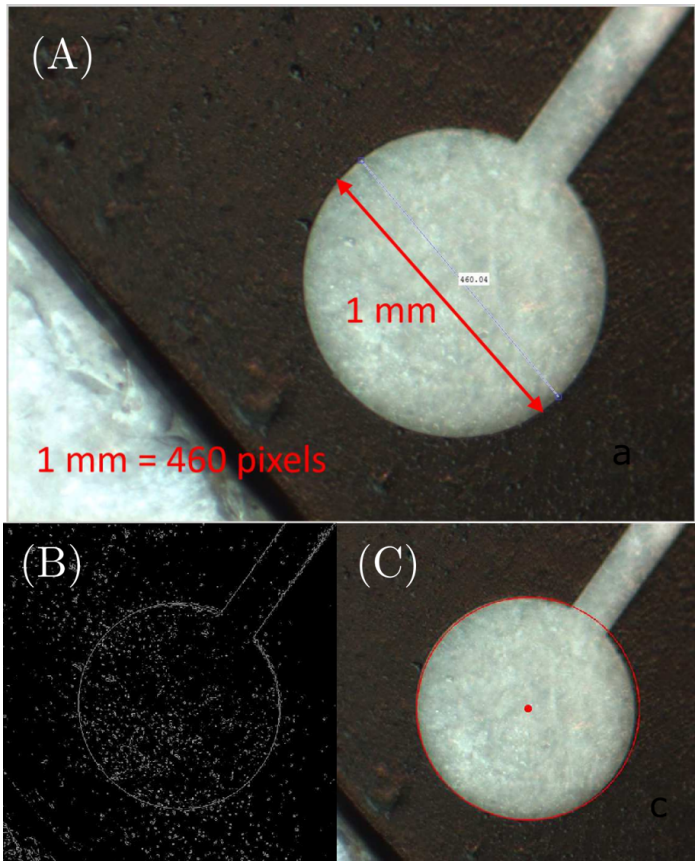

Figure 4.15: Single Circle Photomask marker: (A) Circle definition and pixels conversion. (B) Processed image. (C) Circle center identification

Using the new marker, the tracking results were substantially improved. Figure 4.16 (A) shows the position of the marker center over 40 pictures acquired while the continuum robot tip was kept stationary. The plot shows a maximum deviation of 1 μm along y direction and 2 μm along x direction. Figure 4.16 (B) shows the result of tracking the center circle during micro-motion of a single segment continuum robot. The plot shows a significant improvement in motion tracking compared to the result of the same experiment when using

the *X* marker (Figure 4.2 (B)).

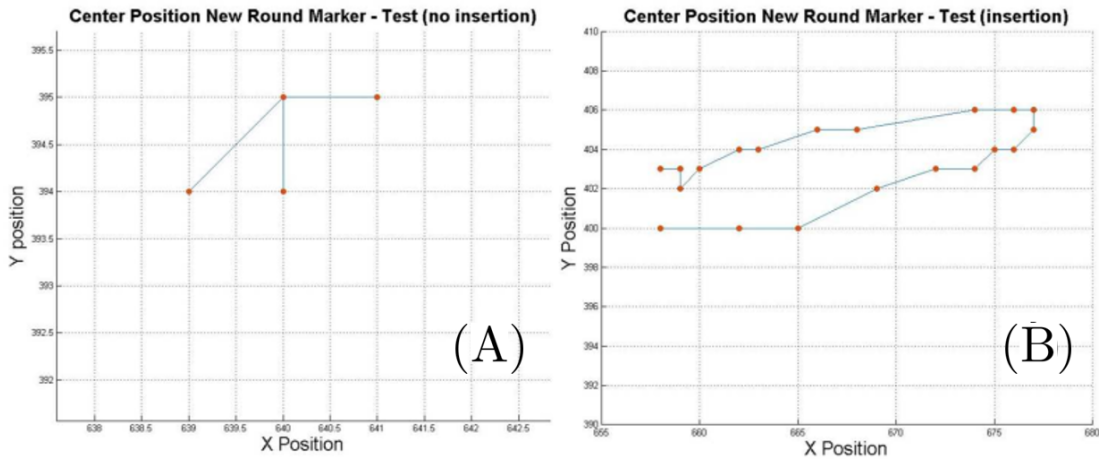

Figure 4.16: Results of Single circle marker strategy: (A) Stationary marker test results. (B) Tracking result for micro-motion.

Once the new marker segmentation has been defined for position tracking, we needed to track the orientation of the marker . We have addressed this requirement by designing a final new marker geometry as explained in the next session.

4.9 Micro-motion Tracking

As shown in Figure 4.17, different geometries were designed and tested together with an 144 LED Microscope Ring Illuminator mounted on the camera for optimal lightning condition and avoid any shadow on the marker. The final new marker was defined by three circles of 250 μm in radius, located in a specific pattern that uniquely identify marker position and orientation as shown in Figure 4.18 (B).

Given the new marker, the following steps are applied following the previous circle segmentation procedure in order to define the position and orientation of the marker:

- Each image is converted to B/W and each circle is segmented using the Hough circle method to obtain the centers of all markers.
- Vectors are defined between all circle pairs

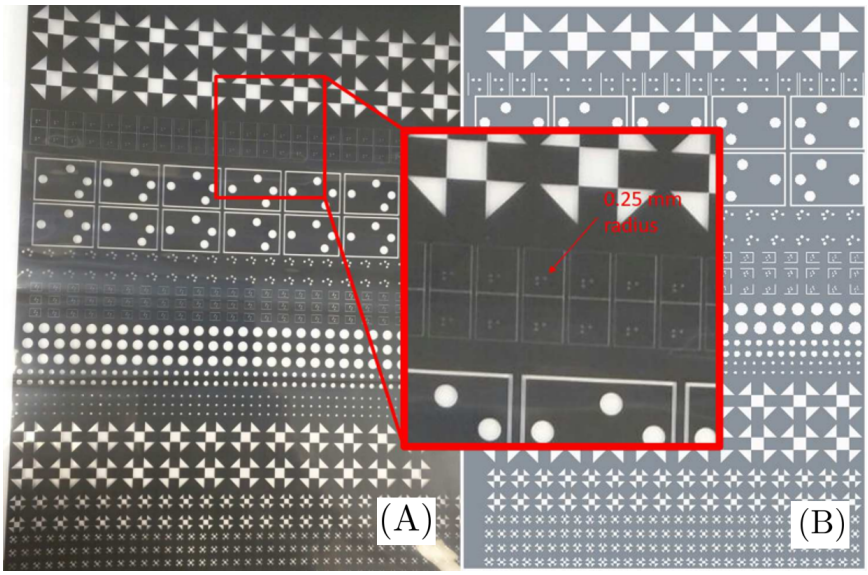

Figure 4.17: Tested designs of markers made out of photomask material: (A) Photomask printed sheet (B) Photomask sheet cad model

- The lengths of the vectors and relative angles between them are used to prune and sort the vectors to match the known marker template.
- Using the sorted vectors matching the marker template, the center and orientation of the marker frame relative to camera frame are calculated.

Once the image segmentation method for the new final marker is defined, the next section presents the experimental evaluation for asses the robustness of such marker and image segmentation framework.

4.10 Experimental Evaluation

4.10.1 Vision Tracking Accuracy

One challenging aspect of this work has been the evaluation of accuracy and repeatability of the micro-motion tracking method. There are several devices on the market for micro-motion tracking. Due to the high sensitivity of the entire experimental apparatus to vibration, it has been impossible to design or use any manually actuated device in order

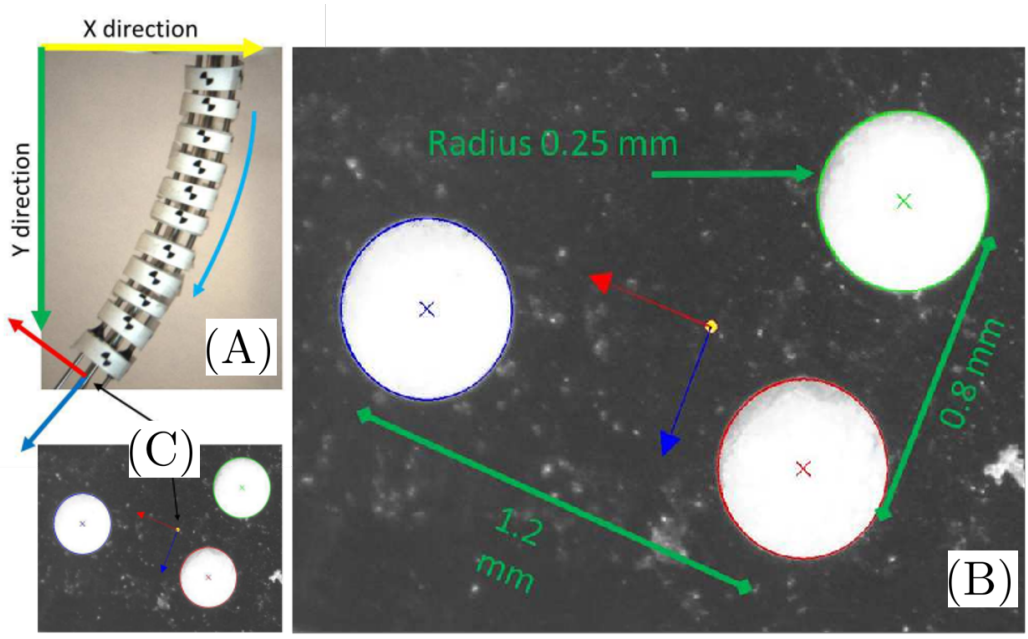

Figure 4.18: Three circles marker: (A)(C) Frame correspondence between marker frame and EE Frame (blue and red arrows), robot/camera frame(yellow and green arrow). (B) Three circles marker specifications

to compare the real motion displacements against the measurements obtained from our method.

Due to these difficulties, in order to have a way to evaluate the accuracy and repeatability of the presented micro-motion tracking method, we designed two sets of experiments. The first experiment used 6 sets of 45 pictures of the marker taken while the marker was attached to a fixed frame. *Box plots* of the X and Y coordinate values over the 6 sets are reported in Figure 4.19. The boxes contain samples between the first and third quartiles of the data. The box plot shows an overall maximum error range over the measurements of $0.8\mu m$ in the X direction and $0.5\mu m$ in the Y direction. The marker center position in one set of the experiments is shown in Figure 4.20, it shows that the center marker positions acquired from the segmentation method has an error in repeatability of $\pm 0.4\mu m$ in the Y direction and $\pm 1.4\mu m$ in the X direction. This first set of experiment was designed to provide a baseline for defining the repeatability of the image processing method described

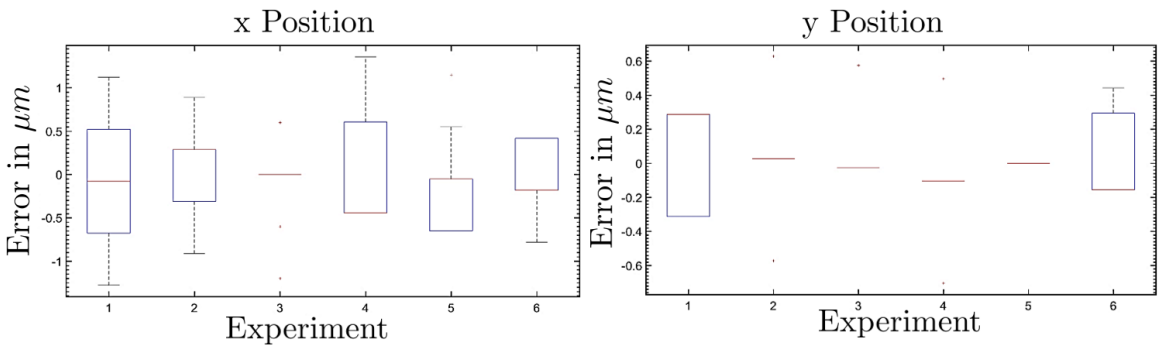

Figure 4.19: Marker center position error on X and Y direction respectively along 6 set of experiments

in the previous sections.

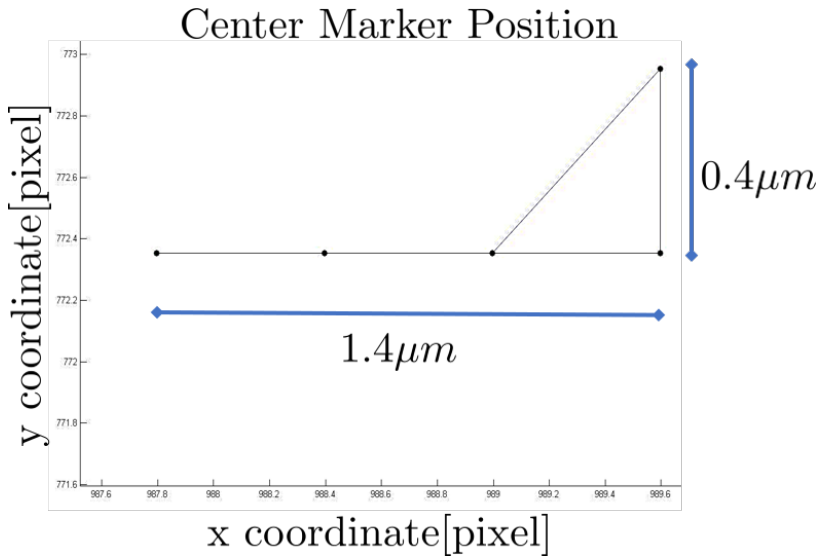

Figure 4.20: Marker tracking result over 1 set of experiment

The second set tested the micro-motion tracking accuracy. A multi-circle tracking marker, rigidly attached to a Parker Micrometer Cartesian Stage M4434, was moved repetitively back and forth 200 microns($\pm 2\mu m$ Parker stage accuracy) in the Y direction. A picture was acquired at every pose for a total of 30 pictures. Every picture was processed and the locations of the marker centers recorded. Figure 4.21.A displays X and Y coordinates for the 30 images. The Y component(diamond) moves about $200\mu m$ between each image and the X component(star) maintains the same value, accordingly with the

experiment setup. Figure 4.21.A shows the vertical distance between the markers' centers at each consecutive image, varying between 202.8μm and 203.5μm.

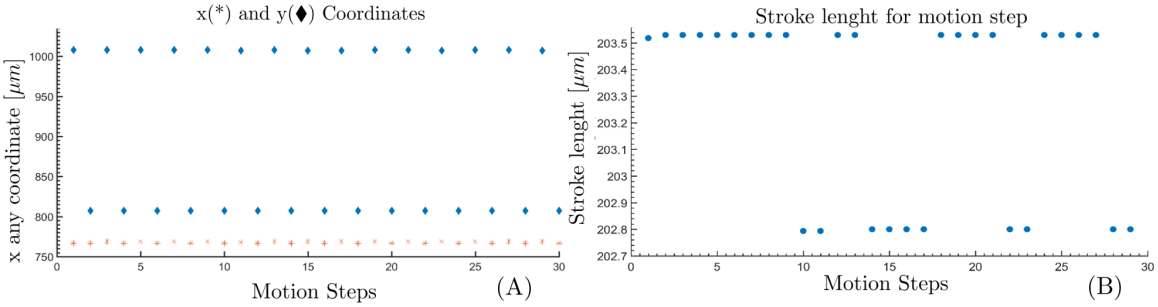

Figure 4.21: Evaluation measurements: (A) Stroke length for motion step, (B) X(*) and Y(diamond) coordinates of the marker center position

In conclusion, we have verified that the positional tracking accuracy is better than 1μm for a fixed and a slowly moving marker. The results in Figure 4.21 also verify this tracking accuracy for a micrometric linear stage with an estimated error of $\pm 0.2\mu m$ due to user error when rotating the micrometer.

4.10.2 Micro-Scale Motion via Equilibrium Modulation

To evaluate the feasibility of micro-motion via equilibrium modulation and to assess the end effector accuracy and repeatability we have used the experimental setup of Figure 4.1 and induced equilibrium modulation using the modulation wires in 5 different bending configurations of the continuum segment. Each configuration is identified by two parameters δ and θ_L as defined in [26]. θ_L is the angle between the horizon and the normal to the end disk of the segment while angle δ is the angle of the plane in which the segment bends. While keeping $\delta = 90$ we tested 5 different configurations as shown in Figure 4.22.C.

To evaluate repeatability, we carried out 10 sets of experiments for each configuration. During a single experiment the 3 insertion wires were inserted using a speed of 0.5 mm/s. The wires were stopped at increments of 1 mm insertion to allow image acquisition of the multi-circle marker for a total of 45 images per experiment.

The motion tracking results using multi-circle marker are shown in Figure 4.23 and

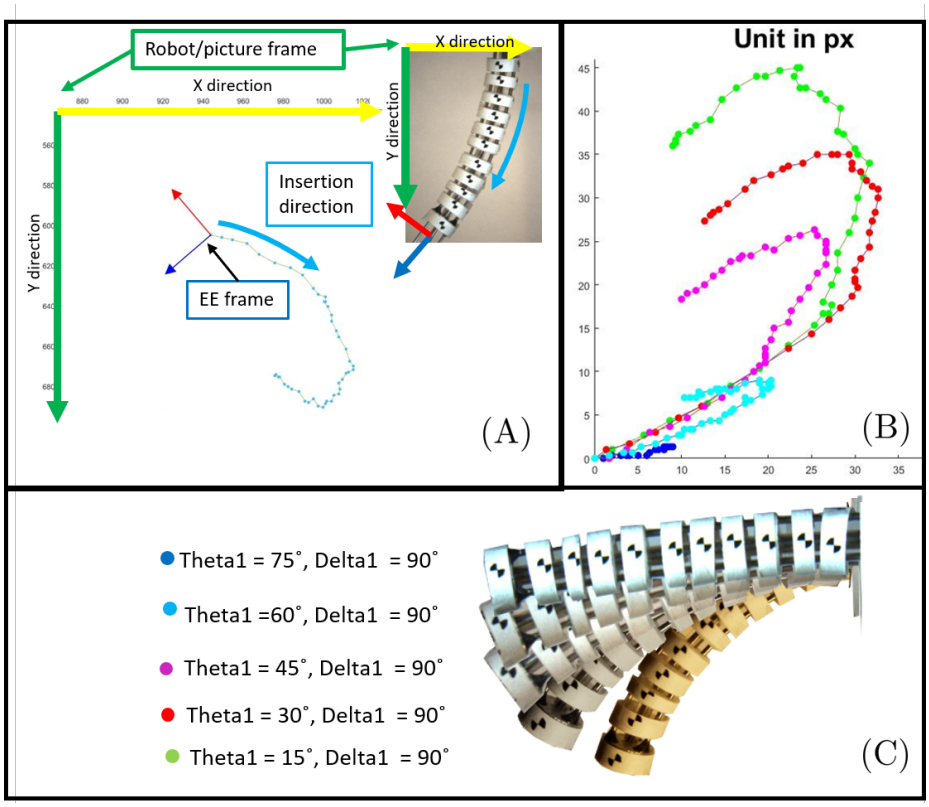

Figure 4.22: Micro-scale motion via equilibrium modulation: (A) Frames assignment for micro-motion tracking (B) Micro-motion tracking result example for each CR configuration (C) CR configurations

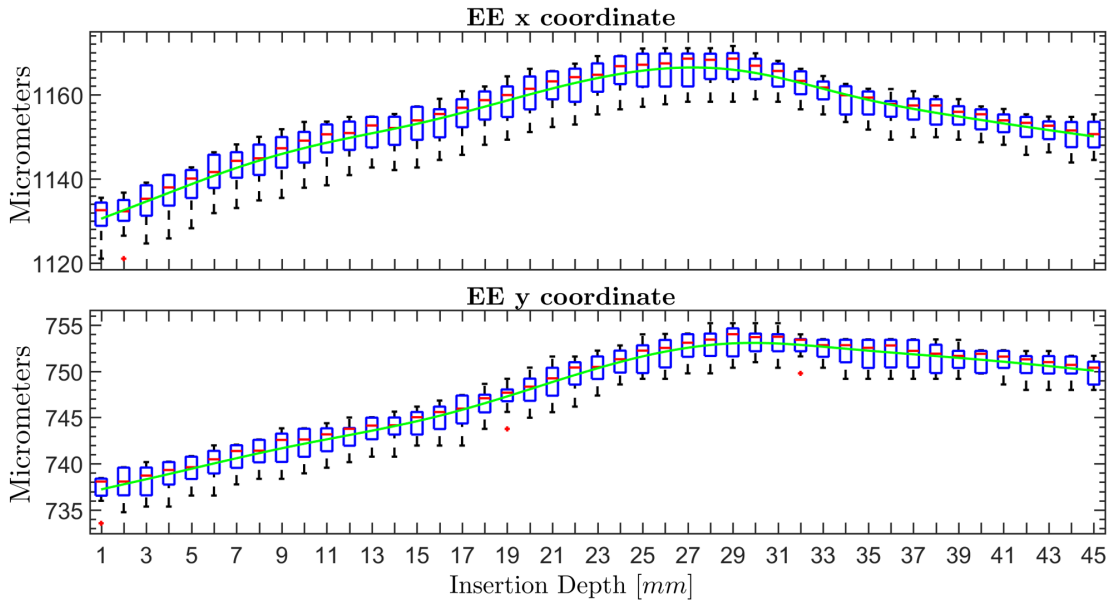

Figure 4.23: Experiment result: X and Y coordinate box plot of micro-motion tajectory in $\theta = 60^{\circ}$ configuration

Table 4.3. Figure Figure 4.23 shows the *box plot* for the X and Y coordinate values of the marker center over the entire insertion travel, for $\theta_L = 60^\circ$.

Table 4.3 summarizes the results from the 5 configurations reporting the largest and smallest amount of error along the X and Y directions that correspond to largest and smallest squares of the box plots, it also reports the value of the standard deviation of the overall error values in the 10 trials.

Table 4.3: Position variations (in μm) for 10 repetitions per each of the 5 continuum robot configurations of Figure 4.1.C

Config.	Max/Min X-error†	STD on X	Max/Min Y-error	STD on Y
①	16/9	6.9	3.5/1	1.3
②	8/3	4.03	3/1.5	1.48
③	24/12	10.02	12/10	6.76
④	12/1	5.40	7/1	3.29
⑤	40/26	21.35	31/14	16.20

† The linear actuators used to drive the NiTi wire have a manufacturer-specified backlash of 200 microns

Figure 4.24 shows a polynomial spline fit, based on the boxplot analysis, along the X and y direction for the 5 different CR configurations over the 10 experiments. We note that these motion results were obtained despite the use of the Velmex linear slides with plastic nuts having backlash of $200\mu m$.

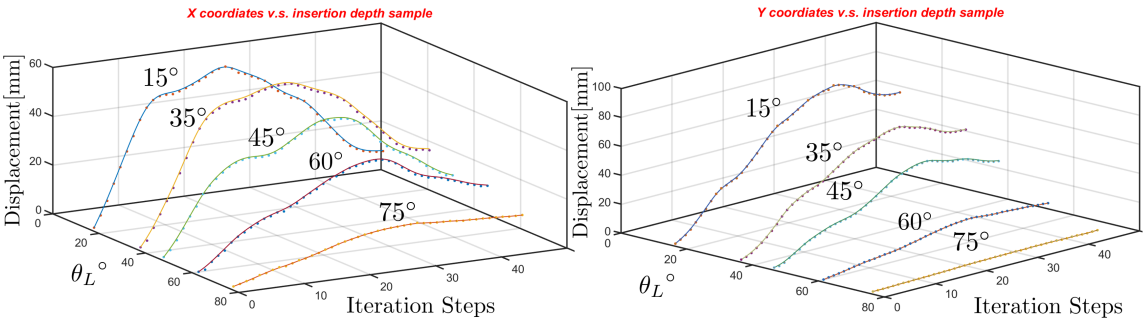

Figure 4.24: Mciro-motion trajectories: polynomial spline fitting of X and Y coordinates trajectory obtained over the 10 set of experiments in the 5 different CR configurations

4.11 Conclusion

Different tracking markers design, manufacturing techniques, image segmentation method were presented.. Using custom markers and image processing algorithms we demonstrated tracking accuracy with errors less than $1\mu m$. We also evaluated a CREM prototype and showed that the robot can move with high repeatability of less than $10\mu m$ while the motion resolution is sub $2\mu m$. We observe (Figure 4.22.B) that in early stages of equilibrium modulation wire insertion, a bent continuum segment moves in a direction of straightening its shape. As the wires are inserted deeper a turning point occurs in which the monotonous relationship between wire insertion and segment straightening is reversed: further insertion of the wires corresponds with an effect of "turning point" during which the segment recovers some of its bent shape. This behaviour led us to the next chapter of this thesis where the efforts over the modeling for the micro-motion and the investigation for the source of the turning point phenomenon are presented.

CHAPTER 5

MODELING CREM KINEMATICS

5.1 Introduction

Most works on kinematic modeling assume circular bending of the CR segments [81, 111, 112]. Few exceptions include [113]which addressed the exact kinematics and statics of multi-backbone CRs and [114, 115] who addressed the exact statics and dynamics of a continuum robot having a single central backbone actuated by wires. Works on control of continuum robots primarily include works on position control and motion control. These robots require actuation compensation to overcome flexibility effects and modeling inaccuracies. Friction modeling [116], backlash identification and cancellation [117][64], extension of actuation lines [118], and kinematic coupling between serially-stacked segments [3] have been investigated in order to modeling motion compensation for CR. Furthermore, extensive works have been done over closed-loop control strategies which include the use of sensors and multiple control loops closed at different levels. For example, researchers have investigated single-camera vision algorithms [119], multi-camera vision methods [120], string pots and encoders [121], and electro-magnetic trackers [122] to provide information about the current configuration of the continuum manipulator.

To the best of our knowledge, there have been no prior works on modeling and control for equilibrium modulation of continuum robots. As it was observed in the previous chapter through EE tracking during experiments, a counterintuitive turning point behavior occurs during insertion of the insertion wires. This chapter proposes new modeling and closed-loop control approaches for continuum robot with equilibrium modulation, explaining the

"turning point" behaviour, enabling unprecedented fine motion at the micro scale.

In section 5.2 is presented the first approach on modeling the CREM system based on moment coupling between the portion of the continuum segment that contains the insertion wires during micro-motion and the empty part of it. Section 5.5.2 presents an energy minimization approach that provides insight into *why* the turning point behavior occurs and predicts an *ideal turning point behavior*, but in experimental data (as shown in Figure 4.22.A) on page 69, we observe that the tip position does not completely return to the starting point after the insertion wires are fully inserted. We call this the *observed turning point behavior*. We believe this is caused by unmodeled energy dissipation (e.g. friction, hysteresis), which are nontrivial to incorporate into a mechanics model. For this reason, in section 5.5.3 we present a purely kinematics-based model that modifies one of the kinematic model parameters (the bending angle β) to replicate the observed turning point behavior. Finally, in section 5.6.1 we present a third approach based on an experimental data which provides empirical derivation of the micro-motion Jacobian, which accounts for unmodeled effects that may shift the turning point from its theoretical value.

5.2 Simplistic Moment-coupling Effects approach

This section presents the first approach for modeling the CREM based on internal moment coupling of the continuum segment when equilibrium modulation is active. For a thorough presentation of the applied method and for a deep explanation of the results, we refers the reader to [109]. To motivate the modeling approach taken we will first refer the readers to [2] where a generalized modal approach to the kinematics of continuum robots was presented. In practice, when the constraint wires were not inserted, the continuum segment bends in a constant curvature and the kinematics was solved in [2]. For a given insertion depth of the constraint wires, the radius of curvature was no longer constant throughout the segment length. Using the approach in [2], it was trivial to modify the kinematics for a given profile of radius of curvature along the length of the continuum

segment. We will therefore focus below on presenting the preliminary approach of Wang et al. [109] to modeling the equilibrium shape for a given insertion depth of the constraint wires.

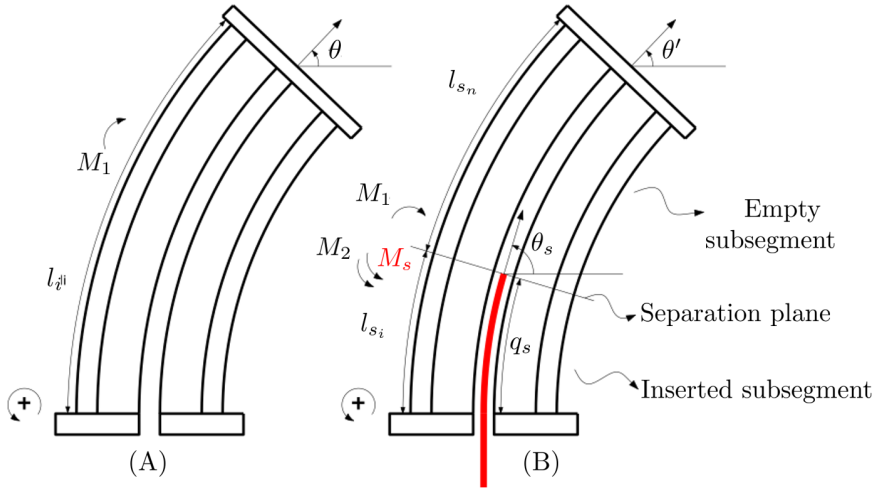

Figure 5.1: Example of a bent snake segment inserted with a stiff wire

Figure 5.1.A shows a continuum segment that has no constraint wires inserted. Figure 5.1.B shows the equilibrium shape when a stiff constraint wire was inserted in the primary backbone of a multi-backbone continuum segment. A separation plane may be defined up to the insertion point, dividing the segment into two sub-segments - *Inserted* and *Non-inserted*. It was also assumed that the two sub-segments each have constant curvatures, but the two curvature values were different. The angles θ', θ_s and θ_0 denoted the end-disk angle, the bending angle at the separation plane and the tangent angle at the end disk, respectively, while θ denoted the tip angle before insertion of the micro-motion wire. The moment M_1 denoted a reaction produced by the empty subsegment and it was applied at the separation plane. In addition, M_1 was the same as the moment along the entire segment when no wire was inserted as in Figure 5.1.A. M_2 denotes the moment produced by the backbones of the *Inserted* sub-segment and M_s denotes the moment produced by the inserted stiff wire. Writing M_1, M_2 and M_s in a torsional spring format, according to [109] we obtain:

$$M_1 = k_0(\theta - \theta_0), \quad k_0 = \frac{E_p I_p}{L} + \sum_i \frac{E_i I_i}{l_i} \tag{5.1}$$

$$M_1 = k_1(\theta' - \theta_s), \quad k_1 = \frac{E_p I_p}{L - q_s} + \sum_i \frac{E_i I_i}{l_{n_i}} \tag{5.2}$$

$$M_2 = -k_2(\theta_s - \theta_0), \quad k_2 = \frac{E_p I_p}{q_s} + \sum_i \frac{E_i I_i}{l_{s_i}} \tag{5.3}$$

$$M_s = -k_s(\theta_s - \theta_0), \quad k_s = \frac{E_s I_s}{q_s} \tag{5.4}$$

where $E_p I_p$ and $E_i I_i$ denote the bending stiffness of the central backbone and the i^{th} secondary backbone, respectively. Symbol l_{s_i} denotes the length portion of the i^{th} secondary backbone that belongs to the *Inserted* subsegment and l_{n_i} denotes the length portion that belongs to the *Non-inserted* subsegment. L and L_i denote the lengths of the central backbone and the i^{th} secondary backbone, i.e. $L_i = l_{s_i} + l_{n_i}$ Referring to Figure 5.1.B we use the following static equilibrium equation:

$$M_1 + M_2 + M_s = 0 \tag{5.5}$$

To obtain the equilibrium shape, we seek a solution for θ' given $\{\theta, \delta_i, q_s\}$ as the following:

$$\theta_s = \frac{k_1\theta' + k_2\theta_0 + k_s\theta_0}{k_1 + k_2 + k_s} \tag{5.6}$$

$$\theta' = \frac{k_0}{k_1}(\theta - \theta_0) + \theta_s = f_{\theta'}(\theta_s) \tag{5.7}$$

Equations (5.6) and (5.7) present an idealized model ignoring friction and modeling uncertainty. However, as discussed in [83, 123], unmodeled uncertainties may occur, including friction and strain along the actuation lines, perturbations from the circular-bending shape of the individual segments, deviations in the cross section of the backbones during bending, and uncertainties in the elastic properties of the NiTi backbones. To

address these uncertainties, and inspired by [83, 123], an uncertainty term $\lambda(q_s, \theta, \mathbf{k}_\lambda)$ is introduced as a function of variables $\{q_s, \theta\}$ and a vector representing the values of the parameters denoted as $\mathbf{k}_\lambda \in \mathbb{R}n_k$. Then the static equilibrium equation (5.5) and the solution equation (5.6) are updated as the following:

$$M_1 + M_2 + M_s = \lambda(q_s, \theta, \mathbf{k}_\lambda) \tag{5.8}$$

$$\theta_s = \frac{k_1\theta' + k_2\theta_0 + k_s\theta_0 - \lambda}{k_1 + k_2 + k_s} \tag{5.9}$$

As a result of the equilibrium shape modeling, we are able to solve the equilibrium tip bending angle θ' and the bending angle at the separation plane θ_s given the nominal tip bending angle θ, the bending plane angle δ, and the insertion depth q_s.

Then referring to the definition of *configuration space* variable ψ in [2] and allow us to introduce a new *equilibrium configuration space* variable ϕ, defined as:

$$\phi \triangleq [\theta_s, \theta_r]^{\mathrm{T}}, \quad \psi \triangleq [\theta, \delta]^{\mathrm{T}} \tag{5.10}$$

$$\theta_r \triangleq \theta' - \theta_s + \pi/2 \tag{5.11}$$

where θ_r represents the *relative* bending angle which is prepared for the kinematic modeling for later sections. The equilibrium shape modeling may then be described as a mapping $\mathcal{F}_{\mathrm{eqm}}$ which provides ease in deriving the Jacobians in later sections:

$$\boxed{\phi = \mathcal{F}_{\mathrm{eqm}}(\psi, q_s, \mathbf{k}_\lambda), \quad \phi \in \mathbb{R}2, \psi \in \mathbb{R}2, \mathbf{k}_\lambda \in \mathbb{R}n_k} \tag{5.12}$$

Equation (5.12) is the key equation resulting in the equilibrium pose of the end disk of a continuum segment for any given wire insertion length. This equation is next used to derive micro-motion instantaneous kinematics Jacobians that are necessary for control purposes. Note that this model includes a parametrization of modeling uncertainty $\mathbf{k}_\lambda$ and will be used for kinematic identification and calibration of micro-motion models these robots.

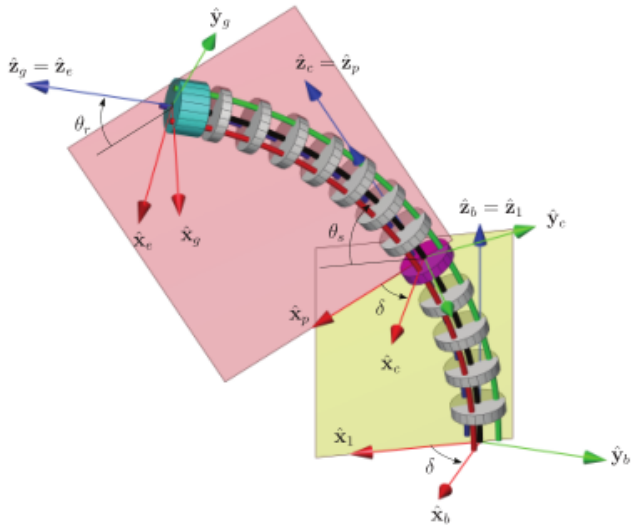

Figure 5.2: A single segment treated as two serially connected sub-segments for a given micro-motion wire insertion depth.

We assumed that the constraint wires were inserted in synchrony to depths corresponding to arc length $s = q_s$ along the central backbone. To reflect this change, we will define the augmented joint space vector as $\mathbf{q} = [q_1, q_2, q_3, q_s]^T$.

Table 5.1 and Figure 5.2 present the nomenclature used in this section. The position and the orientation of the insertion frame $\{C\}(q_s)$,

Once the homogenous transformation $\mathbf{T} \in \mathrm{SE}(3)$ that represents the location and orientation of the EE is calculated as:

$$\mathbf{T} = \begin{bmatrix} {}^{b}\mathbf{R}_g & {}^{b}\mathbf{g} \\ \mathbf{0} & 1 \end{bmatrix} = \mathbf{T}(\phi, \delta, q_s) \tag{5.13}$$

it possible to derive the full differential kinematic relation, expressed as:

$$\begin{aligned} {}^{b}\Delta_{\mathbf{T}} = \;& \mathbf{J}_{\mathbf{x}\phi}\, \mathrm{d}\phi + \mathbf{J}_{\mathbf{x}\delta}\, \mathrm{d}\delta + \mathbf{J}_{\mathbf{x}q_s}\, \mathrm{d}q_s \\ & \mathbf{J}_{\mathbf{x}\phi} \in \mathbb{R}6 \times 2,\ \mathbf{J}_{\mathbf{x}\delta} \in \mathbb{R}6,\ \mathbf{J}_{\mathbf{x}q_s} \in \mathbb{R}6 \end{aligned} \tag{5.14}$$

In (5.14), the Jacobian matrix $\mathbf{J}_{\mathbf{x}\phi}$ relates the small change in equilibrium bending

Table 5.1: Nomenclature for Kinematic Modeling

Symbol	Description
Frame {F}	designate a right-handed frame with unit vectors $\hat{\mathbf{x}}_f, \hat{\mathbf{y}}_f, \hat{\mathbf{z}}_f$ and $\mathbf{f}$ as its origin.
Frame {B}	the base disk frame with $\mathbf{b}$ located at the center of the base disk, $\hat{\mathbf{x}}_b$ passing through the first secondary backbone and $\hat{\mathbf{z}}_b$ perpendicular to the base disk.
Frame {1}	characterizes the plane in which the snake segment bends, $\hat{\mathbf{z}}_1 = \hat{\mathbf{z}}_b$ and $\hat{\mathbf{x}}_1$ passing through with the project point of the end disk center. The angle δ is defined as from $\hat{\mathbf{x}}_1$ to $\hat{\mathbf{x}}_b$ about $\hat{\mathbf{z}}_b$ according to right hand rule.
Frames {E} & {G}	Frame {E} is defined with $\hat{\mathbf{z}}_e$ as the normal to the *end* disk and $\hat{\mathbf{x}}_e$ is the intersection of the bending plane and the end disk top surface. Frame {G} is the *gripper* frame that has the same $\hat{\mathbf{z}}$ as {E}, i.e. $\hat{\mathbf{z}}_g = \hat{\mathbf{z}}_e$, but $\hat{\mathbf{x}}_g$ is passing through the first secondary backbone. It can be obtained by a rotation angle $(-\sigma_{1e})$ about $\hat{\mathbf{z}}_e$.
Frames {P}(q_s) & {C}(q_s)	associated with the micro insertion arc length q_s. These frames are defined in a manner similar to the definition of frames {E} and {G} but for a specific arc insertion length q_s as opposed to the full length of the robot segment L. The $\hat{\mathbf{x}}_c - \hat{\mathbf{y}}_c$ plane is the insertion plane as in shown in the planar case in Figure 5.1

angles $\phi = [\theta_s, \theta_r]^{\mathrm{T}}$ to the differential motion vector, the second Jacobian $\mathbf{J}_{\mathbf{x}\delta}$, relates the small change in the bending plane angle δ to the differential displacement ${}^b\Delta_{\mathbf{T}}$, the third Jacobian $\mathbf{J}_{\mathbf{x}q_s}$, relates the change in the insertion depth q_s to the end-effector pose $\mathbf{x}$, assuming ϕ does not change.

Finally, the full differential kinematics that relates small change in $\{\psi, q_s, \mathbf{k}_\lambda\}$ to the differential displacement ${}^b\Delta_{\mathbf{T}}$ is obtained:

$$
\begin{aligned}
{}^b\Delta_{\mathbf{T}} = \; & \underbrace{\left[\begin{array}{c:c} \mathbf{J}_{\mathbf{x}\phi}\mathbf{J}_{\phi\theta} & \mathbf{J}_{\mathbf{x}\phi}\mathbf{J}_{\phi\delta} + \mathbf{J}_{\mathbf{x}\delta} \end{array}\right]}_{\mathbf{J}_M} \mathrm{d}\psi + \\
& \underbrace{\left[\mathbf{J}_{\mathbf{x}\phi}\mathbf{J}_{\phi q_s} + \mathbf{J}_{\mathbf{x}q_s}\right]}_{\mathbf{J}_\mu} \mathrm{d}q_s \; + \; \underbrace{\mathbf{J}_{\mathbf{x}\phi}\mathbf{J}_{\phi\mathbf{k}_\lambda}}_{\mathbf{J}_{\mathbf{k}}} \mathrm{d}\mathbf{k}_\lambda
\end{aligned}
\tag{5.15}
$$

Therefore, $\mathbf{J}_M$ is defined as the *Macro* motion Jacobian, $\mathbf{J}_\mu$ is defined as the *Micro* motion Jacobian and $\mathbf{J}_{\mathbf{k}}$ is defined as the *Identification* Jacobian.

5.3 Simulations Results of Macro and Micro Motion

In the this section are reported the results from the macro-micro motion simulation based on the framework described above. For more in depth explanation of each simulation

case and for a more thorough description of the algorithm used for each simulation method, the reader is addressed to [109].

In order to catch the "turning point" behaviour aforehand mentioned using the modeling framework presented in the previous section, an uncertainty term λ is introduced in (5.8) as a function of $\{\theta, q_s\}$, parameterized by $\mathbf{k}_\lambda$. A simulation with the modeling uncertainty is conducted at $\theta = 30^\circ$ (Figure 5.3.A), and the zoom-in tip trajectory is shown in Figure 5.3.C, alongside a simulation result at an ideal condition in Figure 5.3.B. The comparison showed that even a simplified linear function of λ created a nonlinear hysteresis behavior on the tip micro motion. In fact, the experimental results in later sections shown similar behavior on the real robot.

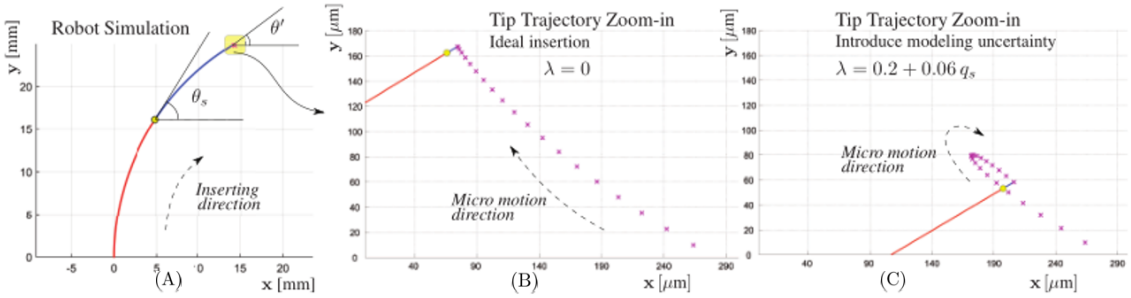

Figure 5.3: Simulations of robot wire insertions for continuum robot micro motion: (a) the entire segment when wire were inserted; (b) the zoom-in view of the tip micro motion assuming ideal condition, i.e. λ; (c) the zoom-in view of the tip micro motion assuming a linear uncertainty function.

Figure 5.4, where A and B shows the micro motion Jacobians computed for both the ideal case and the case with modeling uncertainty. Comparing Figure 5.4.A and B, we can observe how the modeling uncertainty (for example friction effects) is affecting the micro motion Jacobian significantly. While Figure 5.4.A and B shows the motion Jacobian and how the modeling uncertainty affected the motion, Figure 5.4.C reveals how the error of parameters of modeling uncertainty affect the tip position, which was the fundamental relation that we relied upon on to correct $\mathbf{k}_\lambda$.

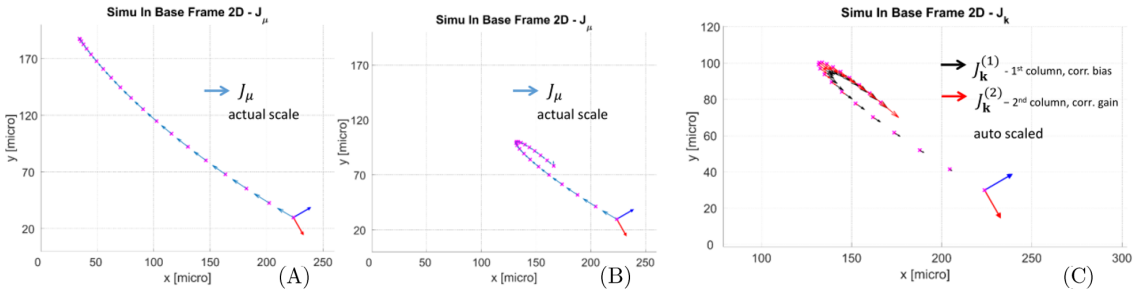

Figure 5.4: Tip velocity based on micro-motion Jacobians: (a) Using micro motion Jacobian for $\lambda = 0$; (b) Based on micro motion Jacobian in for $\lambda \neq 0$; (c) The effect of changes in $\mathbf{k}_\lambda$ on the instantaneous kinematics is used for kinematic identification

5.4 Conclusion

The first modeling attempt for the new concept of CREM, continuum robot capable of multi-scale motion, was presented in this chapter. A simplified kinematics model based on moment coupling effect within the mechanical structure of the continuum segment was discussed. The model approach led to utilize an uncertainty parameter which could compensate for the mechanical losses generated in the modeling due to the simplified model assumptions. Despite the parameters inaccuracy, the modeling framework was validated experimentally and it shows an RMS error in position of $6\mu m$ between the experimental data and the model generated trajectory over the entire EE micro-motion path. The necessity to have a more complete and accurate models for control purpose highlighted the needs to investigate new modeling approaches which are presented in the following chapter.

5.5 Modeling Micro Motion Kinematics

In the previous section we have demonstrated a method that could replicate the turning point behaviour observed in the experimental result of section 4.9. *Although we were able to replicate the behaviour, it was not explained why or how this phenomenon is generated.* This explanation is presented via an energy-minimization approach and a purely kinematics-based approach in this section. However, even if we do not use these two

models for control purpose, we believe the exposition and analysis herein provides important insight into the counterintuitive micro-motion behavior. For the purpose of control, Section 5.6.1 provides an approach that directly derives the micro-motion Jacobian from experimental data. This work was presented in [124].

5.5.1 Kinematic Assumptions and Notation

Although our formulation in Section 5.6.1 allows spatial macro-motion, in this section we utilize micro-motion within a single bending plane only. The reader is referred to [3] for a spatial model of continuum robot kinematics. In this section, we introduce the planar kinematic modeling assumptions and notation for the micro-motion, i.e. when the insertion wires are inserted through the secondary backbones.

Figure 5.5 shows the continuum segment before and after the insertion of the micro-motion wires at s insertion depth. For simplicity of description, we treat the continuum robot as two different consecutive constant-curvature subsegments. The first (*proximal*) subsegment is defined from the base disk of the continuum segment to the insertion plane generated by the tips of the insertion wires. The second (*distal*) subsegment is defined from the insertion plane to the end disk. The solid (black) outline refers to the continuum segment before the insertion of the wires. The dashed (blue) outline identifies the inserted proximal subsegment while the dotted (red) outline identifies the empty distal subsegment after insertion.

The nomenclature henceforth used is listed herein. Subscripts p and d will designate properties of the proximal and distal subsegments. Also, subscripts e and f will denote the states where the *proximal* subsegment is empty or filled with insertion wires, respectively:

- s: insertion depth arc length along the central backbone (measured from the base disk).
- Δ_i: the radial offset of the *i-th* secondary backbone from the primary backbone.

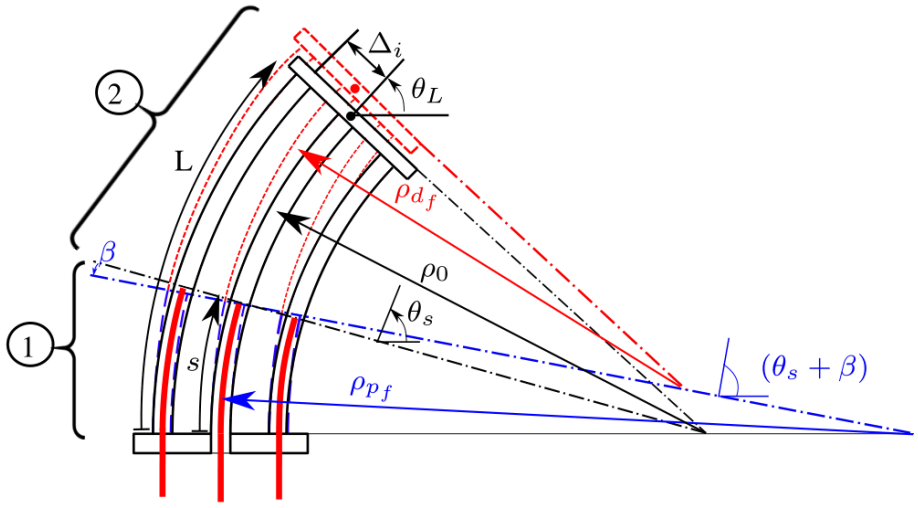

Figure 5.5: Modeling micro motion using two circular-bending subsegments. ① is the proximal subsegment terminating with the insertion plane passing through the tips of the three insertion wires. ② is the distal subsegment. Segment in solid lines is before insertion of modulation wires. Segment in dashed lines is after insertion of said wires.

- L: continuum segment central backbone length.
- L_i: length of the i^{th} secondary backbone of the continuum segment.
- ρ_0: radius of curvature of the continuum segment prior to insertion of modulation wires.
- ρ_p and ρ_d: radii of curvature of the proximal and distal segments, respectively.
- θ_0: the angle of the upward-pointing normal to the base disk ($\theta_0 = \pi/2$).
- θ_L: the continuum segment end disk angle.
- β: the change in the angle of the insertion plane when the modulation wires are inserted.

We also make the following kinematic assumptions:

- The radius of curvature of each continuum segment are constant at each insertion step.

- The bending angle θ_L is constant through the entire insertion process, as shown in [26].

- The circular distal and proximal subsegments are tangent.

To identify the shape of the continuum segment during the insertion process, the following equations are derived in order to obtain the radius of curvature of the proximal and distal subsegments and to predict the EE micro-motion. We first present an energy-minimization approach that predicts a turning-point behavior similar to what was experimentally observed in the Chapter 4.

5.5.2 Energy Minimization Approach

We now provide a simple mechanics model that predicts the turning point via energy minimization. We make a simplifying assumption that the tubes and intermediate disks making up the MBCR structure (without any insertion wires) can be modeled as a single tube with bending stiffness k_t and precurvature u_0. These two parameters are a direct outcome of the macro-motion equilibrium configuration at which micro-motion is generated via equilibrium modulation. This precurvature is related to the bending angle:

$$u_0 = \frac{1}{\rho_0} = \frac{\theta_L - \theta_0}{L} \tag{5.16}$$

We next consider the change in elastic energy relative to macro-motion equilibrium configuration at which there are no wires inserted. We model the insertion wires as a single beam with bending stiffness k_w and we assume straight wires. Using these assumptions, the curvature of the proximal subsegment with insertion wires is $u_p = \frac{1}{\rho_p}$ and the curvature of the distal subsegment without insertion wires is $u_d = \frac{1}{\rho_d}$. With these simplifying assumptions, the change in bending energy relative to the macro-motion equilibrium configuration

is given by:

$$\Delta E = \frac{1}{2}\int_0^s \left(\underbrace{k_t\left(u_p - u_0\right)^2}_{\text{proximal}} + \underbrace{k_w\left(u_p\right)^2}_{\text{wires}} \right) ds + \frac{1}{2}\int_s^L \underbrace{k_t\left(u_d - u_0\right)^2}_{\text{distal}} ds \tag{5.17}$$

Integration gives:

$$\Delta E = \frac{1}{2}sk_t(u_p - u_0)^2 + \frac{1}{2}sk_w u_p^2 + \frac{1}{2}(L-s)k_t(u_d - u_0)^2 \tag{5.18}$$

We seek the unknown curvatures u_p and u_d that minimize the energy for a fixed end-disk angle. The rationale for the fixed end-disk angle stems from the parallel routing of all the backbones as was shown in [2]. The corresponding constrained optimization problem is therefore stated as:

$$\min_{u_p,u_d} \Delta E \quad \text{s.t. } \theta_L = Lu_0 + \theta_0 \tag{5.19}$$

where the constraint is given by solving (5.16) for θ_L.

We solve (5.19) with a Lagrange multiplier using the following Lagrangian and conditions of optimality:

$$V = E + \lambda\left(\theta_L - Lu_0 - \theta_0\right) \tag{5.20}$$

$$\frac{\partial V}{\partial u_p} = 0, \quad \frac{\partial V}{\partial u_d} = 0, \quad \frac{\partial V}{\partial \lambda} = 0 \tag{5.21}$$

Solving these equations leads to the following result:

$$\begin{aligned} u_p = \frac{k_t u_0 - \lambda}{k_t + k_w}, \quad u_d = \frac{k_t u_0 - \lambda}{k_t} \\ \lambda = \frac{-sk_t k_w u_0}{L(k_t + k_w) - sk_t} \end{aligned} \tag{5.22}$$

Figure 5.6B shows the results for the tip motion as the insertion wires are inserted from $s = 0 \ldots L$. The plot shows multiple leafs for different θ_L and different ratios of $\frac{k_t}{k_w}$. We

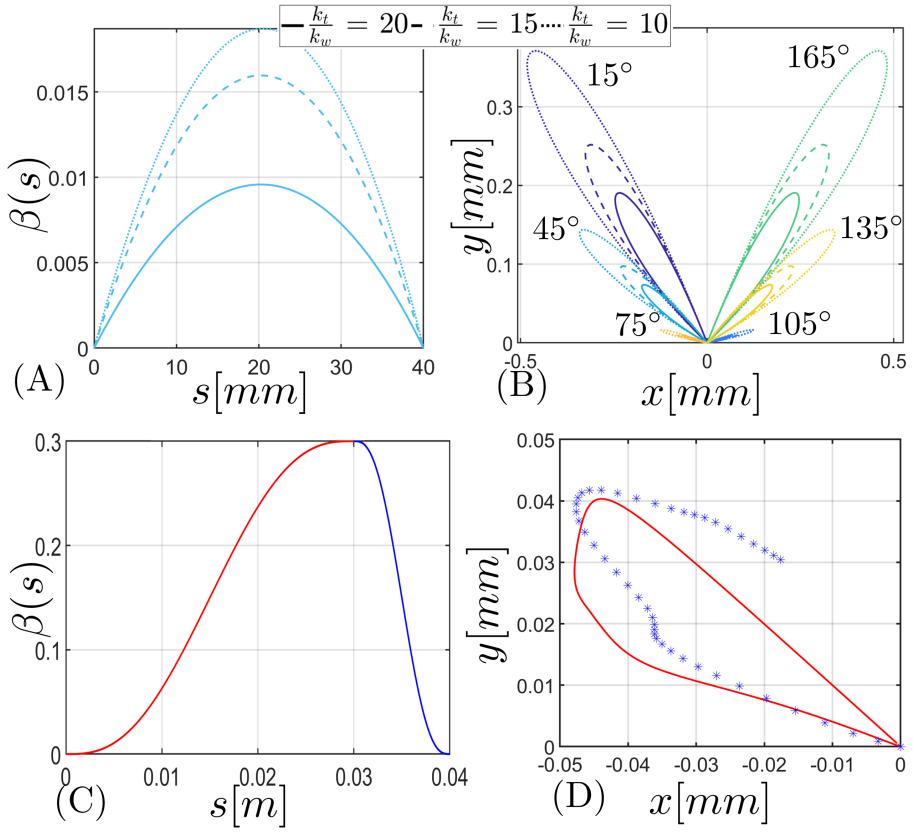

Figure 5.6: (A) $\beta(s)$ for $\theta_L = 45°$ and for different stiffness ratio $\frac{k_t}{k_w}$, (B) Change in tip position predicted by the energy model as the insertion wires are inserted. Plots are shown for different θ_L angles and stiffness ratios $\frac{k_t}{k_w}$, (C) $\beta(s)$ designed as two quintic polynomials (D) experimental (asterisks) and theoretical tip motion (solid line) using $\beta(s)$ shown in C for $\theta_L = 45°$.

note that each leaves shows a symmetric behavior where the tip of the continuum segment reverses direction of motion at a turning point $s = \frac{L}{2}$. As the wire stiffness is increased, the amount of tip motion is increased as expected.

In Section 5.5.3 we explain this turning point phenomenon due to a change $\beta(s)$ in the equilibrium angle θ_s of the proximal subsegment. These two angles are shown in Figure 5.5. The angle $\beta(s)$ may be obtained if either u_p or u_d are given. Referencing Figure 5.5, we have:

$$\theta_s + \beta = su_p + \theta_0 \tag{5.23}$$

We then substitute $\theta_s = \theta_0 + su_0$ (the angle θ_s before deformation due the inserted wires has occurred) to get:

$$\beta(s) = s(u_p - u_0) \tag{5.24}$$

Similarly, we can have from Figure 5.5:

$$\theta_L = \theta_s + \beta + (L-s)u_d \tag{5.25}$$

Substituting $\theta_L = \theta_s + (L-s)u_0$, (the angle θ_L prior to insertion of the wires), we have:

$$\beta(s) = (L-s)(u_0 - u_d) \tag{5.26}$$

Figure 5.6.A shows the profiles of $\beta(s)$ for the tip motion leafs shown in Figure 5.6.B. This figure assumes no frictional losses.

The following subsection uses this $\beta(s)$, along with the kinematic constraints of the continuum robot to explain how the turning point behavior occurs.

5.5.3 Explaining the Source of the Turning Point Behavior Through Kinematic Constraints

Subsection 5.5.2 explained the source of the turning point behavior through an energy minimization argument. It resulted in a predicted change $\beta(s)$ of the tangent angle at the end of the proximal segment, but it did not explain internally what happens from a point of view of kinematic constraints. This section offers this explanation and also shows how the observed turning point behavior from experimental results may be explained by adjusting $\beta(s)$.

When the continuum segment is empty at its initial macro configuration, the arc length along the central backbone corresponding with the insertion plane at insertion depth s is easily obtained assuming circular bending:

$$s = \rho_0 \left(\frac{\pi}{2} - \theta_s \right) \tag{5.27}$$

and consequently the radius of curvature associated with it:

$$\rho_0 = \frac{s}{\frac{\pi}{2} - \theta_s} \tag{5.28}$$

For a given s position of the insertion plane, we can calculate the length of the i^{th} secondary backbone of the proximal segment $L_{i_{p,e}}$ when empty as:

$$L_{i_{p,e}} = (\rho_0 - \Delta_i) \left(\frac{\pi}{2} - \theta_s \right) \tag{5.29}$$

where the radial offset is given by $\Delta_i = r\cos((i-1)\pi)$, $i = 1,2$, and r is the pitch circle radius of the spacer disks.

When the micro-motion wires are inserted through the secondary backbones, the proximal subsegment straightens and results in a change in the bending angle of the proximal segment θ_s. Its radius of curvature changes from the initial ρ_0 to $\rho_{p,f}$. This change is

shown in Figure 5.5 by β, ρ_0 and $\rho_{p,f}$. Therefore, equation (5.27) becomes:

$$s = \rho_{p,f}\left(\frac{\pi}{2} - \theta_s - \beta\right) \tag{5.30}$$

The new radius of curvature of the proximal segment is:

$$\rho_{p,f} = \frac{s}{\frac{\pi}{2} - \theta_s - \beta} \tag{5.31}$$

Recalling (5.28), $\rho_{p,f}$ may also be expressed as:

$$\rho_{p,f} = \rho_0 + \frac{s\beta}{\left(\frac{\pi}{2} - \theta_s - \beta\right)\left(\frac{\pi}{2} - \theta_s\right)} \tag{5.32}$$

which shows that the proximal segment straightens.

The lengths of the secondary backbones in the proximal continuum segment, designated by $L_{i_{p,f}}$, are given by:

$$L_{i_{p,f}} = \left(\rho_{p,f} - \Delta_i\right)\left(\frac{\pi}{2} - \theta_s - \beta\right) \tag{5.33}$$

using $\rho_{p,f} = \rho_0 + \Delta\rho$, eq. (5.33) may be rewritten as:

$$\begin{aligned} L_{i_{p,f}} = & \underbrace{\left(\rho_0 - \Delta_i\right)\left(\frac{\pi}{2} - \theta_s\right)}_{L_i} + \\ & \Delta\rho\left(\frac{\pi}{2} - \theta_s - \beta\right) - \left(\rho_0 - \Delta_i\right)\beta = \\ & L_i + \Delta\rho\left(\frac{\pi}{2} - \theta_s - \beta\right) - \left(\rho_0 - \Delta_i\right)\beta \end{aligned} \tag{5.34}$$

Initially, when the insertion depth of the modulation wires is $s = 0$, the proximal and distal subsegments have a common radius of curvature. The length of the i^{th} secondary backbone of the distal subsegment is:

$$L_{i_{d,e}} = \left(\rho_0 - \Delta_i\right)\left(\theta_s - \theta_L\right) \tag{5.35}$$

The length of the continuum segment backbones is fixed when only micro-motion control is used. This length is given by:

$$L_{i_{\theta_L}} = (\rho_0 - \Delta_i)(\theta_0 - \theta_L) \tag{5.36}$$

Therefore, with increased insertion depth of the modulation wires, the distal segment must curl as the proximal segment straightens. In the following, we analyze the effect of the increased depth of the modulation wires on the curvature of the distal segment.

When the proximal continuum segment is filled with the insertion wires, the length of the secondary backbones of the distal continuum segment can be written as the difference between the CR segment backbone length and the length of the proximal subsegment:

$$L_{i_{d,f}} = L_{i_{\theta_L}} - L_{i_{p,f}} \tag{5.37}$$

Equation (5.37) can be also written using the radius of curvature of the distal subsegment and its bending angle:

$$L_{i_{d,f}} = \left(\rho_{d,f} - \Delta_i\right)(\theta_s + \beta - \theta_L) \tag{5.38}$$

Comparing (5.37) and (5.38) while using (5.34) and (5.36) results in:

$$\rho_{d,f} = \rho_0 - \frac{(\rho_s - \rho_0)\left(\frac{\pi}{2} - \theta_s - \beta\right)}{(\theta_s + \beta - \theta_L)} \tag{5.39}$$

This equation shows that distal segment curls as a result of the inserted wires in the proximal segment.

The above energy minimization and kinematic equations provides insight into the reason for the turning point. However, due to unmodeled energy dissipation, it does not exactly replicate the observed turning point of a physical system with friction. The observed turning point behavior can be recovered with an experimental-based modification to $\beta(s)$.

To demonstrate that our approach can replicate the turning point behavior, $\beta(s)$ was

modified and designed based on results presented in [108] using EE tracking. From this experimental data, it was observed that the turning point happened consistently for our prototype close to 75% of the insertion length. Using two quintic polynomials for modeling $\beta(s)$ as shown in Figure 5.6C, we simulated the tip motion as shown by the solid line in Figure 5.6D, which exhibits a similar behavior to our experimental data shown by asterisks. An accurate representation of kinematics using experimental data is presented in section 5.6.1.

5.6 Experimental Approach to Differential Micro-Motion Kinematics and Control

Although the kinematic model above provides insight into the turning point behavior, for purposes of control it still requires derivation of the micro-motion Jacobian and calibration of $\beta(s)$ across the entire workspace. In the next sections, we present an experimental approach that is more convenient for control since it can directly determine the micro-motion Jacobian from experimental data without going through a kinematics/mechanics model.

5.6.1 Experimental-based kinematic modeling

During micro-motion control, the modulation wire depth s is changed to affect a minute change in the EE position $\mathbf{p} = [x, z]^{\mathrm{T}}$ where x and z are the horizontal vertical coordinates of the EE in frame $\{R\} \triangleq \{\hat{\mathbf{x}}_r, \hat{\mathbf{y}}_r, \hat{\mathbf{z}}_r\}$ as depicted in Figure 3.1. For the purpose of the following discussion, this frame has its $\hat{\mathbf{x}}_r$ axis as the projection of the bent backbone on plane of the base disk and its $\hat{\mathbf{z}}_r$ axis perpendicular and at the center of the base disk. These coordinates are obtained through a microscope tracking setup as described in [108], which results in the coordinates in camera frame $\{C\} \triangleq \{\hat{\mathbf{x}}_c, \hat{\mathbf{y}}_c, \hat{\mathbf{z}}_c\}$, as shown in Figure 3.1. It is assumed that the transformation from the camera frame {C} to {R} is known. In the following, we explain our process for empirical modeling the micro-motion kinematics. This process will be repeated for the x and z coordinates in frame {R}, but since the process

is identical, we will illustrate the process only for the x coordinate.

In the following, we adapt a modal approach first presented in [125] within the context of modeling the kinematics of soft robots. Let $x(s)$ be the x-coordinate of the EE micromotion path, $s \in [0 \dots L]$. For a given macro motion configuration characterized by θ_L in the bending plane, the local tangent to the curve $c = (s, x(s))$ is designated by x':

$$x' = \frac{dx}{ds} \text{ where } x' = x'(\theta_L, s) \tag{5.40}$$

For a fixed θ_L, a modal representation for $x'(s)$ may be used

$$x'(\theta_L, s) = \psi(s)^{\mathrm{T}} \mathbf{a}, \;\; \mathbf{a}, \psi \in \mathbb{R}^n \tag{5.41}$$

where ψ and $\mathbf{a}$ are the modal basis and coefficients. Since the EE micromotion path is smooth and requires a low order polynomial to approximate it, we use a monomial basis:

$$\psi(s) = \left[1, s, s^2, ..., s^{n-1}\right]^T \tag{5.42}$$

To find the modal coefficients $\mathbf{a}$, a data matrix $\mathbf{\Phi}$ containing $x'(s)$ for z different CR configurations with r insertion depths $s = s_1, s_2, \dots s_r$ was constructed. The entries of $\mathbf{\Phi}$ were filled based on the finite difference approximation of the local tangent to the experimental data $x(s, \theta_L)$.

$$\mathbf{\Phi} = \begin{bmatrix} x'(s_1, \theta_{L_1}) & \cdots & x'(s_1, \theta_{L_z}) \\ \vdots & \ddots & \vdots \\ x'(s_r, \theta_{L_1}) & \cdots & x'(s_r, \theta_{L_z}) \end{bmatrix} \in \mathbb{R}^{r \times z} \tag{5.43}$$

Since the elements of $\mathbf{a}$ depend on θ_L, we aggregate the modal approximations of a_i such that:

$$\mathbf{a}(\theta_L) = \mathbf{A}\,\boldsymbol{\eta}(\theta_L), \quad \mathbf{A} \in \mathbb{R}^{n \times m}, \quad \boldsymbol{\eta} \in \mathbb{R}^m \tag{5.44}$$

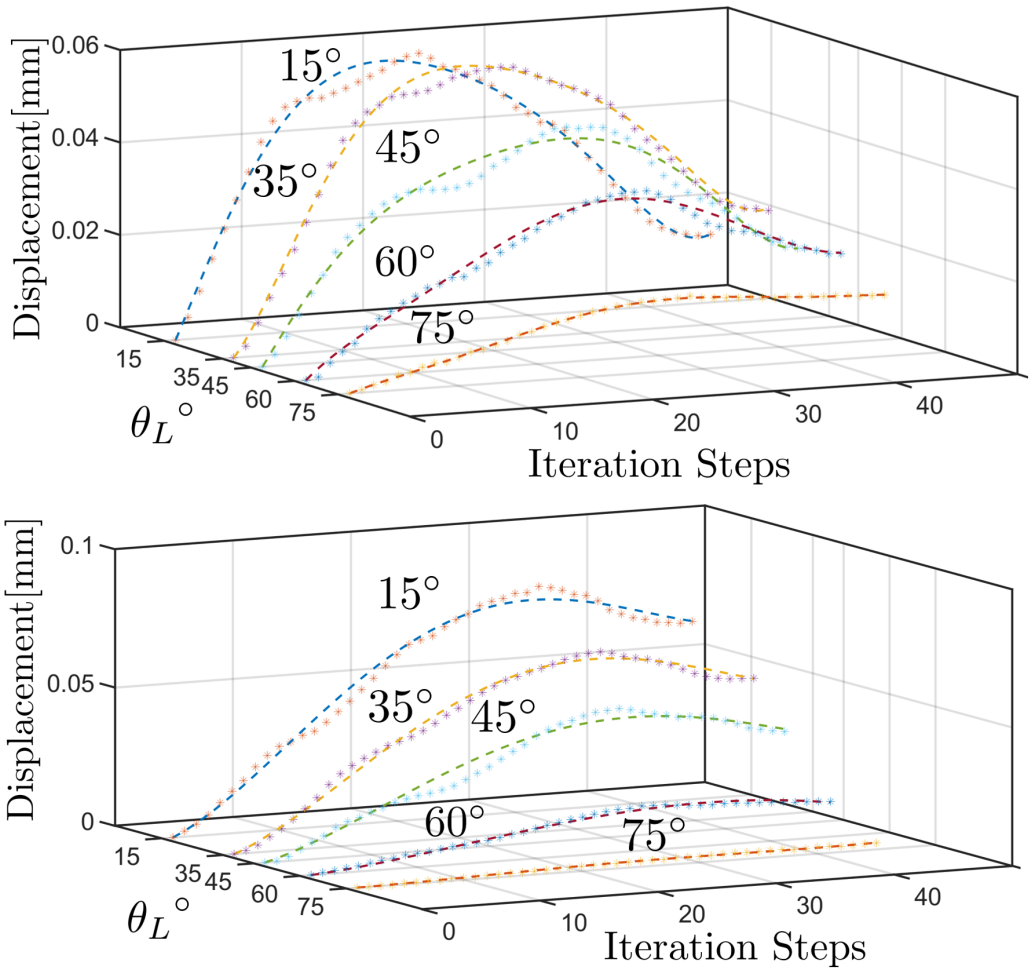

Figure 5.7: x and z end effector coordinates over the full insertion length at 5 different CR configurations

where $\boldsymbol{\eta}(\theta_L) = \left[1, \theta_L, {\theta_L}^2, \ldots, {\theta_L}^{m-1}\right]^{\mathrm{T}}$.

The tangent curve $c = (s, x(s))$ can therefore be obtained by the following modal approximation:

$$x'(\theta_L, s) = \boldsymbol{\psi}(s)^{\mathrm{T}} \mathbf{A}\, \boldsymbol{\eta}(\theta_L) \tag{5.45}$$

Assuming z experiments corresponding macro configuration angles $\theta_1 \ldots \theta_z$ and where the insertion depth is changed with r values, the i^{th} column of $\boldsymbol{\Phi}$ is given by:

$$\boldsymbol{\Phi}^i = \begin{bmatrix} x'(\theta_{L_i}, s_1) \\ \vdots \\ x'(\theta_{L_i}, s_r) \end{bmatrix} = \begin{bmatrix} \boldsymbol{\psi}^{\mathrm{T}}(s_1) \\ \vdots \\ \boldsymbol{\psi}^{\mathrm{T}}(s_r) \end{bmatrix} \mathbf{A}\boldsymbol{\eta}(\theta_{L_i}) \tag{5.46}$$

and the full $\boldsymbol{\Phi}$ matrix is given by:

$$\boldsymbol{\Phi} = \underbrace{\begin{bmatrix} \boldsymbol{\psi}^{\mathrm{T}}(s_1) \\ \vdots \\ \boldsymbol{\psi}^{\mathrm{T}}(s_r) \end{bmatrix}}_{\boldsymbol{\Omega}_{[r\times n]}} \mathbf{A}_{[n\times m]} \underbrace{\begin{bmatrix} \vdots & \vdots & \vdots \\ \boldsymbol{\eta}(\theta_{L_1}) & \ldots & \boldsymbol{\eta}\left(\theta_{L_z}\right) \\ \vdots & \vdots & \vdots \end{bmatrix}}_{\boldsymbol{\Gamma}_{[m\times z]}} \tag{5.47}$$

This is a matrix equation with $\mathbf{A}$ as the unknown. It can be rewritten using Kröneker product as:

$$\left[\boldsymbol{\Gamma}^{\mathrm{T}} \otimes \boldsymbol{\Omega}\right] \mathrm{vec}(\mathbf{A}) = vec(\boldsymbol{\Phi}) \tag{5.48}$$

where the symbol $\otimes$ indicates the Krönecker's matrix product and $\mathrm{vec}(\mathbf{A})$ is a vector sequence of all the columns of $\mathbf{A}$. Equation (5.48) is a linear equation with a vector unknown, which can be solved using the pseudoinverse of $\left[\boldsymbol{\Gamma}^{\mathrm{T}} \otimes \boldsymbol{\Omega}\right]$. Finally, given the solution to $\mathbf{A}$, one can calculate $c = (s, x(s))$ by substituting θ_L and s in (5.45). Finally, the EE coordinate $x(s)$ may be obtained as:

$$x(\theta_L, s) = \int_0^s x'(\theta_L, s) = \int_0^s \boldsymbol{\psi}(s)^{\mathrm{T}} \mathbf{A}\, \boldsymbol{\eta}(\theta_L) ds \tag{5.49}$$

Taking the time derivative of (5.49) using the chain rule:

$$\begin{aligned}\dot{x}(\theta_L, s) = &\frac{\partial}{\partial s}\left(\int_0^s x'(s,\theta_L)ds\right)\dot{s} + \\ &\frac{\partial}{\partial \theta_L}\left(\int_0^s x'(s,\theta_L)ds\right)\dot{\theta}_L\end{aligned} \tag{5.50}$$

The first term in the equation above includes micro motion speed due to the insertion wires and the second term includes the effect of a change in the macro-motion configuration on the micro-motion speed. We will next consider the scenario where the macro-motion configuration is held fixed when one invokes the micro-motion control. Therefore (5.50) can be rewritten as:

$$\dot{x}(\theta_L, s) = \psi(s)^{\mathrm{T}}\mathbf{A}\boldsymbol{\eta}(\theta_L)\dot{s} = \mathbf{J}_{\mu_x}\dot{s} \tag{5.51}$$

where $\mathbf{J}_{\mu_x}$ is the micro-motion Jacobian matrix for the x coordinate. Repeating this process for the z coordinate will also result in similar equations and a Jacobian $\mathbf{J}_{\mu_z}$.

This method was experimentally validated with our system described in section 6.2. For each $\theta_L \in [15°, 35°, 45°, 60°, 75°]$ we moved our robot through 45 EE poses and the EE position was segmented using our method in [108]. Figure 5.7 presents the segmented EE coordinates using asterisk markers. The numerically integrated curve using (5.45) is shown with dashed lines. Table 5.2 presents the root mean squared error between the observed EE micro-motion paths, obtained in [108] and shown as solid lines. These results suggest that the modeling approach we presented can represent the robot kinematics well.

θ_L	15°	35°	45°	60°	75°
x	0.8 (3.3)	0.5 (2.6)	1.1 (3)	1 (2)	0.2 (0.3)
y	0.6 (4.4)	0.3 (3.5)	3.7 (3.9)	1.9 (1.2)	0.5 (0.3)

Table 5.2: Root mean squared error (maximum error) [μm] between measured and modeled EE micro-motion paths.

5.6.2 Redundancy Resolution definition

A smooth transition from macro-motion to micro-motion and viceversa, is required for control purpose of a robot with multi-scale motion capabilities. In this section, a weighted-pseudoinverse redundancy resolution method is adapted to allow this smooth transition. The approach presented adopts prior approaches for macro/micro motion resolution such as in [97, 56] while using the micro-motion Jacobians $\mathbf{J}_{\mu_x}$ and $\mathbf{J}_{\mu_z}$. Defining $\dot{\mathbf{p}}_\mu$ as the EE velocity when the micro-motion control regime is enacted, the micro-motion kinematics is given by:

$$\dot{\mathbf{p}}_\mu \triangleq \begin{bmatrix} x'_\mu \\ z'_\mu \end{bmatrix} \dot{s} = \begin{bmatrix} \mathbf{J}_{\mu_x} \\ \mathbf{J}_{\mu_z} \end{bmatrix} \dot{s} = \mathbf{J}_\mu \dot{s} \tag{5.52}$$

where the second term in (5.50) has been neglected for simplicity. When simultaneously enabling macro and micro-motion control, this term may be neglected also for practical considerations. Backlash and motion losses at the macro-scale actuators can overwhelm the motion generated by this second term. Therefore, considering second-order effects due to this term is an unnecessary complication in applications where online feedback is used for control such as in our work.

Similarly, we will use $\dot{\mathbf{p}}_m$ to designate the EE velocity when only the macro-motion control is enacted. We will restrict the macro-motion kinematics to maintain motion in the bending plane because of the need to maintain the motion of the robot within the imaging plane of the B-mode OCT probe. Referring to [2], which defines a configuration-to-task-space Jacobian, $\mathbf{J}_{x\psi}$, we can construct a reduced configuration space Jacobian $\tilde{\mathbf{J}}_{p\theta_L} \in \mathbb{R}^{2\times 1}$ expressing the EE speed in the $x-z$ coordinates of the bending plane. Taking the appropriate sub-matrix of $\mathbf{J}_{x\psi}$ and transforming it into the frame of the bending plane, using this notation, we define the macro-motion kinematics as:

$$\dot{\mathbf{p}}_m \triangleq \begin{bmatrix} \dot{x}_m \\ \dot{z}_m \end{bmatrix} = \tilde{\mathbf{J}}_{p\theta_L} \dot{\theta}_L \tag{5.53}$$

The joint speeds may be obtained using the configuration-to-joint-space Jacobian $\mathbf{J}_{q\psi}$ defined in [2]. Since we reduced our model to planar motion within the bending plane of the robot, we define $\tilde{\mathbf{J}}_{q\theta_L} \in \mathbb{R}^{3\times 1}$ as the first column of $\mathbf{J}_{q\psi}$ such that

$$\dot{\mathbf{q}}_m = \tilde{\mathbf{J}}_{q\theta_L}\dot{\theta}_L, \quad \dot{\mathbf{q}}_m \in \mathbb{R}^{3\times 1} \tag{5.54}$$

where $\dot{\mathbf{q}}_m$ is the macro-motion joint speeds. Using (5.54) and (5.53) one obtains

$$\dot{\mathbf{p}}_m = \tilde{\mathbf{J}}_{p\theta_L}\tilde{\mathbf{J}}^{\dagger}_{q\theta_L}\dot{\mathbf{q}}_m = \mathbf{J}_{pq}\dot{\mathbf{q}}_m \tag{5.55}$$

We next define the augmented joint-space vector which includes the joint speeds for macro and micro-motion:

$$\mathbf{q}_a = \begin{bmatrix} q_m \\ s \end{bmatrix} \tag{5.56}$$

Therefore the combined EE speed in the bending plane may be expressed as:

$$\dot{\mathbf{p}} = \mathbf{J}_{pq}\dot{q}_m + \mathbf{J}_{\mu}\dot{s} = \begin{bmatrix}\mathbf{J}_{pq} \mid \mathbf{J}_{\mu}\end{bmatrix}\dot{q}_a \tag{5.57}$$

For a given desired EE speed, $\dot{\mathbf{p}}$, the above equation may be solved using a weighted pseudo-inverse solution:

$$\dot{q}_a = \mathbf{W}_a^{-1}\mathbf{J}_a^T\left(\mathbf{J}_a\mathbf{W}_a^{-1}\mathbf{J}_a^T\right)^{-1}\dot{p} \tag{5.58}$$

where $\mathbf{J}_a = \begin{bmatrix}\mathbf{J}_{pq} \mid \mathbf{J}_{\mu}\end{bmatrix}$ and $\mathbf{W}_a$ is a weight matrix defined as:

$$\mathbf{W}_a = \begin{bmatrix} \mathbf{W}_m & 0 \\ 0 & W_{\mu} \end{bmatrix} = \begin{bmatrix} w_{m1} & & & \\ & w_{m2} & & 0 \\ & & w_{m3} & \\ & 0 & & w_{\mu} \end{bmatrix} \tag{5.59}$$

The submatrix $\mathbf{W}_m$ is the weighted matrix of the coefficients related with the macro motion while W_μ is the coefficient related with the micro motion.

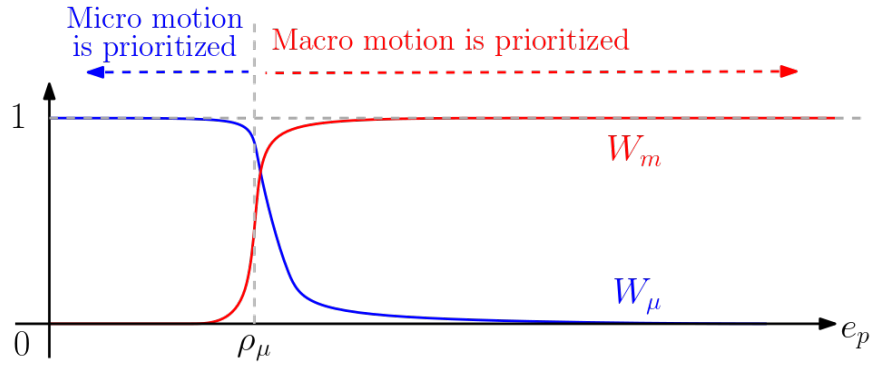

Figure 5.8: Weight coefficients plot

These weights are determined based on proximity to the target EE position, as graphically presented in Figure 5.8 and (5.60) and (5.61).

$$\mathbf{W}_m = \frac{1}{2}\left(1+\tanh\left(n\left(\|e_p\|-\rho_\mu\right)\right)\right) \tag{5.60}$$

$$W_\mu = \frac{1}{2}\left(1-\tanh\left(n_\mu\left(\|e_p\|-\rho_\mu\right)\right)\right) \tag{5.61}$$

where ρ_μ is a threshold radius below which the redundancy resolution will use mostly micro-motion control and above which it will mostly use macro motion control.

5.7 Conclusion

This chapter presented the efforts on solving the problem of multi-scale manipulation. The first simplistic approach using a moment-coupling effect offers initial insights on the *turning point* behaviour. A new approach for micro-motion using equilibrium modulation of CRs was then presented. The work was motivated by the potential benefits of using CR for in-situ inspection and image-based biopsy. Two more approaches for explaining the turning-point phenomenon, unexplained in prior literature, have been presented. The first approach arrives at the source of this behavior from an energy conservation standpoint. The

second approach replicates this behavior through insights into the constrained kinematics of multi-backbone CR. An approach to empirical modeling of micro-motion kinematics has been presented based on a closed-form modal interpolation maps.

This work is a first key step for future development of new robotic assistants that can offer multi-scale manipulation for surgery and for image-based biopsy. Several challenges remain unaddressed by this work. Motions requiring direction reversal can induce undesirable hysteretic effects. Modeling of these hysteretic effects is difficult therefore solutions using in-situ micron-level EE tracking will be needed. Nevertheless, applications such as generating a 3D OCT scan can be planned and achieved while avoiding direction reversal - therefore avoiding the negative effects of hysteresis.

CHAPTER 6

VOLUMETRIC OCT AND OCT-GUIDED VISUAL SERVOING

6.1 Introduction

In this chapter we demonstrates a system-level integration and validation of 3D OCT using an external commercial OCT probe and the feasibility of integrating a custom B-mode probe that can be easily integrated within the robot to obtain the volumetric OCT. Furthermore, for control purpose, in the previous chapter we have presented our effort to define a modal approach to capture the micro-motion kinematics model from experimental data. In this chapter we demonstrate micro-macro motion control with an application of OCT-guided injection. This work was published in [126, 124]

6.2 Experimental Setup and System Integration

Figure 6.1 shows the experimental setup and system integration framework used in our study. This setup was used to validate our modeling approach, to demonstrate the feasibility of generating 3D OCT volumes using CREM micro-motion, and to validate our approach for micro-motion closed-loop control using OCT feedback.

The continuum robot actuation unit is shown as item ① in Figure 6.1A and the continuum robot segment is shown as item ③ in Figure 6.1B. For our experiments, we used a commercial external OCT probe and a custom miniature B-mode OCT probe that was embedded within the robot. The custom B-mode OCT probe is shown as item ② in Figure 6.1B. It is a modification of the probe design first presented in [127]. Relative

to the previous design, this probe used closed-loop position control with custom control electronics enclosed in an Arduino-based control box shown as item ⑤ in Figure 6.1A and presented in depth in Chapter A. The probe was actuated by a voice coil actuator (H2W NCM02-05-005-4JBMC) shown in Figure 6.1C. The external OCT probe (Thorlabs Telesto-II-1325LR-5P6 3.5 to 7mm imaging depth with 5.5 to 12.0μm Axial Resolution in Air) is shown as item ⑥ in Figure 6.1A and also as item ③ in Figure 6.1D.

The commercial probe was used for proof of concept for 3D volumetric OCT with a calibrated system that can provide quantifiable data about the accuracy of our 3D OCT and micro-motion resolution and for demonstrating closed-loop visual servoing in OCT image space. The custom OCT probe was used for testing the feasibility of embedding a custom B-mode OCT probe within the robot for generating 3D OCT scans.

In addition to the continuum segment, the setup used a custom-made planar robot shown as item ① in Figure 6.1B. This robot was comprised of two orthogonally-aligned linear stages (VELMEX A1506B-S1.5 equipped with a 4.5" 20 turns/inch travel lead screw). These stages were driven by two DC gearmotors (Maxon Motor RE16 4.5W equipped with a planetary gearhead GP16A 19:1 and an MR encoder with 256 counts per turn) and controlled by our Arduino-based control box (⑤ in Figure 6.1A). The need for adding this planar actuation unit is explained in section Section 6.4.

The control system implementation used four computers. One computer served as a high-level controller (HLC) (item ① in Figure 6.1E) and three additional computers served the following auxiliary functions. The first computer (item ②) was used as a MATLAB Realtime low-level controller for the continuum robot. The second computer (item ③) was used for OCT image acquisition and online image segmentation in MATLAB. A third computer (item ④) was used as a mid-level controller (MLC) for acquiring EE position data from the second computer and for sending the control-reference signal for the Arduino-based controller of the OCT and planar robot. Although this function would have been possible to implement on the same machine as the high-level controller, we chose a separate

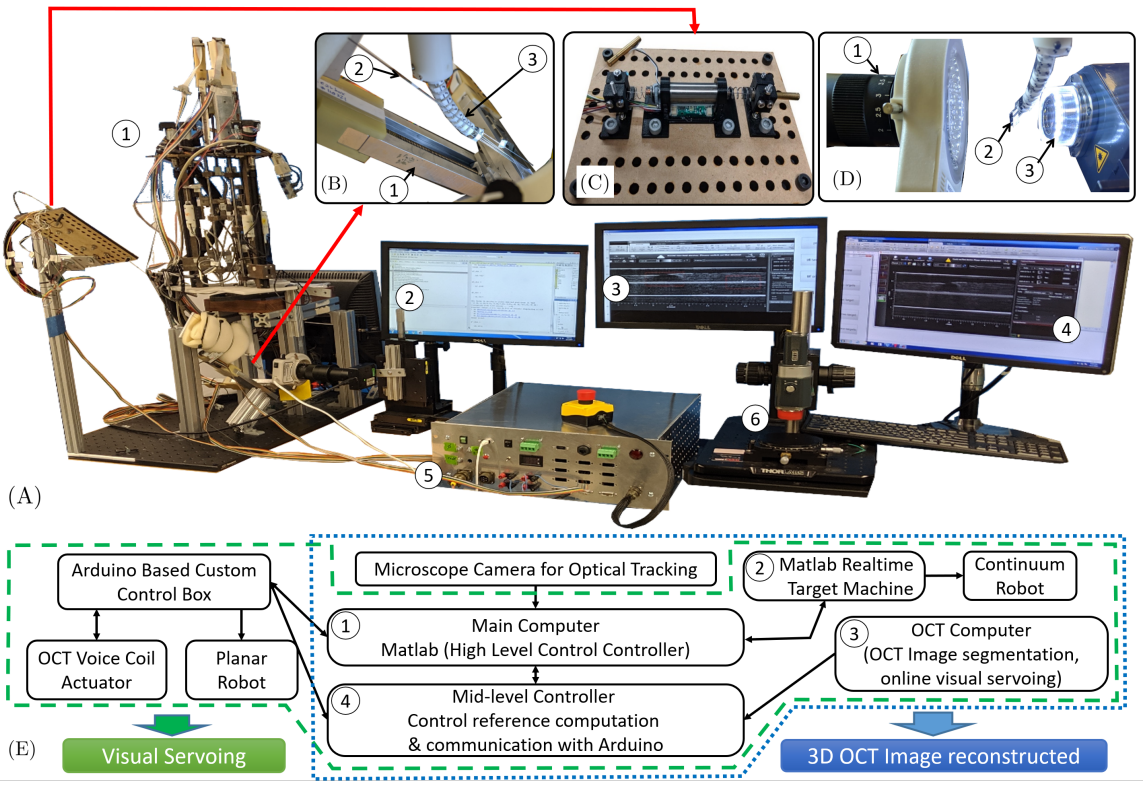

Figure 6.1: Experimental setup: (A)①-CREM system ②-Main Computer ③-OCT Computer ④-Mid-level controller (Control reference computation and communication with Arduino) ⑤-OCT/linear-slides Arduino Based control box ⑥-OCT commercial probe Thorlabs Telesto-II-1325LR-5P6 (B) OCT probe embedded setup: ①-Custom made OCT probe deployed within the CR segment ②-Velmex linear slide ③-CR (C) Voice coil OCT actuation unit (D) External OCT setup: ①-Micro-tracking camera ②-CR ③-Commercial OCT (E) System integration diagram

computer due to MATLAB incompatibility issues.

Data communication between these computers for visual servoing and 3D OCT generation were carried out as the following. The HLC computer obtained the EE position via a microscope camera using MATLAB image acquisition toolbox. This information is used only for 3D OCT volume generation. The acquired scans are synchronized with robot position information using time-stamped user datagram protocol (UDP) messages relayed to the MLC and the MATLAB Realtime target machine. For visual servoing, the OCT image segmentation data is relayed to the MLC via UDP communication. The low-level control frequency on the MATLAB Realtime target machine for controlling the continuum robot was 1KhZ. The MLC obtained image segmentation data and relayed the reference control signal to the Arduino at 30Hz. In turn, the Arduino-controller using HiLetgo ESP32 microcontroller implemented its own low-level PID control for the voice-coil actuator and the planar robot.

6.3 Micro-Motion for Volumetric OCT Imaging

This section details the validation of our approach for achieving volumetric OCT reconstruction via micro-motion. While the final goal is to obtain a volumetric scan of a vessel using a custom-made OCT probe integrated inside the CR, we first validated feasibility using an external commercial OCT probe. These experiments were first reported in [126] and they provide an ideal baseline for expected performance where OCT image aberrations are minimized due to the use of a commercial OCT probe. This section also details validation using our own CR with a custom B-mode OCT probe that is a modification of the design first presented in [128].

6.3.1 3D image reconstruction using commercial OCT probe

The setup used is shown in Figure 6.1A. We used the external OCT probe for these experiments. The CR segment was bent to $\theta_L = 60^\circ$ using macro-motion control and the

macro motion joints were held fixed. The CR segment was used to carry an OCT scanning sample on its tip while the OCT probe was fixed perpendicularly to the samples. By inserting three equilibrium modulation wires, micro-motion was used to move the sample perpendicular to the scanning plane of the probe (we will refer to the motion as normal motion direction (NMD)). During micro-motion, every $\Delta s = 0.5mm$ of insertion depth the HLC machine (① in Figure 6.1E) recorded a B-mode OCT scan image together with the robot configuration joint values. At the same micro-motion tip tracking was used based on the method presented in [108] to record the motion profile of the EE and the CR joint values. At the end of each experiment, MATLAB image segmentation using Canny filter and/or Hough circles was used to construct the 3D images.

Three samples were used in three experiments to test feasibility of our method on different materials and shapes. First, a metric brass screw (0.8*mm* diameter, 0.2*mm* pitch) was scanned, Figure 6.2.B. A profile image of the screw was taken to compare to the known screw pitch geometry (Figure 6.2B ①-②). Micro-motion was initiated to generate a 3D scan which was reconstructed in Figure 6.2B ③-⑤. The pitch measurement, based on the profile image (Fig 6.2B ①-②) was $209.85\mu m$ while based on the 3D scan reconstruction it was $210.75\mu m$ based on analysis of Figure 6.2B ④. This designates an average error of 0.5%. The micro motion displacement shown in Figure 6.2B ③-⑤ corresponded with $92\mu m$ motion in NMD and 89 scans. Therefore, the NMD resolution was $1.03\mu m$.

In the second experiment, we used a multilayer cellophane tape with an additional layer of double-sided tape on top, Figure 6.3 ②-③. The double-sided tape was added to simulate a thicker layer at the top of the sample. This experiment was motivated by a future application of 3D retinal layer reconstruction. Results of the 3D reconstruction are shown in Figure 6.3 ④-⑥. The thickness of the layers measured based on a single OCT image (Figure 6.3 ①) had an average of $71.7\mu m$ while the thickness measured from the reconstructed model had an average of $67.4\mu m$. The average error is circa 6%. According to the tape supplier, the tape layer has an average thickness of $70\mu m$, including the glue layer.

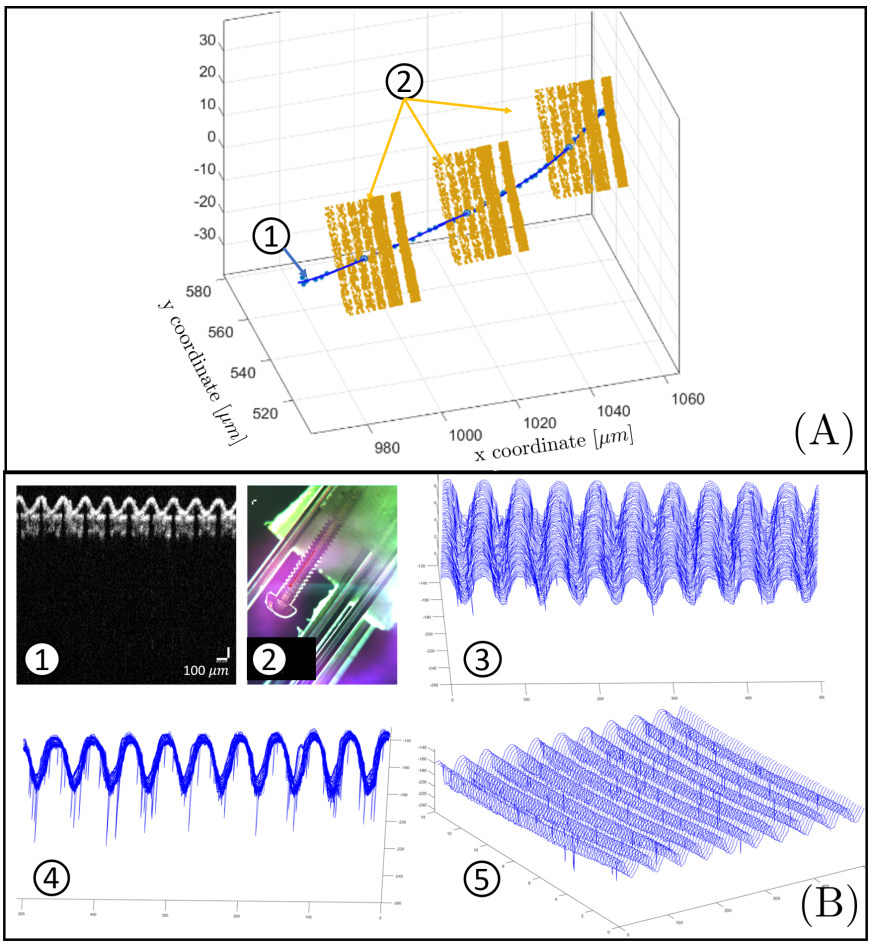

Figure 6.2: (A)The plot shows an example of the images acquisition along the robot EE micro-motion path,①- Robot EE path ②–(B) Multilayer cellophane tape images at 3 sample micro-insertion depths along the motion path. Screw pitch reconstruction: ①-OCT Image ②-Screw sample image (OCT camera view) ③-⑤ Different views of the reconstructed profile

The last experiment aimed to simulate the reconstruction of a capillary blood vessel as an artificial channel generated in Agar, Figure 6.4. The channel was created by placing a $220\mu m$ NiTi wire in the liquid Agar. After solidification, the wire was removed, and the sample scanned. The average area measured using the B-mode OCT images as in Figure 6.4 ① was $2.4746e+04\mu m^2$. The cross-sectional area average for the 3D reconstructed model was measured at $2.6329e+04\mu m^2$ which represents an average deviation of 6%.

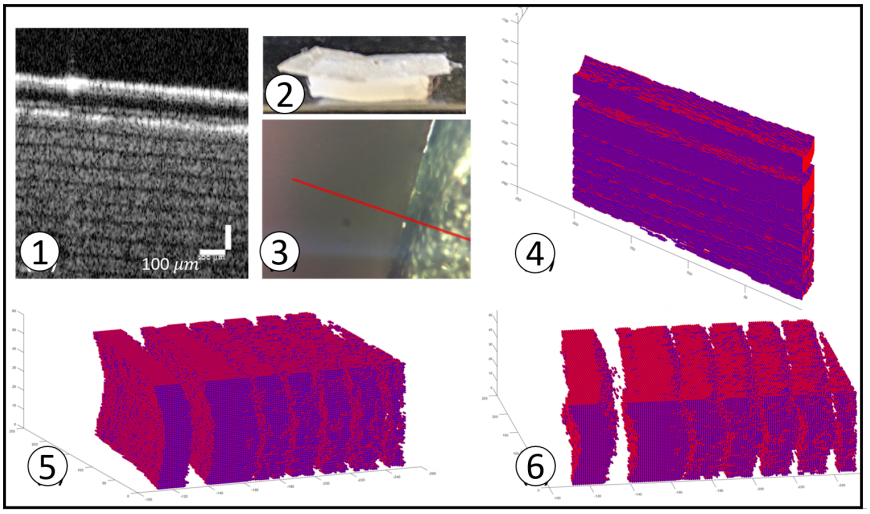

Figure 6.3: Multilayer cellophane tape reconstruction ①-OCT Image ②-Side view of the multilayer cellophane tape with the double-sided tape added on top ③-Multilayer tape Sample image (OCT camera view) ④-⑥-Different views of the reconstructed profile.

6.3.2 3D reconstruction of an optic nerve blood vessel

This section shows the experimental result for a 3D OCT reconstruction of an organic tissue. A freshly harvested retinal optic nerve in a cadaveric swine eye was used as a scanning sample as shown in Figure 6.5A.③. Figure 6.5A.① shows the first OCT scanned image before that the micro-motion is enabled while Figure 6.5A.② shows the last scanned image after the micro-motion scanning is completed. It is possible to notice how a vessel branch in Figure 6.5A.① bifurcates by the end of the scanning. The 3D reconstruction, Figure 6.5A.④-⑤, shows the corresponding anatomy in Figure 6.5A.① and Figure 6.5A.② while the branching of the scanned vessel is clearly visible.

6.3.3 Volumetric OCT using a miniature OCT probe

After testing the robustness of the 3D OCT reconstruction using a commercial OCT probe, we established the feasibility of using the custom-made miniature B-mode OCT probe. As shown in Figure 6.1C, the OCT probe was embedded within the CR segment. An agar sample (Figure 6.5B ①) was prepared with a 0.66*mm* tube embedded in it. Once the

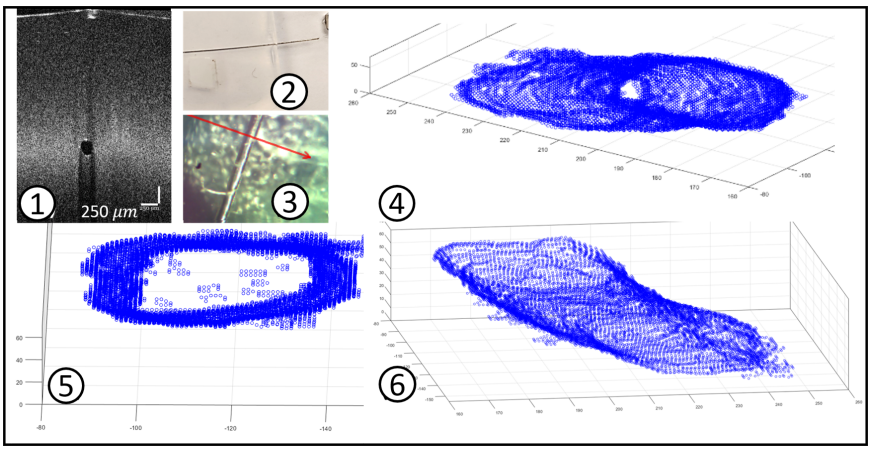

Figure 6.4: Micro Channel reconstruction ①-OCT Image ②-NiTi wire used to create the channel still in the agar sample ③-Channel sample image (OCT camera view) ④-⑥-different views of the reconstructed profile.

agar was solidified, the tube was removed, a channel remained and was used as an imaging target for the probe of a mock up vessel. Using equilibrium modulation, the robot moved the probe perpendicular to the scan direction of the custom miniature OCT probe. Results of the 3D reconstruction are shown in Figure 6.5B ③-④. The average area measured using three B-mode OCT images as in Figure 6.5B ② is $0.32892mm^2$ while the area calculated using the 3D reconstruction is $0.31341mm^2$ which represents an average deviation of 10%.

6.4 OCT-GUIDED VISUAL SERVOING

This section presents the experimental validation of our proposed mixed-feedback control that uses OCT image feedback and the CR joint-space. The experimental setup used for this evaluation is shown in Figure 6.1. We used the commercial OCT probe for these experiments. The aim of the experiment was to mimic an automated blood vessel injection by driving a needle (made out of a NiTi wire $0.4mm$ in diameter and carried by the CR segment) into a mockup vessel ($0.16mm^2$ cross sectional area) inside an agar sample(carried by a linear slide actuator) as shown in Figure 6.7A.

OCT-guided visual control was achieved by using a custom computer code for OCT image segmentation. An online (interactive rate $\approx 30Hz$) image segmentation was achieved

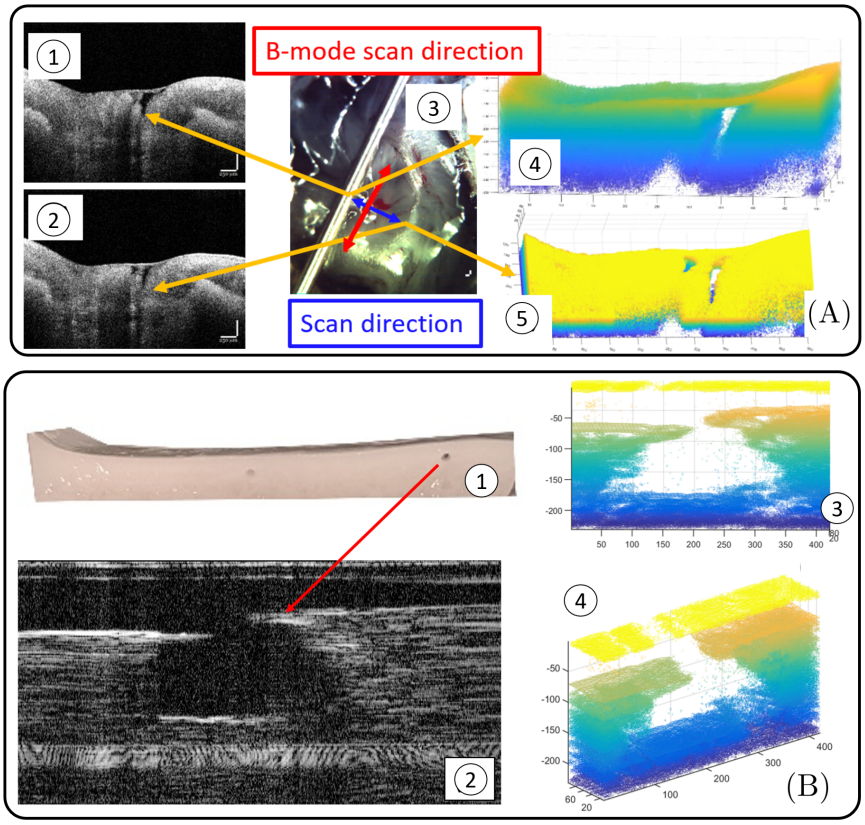

Figure 6.5: (A) 3D reconstruction of a branching in an optic nerve of a swine cadaver retina. ①-②-First and last OCT scanned images. ③-Microscope view of the sample showing the B-mode scan direction (red) and micro-motion scan direction (blue). ④-⑤-Two views of the 3D OCT reconstruction model showing the corresponding anatomy in ① and ② (B) 3D OCT reconstruction using a custom made OCT B-mode probe integrated within the CR. ①-Mock up vessel generated in Agar Sample ②-Vessel OCT image ③-④-Volumetric reconstruction of the scanned sample

using a cross-correlation template matching with manual initialization. At the beginning of the experiment, the user defined the two templates for the two tracking targets (vessel and needle tip) by mouse selection as shown in Figure 6.7.B by two red rectangles. The template matching uses online segmentation and tracking of the mockup vessel and the NiTi needle as viewed in the OCT system.

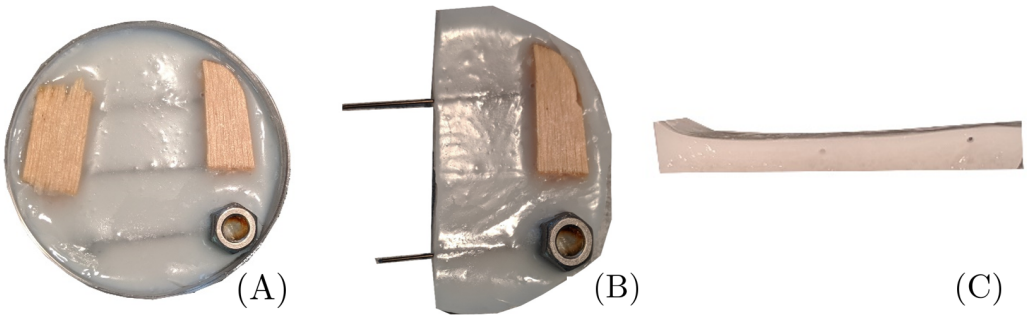

Figure 6.6: Agar channel model showing: (A) the top view of the agar model with 3 embedded 0.66*mm* tubes, (B) the sliced agar showing one tube removed and two remaining, (C) the side view of the agar sample

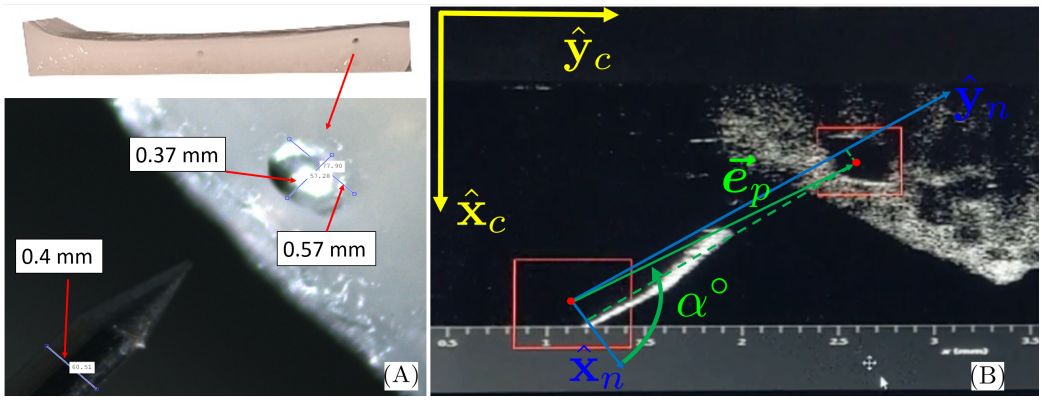

Figure 6.7: (A) Microscope view of the needle tip and the agar vessel mockup. (B) OCT scan image and visual servoing frames definition.

6.4.1 Experimental Validation of OCT-Guided Visual Servoing

The experiment procedure requires user input for choosing two tracking target templates via mouse selection on a Matlab2016a window that acquires the OCT image from a commercial OCT control software. The OCT image in Figure 6.7B shows the result of the tracking method (two red squares) and the frame definitions. The picture frame is identified by $(\hat{\mathbf{x}}_c, \hat{\mathbf{y}}_c)$ while $(\hat{\mathbf{x}}_n, \hat{\mathbf{y}}_n)$ identifies the needle tip frame. Since the OCT image was starting to distort when the needle is piercing the agar sample, the origin of the needle frame was chosen with a specified offset along the needle axis and is accounted for in the tracking code. Once the two target points were chosen, the control code uses micro-motion to close the error in position along the $\hat{\mathbf{x}}_n$ direction and consequently along $\hat{\mathbf{y}}_n$ direction using macro-motion. To avoid laceration of the mockup tissue caused by the sideways motion of the needle, the HLC uses first micro-motion followed by macro-motion.

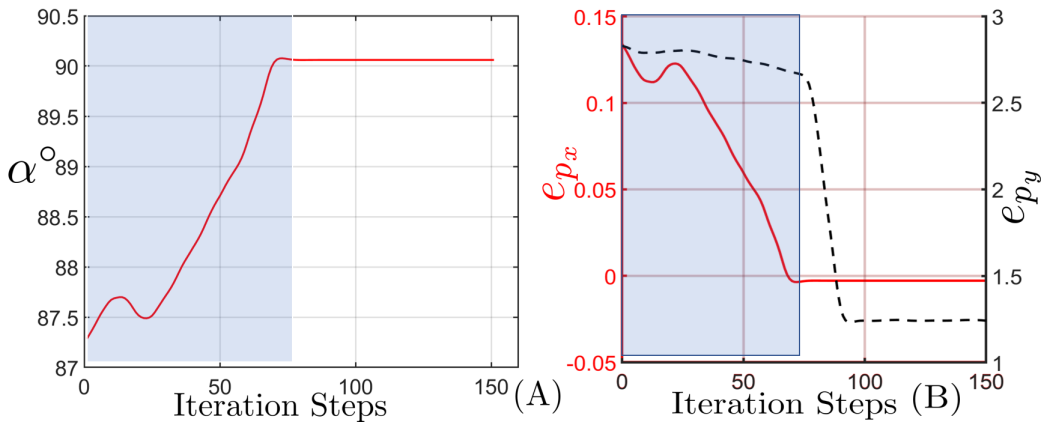

Figure 6.8: (A) Gamma angle, (B) Components of $\mathbf{e}_p$ in $\{\hat{\mathbf{x}}_n, \hat{\mathbf{y}}_n\}$ frame as shown in (B). Solid line referring to the left y-axis is e_{p_x} in $[mm]$ and dashed line referring to right y-axis is e_{p_y} in $[mm]$.

The tracking results of the two red square centers are shown in Figure 6.7C-D. The vector $\mathbf{e}_p$ indicates the position vector of the center of the vessel's red square from the origin of the needle frame. Figure 6.7C presents the tracking result of the relative angle α between $\mathbf{e}_p$ and $\hat{\mathbf{x}}_n$. Figure 6.7D presents the tracking results of the components of $\mathbf{e}_p$ along $\hat{\mathbf{x}}_n$ and $\hat{\mathbf{y}}_n$. The blue shaded area indicates the portion of the process where only the micro-

motion is enabled. We used two thresholds for position convergence. When using macro-motion we used $300\mu m$ and when using micro-motion we used $5\mu m$ as the corresponding convergence threshold radii from the target location. The final position error between the two centers calculated in the needle frame $(\hat{\mathbf{x}}_n, \hat{\mathbf{y}}_n)$ is $0.0028mm$ along $\hat{\mathbf{x}}_n$ and $0.2683mm$ along $\hat{\mathbf{y}}_n$. The considerable difference of the magnitude in the error directions came from the different motion profile associated with each direction. The first one is completely controlled by micro-motion using the equilibrium modulation while the piercing direction is controlled by macro-motion actuation of the linear stage of the planar robot that has a manufacturer specification of backlash of $200\mu m$. The need for the linear stage comes from the missing third degrees of freedom of the single segment CR which would prevent the straight motion for the injection process. The data flow and control scheme is summarized in Figure 6.1E, grouped by the green dashed line.

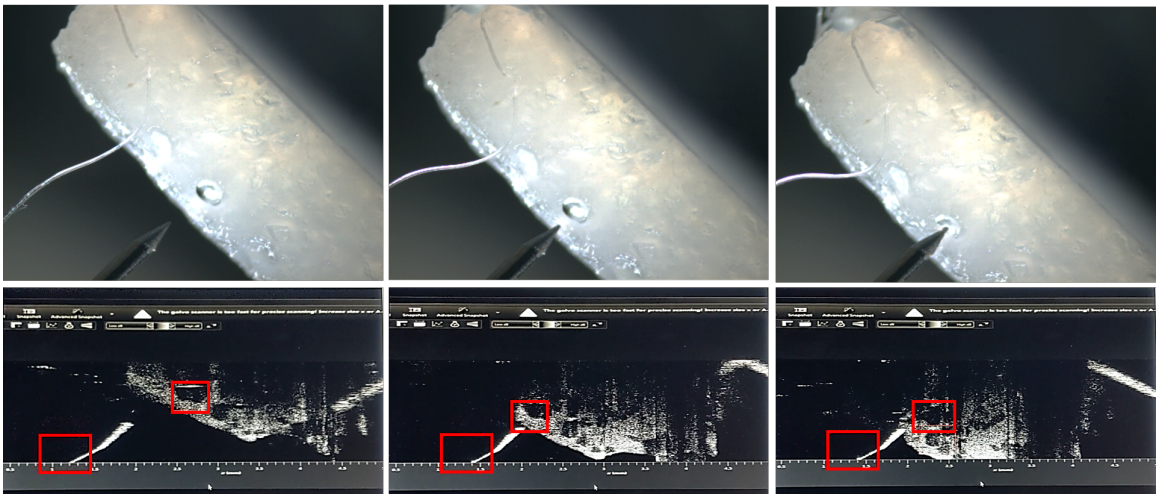

Figure 6.9: A film strip of three images from the microscope and their corresponding images from the OCT. The images show also the segmentation of the target and the needle and the process of visual servoing of the needle to reach the channel.

6.5 Conclusion

This chapter presented a feasibility verification of 3D OCT through a system-integration endeavour that used both a commercial (external) and a miniature (internal) OCT probes.

Results showed that 3D OCT volumes may be obtained with 1 micron slices if accurate position feedback is used. If no accurate EE tracking is available, the experimentally derived micro-motion kinematics can produce accurate position estimates less than $5\mu m$. We also presented a demonstration of closed-loop OCT-guided servoing using both macro and micro motion for guiding a needle into an agar channel. The RMS error using our modeling approach was less than 1.2 microns, which could be used for generating a lower-resolution 3D OCT scan that would still be useful since each image slice still retains its high resolution.

CHAPTER 7

PRELIMINARY DESIGN EXPLORATION AND MODELING OF AN APCR DEVICE

Robotic-assisted ophthalmic surgery has been investigated for the past 30 years. This surgical domain presents several challenges in term of precision requirements, limited perception and intraocular dexterity. Achieving extreme precision in retinal surgery is difficult due to physiological hand tremor, which has been estimated around 14 to 142μm in [129]. Surgical perception during retinal surgery is limited due to limited visualization through the dealated iris, limited depth perception through the microscope, and limited force/tactile feedback due to the very small intraocular interaction forces being masked by the weight of instruments and contact forces with the scleral access ports. Finally, the tools used during retinal surgery are limited in articulation since they are mostly rigid instruments (long narrow rigid rod of circa 900μm in diameter) without an articulated tip, offering the standard 4 Dof of rotating and translating along the shaft and tilting in two directions. Control of the approach angles of the tools with respect to anatomical targets within the eye is not possible when the scleral access port has been pre-determined.

To overcome the problem of precision, several groups proposed different robot architectures that are able to filter hand tremors. For example, a telemanipulated robotic solution was proposed in [130, 131, 132, 133], while more commonly, hand-held devices [134] or hand-on-hand robotic system [135][64] are used to actively filter the undesired movements. Moreover, in [61, 136] axial (depth) tool stabilization is achieved by filtering the tremor of an OCT-tracked device. To overcome the perception challenges researchers have explored devices with force sensing[137], augmented reality [138], and OCT feedback [139, 140].

To address the challenge of intraocular dexterity, Wei et al. [130, 141] proposed and demonstrated continuum robots with intraocular bending. Kutzer et.al [15] presented a design of a continuum robot similar to our design in section 2.6 on page 28, but the device diameter was 5.99 mm and was limited to having a single continuum segment.

In retinal membrane pealing, for instance, a forceps is used to lift an epiretinal membrane or internal retinal layer of 50μm in average [142]. Those membranes are semitransparent which makes very difficult to identify and then grab them using the surgical tool. To overcome those limitation, Yu et al [139], for example, used a B-mode OCT probe for depth perception feedback for membrane pealing but macked a distal wrist. Wei et al [141] demonstrated that increasing by a single degrees of freedom of intraocular side-bending motion, the distal orientational dexterity is improved between 36% to 57%.

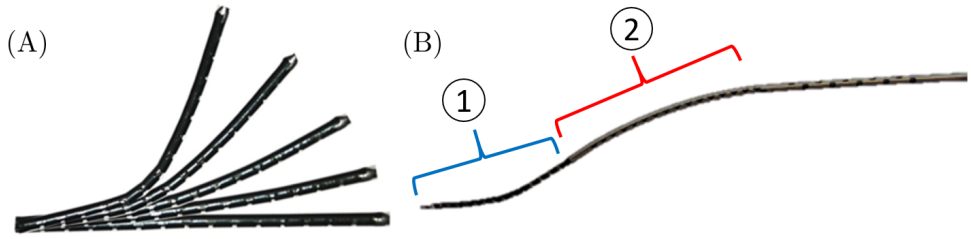

Figure 7.1: APCR prototype: (A) First prototype built, showing different bending angles (B) Two segment APCR prototype ① distal segment ② proximal segment.

The previous works reviewed above do not address the *combined* challenge of dexterity, miniaturization and deployability of sensory technologies such as OCT or confocal microscopy. In this chapter we present the design and modeling efforts of a new device able to provide 4 DoF of intraocular motions provided by two continuum segments while maintaining a working channel for OCT deployment.

The design presented here uses antagonistic pairs of superelastic tubes. This design improves upon that of Oliver-Butler et al [65]who presented a 2 DOF continuum robot for minimally invasive surgery with an external diameter of 7.2 mm, which is not suitable for ophthalmic applications. Jeong et al [143] have recently presented a 1 Dof single segment continuum robot with an external diameter of 0.4 mm, however, the device has a blind

bore which prevents deployment of tools. Our most recent design (Figure7.1.B) offers an APCR with 2 independently steerable segments, with an external diameter of 0.88 mm (size feasible for ophthalmic surgery) and a working lumen of 0.4 mm in diameter. In Sec. 7.3, this prototype has been used for some preliminary results in [144] within the context of enabling dexterous intravenous navigation for ischemic stroke treatment.

In addition to challenges of achieving mechanical embodiments of multi-segment hollow-bore APCRs, the modeling of the statics of these robots is challenging, yet a necessary requirement for the design of these robots and their associated actuation units. In this chapter we are reporting our design effort to obtain a working 2-Dof 2 segments APCR, and preliminary consideration of constrained kinematic model for intraocular dexterity. As of today, this is an ongoing project and this chapter served as a first step to a complete robotic prototype preliminary testing for surgical applications.

7.1 First 1 DoF APCR Prototype

The first attempt to create an APCR microsnake device that would combined dexterity, miniaturization and hollow bore was built in 2015. Using a *flexure-based* design, the first prototype was made in the ARMA Lab at Vanderbilt University and served as a feasibility study of the flexure-based concept. This type of design relies on the flexible section of its body, generated by the notches, to affect a directional bending. This design uses in 2 concentric Super-elastic NiTi tubes. The inner tube has a outer diameter (OD) of 0.66 mm and inner diameter (ID) of 0.48 mm, while the outer tube has an OD of 0.88 mm and ID of 0.71 mm. The notches width and the desired gap between notches was expected to be 1.2 mm due to early fabrication limits. The notches on the tubes were made using a Dremel tool (fig.7.2A.③) equipped with a diamond cutter disk (fig.7.2B.② which has a thickness of $0.65 \pm 0.03mm$. The fabrication setup shown in Fig. 7.2A uses a DynoLight camera ① for visualization connected to a desktop monitor as shown in fig.7.2B. The Nitinol tube are mounted on a tube holder (fig.7.2A.②) while the Dremel tool is driven using a manually

actuated cartesian stage (fig.7.2A.④).

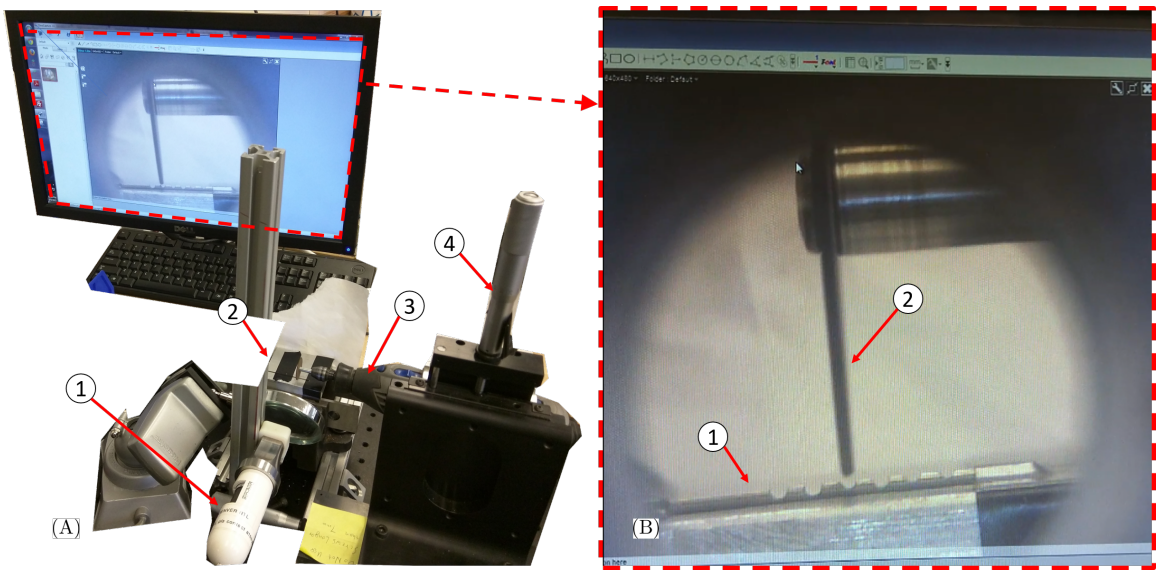

Figure 7.2: Fabrication setup for first Microsnake prototype: A.① Dynolight camera ② Tube holder ③ Dremel ④ Parker XYZ micro-meter cartesian stage - B.① Nitinol tube ② Diamond disk cutter

After a first attempt for inner tube (fig.7.2B) where the notches were obtained using a single diamond disk manually advanced to obtain the desired opening gap, the notches on the outer tube are machined using two adjacent passes with the disk cutter. As shown in the fig.7.2A, there is a cusp in the middle of each cuts. Once the tubes are machined, they are concentrically stacked facing 180° to each other and glued at the distal tip using metal glue, matching the cut at the same height. Figure.7.2C shows the assembled device.

Once assembled, the device is actuated by pushing and pulling on the nitinol tubes. Figure 7.4A-B shows the microsnake protoype bending in both directions. It is clearly visible how the curvature of the device is not constant as it was expected. The close up view in Figure 7.4C shows the inner tube kinking due to high stress concentration and lack of mechanical support to its thin wall.

This first prototype served as a feasibility study for this type of device. Moreover, from this first prototype we realized we had to improve and optimize several critical aspect of the design and fabrication:

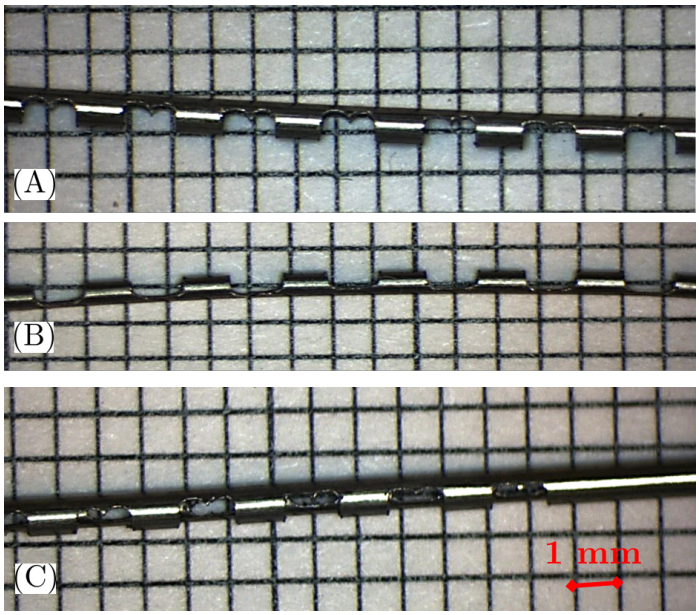

Figure 7.3: Machined and assembled nitinol tubes: A. Outer tube OD 0.88 mm - B.Inner tube OD 0.66 mm - C. Assembled APCR device

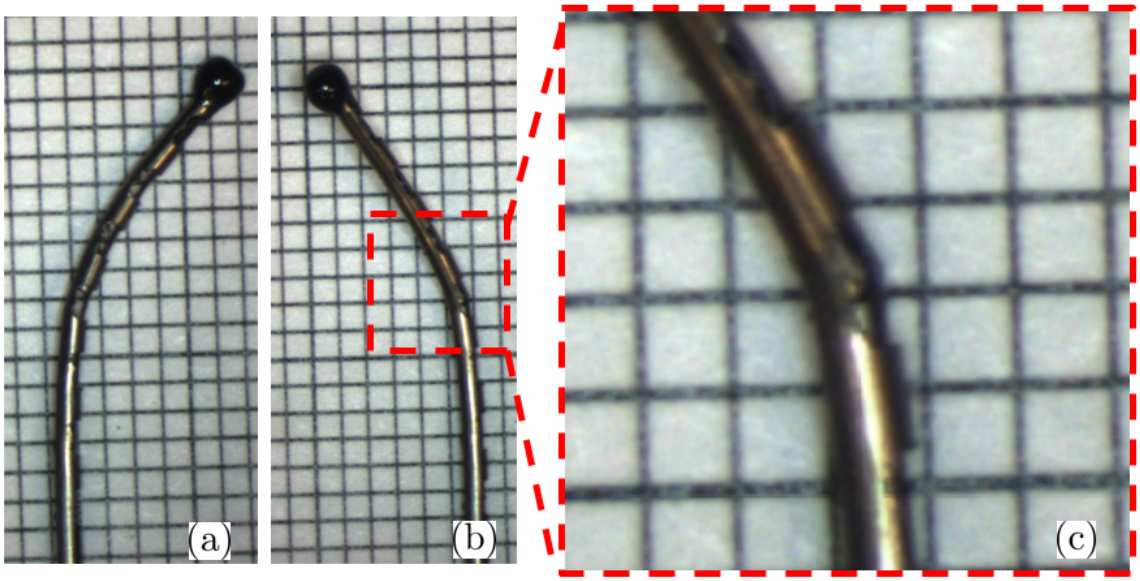

Figure 7.4: Testing of the first prototype: a) right bending b) left bending c) closeup view of the kinked section

- Notch geometry and gap spacing need be improved and optimized
- Mechanical support of thin walls is needed in order to avoid buckling
- Fabrication and assembly process needs to be improved

The next section addresses these problems.

7.2 Two Segment APCR Microsnake

In this section we presents the updated design of the first prototype of the APCR microsnake introduced in the previous section. The new design extends the device to a 2 segment continuum robot using 3 concentrically stacked tubes instead of 2. Each segment can provide 1 DoF and the two consecutive segments are relatively rotated 90° from each other.

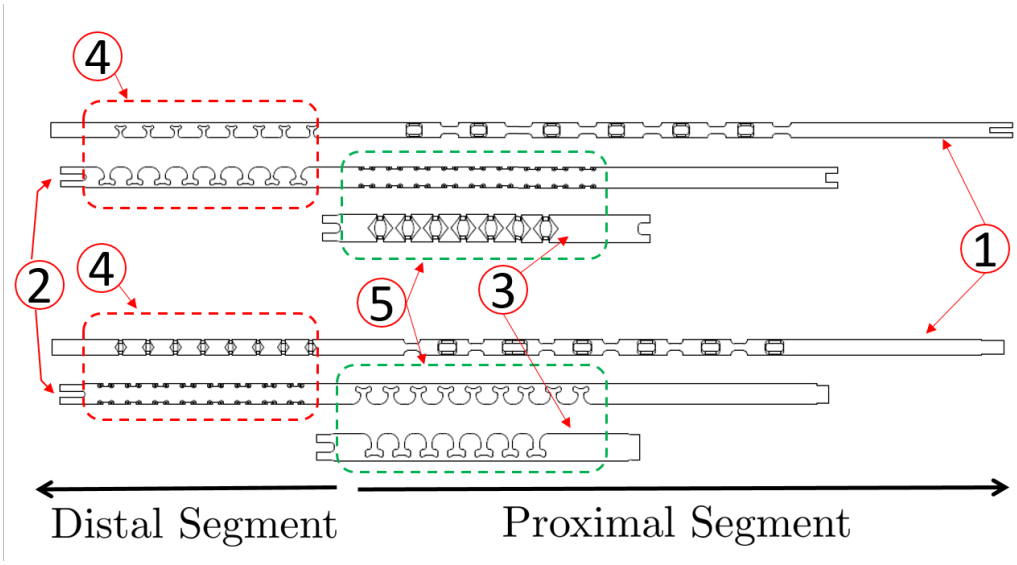

Figure 7.5: 2 DoF APCR design concept

The new design concept is shown in Fig. 7.5. Three thin-walled super-elastic NiTi tubes (Fig. 7.5①②③) are micro-machined using electron discharge machining or femtosecond laser to create a series of flexures designed in a specific way to reduce flexural rigidity of each tube.

According to our design, an innermost tube (Fig. 7.5①) serves as the main support and is proximally notched with bi-directionally alternating flexures that reduce its flexural rigidity so it acts as a passively bending micro-segment in its proximal portion (the portion from the base of the actively steerable segments to an eventual actuation unit). The distal tip of this inner tube has a different flexure pattern consistent with forming an antagonistic bending segment (Fig. 7.5④) with an intermediate tube (Fig. 7.5②). The intermediate tube is housed around and soldered to the distal end of the inner tube. The portion of the intermediate tube, which protrudes past the distal tip of an outer tube (Fig. 7.5③), is also notched with flexures that are circumferentially opposed to the placement of the flexures in the distal portion of the inner tube.

By pushing and pulling the inner tube while holding the intermediate tube fixed at the base of the actuation unit, the second (distal) segment (Fig. 7.5④) of the continuum robot is controllably bent. To add a proximal bending segment (Fig. 7.5⑤), an outer tube (Fig. 7.5③) is added and affixed at its distal tip to the intermediate tube. By pushing and pulling the outer tube, while holding the intermediate tube fixed, the proximal segment of the catheter may be controllably bent. Finally, an angular offset separates the flexure notches in the distal and proximal segments in order to allow 3D bending.

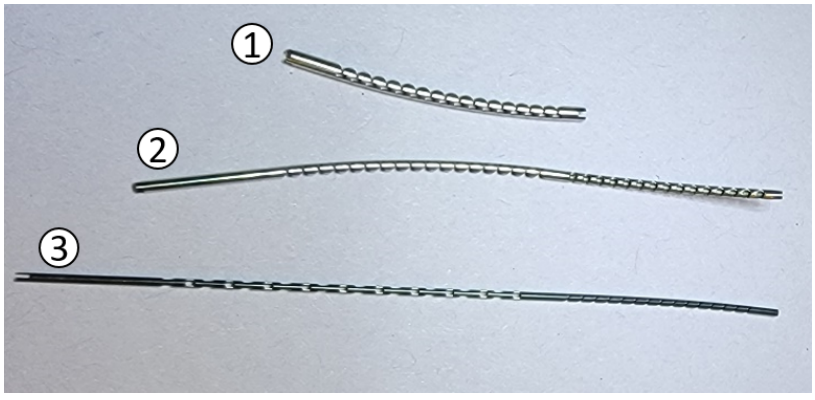

Figure 7.6: New NiTi tubes: ① Outer tube (OD 1.2 mm) ② Intermediate tube (OD 0.88 mm) ③ Inner tube (OD 0.66 mm)

The machined outer tube shown in Fig.Fig. 7.5① has an OD of 1.2 mm and id 0.94 mm; the middle tube ② has an Od of 0.88 mm and ID of 0.71 mm; the most internal tube ③

has an OD of 0.66 mm and ID of 0.48 mm. It was clear from the first test of the previous design that the notches design played a critical role in terms of the continuum segment behaviour. It was crucial to have a better notches design to avoid high stress concentration on the tubes structure that was causing the snake segment to bend in a non circular shape by concentrating the majority of the bending in a single spot along the tube instead to have an equally distributed bending angle on each notch.

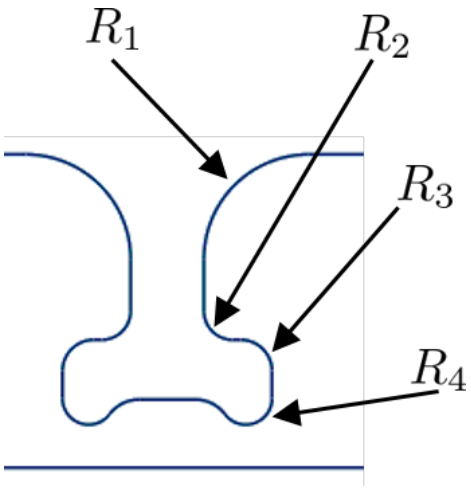

Figure 7.7: Notch geometry model

The technical drawing of new notch geometry is shown in Fig. 7.8. Once the overall new geometry was designed, we defined 4 design parameters R_1, R_2, R_3, R_4 which we used in the ANSYS FEA design parameters optimization (Fig. 7.8) to calculate the best set of parameters that would minimize the stress concentration over the length of the nitinol tubes when bending under a defined load. The optimization was repeated for each of the three tubes.

Furthermore, one of the limitation from the previous design was also related with the fabrication process. Given the more complex notch design and the higher number of features on each tube, an external supplier which provides wire electrical discharge machining (EDM) service was used to fabricate the 3 tubes. Figure 7.9.a shows the result of the EDM machining on the inner tube. The 3 tubes where then assembled concentrically in the lab and accordingly secured on each other following the design scheme.

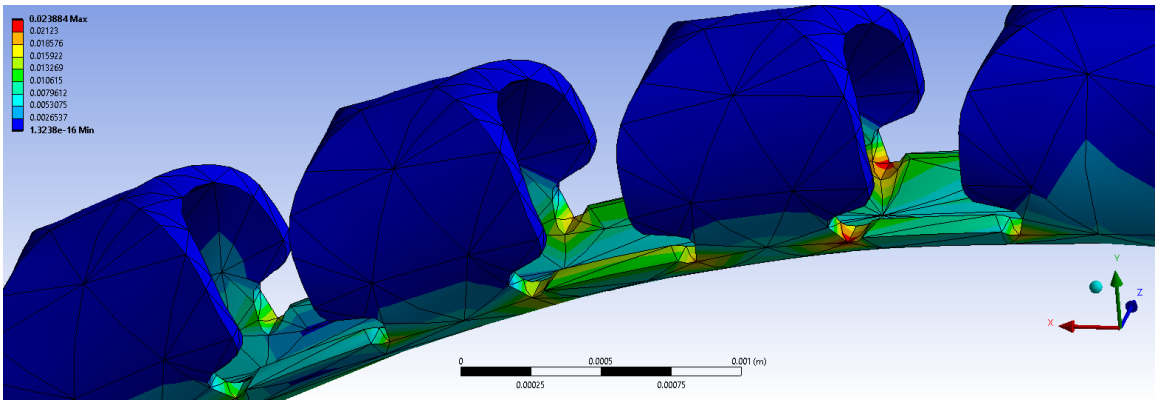

Figure 7.8: ANSYS FEA analysis on the 0.88 mm tube

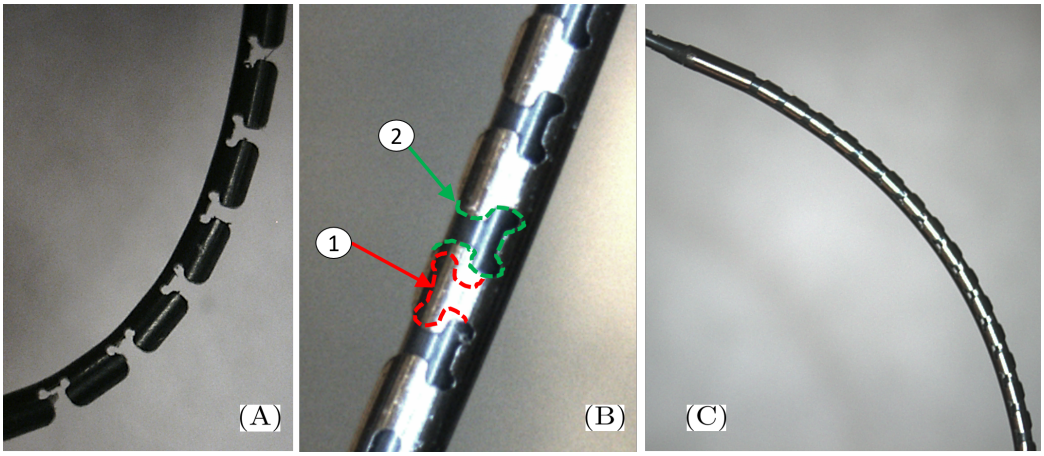

Figure 7.9: A) Close up view of the notched tube machined using EDM - B) Close up view of the concentrically stacked tubes: ① notch profile of the inside tube hidden behind the solid portion of the outside tube, ② notch profile of the outside tube C) Actuated proximal segment.

Differently from the previous design, in order to provide mechanical support to the thin wall of each tube at the notch location, the tubes are still concentrically stacked and facing 180° to each other, but they were shifted longitudinally so that the each notch of the inside tube would be covered by the portion of the outside tube as shown in Fig. 7.9.B. The solder process, even if more technically challenging, was preferred over the prior method, which used metal glue, to offer a stronger bond between tubes and secured their relative tip motion. As a result of the new notch design, Figure. 7.9.C shows the bending curvature of the proximal segment of the new device which presents a smooth and fairly constant curvature along the length of the segment.

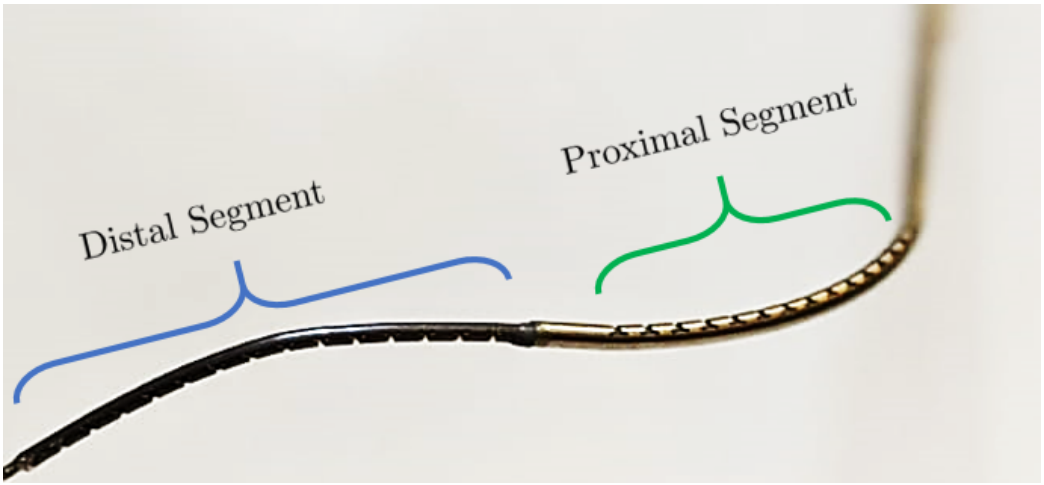

Figure 7.10: 2 Dof APCR flexure-based device

Finally, Fig. 7.10 shows the 2 segment 2 DoF APCR device assembled and actuated at both segments.

7.3 Preliminary results for double articulated micro-catheter for Mechanical Thrombectomy

The first test application of the new device is reported in [144]. The clinical motivation behind this first application is related to the treatment of ischemic stroke which is the usually treat with intravenous thrombolysis with r-tPA. A new approach using endovascular

mechanical thrombectomy was proved [145] safe and effective for treating large vessel occlusions.

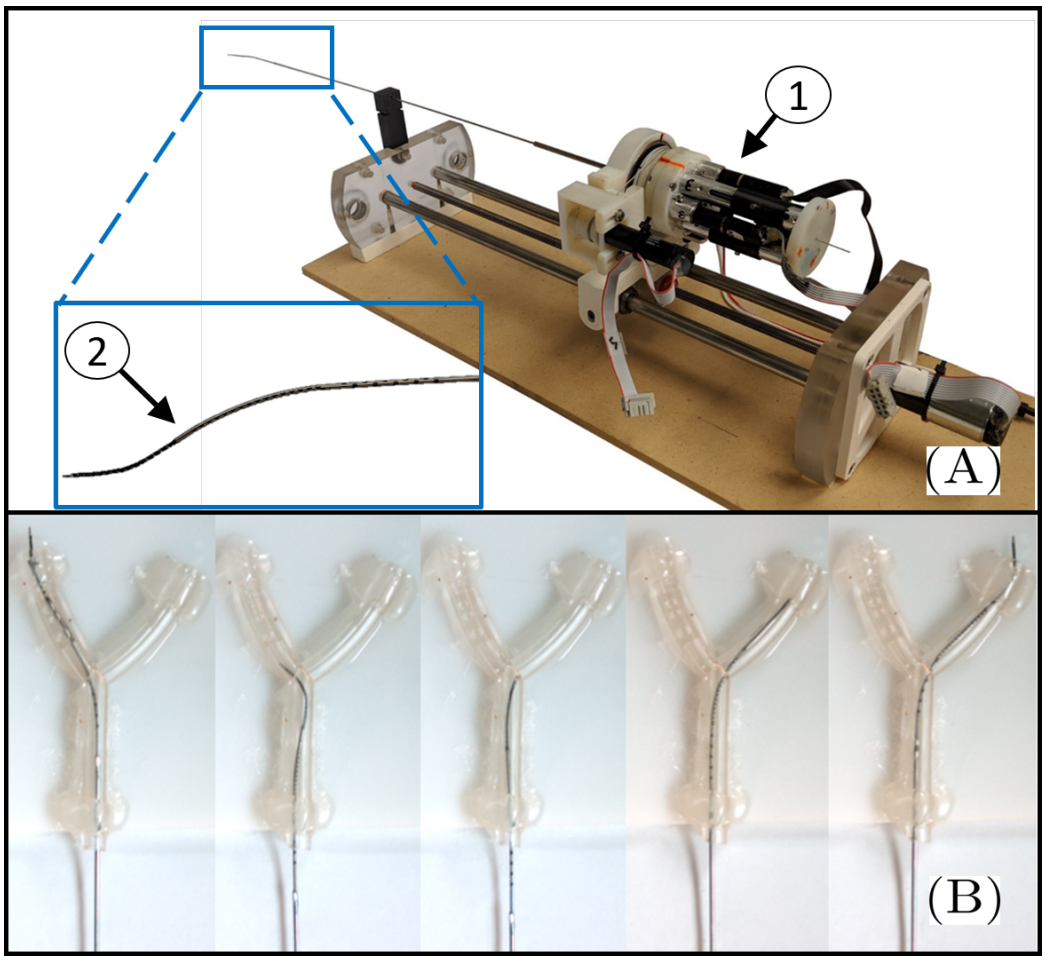

Figure 7.11: Experimental setup: a) ① APCR Actuation unit ② APCR device b) Branch selection using APCR device

Mechanical thrombectomy requires high familiarity with the process and high technical skill to navigate to the portion of the vessel that needs revascularization using passive flexible catheters and a guide wire. The lack of distal control of the current catheters and the naturally tortuous path of the internal carotid artery, make it very hard to reach the middle cerebral artery (MCA). For these reasons, the device presented in this chapter, offers a base platform to provide extra dexterity to the mechanical thrombectomy procedure.

In [144], we propose to use a pre-operative CT scan to define an optimal trajectory to the occlusion site and then use the APCR device to navigate to the target point.

As a first step to a semi-automated navigation process, a preliminary experiment for bifurcated branch selection was conducted. The APCR device was coupled with a 2 DoF actuation unit shown in Fig. 7.11.A① and using a 60° planar bifurcation created using a 3.5 mm ID PTFE tube, shown Fig. 7.11B, the APCR device was inserted while controlled in joint space. While inserting we were able to select the desired branch to follow by steering it, in both direction, as shown in Fig. 7.11.B.

7.4 Kinematic Modeling of the Robotic System

As a first step to an optimized APCR device for intraocular surgical application, this section presents the constrained kinematic derivation of a robotic system comprised of the newly designed APCR snake like robot coupled with a commercial serial arm (SA). In the simulation the APCR system is assumed to be comprised of an actuation unit and a stem section carried by the SA at its EE location as shown in Fig. 7.12.

7.4.1 Nomenclature

For your reference, Below is reported the nomeclature used in this section:

$\hat{\mathbf{u}}$ is a unit vector along vector $\mathbf{u}$. An absence of the superscript for vector $\mathbf{u}$, if not defined seperately, denotes that the position is with respect to and expressed in the frame $\{B\}$.

$[\mathbf{u}]_\times$ is a cross product matrix of vector $\mathbf{u} = [u_x, u_y, u_z]^{\mathrm{T}}$. Using this definition a cross product $(\mathbf{u} \times \mathbf{v})$ can be represented as $[\mathbf{u}]_\times \mathbf{v}$ where $[\mathbf{u}]_\times = \begin{bmatrix} 0 & -u_z & u_y \\ u_z & 0 & -u_x \\ -u_y & u_x & 0 \end{bmatrix}$

$\{A\}$ is a right-handed frame having its origin at point $\mathbf{a}$ and its unit vectors $\hat{\mathbf{x}}_a$, $\hat{\mathbf{y}}_a$, $\hat{\mathbf{z}}_a$

${}^x\mathbf{u}$is position vector of the point $\mathbf{u}$ with respect to and expressed in the frame $\{X\}$. An absence of the left superscript x denotes that the position is with respect to the

world frame.

${}^{x}\mathbf{R}_{y}$ is rotation matrix representing the orientation of the frame $\{Y\}$ with respect to the frame $\{X\}$. An absence of the left superscript x denotes that the rotation matrix is with respect to the world frame.

${}^{x}\mathbf{H}_{y}$ is homogeneous transformation of the frame $\{Y\}$ with respect to the frame $\{X\}$. An absence of the left superscript x denotes that the homogeneous transformation matrix is with respect to the world frame.

${}^{z}\mathbf{v}_{x/y}$ is the linear velocity of the frame $\{X\}$ with respect to frame $\{Y\}$ and expressed in frame $\{Z\}$

$\mathbf{v}_{y}$ is the absolute linear velocity of the origin of the frame $\{Y\}$. Lack of a left superscript means that the vector is described in world frame.

${}^{z}\dot{\mathbf{x}}_{x/y}$ is the twist of frame $\{X\}$ with respect to the frame $\{Y\}$ and expressed a frame parallel to frame $\{Z\}$. This column vector is comprised of the linear velocity, ${}^{z}\mathbf{v}_{x/y}$, followed by the angular velocity ${}^{z}\boldsymbol{\omega}_{x/y}$. Lack of a left superscript means that the vector is expressed in world frame.

$\dot{\mathbf{x}}_{y}$ is the an absolute twist of frame {Y}. It is comprised of the linear velocity, $\mathbf{v}_{y}$, followed by the angular velocity $\boldsymbol{\omega}_{y}$. Lack of a left superscript means that the vector is described in world frame.

$\theta(s)$ is the angle of the central curve tangent in the bending plane at some arc length s along the curve. The $\theta(s=L)$ and $\theta(s=0)$ are denoted by θ_{L} and θ_{0} respectively. Also, the value of θ_{0} is constant and is equal to $\frac{\pi}{2}$

δ_{k} is the right-handed rotation angle measured from the bending plane about $\hat{\mathbf{z}}_{1}$ to a line passing through the central curve and the k^{th} secondary backbone at $s=0$

ψ is the configuration space vector parameterizing the direct kinematics of the continuum segments. $\psi_i = \begin{bmatrix} \theta_{L_i} & \delta_i \end{bmatrix} \in \mathbb{R}^2$ for the $i-th$ continuum segment

$\tilde{\psi}$ is the augmented configuration space vector parameterizing the direct kinematics of the serial arm including the continuum robot. $\begin{bmatrix} q_1 & q_2 & \cdots & q_8 & \theta_{L_1} & \theta_{L_2} \end{bmatrix}^{\mathrm{T}} \in \mathbb{R}^{10}$.

$\tilde{\mathbf{q}}$ is the augmented joint space vector that includes the serial arm joint values followed by the continuum robot joint space vector $\mathbf{q}_{CS}$. $\begin{bmatrix} q_1 & q_2 & \cdots & q_8 & \mathbf{q}_{CS}^{\mathrm{T}} \end{bmatrix}^{\mathrm{T}}$.

$\mathbf{J}_{\tilde{\mathbf{q}}\tilde{\psi}}$ is the Jacobian matrix that maps augmented configuration space velocity, $\dot{\tilde{\psi}}$, to the augmented joint space velocity, $\dot{\tilde{\mathbf{q}}}$

7.4.2 Serial arm kinematic model

In order to derive the direct kinematics from joint space to task space for the serial arm, comprising of the SA the CR stem and consequently its instantaneous kinematic, the frame definition (from frame {B} to frame {7} is generated according the Denavit-Hartenberg (DH) convention and Table 7.1 provides the DH parameters for the Meca500.

Table 7.1: DH Parameters. Length units are in mm. Angular units are in radians.

	$\hat{\mathbf{z}}_{i-1}$ to $\hat{\mathbf{z}}_i$		$\hat{\mathbf{x}}_{i-1}$ to $\hat{\mathbf{x}}_i$	
	along $\hat{\mathbf{x}}_i$	about $\hat{\mathbf{x}}_i$	along $\hat{\mathbf{z}}_{i-1}$	about $\hat{\mathbf{z}}_{i-1}$
Frame	$\mathbf{a}_i$	$\boldsymbol{\alpha}_i$	$\mathbf{d}_i$	$\boldsymbol{\theta}_i$
1	0	$\frac{\pi}{2}$	102	q_1
2	350	0	-40	q_2
3	0	$\frac{\pi}{2}$	40	q_3
4	140	$-\frac{\pi}{2}$	300	q_4
5	37.5	$\frac{\pi}{2}$	10	q_5
6	0	0	0	q_6
7	0	0	q_7	0

For the serial arm, task space is defined by the position and orientation of frame {T} as

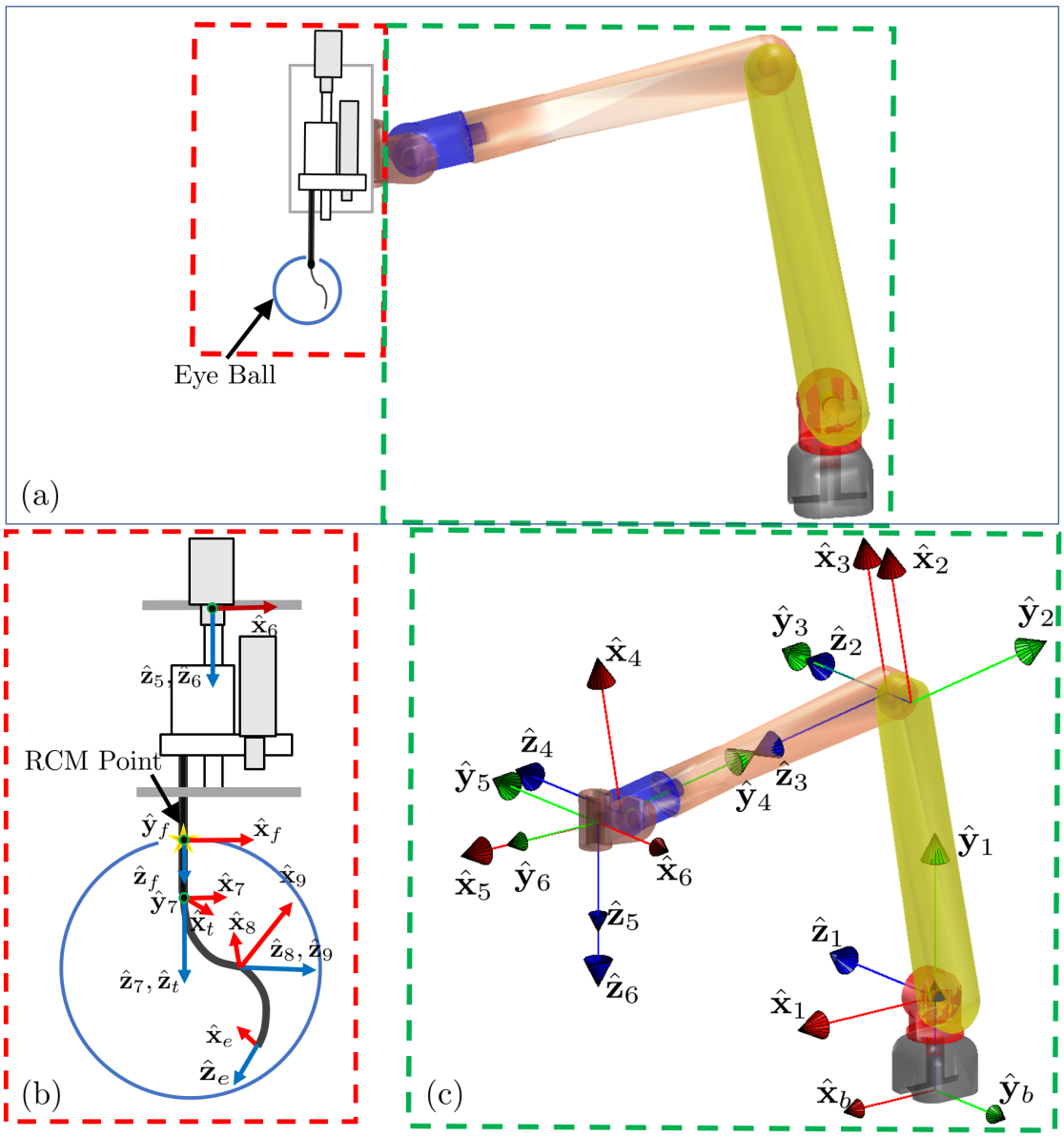

Figure 7.12: System frames assignment

expressed by homogeneous transformation ${}^{b}\mathbf{H}_t$ given as:

$$ {}^{b}\mathbf{H}_t = \begin{bmatrix} {}^{b}\mathbf{R}_t & \mathbf{t} \\ \mathbf{0} & 1 \end{bmatrix} = \prod_{i=1}^{6} {}^{i-1}\mathbf{H}_i \prod_{j=7}^{8} {}^{j-1}\mathbf{H}_j \tag{7.1} $$

where $\mathbf{t}$ is the position vector of the origin of frame $\{T\}$ respect to frame $\{\mathrm{B}\}$ and $\mathbf{R}_t$ is the orientation of frame $\{T\}$ relative to frame $\{B\}$.

The direct kinematics expressed as a moving frame sequence can be given by the post multiplication of the link parameters matrices such that:

$$ {}^{b}\mathbf{H}_6 = \prod_{i=1}^{6} {}^{i-1}\mathbf{T}_i \tag{7.2} $$

where, ${}^{i-1}\mathbf{T}_i$ is the DH link transformation matrix relating the i^{th} coordinate system to the $(i-1)^{th}$ coordinate system for a given set of DH link parameters $\theta_i,\ \alpha_i,\ a_i,\ d_i,\ i = 1 \ldots 6$:

$$ {}^{i-1}\mathbf{T}_i = \begin{bmatrix} c_{\theta_i} & -c_{\alpha_i} s_{\theta_i} & s_{\alpha_i} s_{\theta_i} & a_i c_{\theta_i} \\ s_{\theta_i} & c_{\theta_i} c_{\alpha_i} & -s_{\alpha_i} c_{\theta_i} & a_i s_{\theta_i} \\ 0 & s_{\alpha_i} & c_{\alpha_i} & d_i \\ 0 & 0 & 0 & 1 \end{bmatrix} \tag{7.3} $$

and

$$ {}^{6}\mathbf{H}_8 = \prod_{j=7}^{8} {}^{j-1}\mathbf{T}_j \tag{7.4} $$

is the homogeneous transformation sequence related with the CR stem position and orientation and the joint variable q_7, q_8.

It should be noted here that frame $\{0\}$ is coincident with the base frame $\{B\}$ and frame $\{8\}$ is frame $\{T\}$ defined at the tip of the shaft.

7.4.3 Instantaneous kinematics

The mapping from joint velocities to end effector twist is generated by taking the time derivative of the direct kinematics. The transformation from the end-effector space velocity and joint space velocity is given by the following relationship:

$$\dot{\mathbf{x}}_t = \mathbf{J}_{\mathbf{xq}}\dot{\mathbf{q}} \tag{7.5}$$

For the above definition of $\dot{\mathbf{x}}_t$, the Jacobian matrix, $\mathbf{J}_{\mathbf{xq}} \in \mathbb{R}^{6\times 8}$, is given by the Plücker line coordinates of each joint axis as expressed in a frame parallel to the world frame and centered at the origin of frame {T}:

$$\mathbf{J}_{\mathbf{xq}} = \begin{bmatrix} \hat{\mathbf{z}}_0 \times (\mathbf{o}_8 - \mathbf{o}_0) & \hat{\mathbf{z}}_1 \times (\mathbf{o}_8 - \mathbf{o}_1) & \hat{\mathbf{z}}_2 \times (\mathbf{o}_8 - \mathbf{o}_2) & \hat{\mathbf{z}}_3 \times (\mathbf{o}_8 - \mathbf{o}_3) \\ \hat{\mathbf{z}}_0 & \hat{\mathbf{z}}_1 & \hat{\mathbf{z}}_2 & \hat{\mathbf{z}}_3 \\ \hat{\mathbf{z}}_4 \times (\mathbf{o}_8 - \mathbf{o}_4) & \hat{\mathbf{z}}_5 \times (\mathbf{o}_8 - \mathbf{o}_5) & \hat{\mathbf{z}}_6 \times (\mathbf{o}_8 - \mathbf{o}_6) & \hat{\mathbf{z}}_7 \\ \hat{\mathbf{z}}_3 & \hat{\mathbf{z}}_4 & \hat{\mathbf{z}}_5 & \hat{\mathbf{z}}_6 \quad 0 \end{bmatrix} \tag{7.6}$$

where, $\mathbf{o}_i$, is the position vector of an origin of the i^{th} coordinate system.

7.5 Continuum Robot Kinematics

This section provides the final formulation to compute the pose of the end disk given the configuration space vector. The derivation is based on [26, 84], for brevity we will not report the full derivation but only the final expression of the Jacobian mapping $\mathbf{J}_{\mathbf{x}\psi}$ which provides the mapping from the configuration space velocity $\dot{\psi} = \begin{bmatrix} \dot{\theta}_L & \dot{\delta} \end{bmatrix}^{\mathrm{T}}$ and the generalized twist of the end disk ${}^t\dot{\mathbf{x}}_{g/t} = \begin{bmatrix} {}^t\dot{\mathbf{g}}^{\mathrm{T}}, & {}^t\boldsymbol{\omega}_{g/t}^{\mathrm{T}} \end{bmatrix}^{\mathrm{T}}$, where $g = 8, e$. Referring to

equation 6 in [84], the Jacobian matrix $\mathbf{J}_{\mathbf{x}\psi} \in \mathbb{R}^{6\times 2}$ is given by:

$$\mathbf{J}_{\mathbf{x}\psi} = \begin{bmatrix} L\cos(\delta)\left(\frac{(\theta_L-\frac{\pi}{2})\cos(\theta_L)-\sin(\theta_L)+1}{(\theta_L-\frac{\pi}{2})^2}\right) & L\sin(\delta)\left(\frac{1-\sin(\theta_L)}{\theta_L-\frac{\pi}{2}}\right) \\ -L\sin(\delta)\left(\frac{(\theta_L-\frac{\pi}{2})\cos(\theta_L)-\sin(\theta_L)+1}{(\theta_L-\frac{\pi}{2})^2}\right) & L\cos(\delta)\left(\frac{1-\sin(\theta_L)}{\theta_L-\frac{\pi}{2}}\right) \\ L\left(\frac{(\theta_L-\frac{\pi}{2})\sin(\theta_L)+\cos(\theta_L)}{(\theta_L-\frac{\pi}{2})^2}\right) & 0 \\ -\sin(\delta) & \cos(\delta)\cos(\theta_L) \\ -\cos(\delta) & -\sin(\delta)\cos(\theta_L) \\ 0 & \sin(\theta_L)-1 \end{bmatrix} \tag{7.7}$$

The above mapping is the generalized form for a 2 DoF single segment continuum robot. In our case, the continuum segment has only 1 DoF so we are assuming that the bending plan orientation δ is zero. Consequently we are only considering the first column of $\mathbf{J}_{\mathbf{x}\psi}$. For a 2 segment continuum robot we are identifying two Jacobian matrices $\mathbf{J}_{\mathbf{x}_i\psi_i}$ with $i = 1,2$ which relates the mapping from frame {T} to frame {9} and from frame {10} to frame {E} respectively. The mapping from frame {T} to frame {E} is then give by the following relation:

$$\mathbf{J}_{\mathbf{x}\tilde{\psi}} = \left[\mathbf{S}_{te}\mathbf{J}_{\mathbf{x}_1\psi_1}\middle|\quad \mathbf{S}_{9t}\mathbf{J}_{\mathbf{x}_2\psi_2}\right] \tag{7.8}$$

where $\mathbf{S}_{te}$ is a twist transformation from frame {E} to frame {T} defined as:

$$\mathbf{S}_{te} = \begin{bmatrix} \mathbf{I} & ({}^t\mathbf{p}_9 - {}^9\mathbf{p}_e)_\times \\ \mathbf{0} & \mathbf{I} \end{bmatrix} \tag{7.9}$$

and

$$\mathbf{S}_{9t} = \begin{bmatrix} {}^t\mathbf{R}_9 & 0 \\ \mathbf{0} & {}^t\mathbf{R}_9 \end{bmatrix} \tag{7.10}$$

where ${}^t\mathbf{R}_9$ is the rotation matrix from frame {9} to frame {T} , ${}^t\mathbf{p}_9$ and ${}^9\mathbf{p}_e$ are the vector pose of frame {9} respect to {T} and frame {E} respect to {9}.

7.6 Unconstrained kinematics of the Robotic System

Referring to Fig. 7.12 the robotic system comprised from a serial arm and a 2 DoF two segment CR. We define frames {P} and {T} representing frames {6} and {7} in figure 7.12. Frames {T} and {P} are parallel and separated by the joint variable q_7.

Given the kinematics of the serial arm and the kinematics of the continuum robot, we wish to derive the overall system kinematics and to set the stage for solving the constrained manipulation problem while respecting the fulcrum constraints (frame {F}). In this subsection we derive the overall unconstrained system kinematics which means, referring to Fig. 7.12, we are not considering the conditions of frame {F}. We derive the key mappings used for robot simulations and high-level resolved-rates control. We use the augmented space variables defined in the nomenclature and derive the key kinematic mappings between the augmented joint space velocity $\dot{\tilde{\mathbf{q}}}$, the configuration space velocity $\dot{\tilde{\psi}}$, and the generalized twist of the end effector $\dot{\mathbf{x}}_e$.

The end effector's absolute twist is given by:

$$\dot{\mathbf{x}}_e = \dot{\mathbf{x}}_t + \dot{\mathbf{x}}_{e/t} \tag{7.11}$$

where $\dot{\mathbf{x}}_t$ is the twist of frame $\{T\}$ and $\dot{\mathbf{x}}_{e/t}$ is the relative twist of frame $\{E\}$ with respect to frame $\{T\}$.

The first term in Eq. (7.11) (the twist $\dot{\mathbf{x}}_t$) is given by the serial arm kinematics as $\mathbf{J}_{xq}\dot{\mathbf{q}}$. In the following steps, we derive the expression for the second term of Eq. (7.11) ($\dot{\mathbf{x}}_{e/t}$). The relative twist $\dot{\mathbf{x}}_{e/t}$ is given by the contribution due to the motion of frame $\{T\}$ while the CR is locked and the contribution of motion due to the CR:

$$\dot{\mathbf{x}}_{e/t} = \begin{bmatrix} \mathbf{0} & [\mathbf{t}-\mathbf{e}]_\times \\ \mathbf{0} & \mathbf{0} \end{bmatrix} \dot{\mathbf{x}}_t + \mathbf{B}_t{}^t\dot{\tilde{\mathbf{x}}}_{e/t} \tag{7.12}$$

where the first term is the twist contribution to frame $\{T\}$ due to the angular velocity of

the serial arm acting on an imaginary rigid link from point **t** to point **e**. The twist ${}^{t}\dot{\mathbf{x}}_{e/t}$ is the relative end-effector twist assuming the serial arm is locked and the CR is moving. The matrix $\mathbf{B}_t$ is an adjoint relating the twist in frame $\{T\}$ to a frame centered at **t** and parallel to the world frame. This adjoint matrix is given by:

$$\mathbf{B}_t = \begin{bmatrix} \mathbf{R}_t & \mathbf{0} \\ \mathbf{0} & \mathbf{R}_t \end{bmatrix} \tag{7.13}$$

The relative twist ${}^{t}\dot{\mathbf{x}}_{e/t}$ is due to the continuum robot motion :

$${}^{t}\dot{\mathbf{x}}_{e/t} = \mathbf{J}_{\mathbf{x}\psi}\dot{\psi} \tag{7.14}$$

Assuming that the CR has its own serial kinematics we can write:

$$\dot{\mathbf{x}}_{e/t} = \begin{bmatrix} \mathbf{0} & [\mathbf{t}-\mathbf{e}]_\times \\ \mathbf{0} & \mathbf{0} \end{bmatrix} \mathbf{J}_{\mathbf{xq}}\dot{\mathbf{q}} + \mathbf{B}_t\mathbf{J}_{\mathbf{x}\psi}\dot{\psi} \tag{7.15}$$

now, substituting the relative twist $\dot{\mathbf{x}}_{e/t}$ from equation (7.15) into equation (7.11) and using equation (7.5), we can arrive at the complete arm kinematics simplify into:

$$\dot{\mathbf{x}}_e = \underbrace{\begin{bmatrix} \mathbf{I} & [\mathbf{t}-\mathbf{e}]_\times \\ \mathbf{0} & \mathbf{I} \end{bmatrix}}_{\mathbf{A}_{te}} \mathbf{J}_{\mathbf{xq}}\dot{\mathbf{q}} + \mathbf{B}_t\mathbf{J}_{\mathbf{x}\psi}\dot{\psi} = \mathbf{J}_{\mathbf{x}\tilde{\psi}}\dot{\tilde{\psi}} \tag{7.16}$$

For the above definition of $\dot{\mathbf{x}}_e$, the Jacobian matrix, $\mathbf{J}_{\mathbf{x}\tilde{\psi}} \in \mathbb{R}^{6\times 10}$, is given by:

$$\mathbf{J}_{\mathbf{x}\tilde{\psi}} = \begin{bmatrix} \mathbf{A}_{te}(\mathbf{J}_{\mathbf{xq}})_{SA} & \vert & \mathbf{B}_t\mathbf{J}_{\mathbf{x}\psi} \end{bmatrix} \tag{7.17}$$

The subscript *SA* used in equations (7.17) indicates that the respective quantity is related to the serial arm.

7.7 Constrained kinematics of the Robotic System

In this section we are considering the presence of an incision point $\tilde{\mathbf{f}}$ which applies remote center of motion (RCM) kinematic constraints on the shaft of the serial arm. We use $\mathbf{f}$ to denote the point instantaneously coincident with $\tilde{\mathbf{f}}$. The RCM constrains at the entry point $\tilde{f}$ to allow sliding along and rolling about the longitudinal axis of the robot shaft and two tilting motions while preserving the coincidence of the shaft's longitudinal axis with point $\tilde{\mathbf{f}}$.

The RCM constraints require that the velocity of point $\mathbf{f}$ in a plane perpendicular to the shaft axis $\hat{\mathbf{z}}_t$ should be equal to the velocity of the RCM point $\tilde{\mathbf{f}}$. Defining the linear velocity of the entry point as $\mathbf{v}_{\tilde{f}}$ and the velocity of point $\mathbf{f}$ as $\mathbf{v}_f$, we can express the RCM kinematic constraints as:

$$\mathbf{N}_c \mathbf{v}_f = \mathbf{v}_{\tilde{f}} \qquad , \qquad \mathbf{N}_c = \mathbf{I} - \hat{\mathbf{z}}_t^{\mathrm{T}} \hat{\mathbf{z}}_t \tag{7.18}$$

where the matrix $\mathbf{N}_c$ projects the velocity of point $\mathbf{f}$ along a plane perpendicular to the shaft axis. For an entry point fixed in space, $\mathbf{v}_{\tilde{f}} = \mathbf{0}$ is used in equation (7.18).

The velocity $\mathbf{v}_f$ is given by the kinematics of the serial arm, while considering point $\mathbf{f}$ as the operational point:

$$\mathbf{v}_f = \mathbf{V}_s \mathbf{A}_f \dot{\mathbf{x}}_t \tag{7.19}$$

where, $\mathbf{V}_s = \begin{bmatrix} \mathbf{I} & | & \mathbf{0} \end{bmatrix}$ is the selection matrix that extracts out the linear velocity from the twist and $\mathbf{A}_f$ is the twist transformation matrix shifting the operational point from point $\mathbf{t}$ to point $\mathbf{f}$ and it is defined by:

$$\mathbf{A}_f = \begin{bmatrix} \mathbf{I} & [\mathbf{t}-\mathbf{f}]_\times \\ \mathbf{0} & \mathbf{I} \end{bmatrix} \tag{7.20}$$

Using the serial arm kinematics, we can update equation (7.19) as:

$$\mathbf{v}_f = \mathbf{V}_s \mathbf{A}_f \mathbf{J}_{SA} \dot{\mathbf{q}} \tag{7.21}$$

Equations (7.21) and (7.17) must be solved simultaneously for the joint speeds of the serial arm and the continuum robot in order to satisfy the desired end-effector motion while respecting the entry point constraints. To combine these two linear systems of equations, we use the definitions of the augmented joint space and configuration space variables $\dot{\tilde{\mathbf{q}}}$ and $\dot{\tilde{\psi}}$ as defined in this section's nomenclature. We also define an augmented twist of $\dot{\tilde{\mathbf{x}}}_e$ as $\dot{\tilde{\mathbf{x}}}_e = \begin{bmatrix} \dot{\mathbf{x}}_e^{\mathrm{T}}, & \mathbf{v}_{\tilde{f}}^{\mathrm{T}} \end{bmatrix}^{\mathrm{T}}$. Using these definitions, we can combine equations (7.21) and (7.17) into a single linear system of equations defining the constrained instantaneous direct kinematics:

$$\dot{\tilde{\mathbf{x}}}_e = \mathbf{J}_{\tilde{\mathbf{x}}\tilde{\psi}} \dot{\tilde{\psi}} \tag{7.22}$$

where the augmented jacobian matrix in the above equation is given by:

$$\mathbf{J}_{\tilde{\mathbf{x}}\tilde{\psi}} = \begin{bmatrix} \mathbf{A}_{te}(\mathbf{J}_{\mathbf{xq}})_{SA} & \mathbf{B}_t \mathbf{J}_{\mathbf{x}\psi} \\ \mathbf{N}_c \mathbf{V}_s \mathbf{A}_f (\mathbf{J}_{\mathbf{xq}})_{SA} & \mathbf{0} \end{bmatrix} \tag{7.23}$$

where $(\mathbf{J}_{\mathbf{xq}})_{SA}$ refers to instantaneous direct kinematics Jacobian of the serial arm.

Using the above results, the mapping from the augmented joint space velocity[1], $\dot{\tilde{\mathbf{q}}}$, can be written as:

$$\mathbf{x}_e = \begin{bmatrix} \mathbf{A}_{te}(\mathbf{J}_{\mathbf{xq}})_{SA} & \mathbf{B}_t \mathbf{J}_{\mathbf{x}\psi} \end{bmatrix} \dot{\tilde{\mathbf{q}}} \tag{7.24}$$

Also, since the RCM constraint equations (bottom left side of the matrix in equation (7.23)) include only the joints of the serial arms and since for the serial arm $\psi = \dot{\mathbf{q}}$, we can write:

$$\mathbf{v}_{\tilde{f}} = \begin{bmatrix} \mathbf{N}_c \mathbf{V}_s \mathbf{A}_f (\mathbf{J}_{\mathbf{xq}})_{SA} & \mathbf{0} \end{bmatrix} \dot{\tilde{\mathbf{q}}} \tag{7.25}$$

[1] the augmented joint space vector including the joint speeds of the serial arm followed by the joint speeds of the continuum robot

7.8 Performance Measure: Kinematic Dexterity Measures

In order to evaluate the kinematic dexterity of the robotic system we will use the Kinematic Condition Index (KCI). KCI uses the minimum and maximum singular value of the Jacobian matrices $(\mathbf{J}_{\tilde{\mathbf{x}}\tilde{\psi}})_v$ and $(\mathbf{J}_{\tilde{\mathbf{x}}\tilde{\psi}})_\omega$ where v and ω are identifying the translational and translational portion of the Jacobian matrix. [2].

Through the process of singular value decomposition we can write:

$$\mathbf{J}_i = \mathbf{U}\Sigma\mathbf{V}^{\mathrm{T}} \in \mathbb{R}^{m\times n}, \quad i \in [v, \omega] \tag{7.26}$$

where, Σ is the diagonal matrix of singular values defined as, $\Sigma = diag\begin{pmatrix}\sigma_1 & \sigma_2 & \sigma_3 & \cdots & \sigma_m\end{pmatrix}$, where, $\sigma_1 > \sigma_2 > \sigma_3 > \cdots > \sigma_m$. Using these values, the kinematic dexterity index is given by:

$$I = \text{Kinematic conditioning index (inverse condition number)}(KCI) = \frac{\sigma_{min}}{\sigma_{max}} \tag{7.27}$$

7.9 Preliminary Consideration and Simulation Results

In order to test the derived constrained kinematic, a preliminary test simulation was conducted. The plots in Fig. 7.13 show a screenshot of the robotic system during a path following simulation. The task required the EE to follow the desired path keeping a constant orientation. The desired path has been designed as a circle with the same dimension of the equator of an eyeball and we have constrained the robot with an RCM point located at the superior pole of the eyeball which simulates the entry point during an ophthalmic procedure. The new APCR device, that was built in the ARMA Lab, has a total length of $43\,mm$ and 1.2 mm in diameter. Even if the size of the NiTi tubes are compatible with intraocular procedures, its length is not. According to [146] the size of an

[2] Because of the unit inconsistencies among the in Jacobian matrix $\mathbf{J}_{\mathbf{x}\tilde{\mathbf{q}}}$, the translational $\mathbf{J}_v$ and rotational $\mathbf{J}_\omega$ portions were compared separately and normalized with respect to a characteristic length $||\mathbf{t}-\mathbf{p}||_2$ (the length of link stem).

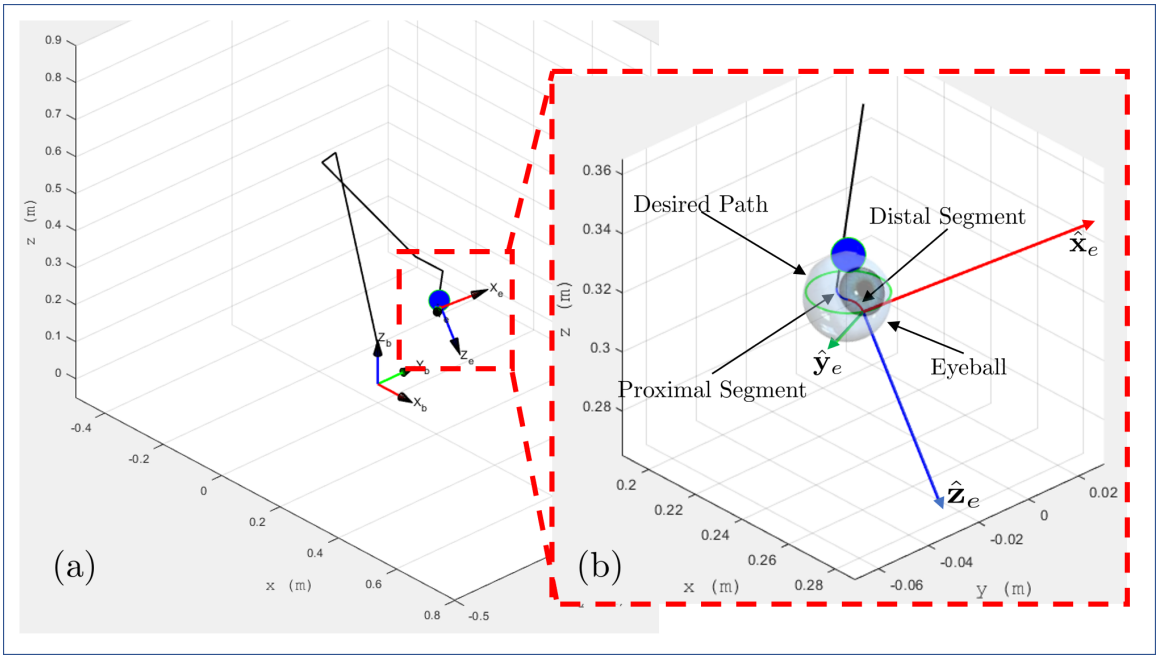

Figure 7.13: Path following: a) Sticks representation of the robotic system while performing the desired task - b) Closeup view of the end effector following the desired trajectory

emmetropic human adult eye has been estimated at $24.2 \times 23.7 \times 24.8mm$ (transverse, horizontal)x(sagittal, vertical)x(axial, anteroposterior) with no significant difference between sexes and age groups.

As a preliminary evaluation of the ability for the APCR device to complete the designed task, we have shortened the length of the CS to simulate 3 scenarios for 3 different CSs length: 8, 6, and 4 mm length. The plots in Fig. 7.14 show the KCI index derived in eq. (7.27) over the 3 CS length.

7.10 Conclusion

This chapter presented the design and modeling efforts of a new APCR device able to offer 4 DoF of intraocular motions provided by two continuum segments while maintaining a working channel for OCT deployment. The prototype of a single segment APCR device was introduced as a pilot model where the new device was built upon. The design limita-

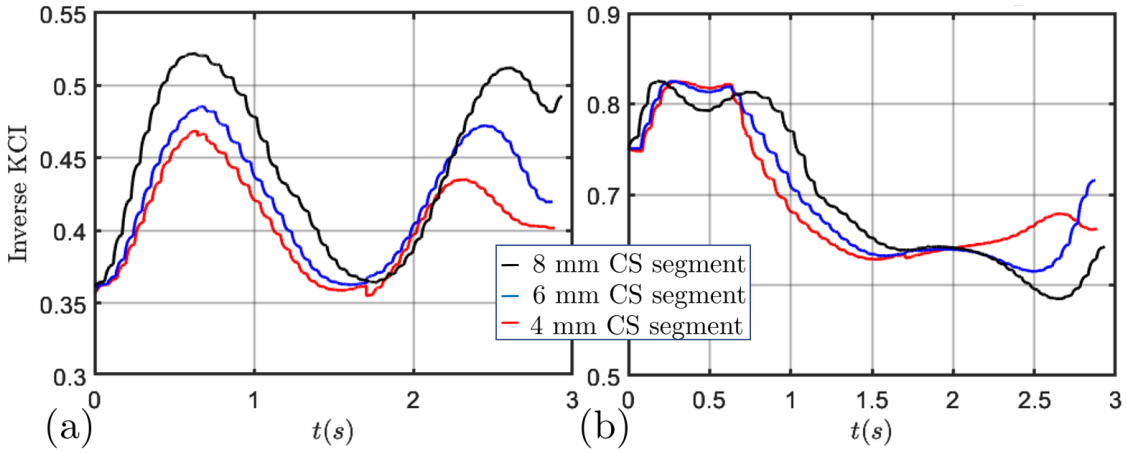

Figure 7.14: a) Translational dexterity b) Rotational dexterity

tions of the prototype were addressed using FEA analysis and new fabrication technologies, which allowed to extend of the new design to a 2 segments APCR. The first testing of the new device within the context of enabling dexterous intravenous navigation for ischemic stroke treatment demonstrated that the device was able to navigate through a mockup artery and was able to choose the path between branches by actively steering. Towards the targeting application of ophthalmic surgery a preliminary derivation of a constrained kinematic model for intraocular dexterity is presented. The derived constrained kinematics has been tested using a task-based simulation where the CR was following the desired path designed to mimic an intraocular trajectory while respecting the RCM constraint.

The simulation has been performed for 3 different lengths of the CSs and the KCI has been reported. The results have shown how the dexterity index is affected by the length of the CSs posing the need for future dimensional optimization of the CS length for a specific application. We believe that even if the design of the device posed several challenges in terms of assembly and fabrication, it was still able to complete the preliminary testing and, as of today, it poses the base of the ongoing project in the ARMA Lab.

CHAPTER 8

STATIC BALANCING OF 3RRR MANIPULATOR

8.1 Introduction

The animal experiment presented in Section 2.7.2 had very important insight not only for the robotic system itself but also for the entire procedure in OR. The weight of the TURBOT is around 6 kg and during the deployment phase, the surgeon was carrying around the unit in order to found the best orientation to access the bladder through the urethra. This operation was cumbersome and tiring for the surgeon to the point that help was needed to accomplish the task. A way around this kind of inconvenient scenarios would be to incorporate the actuation unit on a 6-DoF (at minimum) statically-balanced arm with enough workspace for the task. In this way the surgeon would then only steer the weightless robot in the proper direction.

Moreover, there are many reasons that make the static balancing of a manipulator really important to develop. Some reasons are strictly in terms of economic advantages while others are in terms of mechanical advantages. For example, statically balanced mechanisms have been used for offsetting the physical effort of manufacturing workers in tasks involving payload transfer (e.g. [147]), for offering assistance to patients with weak arms or legs (e.g. [148, 149]) and for supporting surgical or medical imaging instruments [150, 151]. Basically, the static balancing of a manipulator can be defined as the setup of conditions about dimensions and mass parameters of the manipulator which allow, under static conditions, to compensate the weight of each link. This means, do not produce any force or torque at the joint for any configurations of the manipulator.

It is due to define two different ways to have static balancing. A manipulator is called force balanced if the total force acting by the mechanism, on any motion, on the fixed base is constant; this is equal to say that in any configuration, the center of mass of the system remains fixed.

A manipulator is called *statically balanced* in any configuration if the weight of each arm doesn't produce any force of torque at the joints. This condition is also known as *gravity compensation*. The advantages of this condition are many. For example, the need for high-torque actuators in obviated when static balancing is used to offset gravitational torques. This leads to more compact designs with less powerful actuators. There are different ways to achieve static balancing: using masses located in the correct position to counterbalance the mechanism, or using springs to balance the potential energy of the system to the elastic energy of the springs. A review of these methods is available in [152].

This cancellation of gravitational force is accomplished through the strategic placement of elastic elements, the addition of counterweight masses, or a combination of these approaches. Elastic elements can be directly applied to a mechanism's joints only if the mechanism has a very simple geometry (e.g. a single link [153]) otherwise a new sub-mechanisms must be added to the design to generate the desired potential energy functions. Most commonly, these sub-mechanisms are linkages. Most of the literature focuses on balancing of serial linkages (e.g. [147, 154, 155, 156]) and a significant effort has been directed towards balancing of parallel mechanisms. Examples of works focused on parallel mechanism balancing include [157, 158, 159, 160]. Most of these works (with the exception of [160]) produce designs that are too cumbersome for practical implementation.

Many of the mechanisms used in medical robotics require compact designs, portability and a small footprint. It is therefore understandable as to why parallel mechanisms have been considered for many surgical applications. A subset of these surgical applications require holding tools in particular locations for prolonged periods of time (for example,

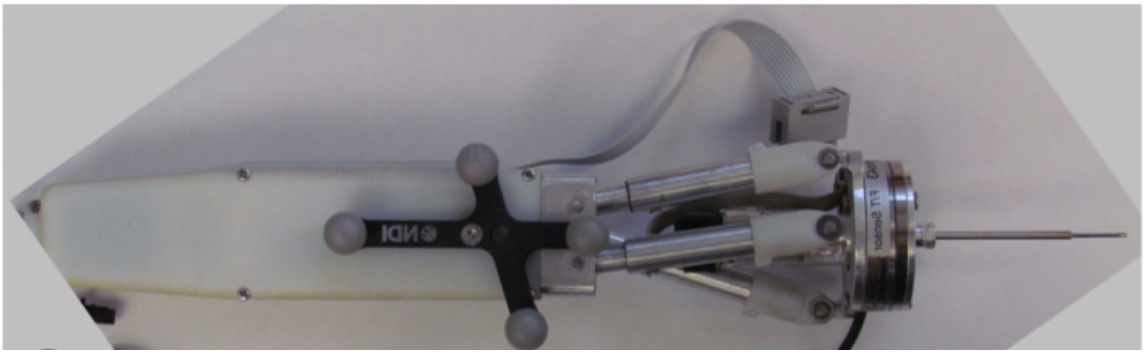

Figure 8.1: Pile's hand held device [1] with hand tremor filtering parallel robot structure.

stabilizing an endoscopic camera or an ultrasound probe). For this reason, there have been a few works considering statically balanced parallel robots for such tasks. Lessard et al [150] proposed a statically balanced planar five-bar linkage mechanisms using masses for manipulating an ultrasound probe for 3D imaging. Pile et al [1] proposed a planar parallel robot for cochlear implant surgery and proposed a methodology for achieving static balancing for these parallel mechanisms using a slider-crack mechanism and a strategic placement of wire-wrapped cams. This work further elaborates on the approach proposed in Pile thesis [160], but focuses on designs where the balancing ia achieved through distributed placement of springs at both active and passive joints of the robot and considers an approach for determining the balancing mechanisms using wire-wrap cams.

8.2 Static Balancing of planar manipulators

Parallel mechanisms have gained use in several applications (e.g. rapid prototyping machines, fast pick-and-place robots, haptic devices and surgical robots) due to their potential benefits of precision, compactness, stiffness and dynamic agility. When attempting to achieve static balancing for these mechanisms, the design task is complicated by the presence of passive and active joints in their kinematic chains. Unlike serial robots where exact static balancing of each joint may be directly decoupled as a sub-problem to be solved by judicious placement of energy storage elements (e.g. [161, 162, 163]), such problem

decomposition is hard to achieve in parallel mechanisms because of the coupled nature of all the closed loop kinematic chains of these mechanisms.

The motivation for statically balanced parallel mechanisms stems from several potential advantages in terms of reducing power and actuators torque requirements, enabling free motion of balanced mechanisms without motors, and safe interaction between humans and machines [164, 165]. For example, statically balanced mechanisms have been used for offsetting the physical effort of manufacturing workers in tasks involving payload transfer (e.g. [166]), for offering assistance to patients with weak arms or legs (e.g. [167, 168] and for supporting surgical or medical imaging instruments [169, 170].

There have been three means for achieving static balancing of parallel mechanisms: a) using counterbalancing masses (e.g. [157, 171]) , b) using springs for energy storage (e.g. [66, 172]), c) using both springs and counterbalance masses (e.g. [173]). We limit this work to solutions using only springs for static balancing due to the drawbacks of counterbalance masses as manifested in increased weight and bulk of the overall parallel mechanism. Such design solutions (based on springs only) are limited to applications where the direction of the gravity vector does not change relative to the base of the parallel linkage.

Although there have been many works in the area of static balancing of parallel linkages, many of the designs proposed are too cumbersome to be attractive for a realistic embodiment. Exceptions to this observation are [174, 175] who proposed and demonstrated a practical embodiment of a six degrees of freedom parallel mechanism with spring-balanced parallelogram linkages. However, if a parallel robot architecture is considered with kinematic chains that do not rely on the use of parallelogram mechanisms, the design solutions are hindered by the presence of passive joints in the kinematic chains. To overcome this, Koser presented a cam-balancing mechanism for serial robots [176] and Kilic et al. presented a wire-wrapped cam mechanism for adjustable stiffness [66].

This chapter presents a practical design alternative for achieving statically balanced parallel mechanisms. Although exact balancing throughout a workspace may be achieved

in particular geometries and with the addition of balancing masses, we avoid the use of such balancing masses in favor of a compact and lightweight design. This design choice is motivated by our envisioned target applications of lightweight parallel robots as hand-held assistive applications in surgery (e.g tremor filtering [177]) or as portable and compact robots for manipulation of a fixed payload (e.g. remote sonography or ultrasound sonography within an MRI bore). The advantage of compactness and design practicality sought in this work comes at a price of achieving only approximate balancing throughout a desired dexterous workspace as opposed to exact balancing.

Given that we can achieve only approximate balancing for a desired workspace, the question of what are the best locations for the placement of balancing springs is addressed in this work. Because of the target application domain, we avoid the use of non-encapsulated spring elements (e.g. a linear spring or a wire passing in air and connecting two links in the mechanism). Such designs offer a risk of injury by potentially grabbing tissue and complicate the task of sterilization using sterile drapes that may also be caught on these springs.

With these sought design traits, we consider two design alternatives: 1) parallel mechanisms using torsional springs in either their active and/or in their passive joints, 2) parallel mechanisms using a combination of linear springs at the base with wire-wrapped cams at the base.

Relative to prior literature, we present a contribution that uses the 3RRR parallel robot architecture as a benchmark application for our design strategy and we illustrate the importance of selecting the possible locations for the balancing springs. We compare the alternative of placing springs in parallel with the active joints v.s. the option of placing the balancing springs in the passive (elbow joints). We also present an approach whereby approximate balancing is achieved throughout a portion of the workspace by deriving a modal approximation of the desired balancing spring torque in a wire-wrapped cam mechanism and adapting the results to produce possible cam implementations using Kilic's closed-form

approach in [66]. In addition, for a given kinematic architecture, we explore the effects of changing the placement of the workspace on the quality of the balancing throughout the target workspace. We believe that this exploration will be useful for guiding the design process for practical compact and lightweight parallel mechanisms for the applications mentioned above.

8.3 Static Balancing Using Spring Elements

We consider the scenario where a unit vector in the direction of gravity is designated by $\hat{\mathbf{g}}$. We assume a parallel robot subject to an external force $\mathbf{f}_e$ and a moment $\mathbf{m}_e$. With this robot having the set of active joints $\mathbf{q}$ and the set of passive joints ϕ, we use τ to designate the actuator torques. We also use $\mathbf{x}$ to denote the pose of the moving platform which is defined as the vector of position and orientation parametrization. For example, $\mathbf{x}$ for a planar robot would be the two Cartesian coordinates and the angle of rotation of the moving platform.

Loop closure constraint equations of the topologically independent loops of a parallel robot may be used to obtain the necessary nonlinear equations relating the passive joints ϕ to the active joints $\mathbf{q}$. By taking a time derivative of these loop closure constraint equations, one can always obtain this instantaneous internal kinematics mapping:

$$\mathbf{A}\dot{\phi} = \mathbf{B}\dot{\mathbf{q}} \tag{8.1}$$

And the Jacobian[1]. associated with the above mapping can be defined as:

$$\dot{\phi} = \mathbf{J}_{\phi q}\dot{\mathbf{q}} \quad , \quad \mathbf{J}_{\phi q} = \mathbf{A}^{-1}\mathbf{B} \tag{8.2}$$

Examples of this approach can be found in [178, 179] for planar and spatial parallel mechanisms.

[1] we use $\mathbf{J}_{xy}$ to designate the Jacobian such that $\dot{\mathbf{x}} = \mathbf{J}_{xy}\dot{\mathbf{y}}$.

Next, we consider the potential energy V_g of the parallel mechanism. With m_i designating the mass of the i^{th} link, h_{ci} denoting the height of its center of mass, m_p the mass of the moving platform and $\mathbf{t}$ the location of the moving platform center (end effector point), one can write:

$$V_g = \sum_{i=1}^{n} \left(m_i g h_{ci}(\mathbf{q}, \phi) + m_p \left(\mathbf{t}^T \hat{\mathbf{g}} \right) \right) \tag{8.3}$$

where n designates the total number of links in the legs, excluding the base and moving platform.

Considering the case where a robot is subject only to gravitational forces, one can write the conditions for static equilibrium as:

$$\boldsymbol{\tau}_g^T d\mathbf{q} - dV_g = 0 \Rightarrow \boldsymbol{\tau}_g = \frac{dV_g}{d\mathbf{q}} \tag{8.4}$$

In the above equation, obtaining V_g only as a function of the active joints $\mathbf{q}$ requires solving a set of nonlinear equations tantamount to solving the direct kinematics or the nonlinear loop closure equations. Instead, we consider $V_g = V_g(\mathbf{q}, \phi, \mathbf{x})$ and we apply the chain rule:

$$\boldsymbol{\tau}_g = \frac{\partial V_g}{\partial \mathbf{q}} + \mathbf{J}_{\phi q}^{\mathrm{T}} \frac{\partial V_g}{\partial \phi} + \mathbf{J}_{xq}^{\mathrm{T}} \frac{\partial V_g}{\partial \mathbf{x}} \tag{8.5}$$

In the general case of a robot having flexible energy storage elements and subject to an external wrench $\mathbf{w}_e$, the virtual work principle leads to:

$$\boldsymbol{\tau}^T \delta\mathbf{q} - \delta V_g - \delta V_e - \mathbf{w}_e^{\mathrm{T}} \delta\mathbf{x} = 0 \tag{8.6}$$

where dV_e is the change of elastic potential energy that is associated with a virtual displacement $d\mathbf{q}$ and $\mathbf{w}_e^{\mathrm{T}} \delta\mathbf{x}$ denotes the work of the robot on the environment. By defining the gravitational torque $\boldsymbol{\tau}_g = \frac{dV_g}{d\mathbf{q}}$ and the torque due to the internal springs $\boldsymbol{\tau}_e = \frac{dV_e}{d\mathbf{q}}$, we obtain:

$$\boldsymbol{\tau} = \boldsymbol{\tau}_g + \boldsymbol{\tau}_e + \left[\mathbf{J}_{qx}^T \right]^{-1} \mathbf{w}_e \tag{8.7}$$

Finally, by expressing the elastic energy V_e as a function of all possible spring locations at the active and passive joints, we can write:

$$V_e = \frac{1}{2}1\left(\tilde{\mathbf{q}}^{\mathrm{T}}\mathbf{K}_q\tilde{\mathbf{q}} + \tilde{\phi}^{\mathrm{T}}\mathbf{K}_\phi\tilde{\phi}\right) \tag{8.8}$$

where $\tilde{\mathbf{q}} = \mathbf{q} - \mathbf{q}_f$ and $\tilde{\phi} = \phi - \phi_f$ designate the spring deflections relative to their unloaded configurations with corresponding joint angles $\mathbf{q}_f$ and ϕ_f and $\mathbf{K}_q$ and $\mathbf{K}_\phi$ are diagonal matrices containing the spring constants installed to the active and passive joints.

The torque due to the elastic elements $\boldsymbol{\tau}_e$ is given by:

$$\boldsymbol{\tau}_e = \frac{dV_e}{d\mathbf{q}} = \frac{\partial V_e}{\partial \mathbf{q}} + \mathbf{J}_{\phi q}^{\mathrm{T}}\frac{\partial V_e}{\partial \phi} = \mathbf{K}_q\tilde{\boldsymbol{q}} + \mathbf{J}_{\phi q}^{T}\mathbf{K}_\phi\tilde{\phi} \tag{8.9}$$

Substituting (8.9) into (8.7) gives the condition for static balancing for a given load $\mathbf{w}_e$:

$$\boldsymbol{\tau} = \boldsymbol{\tau}_g + \mathbf{J}_{\phi q}^{T}\mathbf{K}_\phi\tilde{\phi} + \mathbf{K}_q\tilde{\boldsymbol{q}} + \left[\mathbf{J}_{qx}^{T}\right]^{-1}\mathbf{w}_e = \mathbf{0} \tag{8.10}$$

where $\boldsymbol{\tau}_g$ is given by (8.5).

8.4 Planar 3-RRR Manipulator

To illustrate the approach of the previous section, we use a 3RRR planar parallel robot. We consider two possible layouts for this robot: the *Wide layout (WL)* shown in Fig. 8.2A and *Narrow layout (NL)* shown in Fig. 8.2B. In the wide layout, the three base joint are placed radially with respect to the world frame and equidistantly from each other. In the narrow layout, the three base joints are placed to the left of the world frame $\{\hat{\mathbf{x}}_0, \hat{\mathbf{y}}_0\}$ to mimic an hand-held device with its end effector reaching to the right. We also keep the serial kinematic chains in each leg in an elbow-up configuration to avoid the risk of collision between the elbows and the anatomy, which typically lies below the robot base.

In the following simulation study, we will investigate four possibilities for the place-

ment of torsional springs:

- Mode 0: the baseline case where no springs are used. The actuator torque required for this case will be designated by τ_0.
- Mode 1: balancing springs are installed only at the active joints.
- Mode 2: balancing springs are installed only at the elbow joints.
- Mode 3: balancing springs are installed both at the active and elbow joints.

8.4.1 Kinematics

Equation (8.10) requires the Jacobian matrices $\mathbf{J}_{xq}$ and $\mathbf{J}_{\phi q}$. We therefore derive these Jacobians in this section. Referring to Fig. 8.3, we define $\mathbf{b}_i$ as the locations of the base joints in the base (world) frame $\{\hat{\mathbf{x}}_0, \hat{\mathbf{y}}_0\}$ and ${}^m\mathbf{p}_i$, $i = 1,2,3$ as the location of the corresponding passive joints in the moving platform-attached frame $\{\hat{\mathbf{x}}_t, \hat{\mathbf{y}}_t\}$[2]. We also define $\hat{\mathbf{s}}_i$, as the unit vectors along the actively rotating links at the base and $\hat{\mathbf{n}}_i$ as the unit vectors along the forearms connecting the moving platform passive revolute joints at ${}^t\mathbf{p}_i$ to the elbow passive joints $\mathbf{e}_i$. Finally, we assume the leg lengths $||\mathbf{b}_i - \mathbf{e}_i|| = L_1$ and $||\mathbf{p}_i - \mathbf{e}_i|| = L_2$.

Designating the rotation of the moving frame relative to the world frame as ${}^w\mathbf{R}_t$ and referring to Fig. 8.3, we can write the loop closure equation:

$$\mathbf{t} + {}^w\mathbf{R}_t\,{}^t\mathbf{p}_1 - L_2\hat{\mathbf{n}}_1 - L_1\hat{\mathbf{s}}_1 - \mathbf{b}_1 = 0 \tag{8.11}$$

Taking the time derivative of (8.11) and recalling that the time derivatives ${}^t\dot{\mathbf{p}}_1 = {}^w\boldsymbol{\omega}_t \times {}^t\mathbf{p}_1$, $\dot{\hat{\mathbf{s}}}_1 = \dot{q}_1\hat{\mathbf{z}}_0 \times \hat{\mathbf{s}}_1$, and $\dot{\hat{\mathbf{n}}}_1 = \dot{\phi}_1\hat{\mathbf{z}}_0 \times \hat{\mathbf{n}}_1$ we obtain:

$$\dot{\mathbf{t}} + {}^w\boldsymbol{\omega}_t \times {}^w\mathbf{R}_t\,{}^t\mathbf{p}_1 - L_2\dot{\phi}_1\,(\hat{\mathbf{z}}_0 \times \hat{\mathbf{n}}_1) - L_1\dot{q}_1\,(\hat{\mathbf{z}}_0 \times \hat{\mathbf{s}}_1) = 0 \tag{8.12}$$

[2] we use ${}^t\mathbf{x}$ to designate a vector described in frame $\hat{\mathbf{x}}_t, \hat{\mathbf{y}}_t$ and we omit the left superscript when the vector is described in world frame

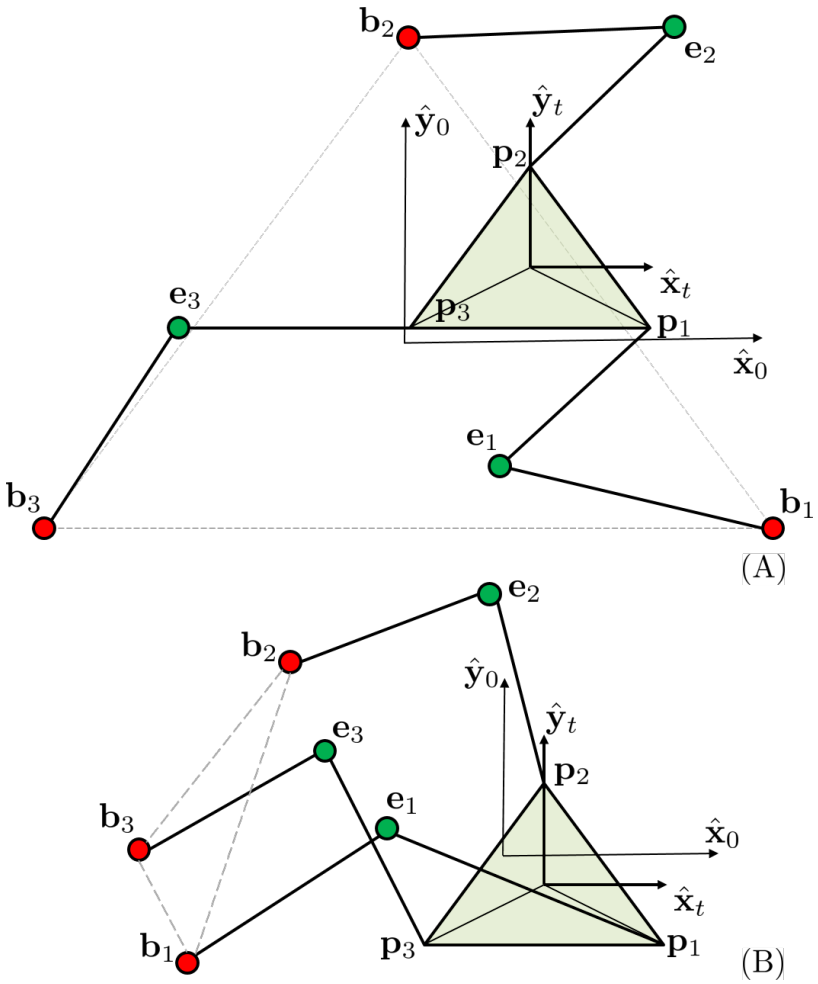

Figure 8.2: 3-RRR Planar manipulator: A) wide (WL) layout B) Narrow (NL) layout. The red and green dots designate the active and passive joints, respectively.

To find the relation between $\dot{\mathbf{q}}$ and task space twist, we define the end effector's reduced-dimension twist as $\dot{\mathbf{x}} \triangleq [\dot{t}_x, \dot{t}_y, \dot{\gamma}]^{\mathrm{T}}$ where the first two terms designate the Cartesian end effector speeds and the third element designates the angular rate of rotation of the moving platform. The passive joint speed $\dot{\phi}_1$ is next eliminated from the above equation by taking a dot product with $\hat{\mathbf{n}}_1$ and using the scalar triple product identity $\mathbf{a}\cdot\mathbf{b}\times\mathbf{c} = \mathbf{c}\cdot\mathbf{b}\times\mathbf{a} = \mathbf{b}\cdot\mathbf{c}\times\mathbf{a}$. These mathematical manipulations allow rearranging (8.12) as:

$$\hat{\mathbf{n}}_1^T \dot{\mathbf{t}} + \left({}^w\mathbf{R}_t\, {}^t\mathbf{p}_1 \times \hat{\mathbf{n}}_1\right)^T \dot{\gamma}\hat{\mathbf{z}}_0 = \hat{\mathbf{n}}_1^T \left(\hat{\mathbf{z}}_0 \times \hat{\mathbf{s}}_1\right) L_1 \dot{q}_1 \tag{8.13}$$

Since the 3RRR is a planar robot, ${}^w\boldsymbol{\omega}_t = \dot{\gamma}\hat{\mathbf{z}}_0$. Rewriting equation (8.13) with all three chains results in the matrix form:

$$\underbrace{\begin{bmatrix} n_{1x} & n_{1y} & \hat{\mathbf{z}}_0^{\mathrm{T}}({}^w\mathbf{R}_t^t\mathbf{p}_1 \times \hat{\mathbf{n}}_1) \\ n_{2x} & n_{2y} & \hat{\mathbf{z}}_0^{\mathrm{T}}({}^w\mathbf{R}_t^t\mathbf{p}_2 \times \hat{\mathbf{n}}_2) \\ n_{3x} & n_{3y} & \hat{\mathbf{z}}_0^{\mathrm{T}}({}^w\mathbf{R}_t^t\mathbf{p}_3 \times \hat{\mathbf{n}}_3) \end{bmatrix}}_{\mathbf{A}} \underbrace{\begin{bmatrix} \dot{t}_x \\ \dot{t}_y \\ \dot{\gamma} \end{bmatrix}}_{\dot{\boldsymbol{x}}} = \underbrace{L_1 \begin{bmatrix} \hat{\mathbf{n}}_1^T(\hat{\mathbf{z}}_0 \times \hat{\mathbf{s}}_1) & 0 & 0 \\ 0 & \hat{\mathbf{n}}_2^T(\hat{\mathbf{z}}_0 \times \hat{\mathbf{s}}_2) & 0 \\ 0 & 0 & \hat{\mathbf{n}}_3^T(\hat{\mathbf{z}}_0 \times \hat{\mathbf{s}}_3) \end{bmatrix}}_{\mathbf{B}} \dot{\mathbf{q}} \tag{8.14}$$

Using the above results, we define the instantaneous inverse kinematics Jacobian $\mathbf{J}_{qx} \triangleq \mathbf{B}^{-1}\mathbf{A}$ such that $\dot{\mathbf{q}} = \mathbf{J}_{qx}\dot{\boldsymbol{x}}$.

It is possible to extract the Jacobian matrix $\mathbf{J}_{\phi x}$ that relates $\dot{\mathbf{x}}$ to the passive joint rates $\dot{\phi}$. To eliminate $\dot{q}_1$ from (8.12) we take the dot product with $\hat{\mathbf{s}}_1$ and using again the cross product identity, which yields:

$$\hat{\mathbf{s}}_1^T \dot{\mathbf{t}} + \left({}^w\mathbf{R}_t\, {}^t\mathbf{P}_1 \times \hat{\mathbf{s}}_1\right)^T \dot{\gamma}\hat{\mathbf{z}}_0 = \hat{\mathbf{s}}_1^T \left(\hat{\mathbf{z}}_0 \times \hat{\mathbf{n}}_1\right) L_2 \dot{\phi}_1 \tag{8.15}$$

Repeating the (8.15) for the three kinematic chains provides $\mathbf{J}_{\phi x}$ such that $\dot{\phi} = \mathbf{J}_{\phi x}\dot{\mathbf{x}}$:

$$\underbrace{\begin{bmatrix} s_{1x} & s_{1y} & \hat{\mathbf{z}}_0^{\mathrm{T}}({}^{w}\mathbf{R}_t^t\mathbf{p}_1 \times \hat{\mathbf{s}}_1) \\ s_{2x} & s_{2y} & \hat{\mathbf{z}}_0^{\mathrm{T}}({}^{w}\mathbf{R}_t^t\mathbf{p}_2 \times \hat{\mathbf{s}}_2) \\ s_{3x} & s_{3y} & \hat{\mathbf{z}}_0^{\mathrm{T}}({}^{w}\mathbf{R}_t^t\mathbf{p}_3 \times \hat{\mathbf{s}}_3) \end{bmatrix}}_{\mathbf{C}} \underbrace{\begin{bmatrix} \dot{t}_x \\ \dot{t}_y \\ \dot{\gamma} \end{bmatrix}}_{\dot{x}} = \underbrace{L_2 \begin{bmatrix} \hat{\mathbf{s}}_1^T(\hat{\mathbf{z}}_0 \times \hat{\mathbf{n}}_1) & 0 & 0 \\ 0 & \hat{\mathbf{s}}_2^T(\hat{\mathbf{z}}_0 \times \hat{\mathbf{n}}_2) & 0 \\ 0 & 0 & \hat{\mathbf{s}}_3^T(\hat{\mathbf{z}}_0 \times \hat{\mathbf{n}}_3) \end{bmatrix}}_{\mathbf{D}} \dot{\phi} \tag{8.16}$$

Where is given by $\mathbf{J}_{\phi x} = \mathbf{D}^{-1}\mathbf{C}$.

Using the above two Jacobians, it is possible to derive $\mathbf{J}_{\phi q}$ such that $\dot{\phi} = \mathbf{J}_{\phi q}\dot{\mathbf{q}}$ as the following:

$$\dot{\phi} = \mathbf{J}_{\phi x}\dot{\mathbf{x}} = \mathbf{J}_{\phi x}\mathbf{J}_{qx}{}^{-1}\dot{\mathbf{q}} \quad \Rightarrow \quad \mathbf{J}_{\phi q} = \mathbf{J}_{\phi x}\mathbf{J}_{qx}{}^{-1} \tag{8.17}$$

In the above derivations, we assume that the robot does not suffer any type of singularity associated degeneracy of any of the matrices **A**, **B**, **C**, **D**. Conditions for degeneracy of these matrices were discussed in the literature including [180, 181].

8.5 Static Balancing Strategy and Simulation Results

Given a dexterous workspace, one can be tempted to design a static balancing solution for the entire dexterous workspace. We do not advocate for this because the solution obtained through this approach will have attenuated effectiveness. Attempting to obtain maximal static balancing throughout the dexterous workspace will demand non-monotonous balancing torque profiles with very large ranges that would effectively require using either an adjustable linkage to change the spring pre-load or incorporating balancing masses in

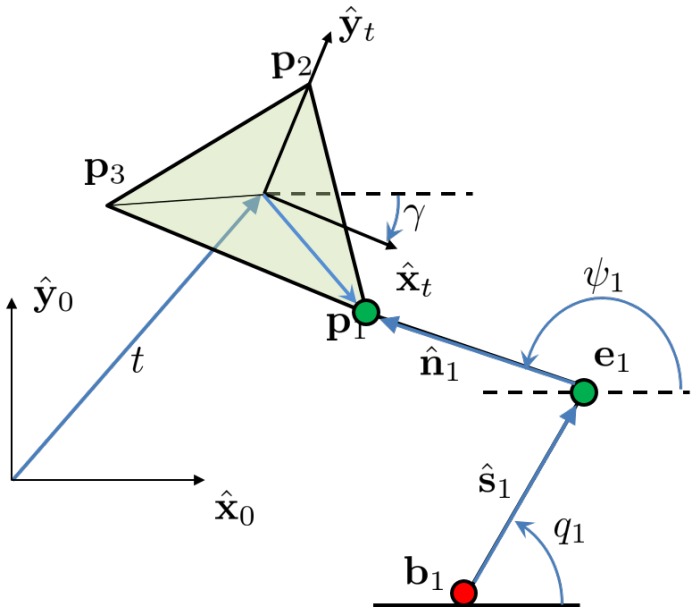

Figure 8.3: Single kinematic chain of 3-RRR Parallel mechanism

addition to springs. In this section, we propose a different design strategy for simplified static balancing implementation by using a task-based design task and identifying the ideal location of the task of the robot.

8.5.1 Task-Based Static Balancing and Sub-workspace Location

The first step towards optimizing the static balancing solution for a given robot is the identification of the dexterous workspace within which the robot can satisfy desired ranges for Cartesian and rotation motions. Within the set of reachable points, a dexterous workspace is admissible if all the points within it can be reached with all desired orientations. In this study, we defined the desired dexterous workspace as the locus of points reachable in every direction from the origin of the world frame such that the moving platform can rotate $\pm 30^{\circ}$. There are a variety of methods that can be used to determine the dexterous workspace for a given robot (e.g. [182]). In our work, we used a hierarchical workspace scan starting with constant-orientation scans. For each constant orientation scan, a recursive depth-first search in the radial direction was used in conjunction with inverse

kinematics to quickly identify the farthest reachable point associated with a particular polar coordinate. The boundary of the dexterous workspace is then determined as the set of points belonging to all the constant-orientation workspaces within the desired orientation range. This dexterous workspace is identified by ① and a dashed blue line in Fig.8.4A and B. In the case of the narrow layout, we limited the scanning range to $\pm 120^{\circ}$ to avoid physical overlap of the base joints and the moving platform.

Since our goal is to offer a static balancing strategy that maintains design simplicity and compactness, we advocate for optimizing the design of the balancing mechanism for a *task-based dexterous sub-workspace*. To illustrate the approach, we used for static balancing design the design task of following a spiral trajectory over a circular area with a diameter of $100mm$. Once the design task has been defined, we search for all the points in the dexterous workspace that are feasible center-points for completing the design task (e.g. following the spiral). Points offset from the boundary of the dexterous workspace such that the robot can satisfy design task are feasible points. The boundary of such dexterous sub-workspace is identified by ② and marked by a dashed red line in Fig.8.4A and 8.4B.

Figure 8.5A-B explain why it is not feasible to use torsional springs and a design strategy that optimizes the design of the balancing springs throughout the entire dexterous sub workspace. The figure shows the mapping of the average torque reduction percentage, using torsional springs at the active joints, in both robot base configurations and constant moving base orientation. The plots show that while in some areas of the dexterous workspace we can obtain partial static balancing, the same set of spring parameters is not suitable for other areas where, actually, the average percentage of torque reduction has a negative value, which means that the required torque at the joints has been increased.

In order to identify the optimal location for the task-based dexterous sub-workspace, we scanned the dexterous sub-workspace for all the moving base orientations, as shown in Fig.8.4A-③ and 8.4B-③, and calculated the required torque at the active joints. The cyan and green asterisks in Fig.8.4A-④-⑤ and 8.4B-④-⑤ are the points with the highest and

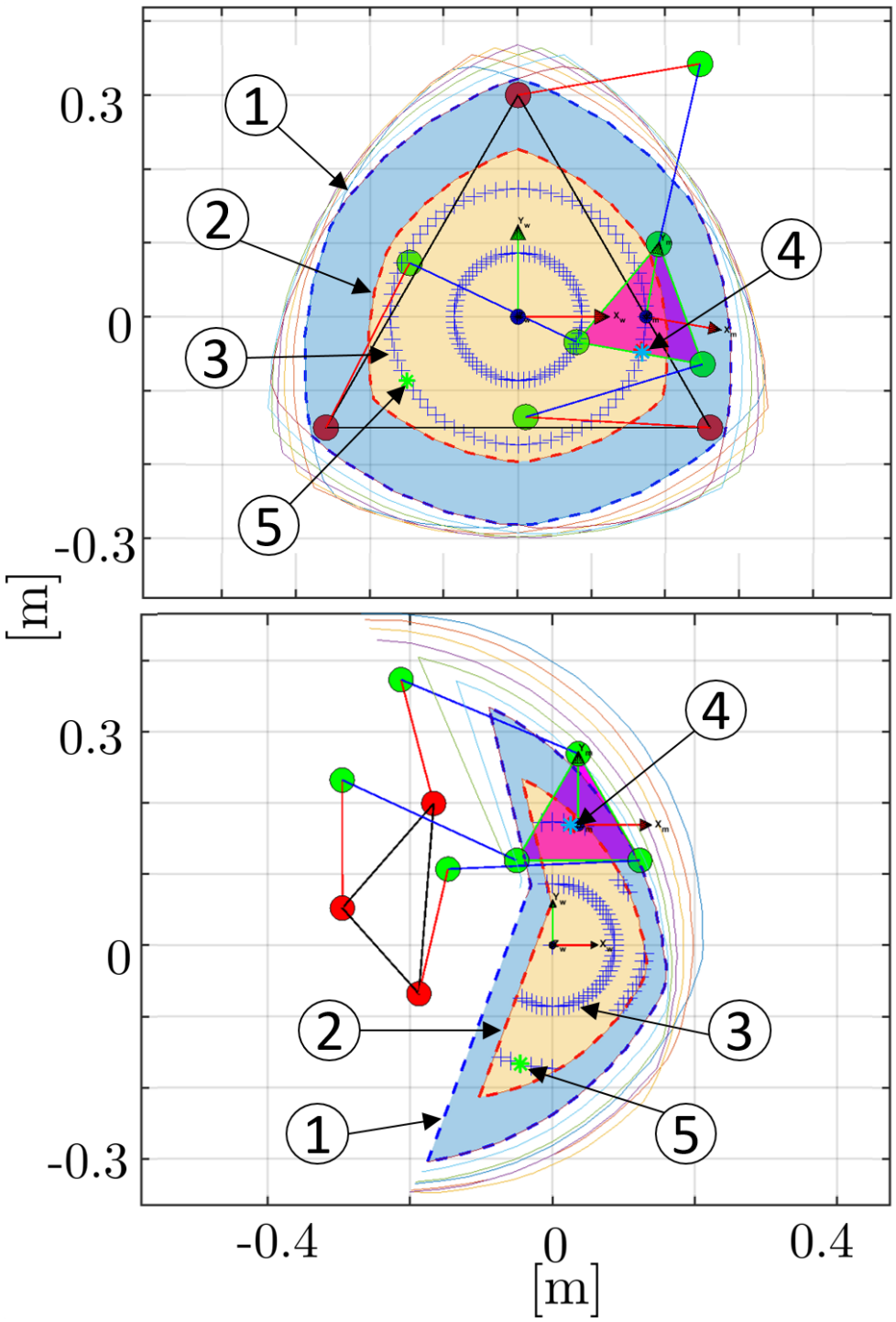

Figure 8.4: A)WL robot configuration. B) NL robot configuration. Both manipulators are placed in the configuration of max percentage of torque reduction - ① Dexterous Workspace ② Dexterous sub-workspace ③ Scanned points for optimal location for the task-based dexterous sub-workspace ④-⑤ Point of maximal and minimal required torque respectively.

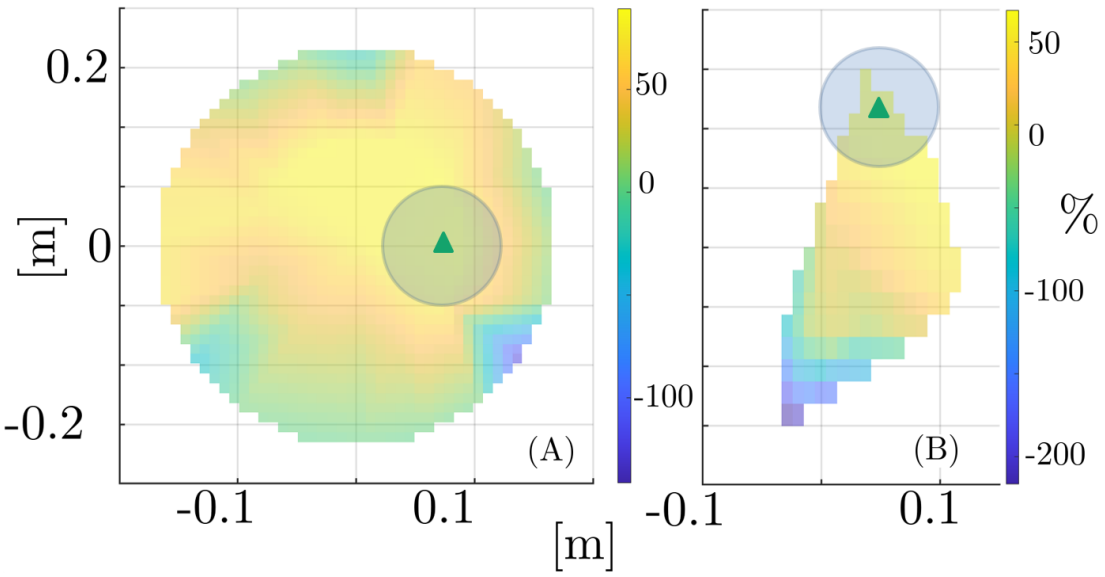

Figure 8.5: Average percentage of torque reduction over the dexterous sub-workspace: A) WL robot configuration for $\gamma = -10^\circ$ B) NL robot configuration for $\gamma = 0^\circ$.

lowest required joint torque norm respectively.

To choose the optimal placement of the task relative to the robot we consider the effect of static balancing gain in reducing the required actuator torques. We identified the optimal location as the point where the highest actuator torque reduction when comparing Mode 0 to Mode 1 with optimized torsional springs.

The robot configurations in Fig.8.4A and 8.4B show the robot at the pose with the most effective counterbalancing contribution. In Fig 8.5.A and 8.5B the location of these points are marked with a green triangle and the light-blue shaded circular area defines the associated task-based dexterous sub-workspace.

8.5.2 Torsional springs optimization

Once the location of the task-based sub-workspace is identified, in order to statically balance the manipulator over such area, we scan such area following a spiral path and calculate the required torque using eq. (8.10).

We fine an augmented torque vector $\breve{\tau} = [\tau_1^{\mathrm{T}}, \ldots, \tau_N^{\mathrm{T}}]^{\mathrm{T}}$ for N sample points along the

design task of following a spiral. We define the cost function $M = \frac{1}{2N}\breve{\boldsymbol{\tau}}^{\mathrm{T}}\breve{\boldsymbol{\tau}}$. We use a nonlinear least squares algorithm (Algorithm 1 to find the design parameters $\tilde{\mathbf{x}}$ that reduces its cost function. Since we are using torsional springs as elastic elements to counterbalance the required torque, the design parameters vector $\tilde{\mathbf{x}}$ includes the initial pre-load of the springs and the stiffness coefficients for each torsional spring. The process is repeated for all the balancing modes introduced in Sec. 8.4 and the results are reported in this section.

Algorithm 1 Nonlinear LS Minimization

Require: $TargetPoses(q, \Phi, \Psi)$ ▷ Data set for minimization process

1: **START** Initialize: $\tilde{\mathbf{x}}$, $M_i \leftarrow 100$ ▷ Minimization parameters vector

2: **while** $M > \varepsilon_\tau$ *and* $iter_i < iter_{max}$ **do**

3: $\quad \breve{\boldsymbol{\tau}}(\vec{x}) = [\boldsymbol{\tau}_1; ...; \boldsymbol{\tau}_N]$, ▷ Aggregated torque vector ▷ N number of Target Poses

4: $\quad \triangle\breve{\boldsymbol{\tau}} = \frac{\partial\breve{\boldsymbol{\tau}}}{\partial\vec{x}} \triangle\vec{x}, \quad \frac{\partial\breve{\boldsymbol{\tau}}}{\partial\vec{x}} = \boldsymbol{J}_A,$

5:

6: $\quad \boldsymbol{J}_A = \begin{bmatrix} \frac{\partial\breve{\boldsymbol{\tau}}_1}{\partial\vec{x}} \\ \frac{\partial\breve{\boldsymbol{\tau}}_2}{\partial\vec{x}} \\ \vdots \\ \frac{\partial\breve{\boldsymbol{\tau}}_N}{\partial\vec{x}} \end{bmatrix}$ ▷ Gradient of cost function

7: $\quad$ Update $\tilde{\mathbf{x}}_{i+1}$:

$$\tilde{\mathbf{x}}_{i+1} = \tilde{\mathbf{x}}_i - \eta \mathbf{J}_A^{+}\breve{\boldsymbol{\tau}}$$

$$M_i = \frac{\breve{\boldsymbol{\tau}}^T\breve{\boldsymbol{\tau}}}{2N}$$

▷ η step-size matrix

8: **end while**

9: $\tilde{\mathbf{x}}^* \leftarrow \tilde{\mathbf{x}}_i$

Ensure: $\tilde{\mathbf{x}}^*$

Figure 8.6 and 8.7 show the required joint torques for the for the WL and NL layouts over the 4 modes defined in section 8.4. Each plot has a dashed green line which represents the norm of the actuation torques required at Mode 0, the solid red lines represent the norm of the joint torques for the three modes, finally the purple dotted lines represent norm of the torque required for the case of the wire-wrapped cams discussed in sec. 8.5.3.

To compare the balancing efficacy of the torsional spring design, the following performance measure e_{τ_i}, was defined:

$$e_{\tau_i} = \sqrt{\frac{1}{N}\sum_{1}^{N}\left(\frac{||\tau_i Mode_c||}{||\tau_i Mode_0||}\right)^2} \quad c = 1,2,3 \tag{8.18}$$

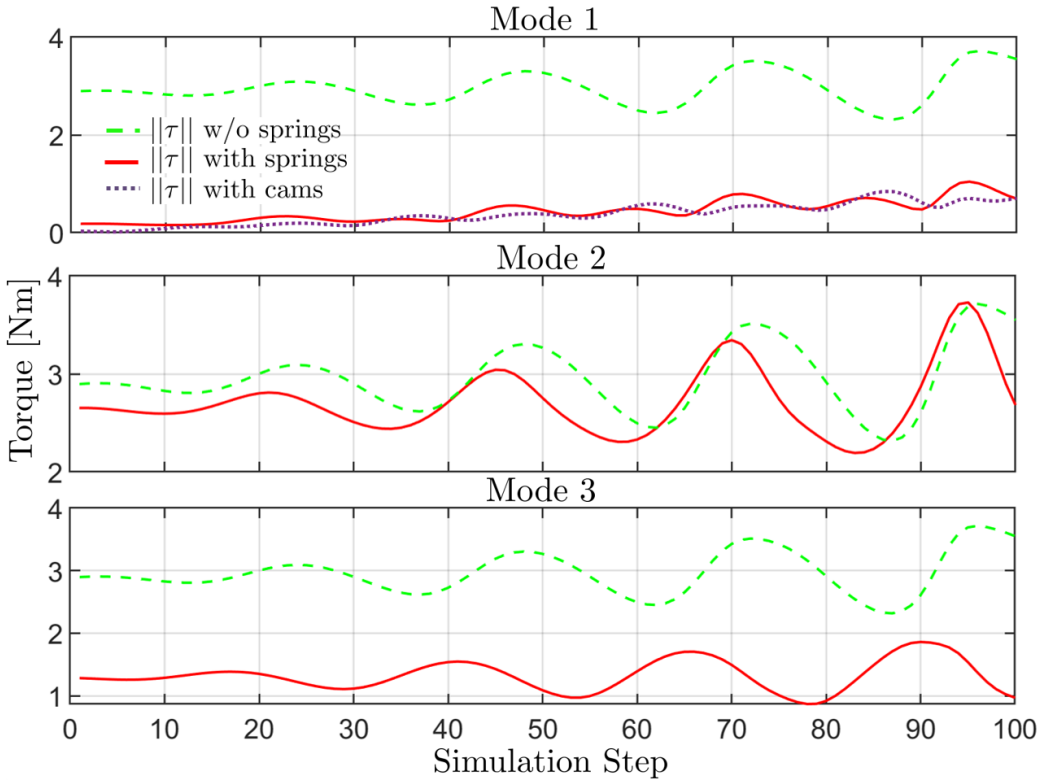

Figure 8.6: Torque norm profiles for WL layout.

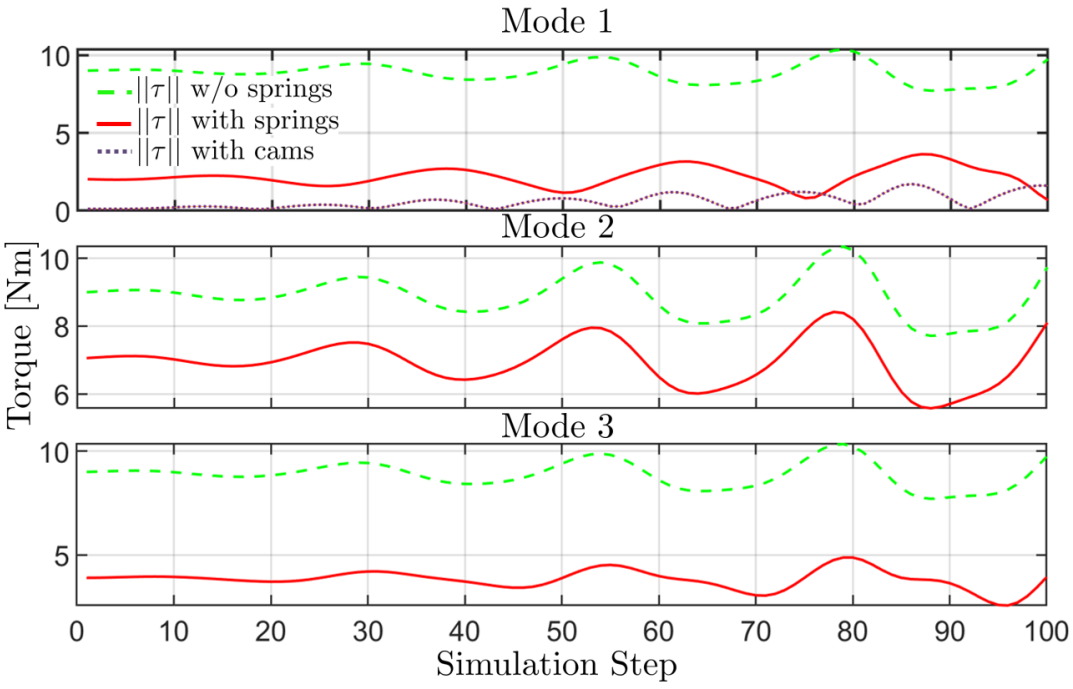

Figure 8.7: Torque norm profiles for NL layout.

where i is the index of the leg, c is an index designating the Mode, and $N = 1500$ is the number of points scanned in the task-based dexterous sub-workspace. Perfect static balancing corresponds with $e_{\tau_i} = 0$; therefore, a larger e_{τ_i} indicates worse balancing performance. Table 8.1 reports this performance measure for all three modes. The lower values designate better static balancing outcomes for each leg.

Table 8.1: e_{τ_i} using torsional springs

Mode	1		2		3	
	WL	NL	WL	NL	WL	NL
e_{τ_1}	0.18	0.12	0.62	0.68	0.94	0.26
e_{τ_2}	0.12	0.66	0.70	0.76	0.08	0.27
e_{τ_3}	0.17	0.37	0.85	0.9	0.29	0.54

Figures 8.8 and 8.9 show the required torque norm ratio $\frac{||\tau_i||}{||\tau_0||}$, where i designates the mode index ($i = 1, 2, 3$) and τ_0 designates the torque without static balancing. The plots are generated over the task-based dexterous sub-workspace.

8.5.3 Wire-Wrapped Cams optimization

In this section, we will compare our method to a more complicated alternative that utilizes wire-wrapped cams. The wire-wrapped cam design concept we are using in this section was developed by Kilic et. al. [66]. In this method, a wire attaches on one end to a translational spring, wraps around an idler pulley, and then wraps around a cam as shown in Fig. 8.10. When the cam rotates, it extends the spring causing a moment about the cam's axis of rotation. Using [66], the cam can be specially designed to generate a desired moment $g(\alpha)$ as a function of cam angle α. In the design shown in Fig. 8.10, the idler and cam centers of rotation are assumed to be horizontally aligned and separated by a distance a along the x axis. The designer is free to choose a as a design parameter. The translational spring constant k, the spring pre-extension u_t, and the idler radius r are also design parameters.

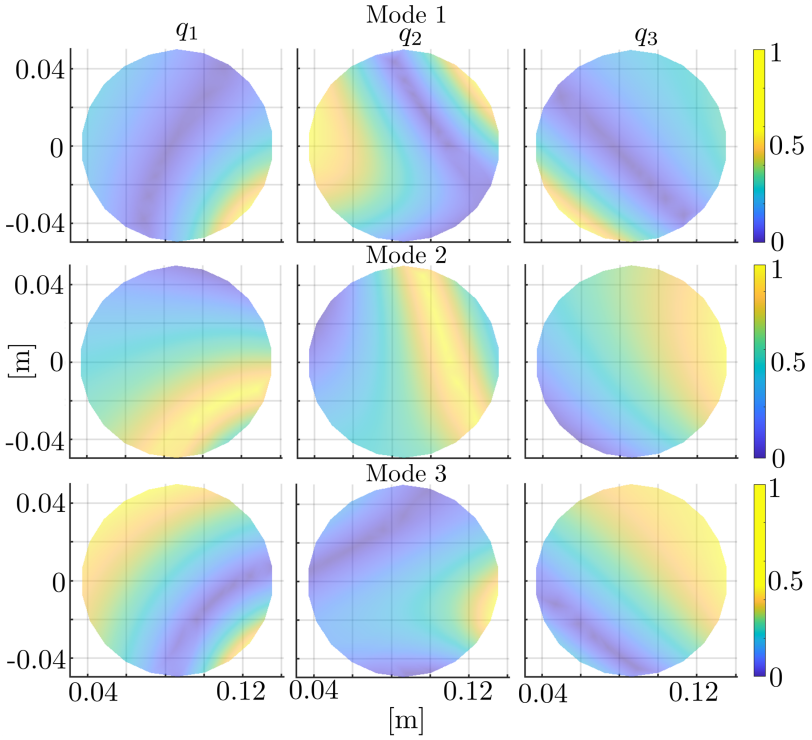

Figure 8.8: Torque norm ratio (with springs/without springs) for WL robot configuration

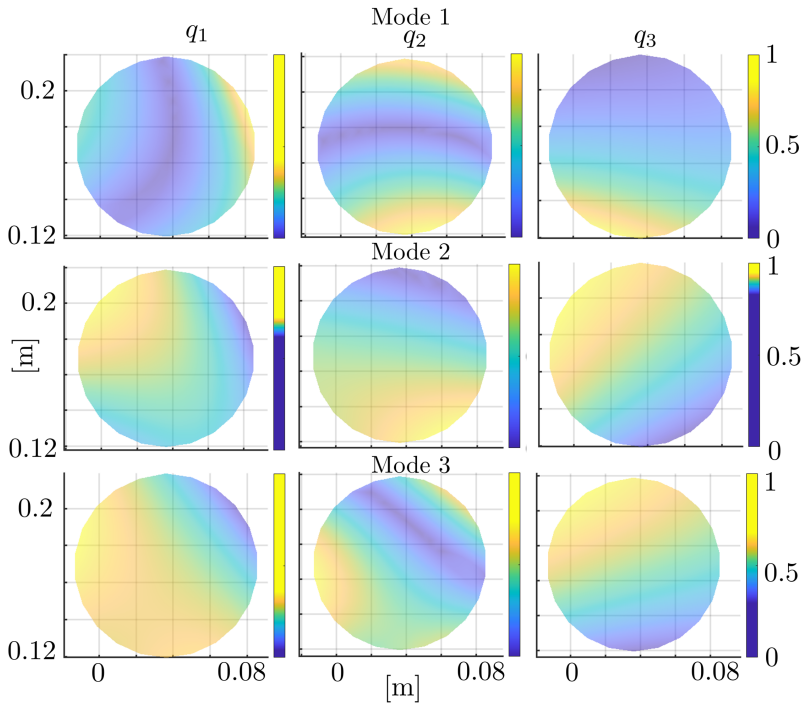

Figure 8.9: Torque norm ratio (with springs/without springs) for NL robot configuration

By rigidly attaching a cam to each active joint in the 3RRR robot as shown in Fig. 8.11, we can offset the gravitational torque on the joints in a section of the workspace.

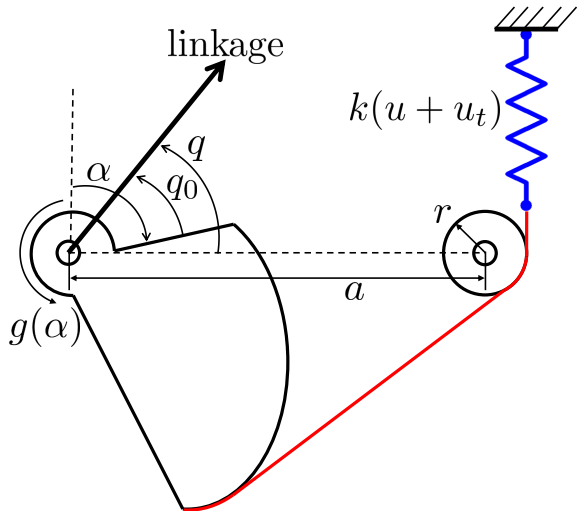

Figure 8.10: Cam design concept and terminology

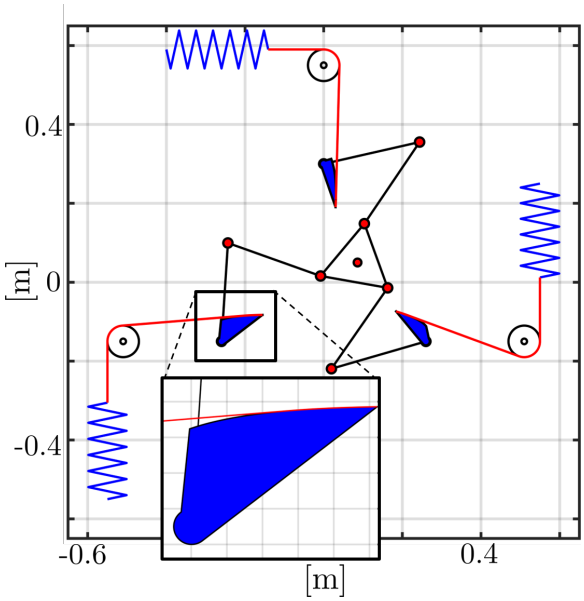

Figure 8.11: 3RRR wire-wrapped cam design concept for the WL case

The equations in [66] require the cam angle α to be defined as shown in Fig. 8.10. Because α is defined differently from the linkage angle q, we must calculate the cam angle

for a given linkage angle using:

$$\alpha = \frac{\pi}{2} - (q - q_0) \tag{8.19}$$

Where the constant angle between the cam and the linkage q_0 is a design parameter. Because the torque on each joint from the wire-wrapped cam is a function only of the angle of the joint it is attached to, we can only achieve approximate balancing. Therefore, we must design a function $\tau_{est}(\alpha)$ that is the best possible estimate of τ. To do this, we chose an n^{th} order polynomial basis for $\tau_{est}(\alpha)$:

$$\tau_{est,i}(\alpha_i) = b_{i,0} + b_{i,1}\alpha_i + b_{i,2}\alpha_i^2 + \cdots + b_{i,n}\alpha_i^n \quad i = 1,2,3 \tag{8.20}$$

In this equation, i represents the joint (and cam) number. We now must choose the modal coefficients $\mathbf{b}_i = [b_{i,0}, b_{i,1}, \ldots, b_{i,n}]^{\mathrm{T}} \in \mathbb{R}^{n+1}$ that minimize the difference between $\tau_{est,i}(\alpha_i)$ and the actual torque on the joint τ_i. If we take measurements of τ_i at N different poses of the robot, we can write the following equation:

$$\underbrace{\begin{bmatrix} \tau_{i,1} \\ \vdots \\ \tau_{i,N} \end{bmatrix}}_{\boldsymbol{\tau}_i} = \underbrace{\begin{bmatrix} 1 & \alpha_{i,1} & \alpha_{i,1}^2 & \ldots & \alpha_{i,1}^n \\ & & \vdots & & \\ 1 & \alpha_{i,N} & \alpha_{i,N}^2 & \ldots & \alpha_{i,N}^n \end{bmatrix}}_{\mathbf{M}_i} \underbrace{\begin{bmatrix} b_{i,0} \\ b_{i,1} \\ \vdots \\ b_{i,n} \end{bmatrix}}_{\mathbf{b}_i}, \quad i = 1,2,3 \tag{8.21}$$

We can now solve for the modal coefficients using the pseudo-inverse of $\mathbf{M}_i$:

$$\mathbf{b}_i = \mathbf{M}_i^{+} \boldsymbol{\tau}_i, \quad i = 1,2,3 \tag{8.22}$$

Because we are trying to balance τ, the desired cam torque as a function of cam angle can

be found using:

$$g_i(\alpha_i) = -\tau_{est,i}(\alpha_i), \quad i = 1,2,3 \tag{8.23}$$

For the both the WL and NL cases, a $\tau_{est,i}(\alpha_i)$ function was calculated from (8.22) using the data from the search inside the task-based sub-workspace corresponding with the optimal location for Mode 1. The result of this analysis is shown in Fig. 8.12.

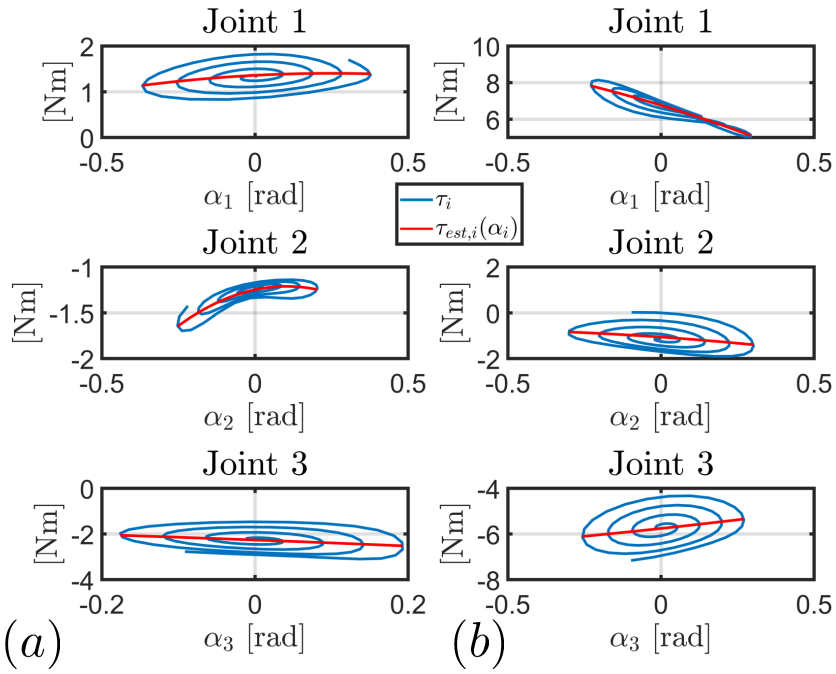

Figure 8.12: Actual torque τ_i vs. least squares torque estimate $\tau_{est,i}$: (a) WL case (b) NL case

Now that the desired torque function $g_i(\alpha_i)$ has been calculated for each cam, we can design the cams using the parameters shown in Table 8.2. The resulting cams for the WL case are shown in Fig. 8.11.

Similarly to the torsional spring case, eq.(8.18) is used for the wire-wrapped cam solution to compare the cam balancing efficacy of the wire-wrapped cam designs, the

Table 8.2: Cam Design Constants

		q_0	a	u_t	r
WL	q_1	2.1567 rad	0.25 m	0.05 m	0.04 m
	q_2	-1.5669 rad	0.25 m	0.065 m	0.04 m
	q_3	-0.1566 rad	0.25 m	0.05 m	0.04 m
NL	q_1	-0.2287 rad	0.0414	0.06 m	0.04 m
	q_2	0.2582 rad	0.0414	0.05 m	0.04 m
	q_3	0.0019 rad	0.0414	0.06 m	0.04 m

following performance measure was created:

$$e_{\tau_i} = \sqrt{\frac{1}{N}\sum_{j=1}^{N}\left(\frac{g_i(\alpha_{i,j}) + \tau_{i,j}}{\tau_{i,j}}\right)^2} \quad i = 1,2,3 \tag{8.24}$$

Table 8.3 shows the values of e_{τ_i} in the case of wire-wrapped cams. Figure 8.13 shows the torque norm ratio $\frac{||\tau_{withcams}||}{||\tau_0||}$ over the task-based dexterous sub-workspace.

Table 8.3: e_{τ_i} using cams

	e_{τ_1}	e_{τ_2}	e_{τ_3}
WL	0.17	0.045	0.16
NL	0.042	0.39	0.11

8.6 Discussion

The simulation results show that the WL layout is easier to balance than the NL layout as indicated by the lower performance measures e_{τ_i}. Also, the worst performance corresponds with the kinematic cain that reaches the biggest extension. The comparison of modes shows that Mode 1 offers the best performance based on Table 8.1. Mode 2 offers the worst balancing performance and Mode 3 does not improve over Mode 1. Therefore, if one limits the design implementation to using torsional springs, these springs should be located at the base of the robot where the active joints are positioned.

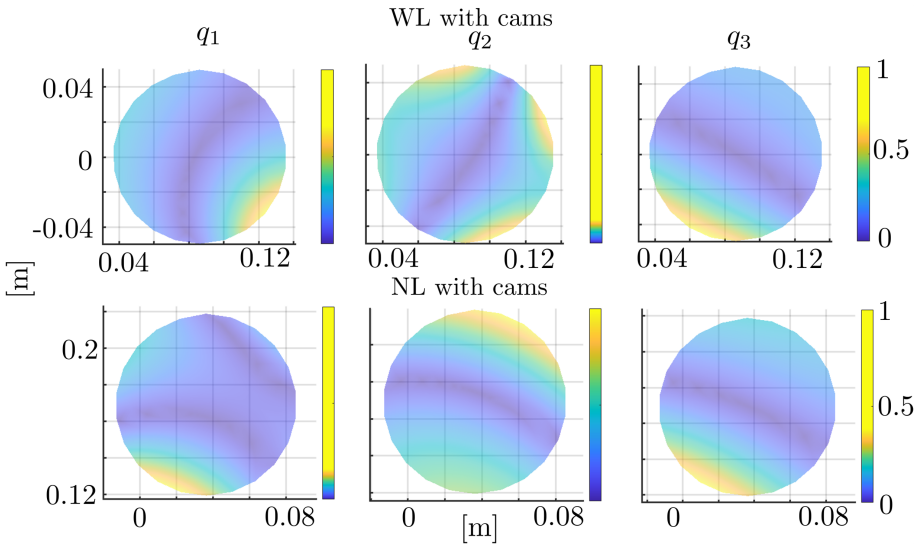

Figure 8.13: Torque norm ratio (with springs/without springs) for WL and NL layouts using wire-wrapped cams.

When comparing the wire-wrapped cam design to the torsional spring design with Mode 1, we observe by comparing the first two columns of Table 8.1 to the corresponding two rows of Table 8.3 that the cam-based balancing marginally improves balancing performance for the WL layout, but offers significant improvement for the NL layout.

Based on these results, if one chooses a WL layout based on an application compatible with this layout, then using a simple balancing solution based on torsional springs can offer significant actuator torque reduction over a task-based workspace. Alternatively, if an application demands the use of the NL layout and the design size limitations can admit the added size and complexity associated with the use of idlers, cams, and linear springs then the cam-based design will offer better balancing performance. If however the size limitations are severe then the use of a simple design with torsional springs can offer effective static balancing over a desired task-based workspace.

For the simple design alternative using torsional springs, changing the location of the dexterous workspace requires redesign of the spring reload and spring constants and, in some aspects of the workspace, may not produce effective balancing as shown in fig. 8.5.The cam-based design alternative effectively locks the location of the dexterous workspace

since it requires a change in design to incorporate a clutch mechanism allowing the cams to disengage while shifting the center of the desired workspace. Such mechanism will ensure that the cams still operate within the range they were designed for. However, the static balancing performance in that case also would not be guaranteed to offer effective balancing.

8.7 Conclusion

This chapter discussed design alternatives for static balancing for parallel mechanisms using elastic elements consistent with applications demanding design compactness, low mass, and simplicity (e.g. as is the case for medical robotics). While it is possible to obtain perfect balancing along a path, it is hard to obtain exact balancing throughout a workspace if one wishes to avoid the use of balancing masses and to maintain design simplicity. We have considered two design layouts for the 3RRR parallel robot and considered the efficacy of static balancing based on the location of torsional balancing springs along the kinematic chains of each design layout. We also compared the performance of these simple designs to a design alternative using wire-wrapped cams. Our design strategy explains how to use the concept of a task-based workspace for the optimal design of balancing spring parameters and for the choice of the workspace location. By using modal fitting for the required torque throughout the task-based design workspace, we are able to adapt recent results for the design of wire-wrapped cams for the balancing of the two possible design layouts. The methodology of this work provides a useful guidance based on the constraints of the application scenario in terms of choosing the design layout, the placement of torsional springs, or the possible use of wire-wrapped cams for balancing.

CHAPTER 9

CONCLUSIONS

9.1 Summary of Findings

Continuum Robots have seen rapid growth in surgical application given their versatility and dexterity in confined spaces and tortuous paths. The design of these robots (in terms of their electro-mechanical design and control) is subject to operational requirements in terms of precision, payload capabilities, workspace, and dexterity. These design properties can be enhanced by *concurrently* considering the design of the continuum robot and its actuation unit.

Chapter 2 reported the design considerations that guided the fabrication of an actuation unit for a continuum robot for Transurethral Resection of Bladder Tumors (TURBT). From the analysis of previous studies and surgeons feedback regarding the needs during TURBT, the design was based on the derived conceptual attributes, which were used for guiding the choice for the most suitable mechanical architecture, and task specifications. These design attributes and design specifications were used to guide the detailed design and component selection for each actuator. The created actuation unit satisfies the required characteristics of ease of sterilization and actuation separability given by the three actuation modules that enhanced the modularity of the whole system and robustness to sensor error. After preliminary testing of the actuation unit to assess its primary functions, the whole robotic system was tested in several phantoms and in-vivo studies where the robot successfully ablated tumors in several critical regions of swine bladders using the laser.

In chapter 3 a new design for continuum robots was presented. The new continuum

robot design enables micro and macro scale motion in a single mechanical embodiment (as opposed to the traditional approach of serially stacked macro and micro manipulators, which is not easy to adapt and miniaturize for surgical applications). This new architecture achieves micro motion by altering the cross sectional stiffness distribution along the length of the continuum segment. To understand and model the micron-motion of CREM robots, a custom *ad-hoc* system for motion tracking was needed to enable micron-level motion tracking - a precision level not available using commercial motion trackers.

The efforts for creating a tracking marker feasible for micro-motion scale, its tracking procedure, and CREM motion testing feasibility was presented in chapter 4. Several markers geometry, fabrication technology, and chromatic scales were tested to finally be able to obtain a tracking accuracy with error less than $1\mu m$. The new tracking procedure enabled testing the new CREM robot and measuring its motion repeatability. Results showed that the robot can achieve motion repeatability of less than $10\mu m$, and its motion resolution was shown to be less than $2\mu m$.

Chapter 5 presented the derivation of the micro-scale motion modeling and kinematics. First, a simplistic approach using moment-coupling effect was presented and shown to be able to replicate the turning-point phenomenon observed in chapter 4. Two other methods were then presented to explain the source of this turning point phenomenon. The first methods relied on energy considerations and the second method relied on the kinematic constraints of these robots. Since both of these methods cannot account for internal friction, a third method using empirically derived Jacobian was presented using a modal approximation of the micro-motion map.

Once the modeling framework was defined, chapter 6 demonstrated a system-level integration and validation of 3D OCT volumes using an external commercial OCT probe and an integrated miniature custom B-mode OCT probe while enabling the micro-scale motion. The result showed that the volumes, reconstructed using the OCT scans and the micro-scale motion, can be generated with a $1\mu m$ slices if using closed-loop control with

position feedback.

Moreover, it was demonstrated that if no visual feedback is used for the 3D OCT reconstruction, using the experimentally derived micro-motion kinematics, the resulting 3D volumes have less than $5\mu m$ of error in position. Using this modeling approach, we presented the first known demonstration of a continuum robot using OCT for visual servoing while utilizing both macro and micro motion for guiding a needle into an agar channel. Using the combined macro and micro motion, the position error of the tip of the needle from the center of the agar channel was reported at less than $3\mu m$ in the longitudinal axis and less than $0.3mm$ in the depth direction.

In chapter 7 a new miniature antagonistic pair actuated continuum robot was presented. The first iteration of a single segment 1-Dof flexure-based design was improved with an extended dexterity design. As a result of such re-design, a new two segments 2-Dof APCR was prototyped and tested on a preliminary exploration of task feasibility within the context of enabling dexterous intravenous navigation for ischemic stroke treatment. The constrained kinematic model aiming at intraocular dexterity was derived, serving, as of today, as the base platform of the ongoing project in the ARMA Lab.

Finally, chapter 8 presented the results for a simplified design of a 3-RRR parallel robot with embedded elastic elements, in 4 different placement modes, aiming at static-balancing conditions. We showed that this simple design choice allows for effective balancing within a desired task-based dexterous sub-workspace.

This new simple design considerations allow an average torque reduction of 84% when using Mode 1, changing the location of the dexterous workspace requires a redesign of the spring reload and spring constants and in some aspects of the workspace may not produce effective balancing.

We further extended the design consideration using wire-wrapped cam design showing that the cam design produces an improvement of an extra 8% in balancing performances when compared with the balancing strategy using torsional springs but at the cost of having

a more complex overall design.

9.2 Future Research Directions

There is a possible significant improvement over the TURBoT system. One main aspect that could generate an immediate and substantial benefit is to further decouple the actuation scheme. As of now the three cylinders in each actuator module are not fully decoupled, only the first and second cylinders are. Decoupling the second and third cylinder with a similar design used for the first two actuators would allow using smaller motors and further decrease the size of the overall actuation unit for a more compact and lighter assembly. Based on the experimental evaluation in the pig study, another important aspect that could be addressed in future research is the visualization modality of the system. A bottleneck of the current system is the actual field of view relying on a simple resectoscope. Implementing an articulated camera or a stereo vision camera would significantly increase the performance of the system. It will allow improved depth perception needed for safer telemanipulation and the use of vision-assisted virtual fixtures [183, 184].

In chapter 3 the CREM concept demonstrated the capabilities of these robots to achieve multi-scale motion by coupling the standard direct-actuation of pushing and pulling the tubular backbones to generate macro motion with indirect actuation whereby altering the equilibrium pose, micro-scale motion is achieved. A future research direction should explore the shortcoming of our modeling framework in that it does not capture the effects of direction reversal of the equilibrium modulation wires (i.e. hysteresis and stiction effects have not been yet fully characterized or modeled).

One of the natural point of improvement in terms of modeling framework is to extend the actual study, limited to a 2D dimension, to a 3D case and explore the possibility of insertion coordination of the insertion wires to generate predefined spatial trajectories. However, the extension to a 3D case presents challenges, not only on the modeling side, but also on the hardware itself. The generated motion, no longer confined on a single

plane, will require at least two cameras to track two markers placed perpendicularly to each other and accordingly registered to be able to reconstruct the correct motion path of a 3D configuration. Also, this solution will increase the computational time and power needed since every step of the online marker tracking will run in parallel for the second marker. The advantages of enabling 3D micro-motion are multiple. Spatially extended motion capabilities would allow a bigger scanning range, and could also generate sweeping motion resulting in a more dense and detailed scanning area over the scanned sample.

Chapter 7 is an exploratory effort for possible use of APCRs in ophthalmic surgery and for intraocular dexterity enhancement. The design consideration posed several challenges in terms of flexure optimization and fabrication process but the device proved its ability to steer in confined spaces making it suitable for surgical application where dexterity, miniaturization, and hollow bore design are required. However, the design needs to be revised for each specific application where the segment length, bending curvature, and bending would be optimized upon it. A natural direction for this work would be to investigate the dimensional syntheses of the continuum segments' length and their relative bending planes based on their clinical application. Moreover, in addition to the challenges of achieving mechanical embodiments of multi-segment hollow-bore APCRs, the modeling of the statics of these robots is challenging, yet a requirement for the design of these robots and their associated actuation units. A modeling approach of the statics of these robots could be explored using the chain method [141] where the two antagonistic tubes are modeled along with their coupling forces.

From the results presented in chapter 8, the static balancing condition obtained for a portion of the dexterous workspace is usually not optimal when we move our manipulator to a different pose throughout the workspace. An extension of this work in the direction of obtaining a solution that would generate statically balanced mechanisms that would generate counterbalancing torque over the entire workspace. Such designs could use an adaptor "clutch" that allows wire-wrapped cams to remain within their working range. Also, the

design would require preload adjustment to extend the degrees of freedom to achieve exact balancing throughout the workspace. However, the static balancing performance, in that case, would not be guaranteed to offer effective balancing.

CHAPTER 10

PUBLISHED WORKS AND PATENT AWARDED

10.1 Chapter 2

- **Del Giudice, G.**, Sarli, N., Herrell, S. D. and Simaan, N (2016). *Design Considerations for Continuum Robot Actuation Units Enabling Dexterous Transurethral Bladder Cancer Resection*. In International Design Engineering Technical Conferences and Computers and Information in Engineering Conference (ASME IDETC). Charlotte,NC,USA

- Sarli, N., **Del Giudice, G.**, De, S., Dietrich, Mary S., Herrell, S. D. and Simaan, N (2018). *Preliminary Porcine in vivo evaluation of a Telerobotic System for Transurethral Bladder Tumor Resection and Surveillance. Journal of Endourology*. **Best paper Award**

- Sarli, N., **Del Giudice, G.**, Herrell, D. S. and Simaan, N. (2016). *A Resectoscope for Robot-Assisted Transurethral Surgery*. ASME Journal of Medical Devices

- Sarli, N., Marien, T., Mitchell, C. R., **Del Giudice, G.**, Dietrich, M. S., Herrell, S. D. et al. (2016). *Kinematic and Experimental Investigation of Manual Resection Tools for Transurethral Bladder Tumor Resection*. The International Journal of Medical Robotics and Computer Assisted Surgery.

- Sarli, N., **Del Giudice, G.**, Herrell, D. S. and Simaan, N (2016). *A Resectoscope for Robot-Assisted Transurethral Surgery*. In 2016 Design of Medical Devices Confer-

ence(DMD'2016). Minneapolis, MN, USA

- Marien, T., Sarli, N., Mitchell, C., **Del Giudice, G.**, Simaan, N. and Herrell, S. D (2015). *Surgeon Resection Performance During Transurethral Resection of Bladder Tumor (TURBT): A Quantified Study*. In 30th annual meeting of Engineering and Urology Society

10.2 Chapters 3, 4

- **Del Giudice, G.**, Wang, L., Shen, J., Joos, K. and Simaan, N., *Continuum Robot for Multi-Scale Motion: Micro-Scale Motion Through Equilibrium Modulation*, IEEE/RSJ International Conference on Intelligent Robots and System (IROS'), Vancouver, Canada, 2017.

- **Del Giudice, G.**, Wang, L., Shen, J., Joos, K. and Simaan, N., *Continuum Robot for Multi-Scale Motion: Micro-Scale Motion Through Equilibrium Modulation*, 6th Annual Surgery, Intervention, and Engineering Symposium, VISE Symposium, Vanderbilt University, Nashville TN, USA. 2017

- **Del Giudice, G.**, Wang, L., Ghandi S., Shen, J., Joos, K. and Simaan, N., *CONTINUUM ROBOTS FOR MULTI-SCALE MOTION: Experimental Integration, Modeling and Preliminary Evaluation*, 7th Annual Surgery, Intervention, and Engineering Symposium, VISE Symposium, Vanderbilt University, Nashville TN, USA.2018

10.3 Chapters 5, 6

- **Del Giudice, G.**, Orekhov A., Shen, J., Joos, K. and Simaan, N., *Investigation of Micro-motion Kinematics of Continuum Robots for Volumetric OCT and OCT-guided Visual Servoing*, IEEE Transactions on Mechatronics. Submitted 2020

- **Del Giudice, G.**, Shen, J., Joos, K. and Simaan, N., *Feasibility of Volumetric OCT*

Imaging using Continuum Robots with Equilibrium Modulation Hamlyn Symposium on Medical Robotics, London, UK. 2019.

- Long Wang, **Giuseppe Del Giudice**, and Nabil Simaan. *Simplified kinematics of continuum robot equilibrium modulation via moment coupling effects and model calibration*. ASME JMR, 11(5), 2019.

- **Del Giudice, G.**, Wang, L., Ghandi S., Shen, J., Joos, K. and Simaan, N., *Continuum Robots for multi-scale motion: feasibility of volumetric OCT imaging reconstruction*, 8th Annual Surgery, Intervention, and Engineering Symposium, VISE Symposium, Vanderbilt University, Nashville TN, USA. 2019 **Best Poster Award**

10.4 Chapters 7

- Colette Abah, **Giuseppe Del Giudice**, Neel Shihora, Rohan Chitale, Nabil Simaan. *Towards semi-automated mechanical thrombectomy: Path planning considerations for a double articulated microcatheter*. Hamlyn Symposium on Medical Robotics, London, UK. 2019.

10.5 Chapter 8

- **Giuseppe Del Giudice**, Garrison Johnston, and Nabil Simaan. "Optimal Balancing of Planar Parallel Robots Using Torsional Springs and Wire-cam Mechanisms",(ASME J. of Mechanisms & Robotics)submitted.

10.6 Patents

- Simaan, N., **Del Giudice, G.**,Wang, L., Joos, M.K., Shen, J.H., *Continuum Robots with Multi-Scale Motion Through Equilibrium Modulation* US patent #10967504 B2, Vanderbilt University, granted 4/6/2021

- Simaan, N., **Del Giudice, G.**, Abah C., Chitale R., VU20009P1 (No. 62/901,114) "SMART MULTI-ARTICULATED CATHETERS WITH SAFETY METHODS AND SYSTEMS FOR IMAGE-GUIDED COLLABORATIVE INTRAVASCULAR DEPLOYMENT"

Appendices

APPENDIX A

HARDWARE IMPLEMENTATION FOR CUSTOM OCT PROBE CONTROL

A.1 Arduino Based Control Box

This section summarizes the mechanical and electrical design of the Arduino Base Control Box and the Custom made B-mode OCT probe Voice Coil Actuator (VCA)(model:NCM02-05-005-4JBH manufactured by H2W) used for the experimental evaluation in Chapter 6. Although this system is the result of many design iterations over the past 5 years, we are presenting the final design used to support the work presented in this thesis.

A.1.1 Background

The actual control box is a re-designed of the first generation control box, shown in Figure A.1. The original box was realized to control the actuation unit of a custom made B-mode OCT probe from [185], synchronizing the signal generated by a commercial OCT engine to the sweeping movement of the B-mode OCT probe. The last design iteration includes updates of the original electronics module and an extra control module to be able to control up to 12 DC motor with their relative encoders.

A.1.2 Overview of Box Redesign

The old box was made out of acrylic material and custom laser-cutted, the new system instead has been placed in an industrial standard enclosure box, to save design time and to ensure high build quality. The internal base has been isolated using an acrylic plastic sheet

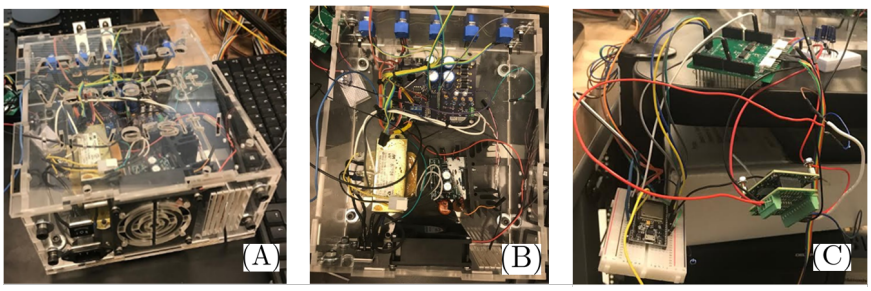

Figure A.1: (A) Old Box overview (B) Old box internal layout (C) First VCA controller prototype

mounted on standoffs within the aluminum enclosure. The PCB, OCT amplifier, power distributions busses, and motor/encoder electronics modules are mounted on this plastic sheet.

A.1.3 Fabrication and Assembly

In order to accommodate all the different components, the base,front, and rear panels are customized and machined using a CNC machine in the A.R.M.A Lab at Vanderbilt University. The ports on the front panel can be broken into 3 categories: VCA ports (to the left), Motor/Encoder ports (to the right/middle), and general ports to the far right. The acrylic sheet mentioned above has been machined using a laser-cutting table. The new box layout accomodates 1 VCA control module, but it has been design to be able to accommodate up to 2 modules; moreover it includes one DC motor control module that can control up to 6 but the design allows to have 2 of these modules in order to control up to 12 motors.

The new control box internal layout is shown in Figure A.2.B. It is possible to identify 4 main areas of interest:

- the front panel (Figure A.2.A-B)
- the rear panel (Figure A.2.C)
- the OCT probe control module (red dashed area in Figure A.2.B)

- the DC motors control module (green dashed area in Figure A.2.B)

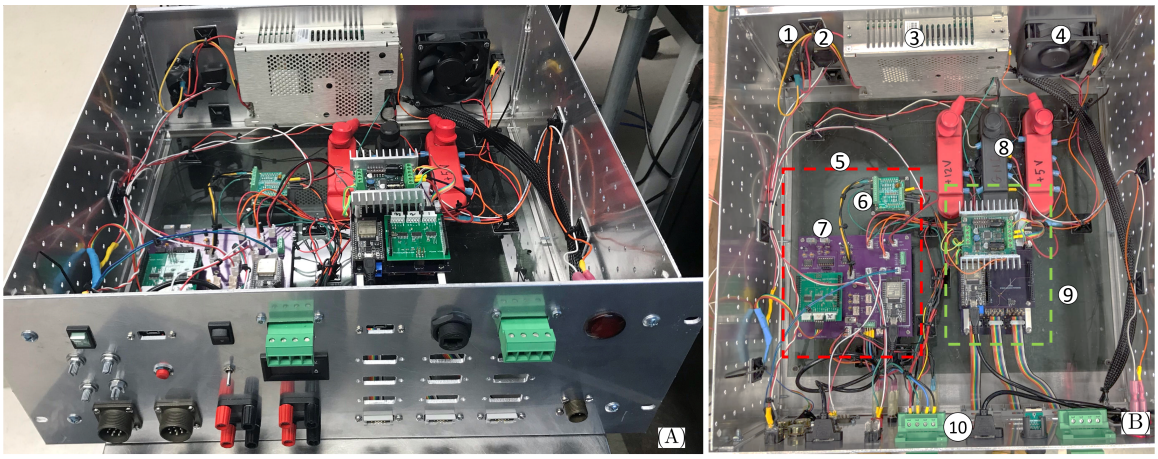

Figure A.2: (A) Overview of Box Contents (B) Internal Layout: ① Box power connector ② OCT Trigger IN ③ Power Supply ④ Cooling Fan ⑤ VCA Control System ⑥ VCA power amplifier ⑦ PCB board ⑧ Power bus bars (5V, 12V, GND) ⑨ DC motors controller ⑩ Front Panel

A.2 Electrical Design

Since the complexity of the system having several input and output, in the electrical design a naming system was implemented to keep track of those connections. Outputs from the PCB are labeled as O1, inputs to the PCB as IN1. Outputs that run to the outside of the box for user access are labeled as X1, for external.

Several redesign goals were made at the beginning of the design phase. Initially, the old box used a wall outlet to provide power. The AC power was passing through an internal transformer, as well as various rectifier and regulator circuits implemented on a custom PCB in order to change the input signal to the corrected output directed to the actuation unit. However, the voice coil that the box was intended to control was being powered off an external dedicated power supply. These two sources of power are replaced by one internal power module that can provide enough power for running the circuit and the voice coil.

Originally, the old box allowed the use of a hand-held OCT probe, which was powered using an old audio amplifier. With the new VCA, a dedicated servo amplifier was needed. The VCA manufacturer suggested to use a B10A04DC servo amplifier. The B10A04DC amplifier was tested with the voice coil to see what current the amplifier would output for a given command voltage. This was done by using an Amp-meter to read the current sent through the voice coil, while sending varying voltages to the amplifier. The results are shown in the following figure.

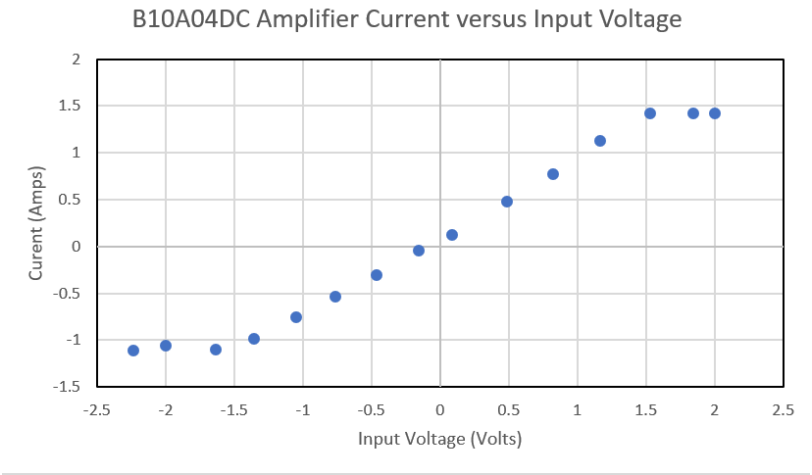

Figure A.3: Amplifier Current Output versus Voltage Command

It is clear that the amplifier experiences saturation of the output current at a very low input voltage for the voice coil. To prevent the sending of too much current to the voice coil, the PCB potentiometers on the current box implementation were adjusted such that the shifted voltage being sent to the amplifier ranges from -4 to 4 volts. All the components and PCBs are powered for a single AC/DC power supply (Emerson Network Power LPQ142-C AC-DC), the rational of choosing this specific model is based on the following needs:

- Ability to provide all the voltage outputs necessary (+12, -12, and +5V)
- Remote inhibit feature, allowing inhibiting of power supply without high power relay.
- Metal Enclosure, for safety and for longevity of components

- Current ratings:
  - The power supply can supply up to 5 amps on the +12V rail, which is what is used to power the amplifiers. This was deemed adequate as the voice coil can draw a maximum of around 2.4 amps, and a typical maxon motor/encoder will draw around .275 amps. The power supply then could handle 6 motors and one voice coil, 2 voice coils, or 12 motors without any issues. You could potentially run more with sufficient testing. The current on the +12V rail was the limiting factor in power supply selection, as the +5V rail can supply up to 12 amps, which is more than enough for the PCB
  - The power supply has no minimum current load rating, which is important becasuse the loads on the +5V and -12V rails are not high, as they are only used for signals

In order to distribute the needed power to each component, the outputs of the power supply are connected to three bus bars in the control box, one for ground, one for +5V and one for +12V output. They make it easy for things not on the PCB to have access to these voltage rails. Basically, it allows one voltage rail to have numerous outputs in the box. Moreover, for extra safety, the power supply is connected to an Emergency Stop switch.

A.2.1 PCB Overview

The custom PCB (Figure A.5.A) allows control of a VCA using an ESP32 microcontroller (Arduino Base coded) together with a B10A04DC servo amplifier, furthermore it uses a Robogaia 3 axis encoder counter board for encoder feedback. Inputs and outputs are done either with screw terminals (IN29, O3-12) or with JST XA1 series PCB connectors (all other IO). This PCB was fabricated by OSH Park.

Figure A.5.B-C show the schematic of the PCB. The PCB receives an input trigger from a commercial OCT engine, in the form of a voltage signal. This signal is converted

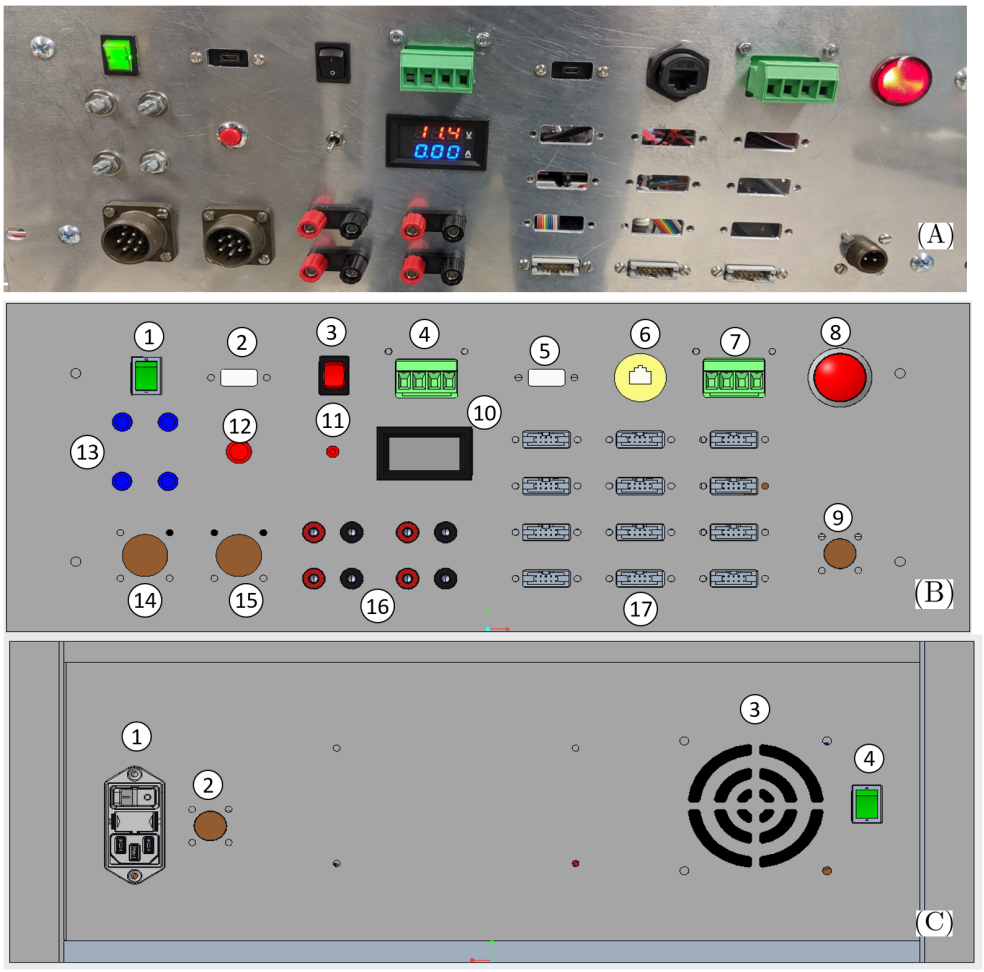

Figure A.4: Box Panels: (A) Front Panel (B) Front panel layout (① Potentimeter and control switch ② Micro-USB port to VCA ③ ESP-32 Power button ④ OCT extra IO ⑤ Micro-USB to DC motor controller ⑥ Dc Motor Controller Ethernet comunication port ⑦ Dc Motor Controller extra IO ⑧ LED power on/off ⑨ Emergency stop ⑩ Current/Voltage Display for OCT Amplifier ⑪ DAC Shape switch ⑫ Reset Button ⑬ Potentiometers ⑭ VCA 1 Out ⑮ VCA 2 Out ⑯ Oscilloscope Outs 4X: DAC, Amplifier Input, Amplifier Current monitor (Output), Square wave ⑰ DC Motors/Encoders output). (C) Back Panel ① Power inlet ② OCT Trigger IN ③ Cooling fan ④ Fan power switch

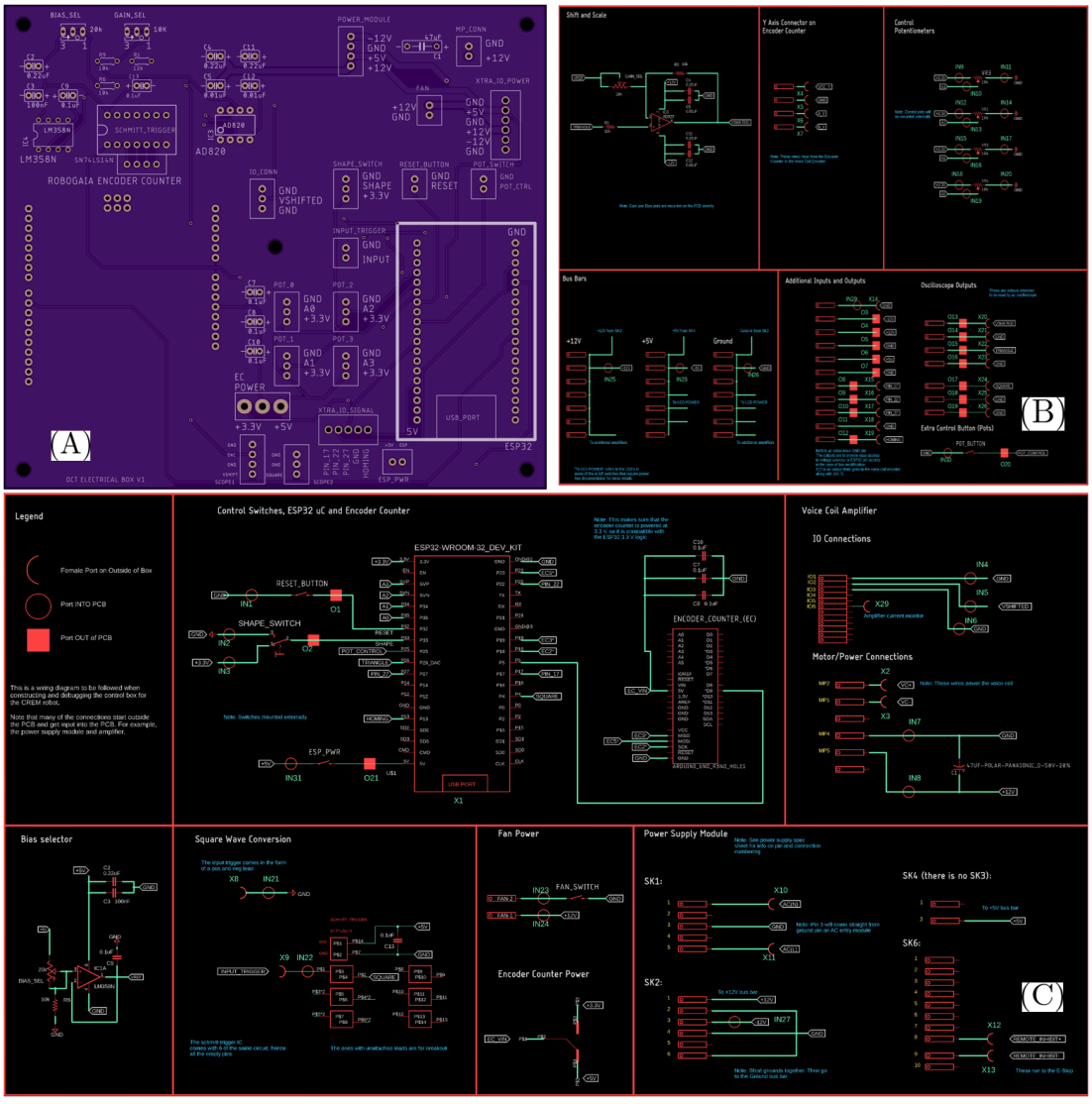

Figure A.5: Custom design PCB: (A) Printed PCB (B-C) Schematic plots

to a square wave using a Schmitt trigger, at this point the microcontroller converts the square wave into a triangle wave which is then amplified in on a shift and scale circuit. The resulting shifted voltage ranges from +10 to -10 volts and it can be modified using the gain selector potentiometer. This shifted voltage is then fed into the motor amplifier, which has outputs leading to the VCA. The PCB also houses connections for potentiometers, switches, outputs for the oscilloscope, and female headers for the Robogaia encoder counter to allow for tweaking of the parameters from outside the control box and for implementation and control of PID control gains. each Trace width was determined by using an online *trace width calculator*, the range goes between 1oz to 2oz thickness based on the current passing through each trace. The power lines on the PCB are rated for 3 amps. The Design Rule Check (DRC) used was based on the guidline of the OSHpark's website. High power traces are contained to the upper right corner of the PCB to prevent crosstalk. Decoupling capacitors are included for powering the EC, all op amps, and the amplifier. Capacitor values were chosen based on values listed in device datasheets. These are physically kept as close as possible to the device they are decoupling. On the PCB there are screw terminals that provide access to +5, +12 and -12 V, as well as ground extra IO options available. There are also screw terminals for 3 additional GPIO pins for the ESP32. GND and the 3 GPIO pins are accessible on the front panel. Also available on the front panel is access to the triangle wave being output from the microcontroller's DAC, the shifted signal coming out of the shift and scale circuit, the square wave generated by the Schmitt Trigger, and the current monitor output of the amplifier.

A.2.1.1 Microcontroller and Encoder Counter

The microcontroller used in this system is an Arduino based HiLetGo ESP32 2.4GHz Dual-Mode WiFi + Bluetooth. It is connected to 4 potentiometers for user control of the generated signal to the VCA, as well as a toggle switch (shape_switch for the triangle wave), a momentary switch (reset_button) and an additional SPST rocker switch

(pot_switch). The wiring diagram in Figure A.5.B-C show which pins on the ESP32 these controls are wired to. There is also another switch designed to let the user choose between powering the ESP32 with 5V from the PCB, or using external USB power. This switch has not been wired in the current box implementation.

The encoders counting task is done by a commercial encoder reading board made by Robogaia. The 3 axis Robogaia Encoder reading board is compatible with the ESP32 microcontroller (Arduino base libraries), and installed on the main PCB, however, the user has the option of powering the Robogaia Encoder Counter with either +3.3 or +5 V. Both options were provided because there was concern that powering the encoder counter with 5V would create logical highs that would be too high for the ESP32's inputs. For this reason, it is preferred to power the counter at 3.3V. This does result in a slower read rate, as noted in the spec sheet for the integrated circuit onboard the encoder counter. To change between voltages, it is possible to use the toggle switch mounted onboard the PCB.

A.2.1.2 DC Motor/Encoder Control Module

As mentioned in Section 6.4.1, the experimental setup uses a Velmex linear stage to achieve insertion of the needle inside the agar. The control of the linear slide is performed by the DC motor control module shown in Figure A.2.B ⑨, grouped by the green dashed line. The module uses an ESP32 microcontroller paired with a Robogaia 3 axis Encoder Counter board and a Sabertooth 2x25 2007 DC motor amplifier. Potentially this setup can control up 12 motors/encoder but as of today only 3 channels are wired.

A.3 Voice Coil motor for OCT Probe actuation unit

The following section presents the efforts on design the actuation unit (AU) (Figure A.6) for a the custom made B-mode OCT probe used in this thesis and originally presented in [185]. The mechanical design together with the electrical and control scheme are summarized in Section A.3.1 and Section A.3.2 respectively. Finally, Section A.3.2 presents

experimental evaluation results of the working actuator.

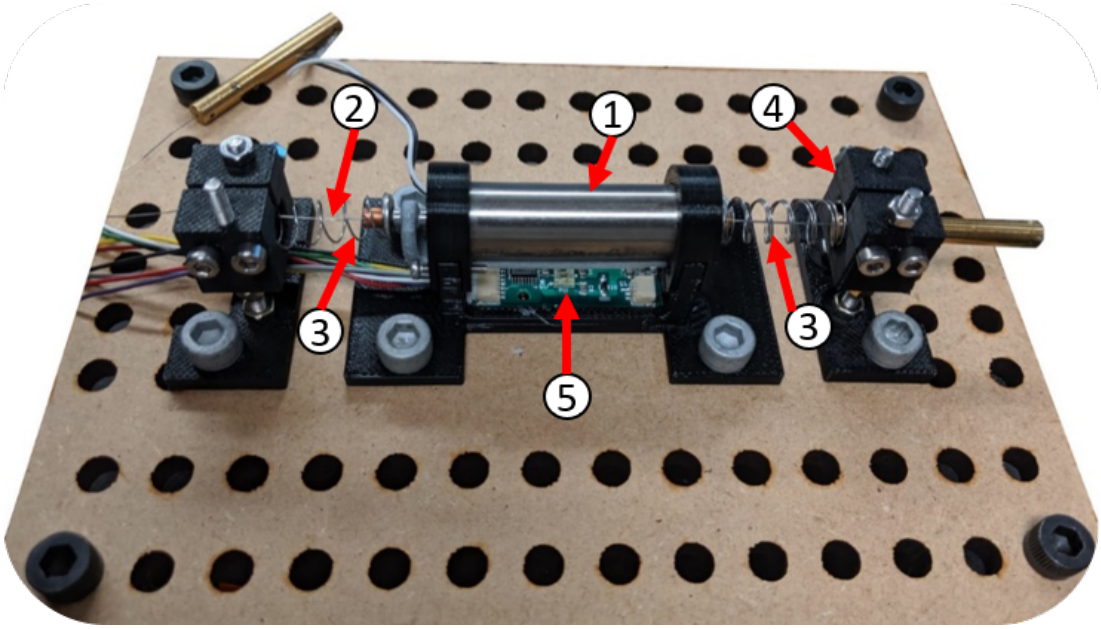

Figure A.6: Custom design VCA: ① Voice coil motor ② NiTi tubes ③ Compression springs ④ Adjustable tube holders ⑤ Optical Encoder Module

A.3.1 Design

The core of the mechanical design is the VCA (model:NCM02-05-005-4JBH manufactured by H2W) shown in Figure A.6 ①. The chosen VCA has an hollow shaft that allow to pass the fiber glass and NiTi tubes ②, used for the OCT probe, concentrically. The stand alone VCA runs in open-loop control mode, doesn't provide any feedback in position for his shaft. Since one of working operational requirement for the custom home made OCT probe is to control the amount of sweeping motion of its tip, a closed-loop control scheme is then required. The shaft position feedback is acquired using an external Optical Encoder Module ⑤ ($30\mu m$ Quadrature Resolution model: OEM-030U-01 manufactured by Moticont) and a linear encoder strip which is rigidly attached underneath the VCA shaft. Two compression springs ③ are used as damping devices. The alignment of the VCA shaft with the OCT probe is adjustable using the two tube holders ④ positioned a the two extremities of the AU.

A.3.2 Control and testing

The control module and electronics has been already discussed in the previous section. The ESP32 microcontroller is an Arduino based device which means it uses C/C++ language. The control code uses open source libraries for device/board compatibilities, however, few custom written libraries have been implemented for PID control scheme integration. The PID gains have been tweaked using autotuning PID libraries available on the Arduino platform, however, since the mechanical performances of the OCT probe may vary with time, the control code allows to adjust each PID gain manually using 3 potentiometers which are not currently wired in the control box.

Figure A.7 shows the results of the testing for the close-loop control of the VCA after that the PID gains were accordingly tweaked. In this experiment, the VCA was commanded to oscillate at a frequency of 30 Hz with an amplitude of 3.4*mm* (purple line), the actual motion (blue line) shows a stroke of $\pm 3.2mm$ which means with an error over the full amplitude of 6

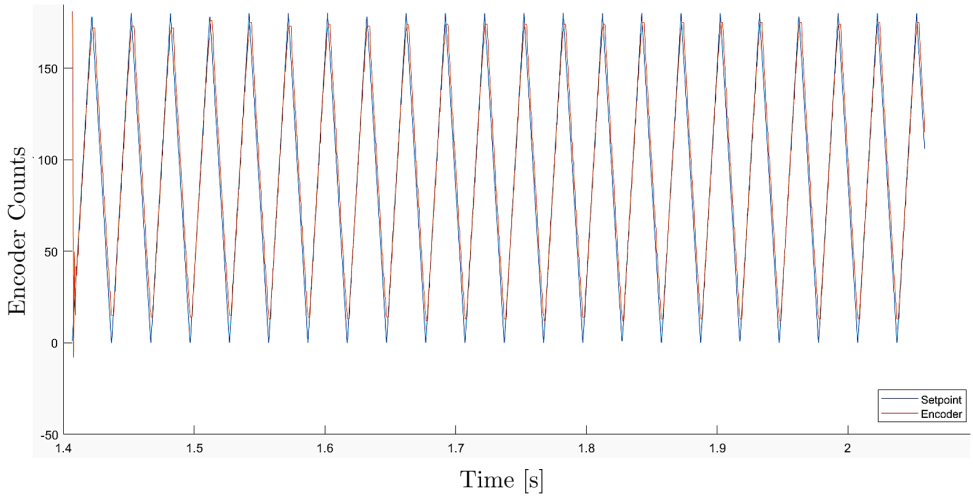

Figure A.7: VCA PID testing result

BIBLIOGRAPHY

[1] Jason Pile and Nabil Simaan. Modeling, design, and evaluation of a parallel robot for cochlear implant surgery. *IEEE/ASME Transactions on Mechatronics*, 19(6):1746–1755, 2014.

[2] Nabil Simaan, Russell Taylor., and Paul Flint. A dexterous system for laryngeal surgery. In *IEEE International Conference on Robotics and Automation, 2004. Proceedings. ICRA '04. 2004*, volume 1, 2004.

[3] Nabil Simaan, Kai Xu, Ankur Kapoor, Peter Kazanzides, Paul Flint, Russell Taylor, and Wei Wei. Design and Integration of a Telerobotic System for Minimally Invasive Surgery of the Throat. *The International Journal of Robotics Research*, 28(9):1134–1153, 2009.

[4] Carlos M Rivera-Serrano, Paul Johnson, Brett Zubiate, Richard Kuenzler, Howie Choset, Marco Zenati, Stephen Tully, and Umamaheswar Duvvuri. A transoral highly flexible robot: novel technology and application. *The Laryngoscope*, 122(5):1067–1071, 2012.

[5] Kai Xu, Dong Qiu, and Nabil Simaan. A pilot investigation of continuum robots as a design alternative for upper extremity exoskeletons. In *2011 IEEE International Conference on Robotics and Biomimetics*, pages 656–662. IEEE, 2011.

[6] Kelly Groom, Long Wang, Nabil Simaan, and James Netterville. Robot-assisted

transnasal laryngoplasty in cadaveric models: Quantifying forces and identifying challenges. *The Laryngoscope*, 125(5):1166–1168, 2015.

[7] Koji Ikuta, Keiichi Yamamoto, and Keiji Sasaki. Development of remote microsurgery robot and new surgical procedure for deep and narrow space. In *2003 IEEE International Conference on Robotics and Automation (Cat. No. 03CH37422)*, volume 1, pages 1103–1108. IEEE, 2003.

[8] Hyun-Soo Yoon, Se Min Oh, Jin Hyeok Jeong, Seung Hwan Lee, Kyung Tae, Kyoung-Chul Koh, and Byung-Ju Yi. Active bending endoscope robot system for navigation through sinus area. In *2011 IEEE/RSJ International Conference on Intelligent Robots and Systems*, pages 967–972. IEEE, 2011.

[9] Jienan Ding, Roger E Goldman, Kai Xu, Peter K. Allen, Dennis L. Fowler, and Nabil Simaan. Design and Coordination Kinematics of an Insertable Robotic Effectors Platform for Single-Port Access Surgery. *IEEE/ASME T Mech*, In press.(99):1–13, oct 2012.

[10] N Simaan, A Bajo, A Reiter, Long Wang, P Allen, and D Fowler. Lessons learned using the insertable robotic effector platform (IREP) for single port access surgery. *J. Robot. Surg.*, pages 1–6, 2013.

[11] W Jong Yoon, Sangtae Park, Per G Reinhall, and Eric J Seibel. Development of an automated steering mechanism for bladder urothelium surveillance. *Journal of medical devices*, 3(1), 2009.

[12] R. E. Goldman, Andrea Bajo, and N Simaan. Algorithms for autonomous exploration and estimation in compliant environments. *Robotica*, 31(1):71–88, March 2013.

[13] Jessica Burgner, Philip J Swaney, D Caleb Rucker, Hunter B Gilbert, Scott T Nill, Paul T. Russell, Kyle D Weaver, and Robert J. Webster. A bimanual teleoperated

system for endonasal skull base surgery. In *2011 IEEE/RSJ International Conference on Intelligent Robots and Systems*, pages 2517–2523. IEEE, sep 2011.

[14] Nicholas Pappafotis, Wojciech Bejgerowski, Rao Gullapalli, J Marc Simard, Satyandra K Gupta, and Jaydev P Desai. Towards design and fabrication of a miniature mri-compatible robot for applications in neurosurgery. In *International Design Engineering Technical Conferences and Computers and Information in Engineering Conference*, volume 43260, pages 747–754, 2008.

[15] Michael DM Kutzer, Sean M Segreti, Christopher Y Brown, Mehran Armand, Russell H Taylor, and Simon C Mears. Design of a new cable-driven manipulator with a large open lumen: Preliminary applications in the minimally-invasive removal of osteolysis. In *2011 IEEE International Conference on Robotics and Automation*, pages 2913–2920. IEEE, 2011.

[16] Moshe Shoham. Miniature bone-mounted surgical robot, January 4 2005. US Patent 6,837,892.

[17] Sharon J Harris, WJ Lin, KL Fan, Roger D Hibberd, Justin Cobb, R Middleton, and Brian L Davies. Experiences with robotic systems for knee surgery. In *CVRMed-MRCAS'97*, pages 757–766. Springer, 1997.

[18] G Brandt, Klaus Radermacher, Stéphane Lavallée, H-W Staudte, and Günther Rau. A compact robot for image guided orthopedic surgery: Concept and preliminary results. In *CVRMed-MRCAS'97*, pages 767–776. Springer, 1997.

[19] N. Sarli, G. Del Giudice, S. De, M. S. Dietrich, S. D. Herrell, and N. Simaan. Turbot: A system for robot-assisted transurethral bladder tumor resection. *IEEE/ASME Trans. Mechatronics*, 24(4):1452–1463, 2019.

[20] Roger E. Goldman, Andrea Bajo, Lara S. MacLachlan, Ryan Pickens, S. Duke Herrell, and Nabil Simaan. Design and Performance Evaluation of a Minimally

Invasive Telerobotic Platform for Transurethral Surveillance and Intervention. *IEEE TBME*, 60(4):918–925, apr 2013.

[21] R. J. Hendrick, S. D. Herrell, and R. J. Webster. A multi-arm hand-held robotic system for transurethral laser prostate surgery. In *2014 IEEE ICRA*, pages 2850–2855, 2014.

[22] Takahisa Kato, Ichiro Okumura, Hidekazu Kose, Kiyoshi Takagi, and Nobuhiko Hata. Tendon-driven continuum robot for neuroendoscopy: validation of extended kinematic mapping for hysteresis operation. *INT J COMPUT ASS RAD*, 11(4):589–602, 2016.

[23] Yeongjin Kim, Shing Shin Cheng, Mahamadou Diakite, Rao P Gullapalli, J Marc Simard, and Jaydev P Desai. Toward the development of a flexible mesoscale mri-compatible neurosurgical continuum robot. *IEEE TRO*, 33(6):1386–1397, 2017.

[24] Johannes Bonatti, George Vetrovec, Celia Riga, Oussama Wazni, and Petr Stadler. Robotic technology in cardiovascular medicine. *Nature Reviews Cardiology*, 11(5):266, 2014.

[25] Awaz Ali, Dick H Plettenburg, and Paul Breedveld. Steerable catheters in cardiology: Classifying steerability and assessing future challenges. *IEEE Transactions on Biomedical Engineering*, 63(4):679–693, 2016.

[26] Nabil Simaan. Snake-like units using flexible backbones and actuation redundancy for enhanced miniaturization. In *Proceedings - IEEE ICRA*, volume 2005, pages 3012–3017, Barcelona, Spain, 2005.

[27] Nima Sarli, Tracy Marien, S Duke Herrell, and Nabil Simaan. Characterization of resection dexterity in transurethral resection of bladder tumor: A kinematic study. In *2015 IEEE International Conference on Robotics and Automation (ICRA)*, pages 5324–5329. IEEE, 2015.

[28] Walid Saliba, Jennifer E Cummings, Seil Oh, Youhua Zhang, Todor N Mazgalev, Robert A Schweikert, J David Burkhardt, and Andrea Natale. Novel robotic catheter remote control system: feasibility and safety of transseptal puncture and endocardial catheter navigation. *Journal of cardiovascular electrophysiology*, 17(10):1102–1105, 2006.

[29] Shawn M Vuong, Christopher P Carroll, Ryan D Tackla, William J Jeong, and Andrew J Ringer. Application of emerging technologies to improve access to ischemic stroke care. *Neurosurgical focus*, 42(4):E8, 2017.

[30] David M. Kwartowitz, S. Duke Herrell, and Robert L. Galloway. Toward image-guided robotic surgery: determining intrinsic accuracy of the da Vinci robot. *International Journal of Computer Assisted Radiology and Surgery*, 1(3):157–165, oct 2006.

[31] Takeharu Kanazawa, Shunji Sarukawa, Hirofumi Fukushima, Shoji Takeoda, Gen Kusaka, and Keiichi Ichimura. Current reconstructive techniques following head and neck cancer resection using microvascular surgery. *Annals of vascular diseases*, 4(3):189–95, jan 2011.

[32] David J Slutsky. The management of digital nerve injuries. *The Journal of hand surgery*, 39:1208–15, 2014.

[33] Chao Chen, Peifu Tang, Lihai Zhang, and Bin Wang. Treatment of fingertip degloving injury using the bilaterally innervated sensory cross-finger flap. *Annals of plastic surgery*, 73:645–51, 2014.

[34] Joern Andreas Lohmeyer, Yasmin Kern, Daniel Schmauss, Felix Paprottka, Felix Stang, Frank Siemers, Peter Mailaender, and Hans-Guenther Machens. Prospective clinical study on digital nerve repair with collagen nerve conduits and review of literature. *Journal of reconstructive microsurgery*, 30:227–34, 2014.

[35] Ryan Cassilly, Michael D Diodato, Michael Bottros, and Ralph J Damiano. Optimizing motion scaling and magnification in robotic surgery. *Surgery*, 136(2):291–4, aug 2004.

[36] Sunil M Prasad, Sandip M Prasad, Hersh S Maniar, Celeste Chu, Richard B Schuessler, and Ralph J Damiano. Surgical robotics: impact of motion scaling on task performance. *Journal of the American College of Surgeons*, 199(6):863–8, dec 2004.

[37] Paurush Babbar and Ashok K Hemal. Robot-assisted urologic surgery in 2010 - Advancements and future outlook. *Urology Annals*, 3(1):1–7, jan 2011.

[38] Minimally invasive cystectomy approaches in the treatment of bladder cancer. *Expert review of anticancer therapy*, 12(6):733–41, jun 2012.

[39] C Freschi, V Ferrari, F Melfi, M Ferrari, F Mosca, and A Cuschieri. Technical review of the da Vinci surgical telemanipulator. *The international journal of medical robotics + computer assisted surgery : MRCAS*, (October), nov 2012.

[40] Albert a Mikhail, Marcelo a Orvieto, Ehab S Billatos, Kevin C Zorn, Edward M Gong, Charles B Brendler, Gregory P Zagaja, and Arieh L Shalhav. Robotic-assisted laparoscopic prostatectomy: first 100 patients with one year of follow-up. *Urology*, 68(6):1275–9, dec 2006.

[41] Jihad H Kaouk, Mihir M Desai, Sidney C Abreu, Francis Papay, and Inderbir S Gill. Robotic assisted laparoscopic sural nerve grafting during radical prostatectomy: initial experience. *The Journal of urology*, 170(3):909–12, sep 2003.

[42] Vincenzo Ficarra, Stefano Cavalleri, Giacomo Novara, Maurizio Aragona, and Walter Artibani. Evidence from robot-assisted laparoscopic radical prostatectomy: a systematic review. *European urology*, 51(1):45–55; discussion 56, jan 2007.

[43] Sanjay Saraf. Robotic Assisted Microsurgery (RAMS): Application in Plastic Surgery. In Vanja Bozovic, editor, *Medical Robotics*. 2008.

[44] M G W Van Den Heuvel and R R W J Van Der Hulst. Robotic assistance in microvascular surgery. In Vanja Bozovic, editor, *Medical Robotics*, chapter 34, pages 471–480. 2008.

[45] Andrew L. Orekhov, Colette Abah, and Nabil Simaan. Snake-like robots for minimally invasive, single port, and intraluminal surgeries. *CoRR*, abs/1906.04852, 2019.

[46] Nabil Simaan, Rashid M. Yasin, and Long Wang. Medical technologies and challenges of robot-assisted minimally invasive intervention and diagnostics. *Annual Review of Control, Robotics, and Autonomous Systems*, 1(1):465–490, 2018.

[47] Jienan Ding, Kai Xu, Roger Goldman, Peter Allen, Dennis Fowler, and Nabil Simaan. Design, Simulation and Evaluation of Kinematic Alternatives for Insertable Robotic Effectors Platforms in Single Port Access Surgery, may 2010.

[48] P. Sears and P. Dupont. A steerable needle technology using curved concentric tubes. In *2006 IEEE/RSJ IROS*, pages 2850–2856, 2006.

[49] R. J. Webster, A. M. Okamura, and N. J. Cowan. Toward active cannulas: Miniature snake-like surgical robots. In *2006 IEEE/RSJ IROS*, pages 2857–2863, 2006.

[50] Colin G Knight, Attila Lorincz, Alex Cao, Kelly Gidell, Michael D Klein, and Scott E Langenburg. Computer-assisted, robot-enhanced open microsurgery in an animal model. *Journal of laparoendoscopic & advanced surgical techniques. Part A*, 15(2):182–5, may 2005.

[51] G Peersman, R Laskin, J Davis, M G E Peterson, and T Richart. Prolonged operative time correlates with increased infection rate after total knee arthroplasty. *HSS*

journal : the musculoskeletal journal of Hospital for Special Surgery, 2(1):70–2, feb 2006.

[52] Magdalena a Lipska, Ian P Bissett, Bryan R Parry, and Arend E H Merrie. Anastomotic leakage after lower gastrointestinal anastomosis: men are at a higher risk. *ANZ journal of surgery*, 76(7):579–85, jul 2006.

[53] James G Fujimoto. Optical coherence tomography for ultrahigh resolution in vivo imaging. *Nat. biotech.*, 21(11):1361–1367, 2003.

[54] C. Reboulet and S. Durand-Leguay. Optimal design of redundant parallel mechanism for endoscopic surgery. In *Proceedings 1999 IEEE/RSJ IROS (Cat. No.99CH36289)*, volume 3, pages 1432–1437 vol.3, 1999.

[55] Robert MacLachlan, Brian Becker, Jaime Cuevas Tabares, Gregg Podnar, Louis Lobes, and Cameron Riviere. Micron: an actively stabilized handheld tool for microsurgery. *IEEE TRO*, 28(1):195–212, February 2012.

[56] Mirko Daniele Comparetti, Alberto Vaccarella, Ilya Dyagilev, Moshe Shoham, Giancarlo Ferrigno, and Elena De Momi. Accurate multi-robot targeting for keyhole neurosurgery based on external sensor monitoring. *P I MECH ENG H*, 226:347–59, 05 2012.

[57] YT Pan, TQ Xie, CW Du, S Bastacky, S Meyers, and ML Zeidel. Enhancing early bladder cancer detection with fluorescence-guided endoscopic optical coherent tomography. *Optics letters*, 28(24):2485–2487, 2003.

[58] Ankur Jain, Anthony Kopa, Yingtian Pan, Gary K Fedder, and Huikai Xie. A two-axis electrothermal micromirror for endoscopic optical coherence tomography. *IEEE journal of selected topics in Quantum electronics*, 10(3):636–642, 2004.

[59] Haoran Yu, Jin-Hui Shen, Karen M Joos, and Nabil Simaan. Calibration and integration of b-mode optical coherence tomography for assistive control in robotic microsurgery. *IEEE/ASME Trans. Mechatronics*, 21(6):2613–2623, 2016.

[60] Yong Huang, Xuan Liu, Cheol Song, and Jin U Kang. Motion-compensated hand-held common-path fourier-domain optical coherence tomography probe for image-guided intervention. *Biom. opt. express*, 3(12):3105–3118, 2012.

[61] Cheol Song, Peter L Gehlbach, and Jin U Kang. Active tremor cancellation by a "smart" handheld vitreoretinal microsurgical tool using swept source optical coherence tomography. *Optics express*, 20(21):23414–23421, 2012.

[62] Cheol Song, Dong Yong Park, Peter L Gehlbach, Seong Jin Park, and Jin U Kang. Fiber-optic oct sensor guided "smart" micro-forceps for microsurgery. *Biomedical optics express*, 4(7):1045–1050, 2013.

[63] Marcin Balicki, Jae-Ho Han, Iulian Iordachita, Peter Gehlbach, James Handa, Russell Taylor, and Jin Kang. Single fiber optical coherence tomography microsurgical instruments for computer and robot-assisted retinal surgery. In *MICCAI*, pages 108–115. Springer, 2009.

[64] Mark Draelos, Gao Tang, Brenton Keller, Anthony Kuo, Kris Hauser, and Joseph A Izatt. Optical coherence tomography guided robotic needle insertion for deep anterior lamellar keratoplasty. *IEEE TBME*, 2019.

[65] Kaitlin Oliver-Butler, Zane H Epps, and Daniel Caleb Rucker. Concentric agonist-antagonist robots for minimally invasive surgeries. In *Medical Imaging 2017: Image-Guided Procedures, Robotic Interventions, and Modeling*, volume 10135, page 1013511. International Society for Optics and Photonics, 2017.

[66] Mehmet Kilic, Yigit Yazicioglu, and Dilek Funda Kurtulus. Synthesis of a torsional

spring mechanism with mechanically adjustable stiffness using wrapping cams. *Mechanism and Machine Theory*, 57:27–39, November 2012.

[67] Giuseppe Del Giudice, Nima Sarli, Stanley D Herrell, and Nabil Simaan. Design considerations for continuum robot actuation units enabling dexterous transurethral bladder cancer resection. In *International Design Engineering Technical Conferences and Computers and Information in Engineering Conference*, volume 50152, page V05AT07A030. American Society of Mechanical Engineers, 2016.

[68] Nima Sarli, Giuseppe Del Giudice, Smita De, Mary S Dietrich, Stanley Duke Herrell, and Nabil Simaan. Preliminary porcine in vivo evaluation of a telerobotic system for transurethral bladder tumor resection and surveillance. *Journal of endourology*, 32(6):516–522, 2018.

[69] Nima Sarli, Giuseppe Del Giudice, Duke S Herrell, and Nabil Simaan. A resectoscope for robot-assisted transurethral surgery. *Journal of Medical Devices*, 10(2), 2016.

[70] Allan J Pantuck, Jack Baniel, Ziya Kirkali, Tobias Klatte, Nazy Zomorodian, Ofer Yossepowitch, and Arie S Belldegrun. A novel resectoscope for transurethral resection of bladder tumors and the prostate. *The Journal of urology*, 178(6):2331–2336, 2007.

[71] U Nagele, M Kugler, A Nicklas, AS Merseburger, U Walcher, G Mikuz, and TR Herrmann. Waterjet hydrodissection: first experiences and short-term outcomes of a novel approach to bladder tumor resection. *World journal of urology*, 29(4):423–427, 2011.

[72] Hans-Martin Fritsche, Wolfgang Otto, Fabian Eder, Ferdinand Hofstädter, Stefan Denzinger, Christian G Chaussy, Christian Stief, Wolf F Wieland, and Maximilian

Burger. Water-jet–aided transurethral dissection of urothelial carcinoma: A prospective clinical study. *Journal of endourology*, 25(10):1599–1603, 2011.

[73] Misop Han and Mark P Schoenberg. The use of molecular diagnostics in bladder cancer. In *Urologic Oncology: Seminars and Original Investigations*, volume 5, pages 87–92. Elsevier, 2000.

[74] Maurizio Brausi, Laurence Collette, Karlheinz Kurth, Adrian P. Van Der Meijden, Wim Oosterlinck, J. A. Witjes, Donald Newling, Christian Bouffioux, and Richard J. Sylvester. Variability in the recurrence rate at first follow-up cystoscopy after TUR in stage Ta T1 transitional cell carcinoma of the bladder: A combined analysis of seven EORTC studies. *European Urology*, 41:523–531, 2002.

[75] K. D. Sievert, B. Amend, U. Nagele, D. Schilling, J. Bedke, M. Horstmann, J. Hennenlotter, S. Kruck, and A. Stenzl. Economic aspects of bladder cancer: What are the benefits and costs? *World Journal of Urology*, 27:295–300, 2009.

[76] Marc F Botteman, Chris L Pashos, Alberto Redaelli, Benjamin Laskin, and Robert Hauser. The health economics of bladder cancer: a comprehensive review of the published literature. *PharmacoEconomics*, 21:1315–1330, 2003.

[77] Wansuk Kim, Cheryn Song, Sejun Park, Jongwon Kim, Jinsung Park, Seong Cheol Kim, Yong Mee Cho, Bumsik Hong, and Hanjong Ahn. Value of immediate second resection of the tumor bed to improve the effectiveness of transurethral resection of bladder tumor. *Journal of endourology*, 26(8):1059–1064, 2012.

[78] Harry W Herr and S Machele Donat. Quality control in transurethral resection of bladder tumours. *BJU international*, 102(9 Pt B):1242–6, November 2008.

[79] Olivier Traxer, Federico Pasqui, Bernard Gattegno, and Margaret S Pearle. Technique and complications of transurethral surgery for bladder tumours. *BJU international*, 94(4):492–496, 2004.

[80] IA Gravagne and ID Walker. Kinematic transformations for remotely-actuated planar continuum robots. In *Proceedings 2000 ICRA. Millennium Conference. IEEE International Conference on Robotics and Automation. Symposia Proceedings (Cat. No.00CH37065)*, volume 1, pages 19–26. IEEE, 2000.

[81] Robert J. Webster III, Bryan A. Jones, R. J. Webster, and Bryan A. Jones. Design and Kinematic Modeling of Constant Curvature Continuum Robots: A Review. *The International Journal of Robotics Research*, 29:1661–1683, jun 2010.

[82] P E Dupont, J Lock, B Itkowitz, and E Butler. Design and Control of Concentric-Tube Robots. *Robotics, IEEE Transactions on*, 26(2):209–225, 2010.

[83] Roger E Goldman, Andrea Bajo, and Nabil Simaan. Compliant motion control for multisegment continuum robots with actuation force sensing. *IEEE Transactions on Robotics*, 30(4):890–902, 2014.

[84] Kai Xu and Nabil Simaan. An investigation of the intrinsic force sensing capabilities of continuum robots. *IEEE TRO*, 24(3):576–587, 2008.

[85] Andrea Bajo, Ryan B Pickens, S Duke Herrell, and Nabil Simaan. Constrained Motion Control of Multisegment Continuum Robots for Transurethral Bladder Resection and Surveillance. In *IEEE International Conference on Robotics and Automation*, pages 5817–5822, 2013.

[86] Bryan A Jones and Ian D Walker. Kinematics for multisection continuum robots. *IEEE Transactions on Robotics*, 22(1):43–55, 2006.

[87] Kai Xu and Nabil Simaan. Intrinsic Wrench Estimation and Its Performance Index for Multisegment Continuum Robots. *IEEE TRO*, 26(3):555–561, jun 2010.

[88] Joseph Edward Shigley and Charles R Mischke. *Machine design fundamentals: a mechanical designers' workbook*. McGraw-Hill Companies, 1989.

[89] Nima Sarli. *Design, modeling and control of continuum robots and dexterous wrists with applications to transurethral bladder cancer resection*. Vanderbilt University, 2018.

[90] David M. Kwartowitz, S. Duke Herrell, and Robert L. Galloway. Update: Toward image-guided robotic surgery: determining the intrinsic accuracy of the daVinci-S robot. *International Journal of Computer Assisted Radiology and Surgery*, 1(5):301–304, feb 2007.

[91] Amir Degani, Howie Choset, Alon Wolf, and Marco A Zenati. Highly articulated robotic probe for minimally invasive surgery. In *Robotics and Automation, 2006. ICRA 2006. Proceedings 2006 IEEE International Conference on*, pages 4167–4172. IEEE, 2006.

[92] A. Bajo, R. E. Goldman, L. Wang, D. Fowler, and N. Simaan. Integration and preliminary evaluation of an insertable robotic effectors platform for single port access surgery. In *2012 IEEE ICRA*, pages 3381–3387, May 2012.

[93] H. S. Yoon, S. M. Oh, J. H. Jeong, S. H. Lee, K. Tae, K. C. Koh, and B. J. Yi. Active bending endoscope robot system for navigation through sinus area. In *2011 IEEE/RSJ International Conference on Intelligent Robots and Systems*, pages 967–972, Sept 2011.

[94] B. L. Conrad, J. Jung, R. S. Penning, and M. R. Zinn. Interleaved continuum-rigid manipulation: An augmented approach for robotic minimally-invasive flexible catheter-based procedures. In *2013 IEEE International Conference on Robotics and Automation*, pages 718–724, May 2013.

[95] Michael C Yip, Jake A Sganga, and David B Camarillo. Autonomous control of continuum robot manipulators for complex cardiac ablation tasks. *Journal of Medical Robotics Research*, page 1750002, 2016.

[96] Wei Luo, Freddy T Nguyen, Adam M Zysk, Tyler S Ralston, John Brockenbrough, Daniel L Marks, Amy L Oldenburg, and Stephen A Boppart. Optical biopsy of lymph node morphology using optical coherence tomography. *Technology in cancer research & treatment*, 4(5):539–547, 2005.

[97] Olav Egeland. Task-space tracking with redundant manipulators. *IEEE Journal on Robotics and Automation*, 3(5):471–475, 1987.

[98] Agathe Hodac and Roland Y. Siegwart. Decoupled macro/micro-manipulator for fast and precise assembly operations: design and experiments. In Bradley J. Nelson and Jean-Marc Breguet, editors, *Proc. SPIE 3834, Microrobotics and Microassembly*, pages 122–130, aug 1999.

[99] Konrad Entsfellner, Gero Strauss, Thomas Berger, Andreas Dietz, and Tim C. Lueth. Micro-Macro Telemanipulator for Middle-Ear Microsurgery. In *Robotics; Proceedings of ROBOTIK 2012; 7th German Conference on*, pages 1–4, Munich, Germany, 2012. VDE.

[100] S. Abiko and K. Yoshida. On-line parameter identification of a payload handled by flexible based manipulator. In *2004 IEEE/RSJ International Conference on Intelligent Robots and Systems (IROS) (IEEE Cat. No.04CH37566)*, volume 3, pages 2930–2935. IEEE, 2004.

[101] Changhyun Cho, Sungchul Kang, Munsang Kim, and Jae-Bok Song. Macro-micro manipulation with visual tracking and its application to wheel assembly. *International Journal of Control, Automation, and Systems*, 3(3):461–468, 2005.

[102] Jungsik Kim, Farrokh Janabi-Sharifi, and Jung Kim. A physically-based haptic rendering for telemanipulation with visual information: Macro and micro applications. In *2008 IEEE/RSJ International Conference on Intelligent Robots and Systems*, pages 3489–3494. IEEE, sep 2008.

[103] Yuki Nagatsu and Seiichiro Katsura. Macro-micro bilateral control using Kalman filter based state observer for noise reduction and decoupling of modal space. In *IECON 2013 - 39th Annual Conference of the IEEE Industrial Electronics Society*, pages 4192–4197. IEEE, nov 2013.

[104] Vladimir T. Portman, Ben-Zion Sandler, and Eliahu Zahavi. Rigid 6-DOF parallel platform for precision 3-D micromanipulation. *International Journal of Machine Tools and Manufacture*, 41(9):1229–1250, jul 2001.

[105] Moshe Shoham. Twisting wire actuator. *Journal of Mechanical Design*, 127(3):441–445, 2005.

[106] Changhai Rul, Xihua Wang, and Shuxiang Guo. A Novel Tool Using SMA Actuator for cell puncturing. In *SICE Annual Conference 2007*, pages 254–258. IEEE, sep 2007.

[107] Yuan Yun and Yangmin Li. A novel design and analysis of a 3-DOF parallel manipulator for micro/nano manipulation. In *2008 IEEE Workshop on Advanced robotics and Its Social Impacts*, pages 1–6. IEEE, aug 2008.

[108] G. Del Giudice, L. Wang, J. H. Shen, K. Joos, and N. Simaan. Continuum robots for multi-scale motion: Micro-scale motion through equilibrium modulation. In *2017 IEEE/RSJ IROS*, pages 2537–2542, Sept 2017.

[109] Long Wang, Giuseppe Del Giudice, and Nabil Simaan. Simplified kinematics of continuum robot equilibrium modulation via moment coupling effects and model calibration. *ASME JMR*, 11(5), 2019.

[110] H. Xu and B. Sun. X-corner detection based on segment test applied in optical pose tracking system. In *International Symposium on Bioelectronics and Bioinformations 2011*, pages 162–165, Nov 2011.

[111] Bryan A. Jones and Ian D. Walker. Kinematics for Multisection Continuum Robots. *IEEE Transactions on Robotics*, 22(1):43–57, dec 2006.

[112] Bryan A. Jones and Ian D. Walker. Practical Kinematics for Real-Time Implementation of Continuum Robots. *IEEE Transactions on Robotics*, 22(6):1087–1099, dec 2006.

[113] Kai Xu and Nabil Simaan. Analytic Formulation for Kinematics, Statics and Shape Restoration of Multibackbone Continuum Robots via Elliptic Integrals. *Journal of Mechanisms and Robotics*, 2:011006, 2010.

[114] William S Rone and Pinhas Ben-Tzvi. Continuum Manipulator Statics Based on the Principle of Virtual Work. In *Volume 4: Dynamics, Control and Uncertainty, Parts A and B*, page 321. ASME, nov 2012.

[115] D Caleb Rucker and Robert J Webster III. Statics and Dynamics of Continuum Robots With General Tendon Routing and External Loading. *IEEE Trans. Robot.*, 27(6):1033–1044, dec 2011.

[116] Samuel B Kesner and Robert D Howe. Force Control of Flexible Catheter Robots for Beating Heart Surgery. In *2011 IEEE International Conference on Robotics and Automation*, pages 1589–1594, Shanghai, China, jan 2011.

[117] Varun Agrawal, William J Peine, Bin Yao, and Seungwook Choi. Control of Cable Actuated Devices using Smooth Backlash Inverse. In *2010 IEEE International Conference on Robotics and Automation*, pages 1074–1079, Anchorage, AK, 2010.

[118] Kai Xu and Nabil Simaan. Actuation Compensation for Flexible Surgical Snake-like Robots with Redundant Remote Actuation. In *IEEE ICRA*, pages 4148–4154, Orlando Florida, 2006.

[119] Jordan M Croom, D Caleb Rucker, Joseph M Romano, and Robert J. III Webster. Visual Sensing of Continuum Robot Shape Using Self-Organizing Maps. In *2010 IEEE International Conference on Robotics and Automation*, pages 4591–4596, Anchorage, AK, 2010.

[120] David B. Camarillo, Christopher R. Carlson, and J. Kenneth Salisbury. Configuration Tracking for Continuum Manipulators With Coupled Tendon Drive. *IEEE Transactions on Robotics*, 25(4):798–808, aug 2009.

[121] Deepak Trivedi and Christopher D Rahn. Model-Based Shape Estimation for Soft Robotic Manipulators: The Planar Case. *Journal of Mechanisms and Robotics*, 6(2):21005, mar 2014.

[122] Ryan S Penning, Jinwoo Jung, Justin A Borgstadt, Nicola J Ferrier, and R Michael. Towards Closed Loop Control of a Continuum Robotic Manipulator for Medical Applications. In *2011 IEEE International Conference on Robotics and Automation*, pages 4822–4827, Shanghai, China, 2011.

[123] Rajarshi Roy, Long Wang, and Nabil Simaan. Modeling and estimation of friction, extension and coupling effects in multi-segment continuum robots. *IEEE/ASME Transactions on Mechatronics*, 2016.

[124] G. Del Giudice, A. Orekhov, J. H. Shen, K. Joos, and N. Simaan. Investigation of micro-motion kinematics of continuum robots for volumetric oct and oct-guided visual servoing. *IEEE Transactions on Mechatronics*, 2020.

[125] Jian Zhang, Jr. Roland, J. Thomas, Spiros Manolidis, and Nabil Simaan. Optimal Path Planning for Robotic Insertion of Steerable Electrode Arrays in Cochlear Implant Surgery. *ASME J. Med. Devices*, 3(1), 12 2008. 011001.

[126] G. Del Giudice, J. Shen, K. Joos, and N. Simaan. Feasibility of volumetric oct imaging using continuum robots with equilibrium modulation. In *2019 HSMR*, 2019.

[127] K Joos, J Shen, J Kozub, and MS Hutson. Apparatus and method for real-time imaging and monitoring of an electrosurgical procedure, 2014.

[128] JH Shen, J Kozub, R Prasad, and KM Joos. An intraocular OCT probe. In *ARVO*, Fort Lauderdale, Florida, 2011.

[129] Cameron N Riviere, R Scott Rader, and Pradeep K Khosla. Characteristics of hand motion of eye surgeons. In *Proceedings of the 19th Annual International Conference of the IEEE Engineering in Medicine and Biology Society.'Magnificent Milestones and Emerging Opportunities in Medical Engineering'(Cat. No. 97CH36136)*, volume 4, pages 1690–1693. IEEE, 1997.

[130] Wei Wei, Roger Goldman, Nabil Simaan, Howard Fine, and Stanley Chang. Design and theoretical evaluation of micro-surgical manipulators for orbital manipulation and intraocular dexterity. In *Proceedings 2007 IEEE international conference on robotics and automation*, pages 3389–3395. IEEE, 2007.

[131] Haoran Yu, Jin-Hui Hui Shen, Karen M. Joos, and Nabil Simaan. Design, calibration and preliminary testing of a robotic telemanipulator for OCT guided retinal surgery. In *2013 IEEE ICRA*, pages 225–231. IEEE, may 2013.

[132] Thijs Meenink, Gerrit Naus, Marc de Smet, Maarten Beelen, and Maarten Steinbuch. Robot assistance for micrometer precision in vitreoretinal surgery. *Investigative ophthalmology & visual science*, 54(15):5808–5808, 2013.

[133] Steve Charles. Dexterity enhancement in microsurgery using telemicro-robotics. 1994.

[134] Cameron N Riviere, Wei Tech Ang, and Pradeep K Khosla. Toward active tremor canceling in handheld microsurgical instruments. *IEEE Transactions on Robotics and Automation*, 19(5):793–800, 2003.

[135] Russell Taylor, Pat Jensen, Louis Whitcomb, Aaron Barnes, Rajesh Kumar, Dan Stoianovici, Puneet Gupta, ZhengXian Wang, Eugene Dejuan, and Louis Kavoussi. A steady-hand robotic system for microsurgical augmentation. *The International Journal of Robotics Research*, 18(12):1201–1210, 1999.

[136] Gyeong-Woo Cheon, Yong Huang, and Jin U Kang. Active depth-locking handheld micro-injector based on common-path swept source optical coherence tomography. In *Optical Fibers and Sensors for Medical Diagnostics and Treatment Applications XV*, volume 9317, page 93170U. International Society for Optics and Photonics, 2015.

[137] Wei Wei and Nabil Simaan. Modeling, Force Sensing, and Control of Flexible Cannulas for Microstent Delivery. *Journal of Dynamic Systems, Measurement, and Control*, 134(4):041004, 2012.

[138] Mark Draelos, Brenton Keller, Christian Viehland, Oscar M. Carrasco-Zevallos, Anthony Kuo, and Joseph Izatt. Real-time visualization and interaction with static and live optical coherence tomography volumes in immersive virtual reality. *Biomed. Opt. Express*, 9(6):2825–2843, Jun 2018.

[139] Haoran Yu, Jin-Hui Shen, Rohan J. Shah, Nabil Simaan, and Karen M. Joos. Evaluation of microsurgical tasks with OCT-guided and/or robot-assisted ophthalmic forceps. *Biom. Opt. Express*, 6(2):457, feb 2015.

[140] Single fiber optical coherence tomography microsurgical instruments for computer and robot-assisted retinal surgery. 12(Pt 1):108–15, jan 2009.

[141] Wei Wei, Roger E Goldman, Howard F Fine, Stanley Chang, and Nabil Simaan. Performance evaluation for multi-arm manipulation of hollow suspended organs. *IEEE transactions on robotics*, 25(1):147–157, 2008.

[142] Jason R Wilkins, Carmen A Puliafito, Michael R Hee, Jay S Duker, Elias Reichel, Jeffery G Coker, Joel S Schuman, Eric A Swanson, and James G Fujimoto. Characterization of epiretinal membranes using optical coherence tomography. *Ophthalmology*, 103(12):2142–2151, 1996.

[143] S. Jeong, Y. Chitalia, and J. P. Desai. Design, modeling, and control of a coaxially aligned steerable (coast) guidewire robot. *IEEE Robotics and Automation Letters*, 5(3):4947–4954, 2020.

[144] Neel Shihora Rohan Chitale Nabil Simaan Colette Abah, Giuseppe Del Giudice. Towards semi-automated mechanical thrombectomy: Path planning considerations for a double articulated microcatheter. 2019.

[145] Mayank Goyal, Bijoy K Menon, Wim H van Zwam, Diederik WJ Dippel, Peter J Mitchell, Andrew M Demchuk, Antoni Dávalos, Charles BLM Majoie, Aad van der Lugt, Maria A De Miquel, et al. Endovascular thrombectomy after large-vessel ischaemic stroke: a meta-analysis of individual patient data from five randomised trials. *The Lancet*, 387(10029):1723–1731, 2016.

[146] Inessa Bekerman, Paul Gottlieb, and Michael Vaiman. Variations in eyeball diameters of the healthy adults. *Journal of ophthalmology*, 2014, 2014.

[147] Marc-Antoine Lacasse, Genevieve Lachance, Julien Boisclair, Jérémie Ouellet, and Clément Gosselin. On the design of a statically balanced serial robot using remote counterweights. In *2013 IEEE International Conference on Robotics and Automation*, pages 4189–4194. IEEE, 2013.

[148] Abbas Fattah, Sunil K Agrawal, Glenn Catlin, and John Hamnett. Design of a passive gravity-balanced assistive device for sit-to-stand tasks. 2006.

[149] Po-Yang Lin, Win-Bin Shieh, and Dar-Zen Chen. A theoretical study of weight-

balanced mechanisms for design of spring assistive mobile arm support (mas). *Mechanism and Machine Theory*, 61:156–167, 2013.

[150] Simon Lessard, Pascal Bigras, Ilian Bonev, Sébastien Briot, and Vigen Arakelian. Optimum static balancing of a parallel robot for medical 3d-ultrasound imaging. 2007.

[151] Jong-Tae Seo, Jae Hong Woo, Hoon Lim, and Byung-Ju Yi. Design of a new counter-balancing stackable mechanism. In *2014 IEEE International Conference on Robotics and Automation (ICRA)*, pages 2372–2377. IEEE, 2014.

[152] Justus Laurens Herder. *Energy-free Systems. Theory, conception and design of statically*, volume 2. 2001.

[153] Nathan Ulrich and Vijay Kumar. Passive mechanical gravity compensation for robot manipulators. In *Proceedings. 1991 IEEE International Conference on Robotics and Automation*, pages 1536–1537. IEEE Computer Society, 1991.

[154] Po-Yang Lin, Win-Bin Shieh, and Dar-Zen Chen. Design of a gravity-balanced general spatial serial-type manipulator. *Journal of Mechanisms and Robotics*, 2(3), 2010.

[155] Ion Simionescu and Liviu Ciupitu. The static balancing of the industrial robot arms: part i: discrete balancing. *Mechanism and machine theory*, 35(9):1287–1298, 2000.

[156] Ion Simionescu and Liviu Ciupitu. The static balancing of the industrial robot arms: Part ii: Continuous balancing. *Mechanism and machine theory*, 35(9):1299–1311, 2000.

[157] Simon Foucault and Cle´ ment M Gosselin. Synthesis, design, and prototyping of a planar three degree-of-freedom reactionless parallel mechanism. *J. Mech. Des.*, 126(6):992–999, 2004.

[158] I Ebert-Uphoff and K Johnson. Practical considerations for the static balancing of mechanisms of parallel architecture. *Proceedings of the Institution of Mechanical Engineers, Part K: Journal of Multi-body Dynamics*, 216(1):73–85, 2002.

[159] Imme Ebert-Uphoff, Cle´ ment M Gosselin, and Thierry Laliberte´. Static balancing of spatial parallel platform mechanisms—revisited. *J. Mech. Des.*, 122(1):43–51, 2000.

[160] Jason Anthony Pile. *Wire-actuated Parallel Robots for Cochlear Implantation with In-vivo Sensory Feedback*. PhD thesis, Vanderbilt University, 2015.

[161] Toshio Morita, Fumiyoshi Kuribara, Yuki Shiozawa, and Shigeki Sugano. A novel mechanism design for gravity compensation in three dimensional space. In *Advanced Intelligent Mechatronics, 2003. AIM 2003. Proceedings. 2003 IEEE/ASME International Conference on*, volume 1, pages 163–168. IEEE, 2003.

[162] Po-Yang Lin, Win-Bin Shieh, and Dar-Zen Chen. Design of a Gravity-Balanced General Spatial Serial-Type Manipulator. *Journal of Mechanisms and Robotics*, 2(3):031003, 2010.

[163] Chunwoo Kim, Doyoung Chang, Doru Petrisor, Gregory Chirikjian, Misop Han, and Dan Stoianovici. Ultrasound probe and needle-guide calibration for robotic ultrasound scanning and needle targeting. *IEEE transactions on bio-medical engineering*, 60(6):1728–34, jun 2013.

[164] Mathijs Vermeulen and Martijn Wisse. Intrinsically Safe Robot Arm: Adjustable Static Balancing and Low Power Actuation. *International Journal of Social Robotics*, 2(3):275–288, March 2010.

[165] John P. Whitney and Jessica K. Hodgins. A passively safe and gravity-counterbalanced anthropomorphic robot arm. In *2014 IEEE International*

Conference on Robotics and Automation (ICRA), volume 6168, pages 6168–6173. IEEE, may 2014.

[166] Marc Antoine Lacasse, Genevieve Lachance, Julien Boisclair, Jeremie Ouellet, and Clement Gosselin. On the design of a statically balanced serial robot using remote counterweights. *Proceedings - IEEE International Conference on Robotics and Automation*, pages 4189–4194, 2013.

[167] Abbas Fattah, Sunil K Agrawal, Glenn Catlin, and John Hamnett. Design of a passive gravity-balanced assistive device for sit-to-stand tasks. *Journal of Mechanical Design*, 128(5):1122–1129, 2006.

[168] Po Yang Lin, Win Bin Shieh, and Dar Zen Chen. A theoretical study of weight-balanced mechanisms for design of spring assistive mobile arm support (MAS). *Mechanism and Machine Theory*, 61:156–167, 2013.

[169] Simon Lessard, Pascal Bigras, and Ilian a. Bonev. A New Medical Parallel Robot and Its Static Balancing Optimization. *Journal of Medical Devices*, 1(4):272, 2007.

[170] Jong Tae Seo, Jae Hong Woo, Hoon Lim, and Byung Ju Yi. Design of a new counter-balancing stackable mechanism. *Proceedings - IEEE International Conference on Robotics and Automation*, pages 2372–2377, 2014.

[171] Alexandre Lecours and C. M. Gosselin. Reactionless two-degree-of-freedom planar parallel mechanism with variable payload. 2, 2010.

[172] L.Ionita I.Ion M. Ene I.Simionescu, L.Ciupitu. Elastic Systems for Static Balancing of Robot Arms. *13th World Congress in Mechanism and Machine Science, Guanajuato, México, 19-25 June, 2011*, 2011.

[173] T. Laliberté, C.M. Gosselin, and M. Jean. Static balancing of 3-DOF planar parallel mechanisms. *IEEE/ASME Transactions on Mechatronics*, 4(4):363–377, 1999.

[174] Imme Ebert-Uphoff, Clément M Gosselin, and Thierry Laliberte. Static balancing of spatial parallel platform mechanisms—revisited. *Journal of Mechanical Design*, 122(1):43–51, 2000.

[175] I Ebert-Uphoff and K Johnson. Practical considerations for the static balancing of mechanisms of parallel architecture. *Proceedings of the Institution of Mechanical Engineers, Part K: Journal of Multi-body Dynamics*, 216(1):73–85, 2002.

[176] Kenan Koser. A cam mechanism for gravity-balancing. *Mechanics Research Communications*, 36(4):523–530, 2009.

[177] Robert A. MacLachlan, Brian C. Becker, Jaime Cuevas Tabares, Gregg W. Podnar, Louis A. Lobes, and Cameron N. Riviere. Micron: An actively stabilized handheld tool for microsurgery. *IEEE Transactions on Robotics*, 28(1):195–212, 2012.

[178] Burton Paul and J Rosa. Kinematics simulation of serial manipulators. *The International journal of robotics research*, 5(2):14–31, 1986.

[179] Nabil Simaan. *Analysis and synthesis of parallel robots for medical applications*. PhD thesis, Technion-Israel Institute of Technology, Faculty of Mechanical Engineering, 1999.

[180] C. Gosselin and J. Angeles. Singularity analysis of closed-loop kinematic chains. *IEEE Transactions on Robotics and Automation*, 6(3):281–290, 1990.

[181] Xiang Chen, Fugui Xie, and Xin-jun Liu. Singularity analysis of the planar 3-rrr parallel manipulator considering the motion/force transmissibility. In Chun-Yi Su, Subhash Rakheja, and Honghai Liu, editors, *Intelligent Robotics and Applications*, pages 250–260, Berlin, Heidelberg, 2012. Springer Berlin Heidelberg.

[182] J-P Merlet. Democrat: A design methodology for the conception of robot with parallel architecture. In *Proceedings of the 1997 IEEE/RSJ International Conference*

on Intelligent Robot and Systems. Innovative Robotics for Real-World Applications. IROS'97, volume 3, pages 1630–1636. IEEE, 1997.

[183] Louis B Rosenberg. Virtual fixtures as tools to enhance operator performance in telepresence environments. In *Telemanipulator technology and space telerobotics*, volume 2057, pages 10–21. International Society for Optics and Photonics, 1993.

[184] Gabor Fichtinger, Peter Kazanzides, Allison M Okamura, Gregory D Hager, Louis L Whitcomb, and Russell H Taylor. Surgical and interventional robotics: Part ii. *IEEE Robotics & Automation Magazine*, 15(3):94–102, 2008.

[185] K Joos and J Shen. Optical coherence tomography probe, 2011.